Fluidelastic instability in heat exchanger tube arrays and a Galerkin-free model reduction of multiphysics systems

Vilas Shinde

FLUIDELASTIC INSTABILITY IN HEAT EXCHANGER TUBE ARRAYS AND A GALERKIN-FREE MODEL REDUCTION OF MULTIPHYSICS SYSTEMS

Vilas Shinde

IMSIA, EDF-CNRS-CEA-ENSTA ParisTech UMR 9219
Mécaniques, Énergétique et Procédés (MEP)

Université Paris-Saclay

This dissertation is submitted for the degree of

DOCTOR OF PHILOSOPHY

in *Computational Fluid Dynamics*

Defense on 17 December 2015, in front of the jury:

Dr. Cyrille Allery	*Université de La Rochelle, France*	*Rapporteur*
Dr. Alain Dervieux	*INRIA, Sophia Antipolis, France*	*Rapporteur*
Dr. Franck Baj	*CEA, Saclay, France*	*Invited*
Prof. Pierre Sagaut	*M2P2 Laboratory, Marseille, France*	*Examiner*
Assoc. Prof. Stéphane Etienne	*Polytechnique Montréal, Canada*	*Examiner*
Prof. Emer. David Weaver	*McMaster University, Canada*	*Examiner*
Dr. Pascal Hémon	*LadHyX, France*	*Examiner*
Dr. Marianna Braza	*IMFT, Toulouse, France*	*Co-advisor*
Dr. Elisabeth Longatte	*EDF R&D, Chatou, France*	*Advisor*

ÉCOLE POLYTECHNIQUE
UNIVERSITÉ PARIS-SACLAY

cnrs

IMSIA
Institut des Sciences de la Mécanique et Applications Industrielles

Doctoral Dissertation Defense

on

FLUIDELASTIC INSTABILITY IN HEAT EXCHANGER TUBE ARRAYS AND A GALERKIN-FREE MODEL REDUCTION OF MULTIPHYSICS SYSTEMS

by

Vilas Shinde

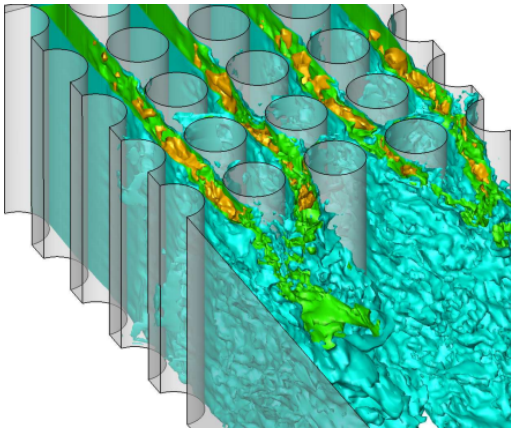

- Thursday, 17 December 2015, 14:00 hrs
- Amphi 2, bâtiment TB, EDF R&D
  1, Avenue du général de Gaulle
  92141 Clamart Cedex

Abstract: Over the last few decades, flow-induced vibrations in heat exchanger tube bundles are studied extensively, especially in order to understand the fluidelastic excitation mechanism. The failure due to fluidelastic instability occurs suddenly, which can pose a serious risk in the plant operations. In this thesis, at first, Computational Fluid Dynamics (CFD) simulations are performed to dynamically predict instability thresholds by using the URANS turbulence modeling. Furthermore, the unsteady nature of the fluidelastic instability is investigated by means of Large Eddy Simulations (LES). A mathematical model for the fluidelastic instability is developed based on the transient interaction between the interstitial flow through an in-line cylinders array and a single cylinder from the array. Secondly, a novel Galerkin-free approach of model reduction for the Navier-Stokes equations is proposed. The method of Galerkin-free ROM is applied to a fluid-structure interaction problem, where the moving mesh is also a part of the solution state vector.

In front of the jury composed of

Dr. Cyrille Allery	*Université de La Rochelle, France*	*Rapporteur*
Dr. Alain Dervieux	*INRIA, Sophia Antipolis, France*	*Rapporteur*
Dr. Franck Baj	*CEA, Saclay, France*	*Invited*
Prof. Pierre Sagaut	*M2P2 Laboratory, Marseille, France*	*Examiner*
Assoc. Prof. Stéphane Etienne	*Polytechnique Montréal, Canada*	*Examiner*
Prof. Emer. David Weaver	*McMaster University, Canada*	*Examiner*
Dr. Pascal Hemon	*LadHyX, France*	*Examiner*
Dr. Marianna Braza	*IMFT, Toulouse, France*	*Co-advisor*
Dr. Elisabeth Longatte	*EDF R&D, Chatou, France*	*Advisor*

Dedicated to the memory of my beloved grandfather
Shri Pralhadrao Kadam,
who taught us to dream and dare.

To raise new questions, new possibilities, to regard old problems from a new angle, requires creative imagination and marks real advance in science.

Albert Einstein

DECLARATION

I hereby declare that except where specific reference is made to the work of others, the contents of this dissertation are original and have not been submitted in whole or in part for consideration for any other degree or qualification in this, or any other University. This dissertation is the result of my own work and includes nothing which is the outcome of work done in collaboration, except where specifically indicated in the text.

Vilas Shinde
17 December 2015

ACKNOWLEDGEMENTS

First, I would like to express my sincere gratitude to my thesis advisers Dr. Elisabeth Longatte, Électricité de France (EDF) and Dr. Franck Baj, Commissariat à l'énergie atomique et aux énergies alternatives (CEA) for their invaluable guidance and continuous support during these years. I owe particular thanks to Dr. Marianna Braza, Institut de Mécanique des Fluides de Toulouse (IMFT), for being my mentor since my master thesis and also for introducing me to the topic of my doctoral thesis.

A special thank to Dr. Patrick Massin, the director of l'Institut des Sciences Mécaniques et Applications Industrielles (IMSIA), for accommodating me in the laboratory. His charismatic personality and remarkable positivity has always been inspiring. I would like to sincerely thank Dr. Marc Boucker, Mécanique des Fluides, Energie et Environnement (MFEE), EDF R&D, Chatou, who provided me timely opportunities to join his team. I thank Mme Marie-Line Cazalon and my fellow labmate Mr. Alexandre Martin for facilitating my work at the IMSIA and the conference travels.

A particular gratitude goes to Dr. Julien Berland, MFEE, EDF R&D, Chatou for his suggestions and cooperation throughout the thesis work. I would like to thank Dr. Enrico Deri and Dr. André Adobes, MFEE, EDF R&D for their guidance and technical discussions. I thank Mr. Jerome Cardolaccia, CEA Saclay for his prompt, informative and practical comments. An extra special thank to him and his colleagues for making the experimental results available.

I wish to express my sincere thanks to Dr. Rémi Bourguet, Massachusetts Institute of Technology (MIT), Cambridge for the technical discussions and guidance. I am thankful to Dr. Yannick Hoarau, ICUBE, Strasbourg and Dr. Thibaut Deloze, AREVA for their kind support in the beginning of this thesis work.

Besides my advisers, I would like to thank the rest of my thesis committee for their invaluable suggestions, which helped me to enrich the thesis content.

I deeply appreciate and acknowledge the financier of the thesis work, Centre national de la recherche scientifique (CNRS) via Agence Nationale de la Recherche (ANR) project Baresafe.

I thank my dear friends Mr. Raju Nimbalkar and Mr. Shrikant Mule for being there for me

and supporting my decisions. Lastly, my heartily thanks go to my parents, *Aai* and *Bappa*, who went through all the sufferings and sacrifices over the years in the pursuit of our education. This work wouldn't have been possible without the support of my loving wife *Namrata* and my adorable brothers *Shrikant* and *Shriniwas*.

ABSTRACT

Heat exchangers are widely used in the power generation industries. The cross-flow type of heat exchangers are more common. The rate of heat transfer is enhanced by operating the heat exchangers at higher flow rates by means of the increased flow turbulence. Although, the high flow rate operations are favoured, there are side effects in terms of the flow-induced vibrations. In the last few decades, the topic (flow induced vibrations in heat exchanger tube bundles) is studied extensively, especially in order to understand the fluidelastic vibration. The preventive measures can be taken in other types of vibration mechanisms, such as the vortex induced vibrations and the acoustic resonance in tube bundles. The turbulence induced vibrations generally take long term to deteriorate the performance of heat exchangers, hence it involves a lesser risk of immediate damage to the heat exchangers. The failure due to the fluidelastic instability occurs suddenly and it can pose a serious risk in the plant operations. Besides the devastating nature of the fluidelastic instability, it is not well understood yet.

In the first part of this thesis, the fluidelastic instability is explored by means of performing numerical simulations. The flow induced vibrations in the heat exchanger tube bundles are reviewed historically. The other mechanisms of vibrations, namely, vortex induced vibrations, turbulent buffeting and acoustic resonance in the tube arrays are briefed. In addition, the theoretical models of the fluidelastic instability are revised in order to understand the different approaches used to model the instability. Computational Fluid Dynamics (CFD) simulations are performed, first by using the Unsteady Reynolds Averaged Navier-Stokes (URANS) approach of modeling the flow turbulence, in order to verify the capability of URANS models to predict the instability thresholds dynamically. Secondly, the transient nature of fluidelastic instability is investigated by means of the Large Eddy Simulations (LES) approach of the turbulence modeling. Although the LES approach is computationally expensive in comparison with the URANS approach, the dynamic interactions between the interstitial fluid flow and a single tube from an in-line tube bundle are well captured by the LES. The post-processing of the LES results is comprised of the dynamics of fluid forces acting on a single cylinder from an array, transient surface pressure profiles on the cylinder and the interstitial velocity flow

fields as a consequence of the increasing flow velocity until the onset of fluidelastic instability. A mathematical model for the fluidelastic instability is developed based on the transient interaction between the interstitial flow through an in-line cylinders array and a single cylinder form the array.

Although there are significant advances in the computers today, the Direct Numerical Simulations (DNS) of large dynamic systems are infeasible. Model reduction also known as Reduced-Order Modeling (ROM) has gained an importance in almost all fields of computational sciences. In the second part of the thesis, firstly, a short introduction to the model order reduction is provided. The Proper Orthogonal Decomposition (POD) and Galerkin projections are commonly used in model reduction of the fluid systems. Almost all reduced-order models derived from the traditional POD-Galerkin ROM require the stability enablers. A novel Galerkin-free approach for model reduction of the Navier-Stokes equations is proposed in this thesis. The method uses the periodicity of the POD time coefficients and a linear interpolation technique in order to construct the off-reference reduced solutions. A test case of the flow past a cylinder at low Reynolds numbers ($Re \sim 125$) is used for the demonstration of the proposed ROM. In the formulation of the proposed Galerkin-free ROM, the variables of a dynamical system are treated independently. Therefore, the method can be conveniently extended for the multi-physics dynamical systems. Lastly, the method of Galerkin-free ROM is applied to a fluid-structure interaction problem, where the moving mesh is a part of the solution state vector. A test case of the vortex induced vibration in a cylinder at Reynolds number $Re = 100$ and the mass ratio as the controlling parameter is considered for the demonstration.

Keywords

Heat exchanger tube arrays, flow induced vibrations, fluidelastic instability, unsteady Reynolds averaged Navier-Stokes turbulence models, large eddy simulations, reduced-order modeling, Navier-Stokes equations, fluid-structure interactions

RÉSUMÉ

Les échangeurs de chaleur sont largement utilisés dans les industries de production d'énergie. Le type d'échangeurs de chaleur à flux croisés sont les plus fréquents. Le taux de transfert de chaleur est amélioré en faisant fonctionner les échangeurs de chaleur à des débits plus élevés au moyen de la turbulence d'écoulement accrue. Bien que, les opérations de débit élevé sont favorisés, il y des effets secondaires en termes de vibrations induites par l'écoulement. Dans les dernières décennies, le sujet (débit vibrations induites dans l'échangeur de chaleur des faisceaux de tubes) a été étudié en profondeur, en particulier afin de comprendre les vibrations fluide-élastique. Des mesures préventives peuvent être prises dans d'autres types de mécanismes de vibration, comme les vibrations induites par vortex et la résonance acoustique dans les faisceaux de tubes. Les vibrations induites par turbulence prennent généralement longtemps à détériorer les structures des échangeurs de chaleur, d'où elle implique un risque moindre de dommages immédiats aux échangeurs de chaleur. L'échec dû à l'instabilité fluide-élastique se produit dans une question d'heures et il peut poser un risque grave dans les opérations de l'usine; alors même que la nature dévastatrice. De l'instabilité fluide-élastique n'est pas encore bien comprise.

Dans la première partie de cette thèse, l'instabilité fluide-élastique est explorée en utilisant des simulations numérique. Les vibrations induites par l'écoulement dans les faisceaux de tubes sont examinés historiquement. Les autres mécanismes de vibrations, à savoir, des vibrations induites par vortex, et par la turbulente et la résonance acoustique dans les faisceaux de tubes sont bien documentés. De plus, les modèles théoriques de l'instabilité fluide-élastique sont examinés. Les simulations de Mécanique des Fluides Numérique (MFN) ou en anglais Computational Fluid Dynamics (CFD) sont réalisées, d'abord en utilisant l'approache Unsteady Reynolds Averaged Navier-Stokes (URANS) pour la modélisation de la turbulence, afin de vérifier la capacité des modèles de URANS à prédire les seuils d'instabilité dynamique. Deuxièmement, la nature transitoire de l'instabilité fluide-élastique est étudiée au moyen de la Simulation Grandes Échelles (Large Eddy Simulation LES) des structure turbulent. Bien que l'approche LES est chère en comparaison avec l'approche URANS, les interactions dy-

namiques entre le flux de liquide interstitiel et un seul tube à partir d'un faisceau de tubes en ligne sont bien capturés par la LES. Le post-traitement des résultats LES composée de la dynamique des forces du fluide agissant sur un seul cylindre dans un groupe, les profils de pression sur le cylindre et les champs d'écoulement de vitesse interstitiels en augmentant la vitesse d'écoulement jusqu'à l'apparition de l'instabilité fluide-élastique. Un modèle mathématique pour l'instabilité fluide-élastique est développé sur la base de l'interaction transitoire entre le débit interstitiel à travers une gamme de cylindres en ligne et une seule forme de cylindre du faisceau.

Bien qu'il y ait des progrès significatifs dans les capacités de calcul, la simulation numérique direct (Direct Numerical Simulation DNS) des grands systémes dynamique sont touhours infaisable. La Réduction de modèles aussi connue comme Reduced Order Modeling (ROM) a acquis une importance dans presque tous les domaines des sciences informatiques. Dans la deuxième partie de la thèse, d'une part, une introduction à la réduction de l'ordre de modèle est fournie. La décomposition en modes propres orthogonaux (Proper Orthogonal Decomposition POD) et les projections de type Galerkin sont couramment utilisées dans la réduction de modèle des écoulement de fluides. Presque tous les modèles d'ordre réduit provenant de la technique POD-Galerkin exigent des l'introduction de stabilisations. Une nouvelle approche de type "Galerkin-free" pour la réduction de modèle des équations de Navier-Stokes est proposée dans cette thèse. La méthode utilise la périodicité des coefficients temporelle de POD et une technique d'interpolation linéaire afin de construire des solutions d'ordre réduit. Le cas test de l'écoulement autour d'un cylindre à faible nombre de Reynolds ($Re \sim 125$) est utilisé pour la démonstration de modéle d'ordre réduit proposé. Dans la formulation de modéle d'ordre réduit "Galerkin-free" POD, les variables d'un système dynamique sont traitées indépendamment. Par conséquent, la méthode peut être facilement étendue aux systèmes dynamiques multi-physiques. Enfin, la technique de Galerkin-free modéle d'ordre réduit est appliquée à un problème d'interaction fluide-structure, où la maille mobile fait partie du vecteur d'état de la solution. Un cas test de vibrations d'induite par vortex d'un cylindre pour un nombre de Reynolds de 100 avec le rapport de masse comme paramètre de contrôle est considéré pour la démonstration.

CONTENTS

List of Figures

List of Tables

PREFACE

Computational Fluid Dynamics (CFD) is a maturing field with applications in a wide range of industries. Generally in industrial applications, the physics of problems are often complex. It involves several phenomena in addition to the flow turbulence such as acoustics, heat transfer, mass transfer, structural vibrations and so on. In such scenarios, an appropriate coupling of the multiple physics is important, besides the principal challenge of modeling the flow turbulence. The number of degrees of freedom involved in such systems grows exponentially, when it comes to take into account the detailed physics of the system. The requirement of computing power and time can be huge, while as in several applications, it is necessary to have a solution within a short amount of time and limited computing resources. The model reduction techniques attempt to reduce the unnecessary degrees of freedom of the high fidelity models and keep only the important features of the system.

The objective of this thesis work is twofold. First, investigation of the flow induced vibrations in the heat exchanger tube bundles, in particular the fluidelastic vibration. Second, model reduction of the fluid-structure interaction problems. In the first part, CFD simulations are performed using both the Unsteady Reynolds Averaged Navier-Stokes (URANS) approach and the Large Eddy Simulations (LES) approach of modeling the flow turbulence. Only single phase flows are considered throughout the work. The fluid-structure interactions are handled by means of an internal coupling between the fluid flow and the solids (the cylindrical tubes of an array). The structures (heat exchanger tubes) are assumed to be rigid and flexibly mounted as the mass on a spring system. The coupling between the fluids and structures is achieved by using the Algebraic Lagrangian Eulerian (ALE) method, which allows large displacements of the computational grid. In the second part, a new method of model reduction is developed for the Navier-Stokes equations. The Proper Orthogonal Decomposition (POD) is used to obtain the basis functions. The method uses a linear interpolation of the reduced basis for the changing control parameter, which leads to a Galerkin-free formulation. Furthermore the Reduced-Order Model (ROM) is extended to fluid-structure interaction problems. Although the test cases considered are in a laminar flow regime, the applicability of the method is in

wide range of multi-physics problems.

The thesis is composed of a total of eight chapters. The first four chapter are dedicated to the flow induced vibrations in tube arrays. The next three chapters are dedicated to the reduced-order modeling. The work is summarized with an outlook in the last chapter. An itemized description of the chapters is provided below.

Chapter 1 **A review on the cross flow induced vibrations and theoretical models of the fluidelastic instability in tube arrays**

The flow induced vibrations in tube bundles and the theoretical models of fluidelastic instability are reviewed in this chapter. The definitions of relevant parameters are provided.

Chapter 2 **Numerical simulation of the flow in tube arrays by using the Unsteady Reynolds Averaged Navier-Stokes turbulence modeling**

The Unsteady Reynolds Averaged Navier-Stokes (URANS) turbulence modeling approach is used to simulate the fluid flow through tube arrays at higher Reynolds numbers ($Re \sim 60000$). The surface pressure profiles on a cylinder from triangular arrays is obtained numerically and compared with the corresponding experimental data. The comparison is done in static configuration between three turbulence models, namely, $k-\varepsilon$ *Linear Production*, $k-\omega$ *Shear Stress Transport* and $k-\varepsilon-\bar{v^2}/k$. A dynamic case of the fluidelastic instability is simulated using the four equation $k-\varepsilon-\bar{v^2}/k$ turbulence model.

Chapter 3 **Analysis of the fluidelastic instability by using the Large Eddy Simulations**

The transient interactions between the interstitial flow in tube arrays and the tubes are simulated by using the Large Eddy Simulation (LES). First, the results are compared with similar experiments. The results are further analysed in order to study the nature of fluidelastic forces acting on a single cylinder oscillating in one degree of freedom (lift direction).

Chapter 4 **A theoretical model of the fluidelastic instability in square inline tube arrays**

The variation of the fluid damping with increasing flow velocity has an effect on the stability thresholds. A theoretical model of fluidelastic instability is derived, taking into account the dynamic interactions between the fluid flow and the array pattern as well as the cylinder oscillations. A relatively simple model in an implicit form of the critical flow velocity under fluidelastic forces is formulated.

Chapter 5 **Introduction to Reduced-Order Modeling**
Model reduction techniques are briefed historically. Mainly, the important definitions are discussed. In addition, the non-linear method of Proper Orthogonal Decomposition (POD) is presented.

Chapter 6 **A Galerkin-free model reduction approach for the Navier-Stokes equations**
A new methodology for building a reduced solution is developed in this chapter. In contrast with the traditional/commonly used POD-Galerkin ROM, the method does not involve the Galerkin projections. The chapter also provides a detailed error and stability analysis of the ROM solution.

Chapter 7 **Model reduction of fluid-structure interactions by using the Galerkin-free POD approach**
The method of Galerkin-free reduced-order modeling, developed in the previous chapter, is extended to fluid-structure interaction problems.

Chapter 8 **Conclusions and outlook**
Finally, concluding remarks and an outlook on the work is provided in the last chapter.

The newly developed Galerkin-free model reduction technique and the results of large eddy simulations (LES) are under review for the publications in journals. The list of research articles produced during the thesis work is provided below.

Journal publications

1. **Shinde, V.**, Marcel, T., Hoarau, Y., Deloze, T., Harran, G., Baj, F., Cardolaccia, J., Magnaud, J.P., Longatte, E., Braza, M., 2014. Numerical simulation of the fluid–structure interaction in a tube array under cross flow at moderate and high Reynolds numbers. Journal of Fluids and Structures 47, 99–113.

2. **Vilas Shinde**, Elisabeth Longatte, Franck Baj, Yannick Hoarau, Marianna Braza, 2015. A Galerkin-free model reduction approach for the Navier-Stokes equations. Journal of Computational Physics. (Accepted)

3. **Vilas Shinde**, Julien Berland, Elisabeth Longatte, Franck Baj, 2015. Analysis of the fluidelastic forces acting on a single cylinder of an in-line tube array using large-eddy simulations. Computers & Fluids. (Submitted)

Conference articles

1. **V. Shinde**, M. Braza, E. Longatte, F. Baj, Y. Hoarau, T. Deloze. Numerical simulation of fluid-structure interaction in square normal cylinder arrays. ERCOFTAC international symposium *Unsteady separation in fluid-structure interaction*. June 17-21, 2013. Mykonos, Greece (Presentation, Paper)

2. **Vilas Shinde**, Elisabeth Longatte, Franck Baj, Marianna Braza, Yannick Hoarau. A model reduction for fluid-structure interaction problems using proper orthogonal decomposition. International Conference on Advanced in Vibrations. March 30-April 1, 2015. Porto, Portugal. (Presentation)

3. **V. Shinde**, E. Longatte, F. Baj, M. Braza, Y. Hoarau. A POD modes interpolation technique for reduced-order modeling of fluid-structure interaction problems. 12e Colloque National en Calcul des Structures. 18-22 Mai 2015. Presqu'île de Giens (Var), France. (Paper, Poster)

4. **Vilas Shinde**, Elisabeth Longatte, Franck Baj. Large Eddy Simulation of fluid-elastic instability in square normal cylinder array. Proceedings of the ASME 2015 Pressure Vessels & Piping Conference. July 19-23 2015. Boston, MA, USA. PVP2015-45136. (Presentation, Paper, Poster)

5. **Vilas Shinde**, Elisabeth Longatte, Franck Baj. LES of cross flow induced vibrations in square normal cylinder array. $22^{ème}$ Congrès Français de Méchanique. 24 au 28 Août 2015. Lyon, France. (Presentation, Paper)

CHAPTER 1

A REVIEW ON THE CROSS FLOW INDUCED VIBRATIONS AND THEORETICAL MODELS OF THE FLUIDELASTIC INSTABILITY IN TUBE ARRAYS

Abstract

The cross-flow induced vibrations in heat exchanger tube bundles are reviewed in this article with a brief introduction to the major types of cross-flow instabilities. Heat exchanger tube bundles in cross-flow arrangements are prone to mainly the vortex induced vibrations, turbulence induced vibrations or turbulent buffeting, acoustic resonance and fluidelastic instability. The later being relatively less understood even though it has a high potential of damage to the tube bundles. The different mechanisms of the fluidelastic instability and associated theoretical developments are presented in brief. In general, the critical flow velocity is expressed as a function of the mass-damping parameter of the tubes in an array. At last, the definitions of the important parameters, namely, tube array orientation, mass, damping, natural frequency of the tubes and critical flow velocity are provided.

Keywords

Heat exchanger tube arrays, flow-induced vibrations, fluidelastic instability

Contents

1.1 Introduction

Heat exchangers are one of the indispensable parts of the process industries, mainly, the power plants, chemical plants and the petroleum refineries. The thermal design of heat exchangers should permit a maximum heat transfer for the main constraints of the space and pressure drop across the equipment. The shell and tube heat exchanger designs are the most common, since they are suited in the high pressure applications (Kakaç et al., 2002). In the shell and tube heat exchangers, as the name suggests, a bundle of tubes is placed in a shell container. Two fluids, one passing through the tubes and the other through the outer shell, exchange the heat through the tube walls. The heat exchange area needs to be maximum for a better efficiency, which justifies the presence of many tubes. In addition, the arrangement of shellside fluid plays an important role in enhancing the heat transfer. The cross-flow arrangement of the shellside fluid results in an increased value of the heat transfer coefficient (film coefficient). Furthermore, it also reduces the deposition of unwanted debris. Although, the heat exchangers operating at high cross-flow velocities are efficient, they give rise to flow induced vibrations.

Flow induced vibrations in heat exchanger tube bundles came into picture in 1960's, after widespread failures reported mostly in the power industry (Nelms and Segaser, 1969). A typical steam generator in a nuclear power plant contains thousands of small diameter tubes with high pressure fluids on either sides. The demand for high efficiency operations makes the tube bundle system susceptible to flow induced vibrations, in addition to the other chronic problems. Since the 60's, the problem of flow induced vibrations has gained an importance because the tube bundles' failure occurred frequently, which has resulted in a huge loss in terms of the lost production cost. Also there are serious safety measures involved, in particular, in the nuclear power stations. Several detailed reviews on the steam generator vibrations are conducted ((Nelms and Segaser, 1969), (Hodge et al., 1974), (Shin and Wambsganss, 1977), (Pettigrew et al., 1978), (Chen, 1978), (Blevins, 1979b), (Païdoussis, 1983a) and (Weaver and Fitzpatrick, 1988a)), which has enhanced the understanding of the mechanisms responsible for the tubes failure. In majority cases, the damage is attributed to the large amplitude vibrations due to fluid flow. The fretting-wear at the baffle contacts and corrosion locations generally acted as an initial point of the breakdown. Figure (1.1) shows damaged tubes due to the excessive flow-induced vibrations. The flow in the parallel (to the tubes axes) configuration is also reported to produce the instabilities, but the cross-flow components of the flow are often held responsible (Païdoussis, 1982). In the steam generators, vibrations due to the tubeside flow are negligible, in comparison with the shellside flow (Shin and Wambsganss, 1977).

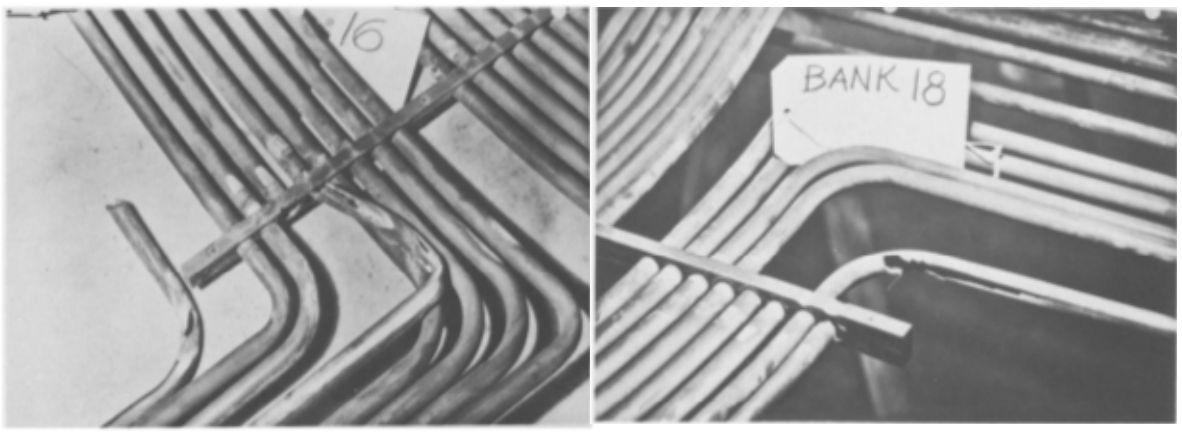

(a) Support bar damage (b) Collision damage

Figure 1.1 Enrico Fermi atomic power plant steam generators. Source:(Shin and Wambsganss, 1977)

1.2 Vibration Mechanisms

The fluid flow through the tube arrays is fairly complex. There exists several excitation mechanisms leading to flow-induced vibrations in tube arrays. Broadly, these are classified as, *Vortex shedding*, *Turbulent buffeting*, *Acoustic resonance* and *Fluidelastic excitations*. In addition, there are other mechanisms which may simultaneously exist, such as the parallel flow turbulent pressure fluctuations, hydraulic noise, structural noise transmitted by the external vibrations, fluctuations in the flow etc.

1.2.1 Vortex shedding / Strouhal periodicity

The fluid flow past a bluff body generates the low pressure alternate vortices behind the body, known as the vortex shedding. The flow past a circular cylinder has been extensively studied physics since a long time. The shedding of vortices results in lift forces in addition to drag forces on the cylinder. The flow depends mainly on the Reynolds number (Re), which is a ratio of fluid inertia forces to viscous forces. The frequency of vortex shedding is normalised by using the flow velocity and cylinder diameter. The resulting dimensionless number is called the Strouhal Number (Sh). Generally the relationships between the forces (drag, lift), Strouhal frequency and the Reynolds number are established empirically. The drag and lift forces beating at Strouhal frequency induce cylinder vibrations in the cylinder. Further, if the Strouhal frequency synchronises with the cylinder's natural frequency, the cylinder resonates and produces large amplitude vibrations, know as vortex-induced vibrations.

The flow through tube arrays forms multiple flow channels passing around the lines (columns) of cylinders. The presence of Strouhal periodicity in tube arrays also results in high amplitude vibrations, when it resonates with the cylinders' natural frequency. The flow instabilities in the tube arrays are largely disputed for the presence of distinct vortex shedding similar to the classical vortex shedding behind a single cylinder. The topic is well reviewed by (Païdoussis, 1983b) and (Weaver and Fitzpatrick, 1988b). Until the early 70's, only the excitations due to vortex shedding were held responsible for the vibrations in tube bundles. The dispute over unanimous values of the Strouhal frequency and its existence in tube arrays led to further investigations of the phenomenon. While summarizing the research work on the existence of vortex shedding in tube arrays, (Païdoussis, 1983b) stated that, the Strouhal periodicity commonly appeared for the first few rows, provided the upstream turbulence had not suppressed it. The appearance of vortex shedding deep within the arrays is found to be dependent on the Reynolds number, array geometry, mechanical properties of the tubes and also the ampli-

tudes of tube vibration. In the later research works, (Weaver et al., 1987), (Fitzpatrick et al., 1988) observed the presence of vortex shedding, if not a flow periodicity even deep within the arrays. In an interesting flow visualization study by (Abd-Rabbo and Weaver, 1986), the development of vortex shedding in arrays is observed similar to the classical vortex shedding behind a single cylinder. The Strouhal periodicity is observed in the closely placed staggered array configurations, which is reported to be absent in the in-line array configurations. Further study on the in-line tube arrays by (Ziada and Oengören, 1992) and (Ziada and Oengören, 1993) has enhanced the understanding of the generation of vortex shedding excitations. The fluid flowing in lanes forms the jet like structures, while the wakes of the cylinders are confined. The vortex-shedding excitations are generated in the first row due to the jet instabilities and persist for couple of rows downstream. The tube pitch ratio and the upstream turbulence has a major impact on the vortex-shedding in the front rows as well as deep in the arrays. The vortex shedding in the staggered (normal triangular) arrangement is studied in (Polak and Weaver, 1995) for various pitch ratios and Reynolds numbers. In a comprehensive work by (Ziada, 2006), the vortex-shedding is shown to be generated by either jet, wake or shear layer instabilities, depending on the tube spacing, upstream turbulence, Reynolds number and the array configuration.

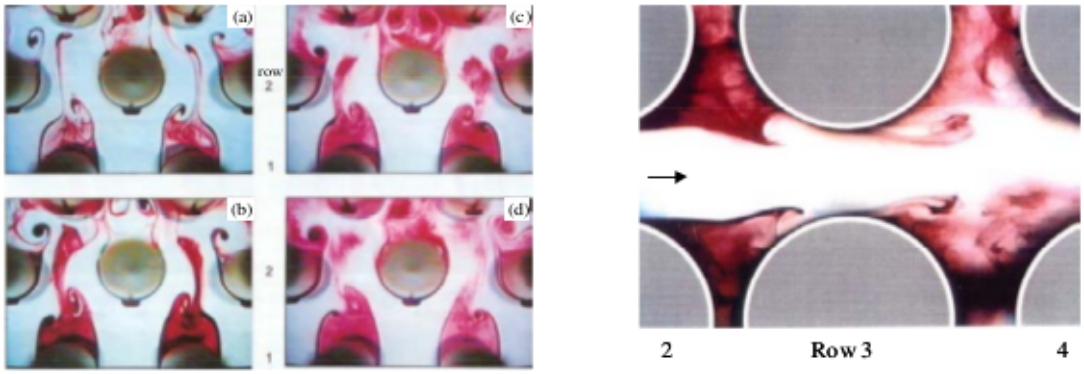

(a) Staggered array (b) In-line array

Figure 1.2 Vortex-shedding in tube arrays. Source: (Ziada, 2006)

Figure (1.2) shows vortex shedding patterns in a staggered and in-line tube array arrangements. The sub-figures in Figure 1.2(a) show the influence of increasing Reynolds number on the flow vorticity. The closely placed cylinders in-line array shown in Figure 1.2(b) shows the shear layer instabilities as the source of Strouhal periodicities.

1.2.2 Turbulent buffeting

The flow in heat exchanger tube arrays is turbulent in almost all industrial configurations. In addition to vortex-shedding / Strouhal periodicity, instabilities due to the flow turbulence are present separately in the flow. They are present in a wide range of frequencies of the flow spectra. If the cylinder natural frequency is in the range of turbulence frequencies, the cylinder is fed with more energy, resulting in high amplitudes of cylinder vibration. The historical development on the topic is provided in the review articles by (Païdoussis, 1983a) and (Weaver and Fitzpatrick, 1988b). The very discussed article by (Owen, 1965) questioned the presence of vortex shedding in the confined arrays. The excitations are attributed to the range of turbulence frequencies and a dominant frequency from the range. The development by (Chen, 1968), is based on the similar concept, but the dominant frequency is used as a vortex shedding frequency. The experimental work by (Weaver and Yeung, 1984) showed the presence of both, the vortex periodicity and the range of turbulence frequencies. Figure (1.3) shows separated peaks for the vortex periodicity and the turbulence range of the spectrum. The experiments were performed in a water tunnel to study the influence of mass ratio on vibrations in all four standard tube bundles with a pitch ratio 1.5. The figure shows a frequency response spectrum for a rotated square array of aluminium tubes and the water flow with an upstream Reynolds number ≈ 1500.

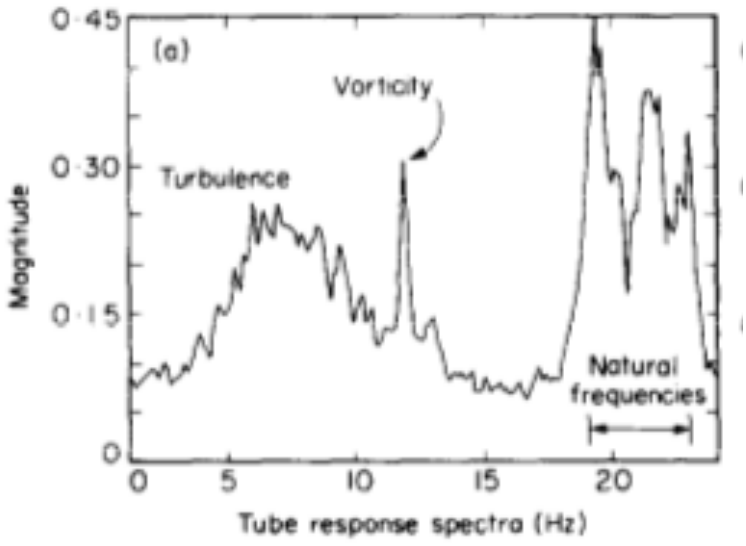

Figure 1.3 Distinct spectral peaks of the vortex shedding and turbulence. Source: (Weaver and Yeung, 1984)

In order to predict the cylinder's vibrational response to the turbulent buffeting, (Pettigrew

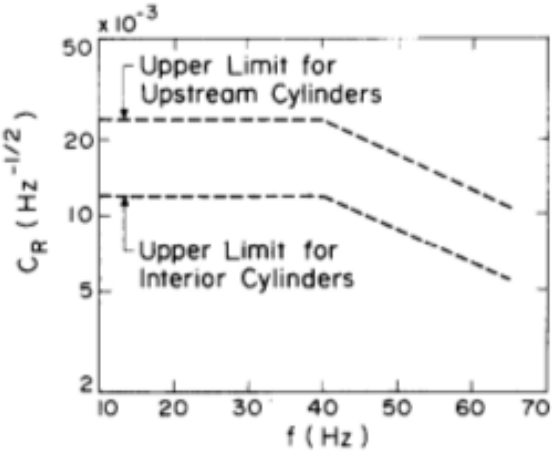

(a) (Pettigrew and Gorman, 1978)

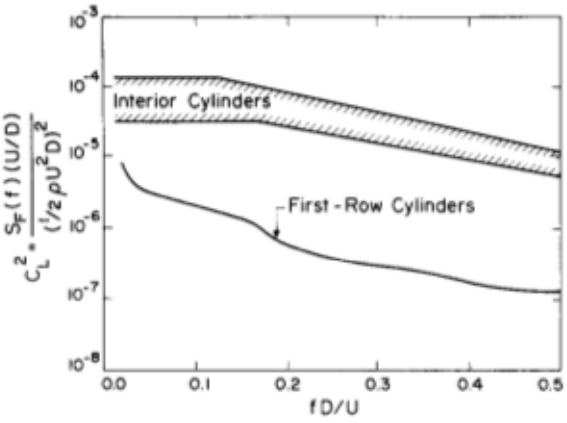

(b) (Blevins et al., 1981)

Figure 1.4 Turbulent correlation coefficients.

and Gorman, 1978) estimated the turbulence spanwise correlations. The random correlation coefficients are used to obtain the power spectral density and thereby the cylinder vibration. On a similar ground, (Blevins et al., 1981) derived an equally simple relation to predict the vibrational response of a cylinder, in a non dimensional form. Figures 1.4(a), 1.4(b) show the plots of random correlation coefficients by (Pettigrew and Gorman, 1978) and (Blevins et al., 1981) respectively. The main difference between Figures 1.4(a) and 1.4(b), as also addressed by (Païdoussis, 1983b), is the difference between the stability limits for the first row or upstream cylinders and the downstream cylinders, which is attributed to the upstream flow turbulence.

In the recent studies on the influence of upstream flow turbulence on the tube array instabilities, (Romberg and Popp, 1998), (Popp and Romberg, 1998) (Rottmann and Popp, 2003) found that, the increased upstream turbulence has a stabilizing effect on the cylinders response. The increase of upstream turbulence intensity resulted in a shift in the instability boundaries of critical velocities to higher values.

1.2.3 Acoustic resonance

The acoustic resonance occurs when the acoustic natural frequencies of the tube bundle shell resonate with the flow periodicity in the tube array. The heat exchanger shells with water like fluids and with compact structures are less susceptible to acoustic resonance, since the speed of sound is relatively high in liquids. On the other hand, the gaseous flows through the tube arrays can undergo acoustic vibration, which may result in an intense magnitude noise. The

phenomenon is briefly reviewed in (Païdoussis, 1983b). Similar to the very vortex shedding and the turbulent buffeting phenomena, the acoustic resonance is also disputed over the source of acoustic excitations, which is discussed in (Weaver and Fitzpatrick, 1988b). An experimental study by (Parker, 1978) showed that the effective speed of the sound reduces because of the presence of tube arrays. Furthermore the acoustic resonance is analysed and compared with the experiments. In (Blevins, 1984), Blevins (1986), it is reported that the vortex shedding acted as a dipole source of the sound. A theoretical development based on Lighthill's analogy is postulated. The acoustic modes of heat exchangers are identified using the finite element technique and compared with experimental data. The acoustic resonance strongly modified the vortex shedding and increased the strength and correlation of the vorticity. In (Fitzpatrick, 1985), the source of acoustic resonance is assumed to be the vortex shedding as well as the turbulent buffeting, in order to predict the flow induced noise. The various methods for predicting the acoustic resonance are compared and design guidelines are formulated in (Ziada and Oengören, 2000) to avoid the acoustic resonance.

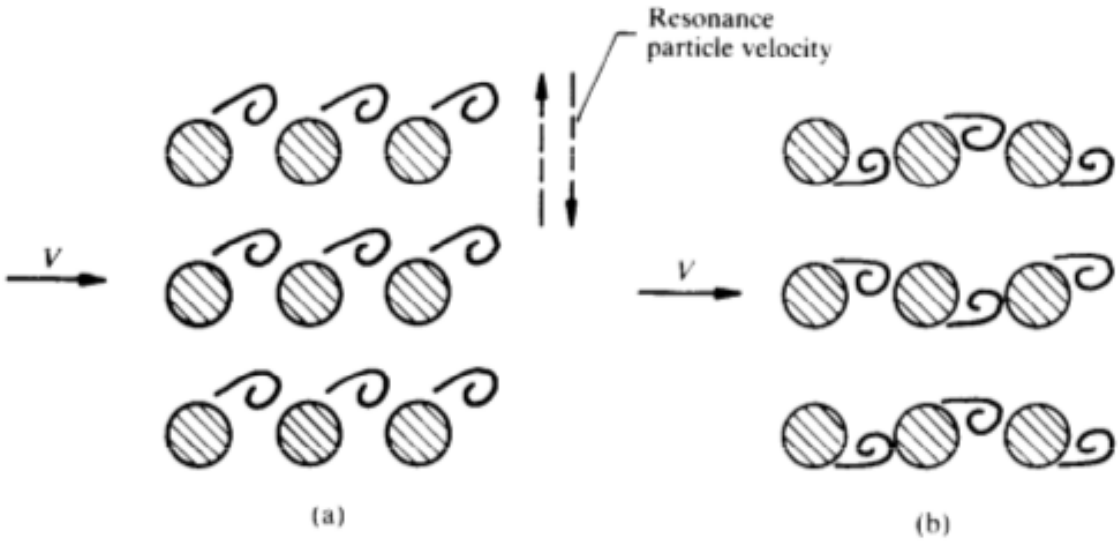

Figure 1.5 Illustration of the vortex shedding under the influence of acoustic resonance. (a) with resonance (b) without resonance. Source: (Ziada and Oengören, 1992)

A comprehensive research work carried out by (Ziada et al., 1989a), (Ziada et al., 1989b), (Oengören and Ziada, 1992), (Ziada et al., 1998), (Ziada and Oengören, 2000) and (Feenstra et al., 2005) has led to an enhanced state of knowledge on the acoustic resonance in tube arrays. The acoustic resonance is studied in both in-line and staggered configurations for different Reynolds numbers and pitch ratios. It is confirmed in (Oengören and Ziada, 1992), that the jet instabilities are responsible for the vortex shedding switch to the shear layer instabilities under

the influence of acoustic resonance. In general, the flow instabilities behind the cylinders are accounted as the excitation source of the acoustic modes in the system. Figure (1.5) shows a schematic illustration of the influence of acoustic resonance (lock-in) on the vortex shedding behind the cylinders. In a recent article, (Ziada, 2006) provided an improved guidelines for the acoustic resonance in tube arrays, detailing its dependence on the tube layout pattern, pitch ratio and Reynolds number. The influence of the acoustic sound field on the lift force in terms of the change in vortex shedding at the onset of acoustic resonance is further studied in (Hanson and Ziada, 2011).

1.2.4 Fluidelastic excitations

The galloping phenomenon of the ice-laden transmission wires due to the wind and the flutter in the aircraft wings are closely linked with the fluidelastic instability in tube arrays. Both the galloping and the flutter instabilities involve either an asymmetry in the associated geometry or/and the interaction with an incident flow with dynamically changing the angle of attack. The fluidelastic instability in tube arrays is also classified under the Movement Induced Vibrations (MIV), since a small movement of the structure (tubes) acts as an origin of the fluidelastic excitations. A small vibration in a tube array excited by the interstitial flow modifies the flow itself and thereby the fluid forces acting on the tubes, which results in the increased vibration, until the array becomes completely unstable. The damage caused by the fluidelastic instability is within a short term and devastating (Weaver and Fitzpatrick, 1988b). Figure (1.6) shows an idealized response of a cylinder from an array under the different excitations mechanisms (Païdoussis, 1983b).

Until the 60's, the flow-induced vibrations due to the fluidelastic instability were attributed to the vortex shedding resonance. In its PhD work (Roberts, 1962), discovered the self-excitation mechanism in a staggered row of cylinders under cross flow, for the vibration in inflow direction. A theoretical development for predicting the critical flow velocity is proposed, which is based on a *jet switching* phenomenon (Roberts, 1966). The flow jet, which is formed due to the cylinders arrangement, oscillates at a relatively lower frequency than the cylinder natural frequency. Later, in the breakthrough work (Connors, 1970), (Connors, 1978) proposed a relatively simple dependency of the critical flow velocity on the structural parameters, i.e. on the mass-damping parameter. The model is developed using a single in-line row of cylinders instead of the staggered arrangement in (Roberts, 1962). (Blevins, 1974) extended the model of (Connors, 1970) for the tube arrays. Although the extended model incorporated the changing damping with respect to the flow velocity, the dependence on the mass-damping parameter remained in the same form. Equation (1.1) is the general form of the fluidelastic

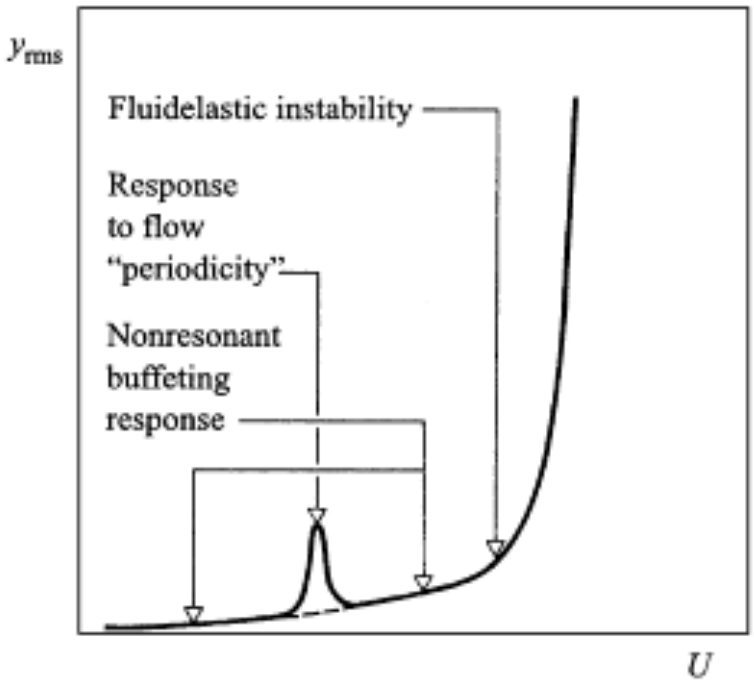

Figure 1.6 Idealized response of a cylinder in an array under cross flow. Source: (Païdoussis et al., 2006)

instability criteria. u_{pc} is the effective critical flow velocity (also called as gap or pitch or intertube velocity). f_n, m and δ represent the cylinder natural frequency, mass of cylinder per unit length and the logarithmic decrement of the cylinder free vibration decrease respectively. Where as D stands for the cylinder diameter. The mechanical variables (f_n, m and δ) can be defined in several ways, but generally they are defined with respect to the fluid medium at rest. K is the constant of proportionality. The exponent a is often taken as 0.5.

$$\frac{u_{pc}}{f_n D} = K\left(\frac{m\delta}{\rho D^2}\right)^a \tag{1.1}$$

A detailed historical development on the topic is reviewed in (Païdoussis, 1983b). The dependence of the critical velocity on the mass-damping parameter is not much disputed, while the value exponent a and the proportionality constant (K) varies depending on configurations. Some of the earlier works is concerned about obtaining an appropriate value of the constant K, e.g. (Pettigrew and Gorman, 1973). (Gibert et al., 1977), (Pettigrew et al., 1978), (Blevins, 1979a). The value of $K_{min} = 3.3$ from the work of (Pettigrew et al., 1978) is widely accepted.

In further investigations for the value of the constant K and in general for the validity of the model (Equation (1.1)) for a wide range of mass-damping parameters, experimental

results showed a wide scatter instead of a single instability boundary as per the Equation (1.1). The experimental work of (Weaver and Lever, 1977) and (Southworth and Zdravkovich, 1975) showed that a single cylinder from an array can become fluidelastically unstable. In the experiments of (Gorman, 1977) the effect of stiffness on the stability limit is tested. In addition to the study on whether the open tube lanes serve as a trigger for the fluidelastic instability is carried out. The results are contradicting with the formulation of (Connors, 1978) (Equation 1.1). Further, in (Weaver and Grover, 1978) the dependence of critical velocity only on the logarithmic decrement is tested, which resulted in a different value of the exponent a for the δ ($a \approx 0.21$). There are many experimental evidences reported against grouping the mass-ratio ($m/\rho D^2$) and logarithmic decrement (δ) together. (Weaver and El-Kashlan, 1981) studied the effect of mass ratio ($m^* = m/\rho D^2$) and damping ratio (ζ) on the instability limits and found different values ($a = 0.29$, $b = 0.21$ respectively for m^* and δ) of the exponents, in a single oscillating cylinder from a rotated/parallel triangular array configuration. In similar studies, (Nicolet et al., 1976), (Heilker and Vincent, 1981), (Chen and Jendrzejcyk, 1981), (Price and Païdoussis, 1989), (Price and Kuran, 1991) obtained different set of values for the exponents in a single as well as multiple oscillating cylinders configurations. (Tanaka et al., 2002) suggested that for the mass ratio $m^* = m/\rho D^2$ smaller than 10, mass and damping should be treated separately.

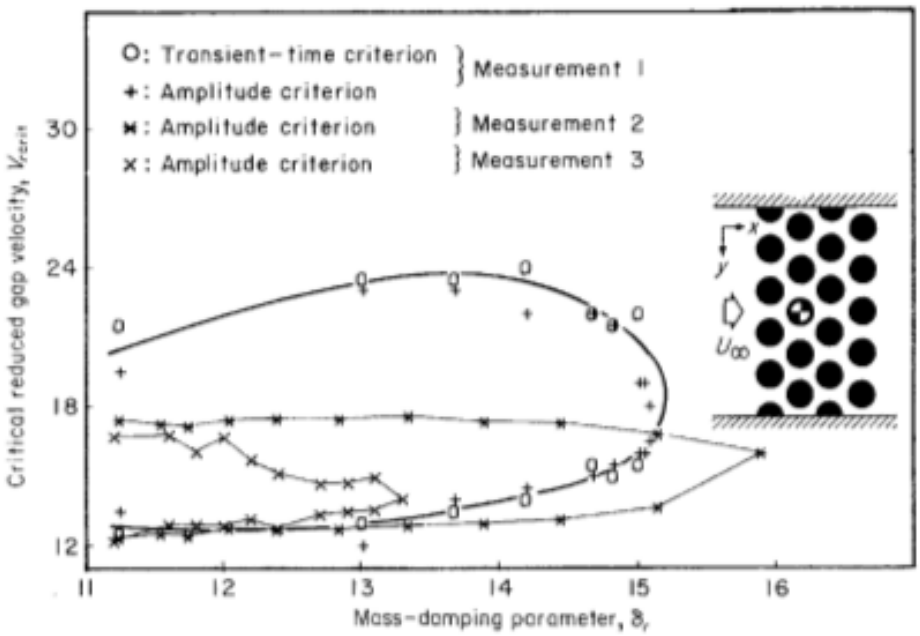

Figure 1.7 Multiple stability limits for a single cylinder from a triangular normal array. Source: (Andjelic and Popp, 1989)

Other set of experiments evidenced the presence of multiple stability limits for a single as well as multiple cylinders from an array, e.g. (Chen and Jendrzejczyk, 1983), (Andjelic and Popp, 1989) and (Austermann and Popp, 1995). The multiple stability boundaries are generally observed for lower values of the mass-damping parameter. This feature of the instability does not reflect in the model of (Connors, 1978) (Equation 1.1). Figure (1.7) shows the multiple stability regions for a single cylinder form a triangular normal array, in the multiple sets of experiments performed by (Andjelic and Popp, 1989).

In attempts to model the fluidelastic instability, several theories have been developed in the past couple of decades, in addition to the pioneering work of (Roberts, 1966) and (Connors, 1978). The parameter space being large, none of the theories holds good in all circumstances. The behaviour of the instability largely changes for different values of the mass-damping parameter. In (Chen, 1983a), the instability is further attributed to the different mechanisms in place, namely, fluidelastic stiffness controlled mechanism and damping controlled mechanism. It is recommended to use difference stability criteria for the different parameter range (Chen, 1983b). In the damping controlled mechanism, the fluid forces act in phase with the velocity of cylinder vibration and there exists a phase lag between the displacement of cylinder and the fluid forces acting on it. The dependence of the instability on phase lag is not fully understood. The finite fluid inertia model by (Lever and Weaver, 1986a) (Lever and Weaver, 1986b), the fluid flow hysteresis effect model by (Price and Païdoussis, 1984), (Granger and Païdoussis, 1996) consider the phase or finite time lag between the fluid forces and the cylinder displacement. In addition to the very clear presence of the multiple stability limits and the independence of the mass ratio and damping ratio in the formation of the mass-damping parameter, there are other parameters that greatly affect the fluidelastic stability limits, namely, orientation of the array, transverse and longitudinal pitch ratios, Reynolds number, position of the cylinder in an array etc. (Chen and Jendrzejcyk, 1981). Further the authors found that the fluidelastic instability may interact with the other excitation mechanisms (e.g. Strouhal periodicity/ Vortex shedding). The flow through tube arrays in steam generators is normally two-phase flow, an additional parameter that influences the stability limits, which can be a separate topic of research in itself and not considered in this study.

1.3 The fluidelastic instability models

The mathematical models of fluidelastic instability can be categorized based on the physical assumptions and methodology used to derive it, namely, jet switch models, quasi-static models, quasi-steady models, semi-analytical models and unsteady models.

1.3.1 Jet switch model

The very first model developed for the fluidelastic instability by (Roberts, 1962) is for a single and a double rows of cylinders in cross flow. It is derived for the instability in the in-flow direction. A slight staggering in the cylinder rows is necessary in developing the wake dynamics and the jet switching instability. Figure 1.8(a) shows the schematic of the jet switch mechanism. The sudden expansion of the flow jet below the separation locations makes it highly transient in nature, while the asymmetry in the geometry creates one small and another big wakes downstream the cylinders. The in-flow oscillations of cylinders favour the jet switching by extracting the energy form the fluidelastic switching of the jet. The author further suggests that the jet switching is possible only if the frequency of jet switching is lower than the cylinder frequency. Further, the occurrence of jet switching is constrained to $u/\omega_n D \geq 2$ condition. Where u, ω_n, D represent the inflow velocity, cylinder angular frequency and its diameter respectively.

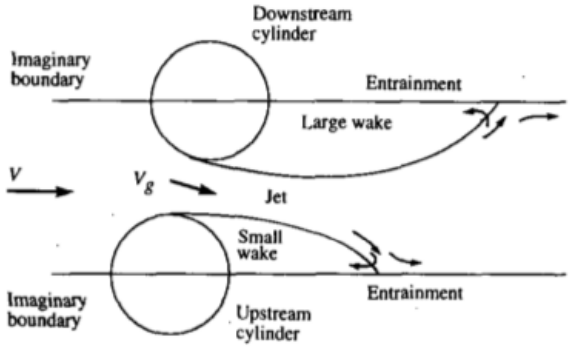

(a) Schematics of Jet-switch mechanism (Roberts, 1962)

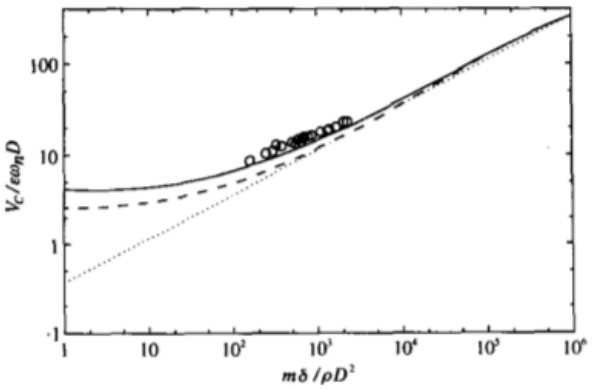

(b) The instability limits by (Roberts, 1966)

Figure 1.8 Schematics of the jet switching mechanism (a) and the instability map of a single cylinder from a row of pitch ratio $p^* = 1.5$ along with the experimental results (b).

The in-flow fluid force as a function of the jet switching mechanism is written as,

$$F_x = \frac{1}{2}\rho u^2 \left\{ 0.717 \left[1 - C_{pb}(x,\tau)\right] - 2\left(\frac{\omega_n D}{u}\right)(1 - C_{pb})_{mean}\frac{dx}{d\tau} \right\} \tag{1.2}$$

Where, C_{pb} represents the theoretical base pressure for the two adjacent cylinders, which is a function of both the displacement (x) and the dimensionless time $\tau = (t\omega_n)$. The solution of the equation of motion by using the in-flow force in Equation (1.2) leads to the stability boundaries as shown in Figure 1.8(b). The simplified form of the solution by neglecting the

damping and unsteady terms from the force F_x leads to,

$$\frac{u_c}{\omega_n \varepsilon D} = K \left(\frac{m\delta}{\rho D^2} \right)^{0.5} \tag{1.3}$$

Where ε represents the ratio of fluidelastic (jet switching) frequency to the cylinders frequency. The symbols, m, ρ and δ stand for the mass per unit length, density of fluid and logarithmic decrement of the cylinder vibration respectively. K is the proportionality constant.

The model shows a poor agreement with the experimental results for the cylinder rows in cross flow (Païdoussis et al., 2010, chap. 5). The model is developed for the motion of cylinders in the in-flow direction, while as the experiments show the dominance of the fluidelastic instability in the flow normal direction. In the theory, instability can not occur if $u_c/\omega_n \varepsilon D \leq 2$.

1.3.2 Quasi-static, quasi-steady models

Similar to Equation (1.3), (Connors, 1970) developed a quasi-static model for the fluidelastic instability in a row of cylinders under cross-flow. The forces (drag and lift) are directly measured by performing experiments. Mainly two types of (whirling) patterns of the adjacent cylinders from a row with pitch ratio $p^* = 1.41$ are observed during real experiments, which are either symmetric or anti-symmetric. The force coefficients are obtained by simulating the dominant patterns of the cylinder oscillations using the static displacement of the adjacent cylinders. In the analysis, the instability found to be more dependent on the transverse direction. Also the effect of jet switching on the instability is found to be negligible. The cross-flow and inflow energy balances based on the measurements led to,

$$\frac{u_{pc}}{f_n D} = K \left(\frac{m\delta}{\rho D^2} \right)^{0.5} \tag{1.4}$$

Where, u_{pc} is the critical pitch velocity, the value of constant $K = 9.9$. In an extension of the model (Equation (1.4)) to the tube arrays, the value of $K = 3.3$ is recommended in (Gorman, 1976) and (Pettigrew et al., 1978). Later, in (Connors, 1978), provided a relation for the value of constant K, in terms of the transverse pitch ratio ($p_y^* = T/D$) as, $K = (0.37 + 1.76 p_y^*)$ for $1.41 < p_y^* < 2.12$. On the same ground, (Blevins, 1974) derived a relation similar to Equation (1.4). The cylinders from a row as well as from an array are assumed to whirl in interdependent orbits, mainly, in out of phase to the adjacent cylinders. The quasi-state formulation resulted

in,

$$\frac{u_{pc}}{f_n D} = \frac{2(2\pi)^{0.5}}{(\overline{C}_x \overline{K}_y)^{0.25}} \left(\frac{m\delta}{\rho D^2} \right)^{0.5} \tag{1.5}$$

Where, $\overline{C}_x = \partial C_x / \partial y$ and $\overline{K}_y = \partial K_y / \partial x$ are the fluid-stiffness terms, provided in the formulation of (Connors, 1970).

In the quasi-steady approach of modeling the interaction between cylinder in motion and fluid around, the instantaneous velocity vector is repositioned for the lift and drag direction, while the effective values of the coefficients are kept the same as in the stationary case. Figure 1.9(a) shows the relative change of the drag and lift directions on a cylinder with a change in the inflow velocity direction. (Blevins, 1979c) used a quasi-steady approach in order to incorporate the effect of the fluid dependent damping in the relation. The logarithmic decrement of the (Connors, 1978) model is given by,

$$\delta = 2\pi \sqrt{\zeta_x \zeta_y} \tag{1.6}$$

where, ζ_x and ζ_y are the damping factors in the inflow x and the cross flow y directions respectively. A considerable work was done by (Whiston and Thomas, 1982), in order to take into account the phase angle between the adjacent cylinders and the details of the intertube flow physics.

(Gross, 1975) used the quasi-steady analysis for the tube arrays, stating that, the instability occurs due to two distinct mechanisms, namely, negative-damping and stiffness controlled. The fluid force is taken proportional to the variation of the lift coefficient linearly with the relative angle between the incident velocity and cylinder position, as shown in Figure 1.9(a). The cylinder is expected to be unstable when the effective damping becomes zero. The model is given as,

$$\frac{u_{pc}}{f_n D} = \frac{m\delta}{\rho D^2 (-\partial C / \partial \alpha)} \tag{1.7}$$

In contrast to the experimental evidences (e.g. (Chen, 1984), (Weaver and Fitzpatrick, 1988b)) the dependence of the critical dimensionless velocity on the mass-damping parameter is linear, against the low values (less than one) of the exponent (a) in the experiments. In the similar analysis, (Price and Païdoussis, 1983) developed a quasi-steady relation between the force and the displacement of a cylinder from the two rows of cylinders. Further, they improved the model by incorporating the dependency of the fluid coefficients on the displacement of the surrounding cylinders by using a constrained modal analysis (Price and Païdoussis, 1986a) as well as importantly, by adding the flow retardation effect in the model (Price and Païdoussis, 1984), (Price and Païdoussis, 1986b). It is suggested that, the instability for the higher values

of mass-damping parameter ($m\delta/\rho D^2$) is stiffness-controlled, on the other hand it is damping controlled for the smaller values of the mass-damping parameter. In an analysis of a single cylinder from an array, the instability is attributed to the negative effective damping of the cylinder, which resulted due to the flow retardation or the phase lag effect. The equation proposed is,

$$\frac{u_{pc}}{f_n D} = \frac{4m\delta/\rho D^2}{(-C_D - \mu D \ \partial C_L/\partial y)} \tag{1.8}$$

where, C_D, C_L are drag and lift coefficients, while μ is the flow retardation parameter. The resulted instability map for different values of the flow retardation is shown in Figure 1.9(b).

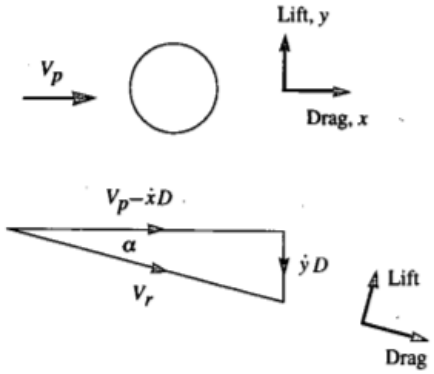

(a) The velocity representation in quasi-steady analysis

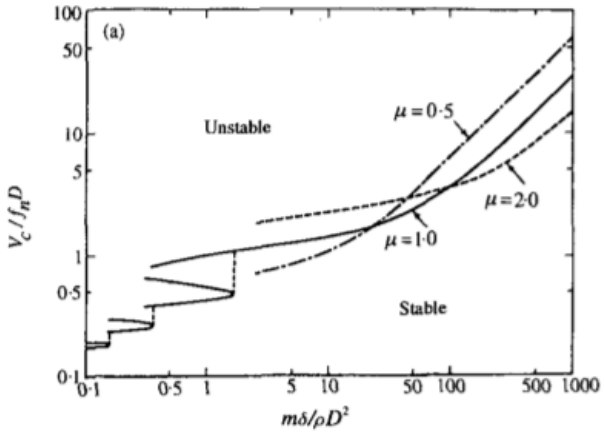

(b) The stability map for a parallel triangular array with $p^* = 1.375$

Figure 1.9 The quasi-steady analysis of (Price and Païdoussis, 1984) (a) velocity representations (b) the stability boundaries for different value of flow retardation parameter.

1.3.3 Semi-analytical models

An analytical approach is adopted in (Lever and Weaver, 1982), in order to model the fluidelastic instability for a single cylinder in an array. It is concluded based on the experimental studies in (Weaver and Grover, 1978) and (Lever and Weaver, 1982) that the instability in a single cylinder is representative for an array since the value of the critical flow velocity remains more of less the same. In addition, the model is developed for the cross flow instabilities only. In the following improvements, (Lever and Weaver, 1986a), (Lever and Weaver, 1986b) incorporated the cylinder motion in the in-flow direction as well, although treated independently. In the model, the authors considered the interactions of the adjacent flow channels with the cylinder displacement. The flow channels are assumed to be inviscid with a resistance term

for the frictional losses. The area of the inviscid stream-tubes is preserved, if it is modified by the movements of the cylinder. The dynamic interaction between the flow tubes and the cylinder displacement resulted in a finite phase lag between the two, due to the fluid inertia. An empirical relation is used to model the phase lag. Figure 1.10(a) shows the idealized flow channels adjacent to the cylinder under consideration.

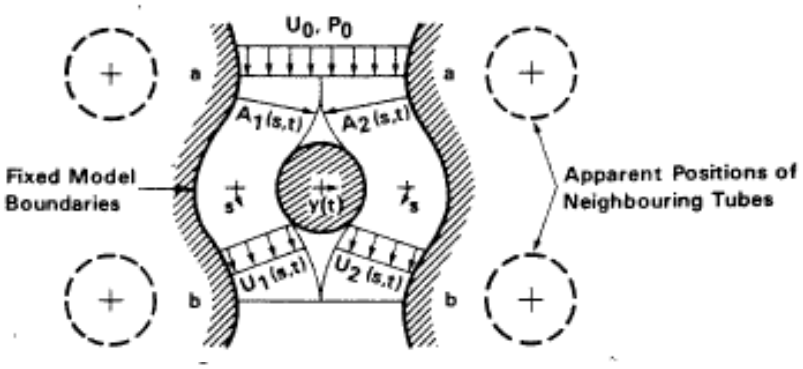

(a) The unit-cell of the model

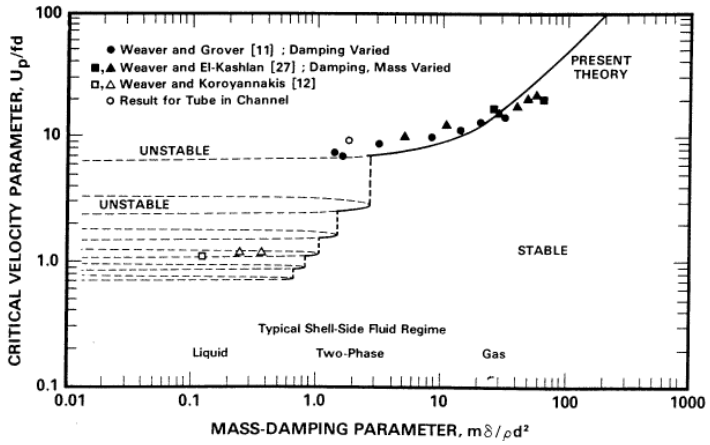

(b) The stability map for a parallel triangular array with $p^* = 1.375$

Figure 1.10 The semi-analytical model of (Lever and Weaver, 1982) (a) flow tubes representations (b) the stability boundaries featuring multiple stable-unstable regions.

The fluid force on the cylinder is derived using the surface pressure for a harmonic vibration in the cylinder, which is decomposed in stiffness and damping terms as,

$$F_p(t) = \underbrace{F_o cos(\theta_o)\frac{y(t)}{y_o}}_{\text{stiffness term}} + \underbrace{F_o sin(\theta_o)\frac{1}{\omega y_o}\frac{dy(t)}{dt}}_{\text{damping term}} \tag{1.9}$$

The damping and stiffness terms of the pressure force $F_p(t)$ (Equation 1.9) are subtracted from

the respective damping and stiffness terms of the motion equation resulting in,

$$lm\frac{d^2y}{dt^2}+\left\{c+\frac{C_D\rho Dlu_o}{2}-\frac{F_o sin(\theta_o)}{\omega y_o}\right\}\frac{dy}{dt}+\left\{k_o-\frac{F_o cos(\theta_o)}{y_o}\right\}y=0 \tag{1.10}$$

where, c is measured damping in still fluid medium and k_o is the structural stiffness. The additional terms in the coefficients of the cylinder velocity and displacement accounts for the flow-induced damping and stiffness respectively. The instability occurs when the effective damping term becomes zero, which leads to the stability criterion in a non-dimensional form for a particular array as,

$$\frac{m\delta}{\rho D^2}+C_1\left(cos(1/u_p^*)-1\right)u^{*3}+C_2 sin(1/u_p^*)u_p^{*2}+\left(C_3+C_4 cos(1/u_p^*)\right)u_p^*=0$$

With

$$u_{pc}^*=C_5u_p^* \tag{1.11}$$

The empirical coefficients C_1 to C_5 are needed for the estimation of the stability threshold. Figure 1.10(b) shows the stability plot for a single cylinder from a triangular array with a pitch ratio $p^*=1.375$. The analytical model in Equation (1.11) shows that the critical reduced velocity is linearly dependent on the mass-damping parameter for high values of the mass-damping parameter, while as the experimental evidence showed the proportionality to be $\left(m\delta/\rho D^2\right)^{0.5}$. The improved versions of the model are proposed in (Yetisir and Weaver, 1988), (Yetisir and Weaver, 1993a), (Yetisir and Weaver, 1993b), taking into account the effect of the neighbouring cylinders. The improved model leads to the exponent 0.5 of the mass-damping parameter as observed experimentally. In these works the interaction between the flow stream tubes and the cylinder are more appropriately taken into account. In a recent attempt, (Khalifa et al., 2013) provided some improvements in the original model by using an empirical phase lag relation based on the Computational Fluid Dynamics (CFD) simulations for a triangular array.

1.3.4 Unsteady models

The unsteady formulation of the fluidelastic models largely depends on the direct experimental measurement of the fluid force coefficients. The dynamic fluid force on a vibrating cylinder in an array is expressed as a function of the intertube flow velocity and the force coefficients for the movements of the neighbouring cylinders. The coefficients are obtained experimentally in order to establish the stability maps. In (Tanaka and Takahara, 1980), (Tanaka and Takahara,

1981) such measurements are performed for an in-line array of pitch ratio $p^* = 1.33$, while as for a similar array with a pitch ratio $p^* = 2.00$ are reported in (Takahara and Ohta, 1982). Figure 1.11(a) shows the cylinders monitored to estimate the model coefficients experimentally. The fluid force on cylinder O (Figure 1.11(a)) is considered to be influenced by the vibrations in the adjacent cylinders (U, R, L, and R) from the same row and column, in addition to the vibration in itself. The total fluid force is considered to be the sum of the inertia due to added mass, damping due to the fluid and stiffness due to the dynamic pressure and displacement.

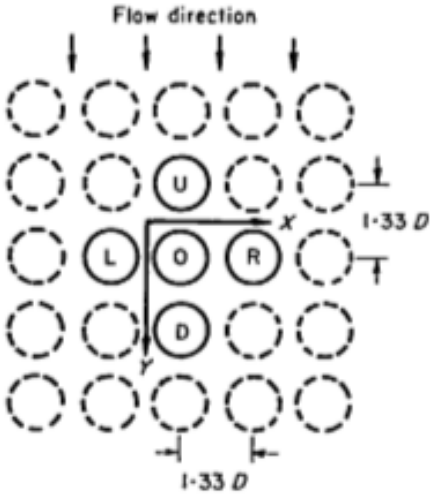

(a) In-line array with $P^* = 1.33$

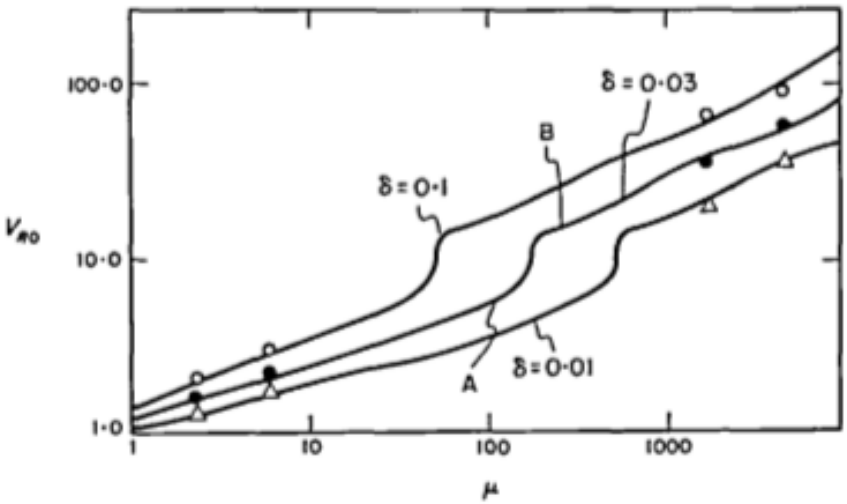

(b) Stability map for different logarithmic damping (δ)

Figure 1.11 The unsteady model of (Tanaka and Takahara, 1981) (a) cylinder array (b) the stability boundaries showing critical reduced velocity against mass ratio ($\mu = m/\rho D^2$) for different values of logarithmic damping (δ).

Further, the fluid force is derived for the steady state motion of the cylinders. The total force on a cylinder is simply the summation of the forces induced by the individual cylinders, since the amplitudes of vibration are assumed small. The total fluid force on cylinder O in Y direction induced by the motion of cylinders O, U, D, L and R is given as,

$$F_Y = \frac{1}{2}\rho u_p^2 \sum_{k=1}^{5} (C_{YkX} X_k + C_{YkY} Y_k) \tag{1.12}$$

where C_{YkX} and C_{YkY} represent the force coefficients in Y direction on the k^{th} cylinder for the motion in X and Y directions respectively. Thus, a coupled system of equations is solved for the monitored cylinders by using the force coefficients measured experimentally. The force is measured experimentally by using the fundamental Fourier coefficients. The measured force is represented in a dimensionless form given as,

$$F = \frac{1}{2}\rho u_p^2 C X_o sin(2\pi f t + \phi) \tag{1.13}$$

where, C is the force coefficient, X_o is the magnitude of imposed displacement, while ϕ represents the phase lag between the displacement and fluid force. The stability map shown in Figure 1.11(b) is established, for a range of mass ratio $1 \leq m/\rho D^2 \leq 10^4$ and different values of the logarithmic decrement δ. It is also pointed out that there exist a discontinuity in the stability boundaries for $50 \leq m/\rho D^2 \leq 500$, indicating the presence of different mechanisms of the instability in these two regions.

(Chen, 1983a) further analysed the instability using the unsteady measurements of forces on the cylinders from a row as well as an array. The presence of two distinct mechanisms of the instability is confirmed. First, similar to the galloping phenomenon resultant of a negative fluid damping, hence called damping-mechanism. Second the flutter type mechanism controlled by the fluid stiffness while the fluid damping is positive. It is called a stiffness mechanism. In addition, (Chen, 1983b) performed an unconstrained analysis for the row and in-line array of cylinders. The presence of multiple stability boundaries for the small values of the mass-damping parameter are uncovered. Also in a discussion on the presence of the discontinuity in the stability boundaries, (Chen, 1983b) attributed it to the sharp change in the phase difference between the fluid forces and cylinder oscillations, rather than to the different mechanisms of the instability. Figure (1.12) shows the stability boundaries and stable-unstable regions as predicted by (Chen, 1983b).

The unsteady models are more reliable in terms of the instability thresholds and investigation of the underlying physics of the fluidelastic instability. On the other had the experimental

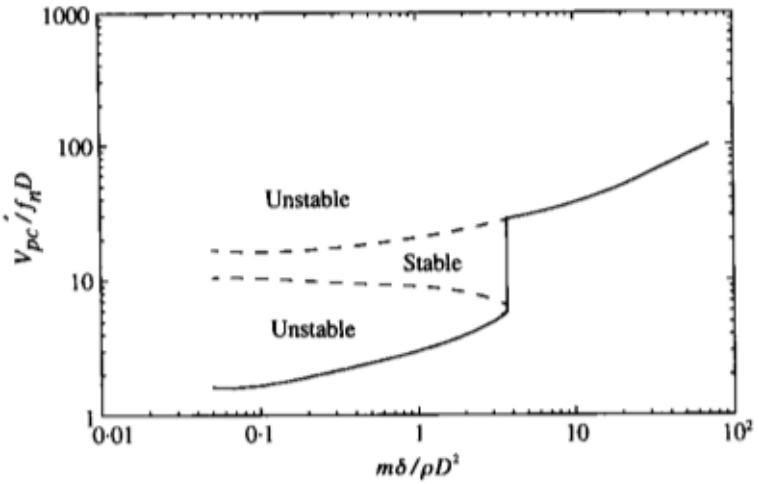

Figure 1.12 The instability limits predicted by (Chen, 1983b) for a row of cylinders ($p^* = 1.33$).

data required is very demanding. In order to reduce these efforts, inverse methods to estimate the forces on cylinders under vibration are developed in (Teh and Goyder, 1981) and (Granger, 1990).

1.4 The parameter space and definitions

The cross flow induced vibrations of tube arrays involve several parameters, mainly, the array orientation, pitch ratio, critical flow velocity, inflow turbulence intensity, tube natural frequency, mass of the tube and damping of the tube vibration. One of the difficulties in comparing different results of the fluidelastic instability threshold is the different definitions of the system parameters. The important parameters and their definitions are discussed in the following section.

1.4.1 Array orientation

There are four principal configurations in which the tube arrays are classified. The physics of the interstitial flow differ with the array configuration and so does the behaviour of the fluidelastic instability. Figure (1.13) shows the four configurations generally used in the design of heat exchangers. Figures 1.13(a) shows a triangular arrangement of the tubes often denoted by 30^o, called as the triangular normal configuration. Rotating the triangular normal array or the inflow direction by 90^o results into the triangular rotated arrangement (60^o), as shown in Figure 1.13(c). Similarly, Figures 1.13(b),(d) show the square arrangements of the tubes in the normal (90^o) and rotated (45^o) configurations respectively. The square arrays Figures

1.13(b),(c) are also known as the parallel configurations, since the flow passage is more-or-less in parallel channels, in comparison with the other two configurations (30^o and 45^o).

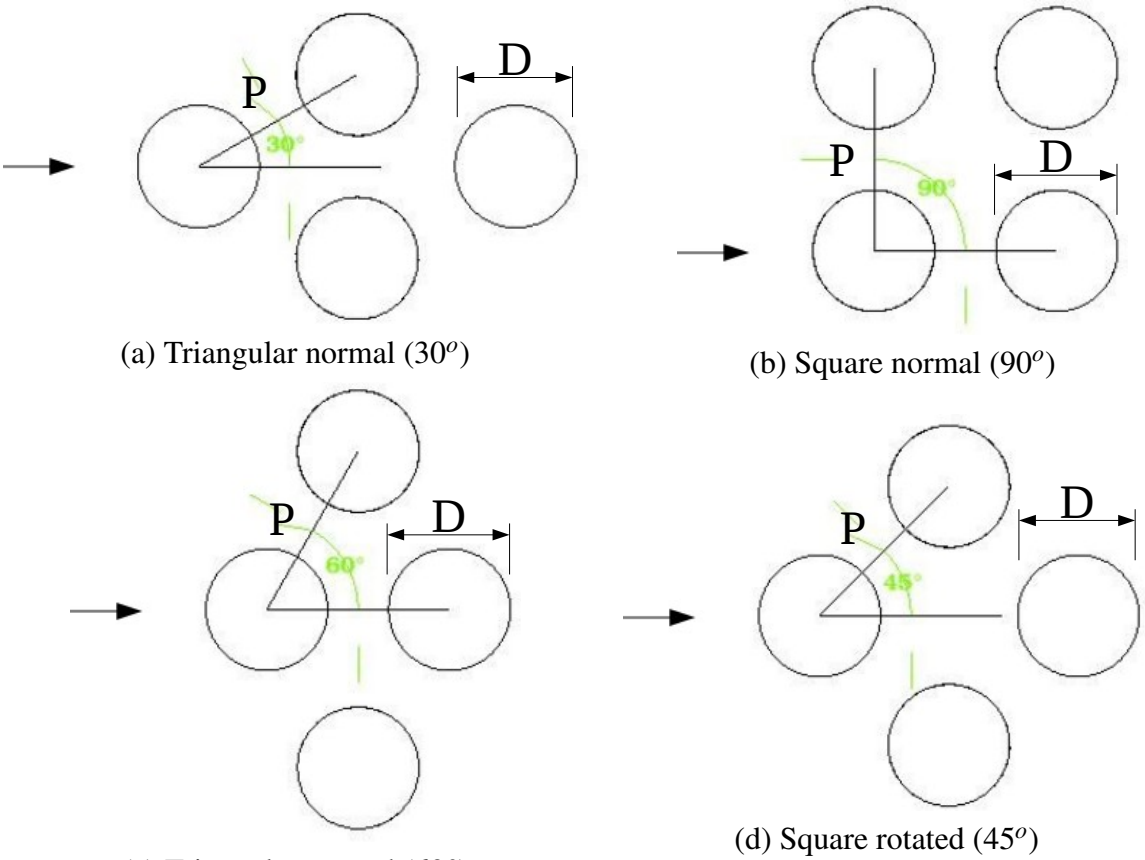

(a) Triangular normal (30^o)

(b) Square normal (90^o)

(c) Triangular rotated (60^o)

(d) Square rotated (45^o)

Figure 1.13 Array Configurations.

The diameter is denoted by D in the Figures 1.13 (a),(b),(c),(d), while as the minimum distance between the two adjacent tubes is called as the pitch distance (P). A non-dimensional pitch is often used, denoted by $p^* = P/D$, also called as a reduced pitch or simply the pitch ratio.

1.4.2 Natural frequency

The free harmonic oscillations are used to estimate the natural frequencies of the tube. The tube can oscillate at several frequencies and in different modes-shapes depending upon its shape and supports. The first natural frequency also known as fundamental frequency is relevant in the cross-flow induced vibration. It is denoted by f_n (or ω_n for angular representation). The value of frequency changes with respect to the surrounding fluid medium and also with

the flow velocity. Although, the value estimated in vacuum (practically in air) remains unchanged for a tube, the value with respect to the fluid medium is more relevant, hence it is commonly used. Further, the frequency f_n varies with the flow velocity, therefore the value used in most of the design guidelines is the frequency in still fluid medium.

1.4.3 Mass of the tube

The mass of the tube is comprised of three quantities, namely, tube material mass, mass of the fluid inside and an additional hydrodynamic mass due to the surrounding fluid medium. The hydrodynamic added mass due to fluid medium is negligible in gases or light weight fluids, while as it needs to be taken into account for heavy fluids. The total/effective mass per unit length m includes the hydrodynamic mass. The motion of the tube in fluid medium is accompanied by the motion of surrounding fluid, which results in to a force on the tube. The hydrodynamic force is taken into account as an additional mass or virtual mass of the tube. A coefficient of the added mass (m_a) is given as,

$$C_m = \frac{m_a}{\rho V} \tag{1.14}$$

where, ρ, V are the fluid density and fluid volume displaced due to tube motion. In the case of a cylinder in an array, the hydrodynamic mass is also influenced by the presence of surrounding tubes. It depends of the pitch ratio (p^*), configuration of the tube array. Figure 1.14(a) shows the effect of pitch ratio and the configuration on the added mass coefficient. The coefficient (C_m) is higher for tightly placed tube arrays (Chen and Chung, 1976), which drops the cylinder natural frequency relatively.

1.4.4 Damping

Damping of the tube vibrations is an important quantity. Also it is the main source of discrepancies in defining the mass-damping parameter. Similar to the mass of the tube, the damping is also categorized in the structural damping and the fluid damping. The commonly used quantity is damping ratio (ζ). It can easily be calculated from the logarithmic decrement (δ) in the vibration time response,

$$\zeta = \frac{1}{\sqrt{1 + \left(\frac{2\pi}{\delta}\right)^2}} \tag{1.15}$$

The values of damping ratio for a tube depends highly on the fluid medium. In addition, the flow velocity has an additional component contributing to the effective damping, usually re-

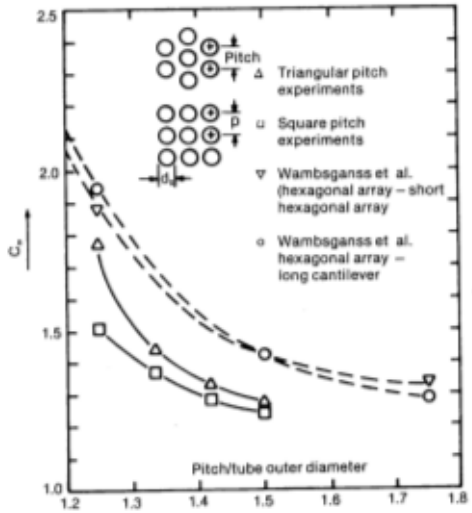

(a) Coefficient of added mass (Moretti and Lowery, 1976)

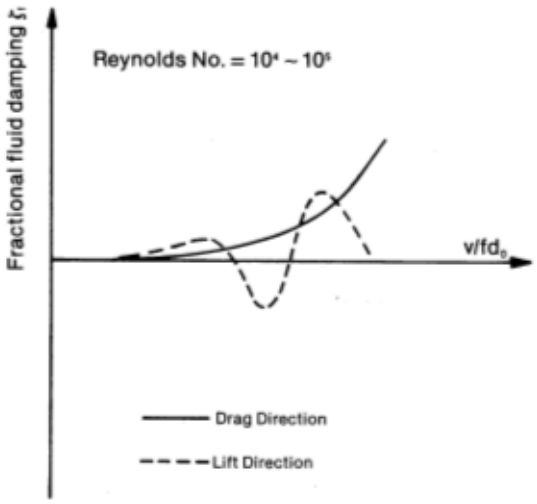

(b) Fluid damping parameter (Singh and Soler, 1984)

Figure 1.14 The coefficients of added mass and damping parameters due to the fluid medium in tube arrays.

ferred as the fluid damping parameter. The dependence of the fluid damping on the natural frequency f_n is studied in (Pettigrew et al., 1973). It is found that the fluid damping decreases with increasing tube natural frequency. In (Chen and Jendrzejcyk, 1981), (Chen and Jendrzejczyk, 1981), the dependence of the damping on flow velocity is studied. The fluid damping is found to increase monotonously in the drag direction, while as in a sinusoidal manner in the lift direction. A general trend of the fractional fluid damping against the reduced velocity is provided in Figure 1.14(b) (Source:(Singh and Soler, 1984)). The sinusoidal trend of the fluid damping in lift direction provides a possibility of total damping becoming zero/negative. The value of effective damping reaching zero is often used as the critical point of the stability limit in the flow-induced vibrations.

1.4.5 The critical flow velocity

The flow velocity between two cylinders of an array separated by the pitch distance (minimum distance) is the characteristic velocity used in the design guidelines for the heat exchanger tube arrays. It is commonly referred as intertube velocity, gap velocity or pitch velocity. The distance between all adjacent cylinders is not necessarily equal, hence sometimes the term gap velocity and the pitch velocity may refer to different quantities. In such cases the minimum gap velocity or the pitch velocity is used. It is denoted by u_p in this work, which stands for

the pitch velocity. The non-dimensional reduced velocity is defined as $u_p^* = u_p/f_n D$ using the tube natural frequency (f_n) and its diameter (D).

In the context of fluidelastic instability, the critical reduced pitch velocity ($u_{pc}^* = u_{pc}/f_n D$) is a velocity beyond which the tube vibration response increases monotonously and suddenly. The value is sometimes obtained by plotting a tangent to the tube response curve a the onset of the fluidelastic instability, as shown in Figure 1.15(a). On the other hand, the critical reduced velocity can be obtained by using a linear extrapolation of the total damping ratio curve for its value to be zero ($\zeta \to 0$). The vibration response is expected to diverge for the negative values of the effective damping ratio. Figure 1.15(b) shows a typical damping response curve of a tube from an array for increasing pitch velocity (u_p).

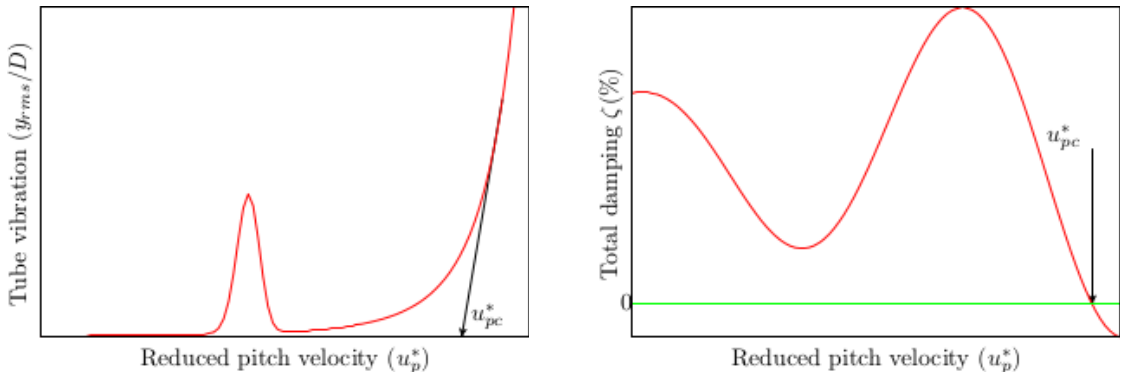

(a) u_{pc}^* based on vibration response (b) u_{pc}^* based on effective damping

Figure 1.15 Critical velocity prediction based on the tube vibration response (y_{rms}) and the effective (total) damping ratio (ζ).

1.5 Conclusion

The flow-induced vibrations in the heat exchanger tube arrays under cross-flow arrangement is reviewed in this article. At the beginning, the major vibration types are briefed, namely, vortex-induced vibration, turbulent buffeting, acoustic resonance and the fluidelastic instability. The damage in the heat exchanger due to turbulent buffeting is long term. On the contrary, the damage due to the fluidelastic instability occurs within a very short time. The fluidelastic instability is explained in terms of the mathematics models used to predict the instability. The unsteady models are more accurate, although they require more experimental data. At last, the definitions of the important parameters for the instability are provided.

CHAPTER 2

NUMERICAL SIMULATION OF THE FLOW IN TUBE ARRAYS BY USING THE UNSTEADY REYNOLDS AVERAGED NAVIER-STOKES TURBULENCE MODELING

Abstract

The unsteady fluid flow through tube arrays is simulated using the Unsteady Reynolds Averaged Navier-Stokes (URANS) turbulence modeling, in 2-D at moderately high Reynolds numbers ($\sim 7 \times 10^4$). At first, a comparison is done between two equation turbulence models ($k-\varepsilon$ Linear Production and $k-\omega$ Shear Stress Transport) and a four equation ($k-\varepsilon-\overline{v^2}/k$) turbulence model. The experimental data published in (Mahon and Meskell, 2009) and (Mahon and Meskell, 2012) are used for the comparison in terms of the azimuthal pressure profile on the cylinder surface. Secondly, a water flow induced vibration of a single tube from a square normal array at $Re \approx 6 \times 10^4$ is simulated using the dynamic Arbitrary Lagrangian Eulerian method. The flow turbulence is modeled using the four equation $k-\varepsilon\overline{v^2}/k$ turbulence model. The tube can vibrate freely in the lift direction only. The value of critical flow velocity shows a fair agreement with the experimental prediction. Although the cylinder response frequency and its damping ratio are in the range of experimental values, variation in these quantities for increasing flow velocities show a poor agreement with the experimental trends.

Keywords

Heat exchanger tube bundles, fluidelastic instability, URANS turbulence modeling

Contents

2.1 Introduction

Cross flow-induced vibrations in heat exchanger tube arrays are investigated since several decades now. In order to explore the exact nature of the fluidelastic instability, many experimental works have been performed in the past (Weaver and Fitzpatrick, 1988a). The fluidelastic mechanism is known to cause a potential damage to the tube bundles in a short span of time (in a matter of hours). The instability and the underlying mechanisms are studied mainly by performing experiments and also by theoretical developments based on the experimental observations. A detailed historical review on the topic is provided in (Païdoussis, 1983a) and recently in (Païdoussis et al., 2010). In addition, due to the recent advent of computers, numerical simulations are performed to study the physics of the fluidelastic instability.

In an industrial configuration, the flow through tube arrays is normally at higher Reynolds numbers. The high Reynolds numbers are also favoured in order to have high rates of heat transfer due to the presence of turbulence. The Direct Numerical Simulations (DNS) of such flows are computationally very expensive and also demand very long time computer simulations. Therefore the DNS are usually restricted to low Reynolds numbers and in general for a small computational domain. The computational efforts are reduced by means of the flow turbulence modeling. The Large Eddy Simulations (LES) approximate the smaller eddies in the flow by means of the turbulent (eddy) viscosity of the flow. In the LES approach, the larger flow turbulence eddies are directly resolved, while the eddies smaller than the computational grid (or the LES filter) are modeled. The approach is inherently 3-dimensional. In the near

wall regions, the computational cost is equivalent to the DNS. The Unsteady Reynolds Averaged Navier-Stokes (URANS) can be used to substantially reduce the computational cost and time. The URANS turbulence models are well suited for the industrial applications, considering the computational resources available and the time constraint. In URANS models, the flow turbulence is completely modeled by means of the Reynolds averaging operation, generally which requires a great deal of validations of the results.

The numerical simulations of the flow through tube arrays are performed using different turbulence modeling approaches. In most cases, the simulations are performed for static configurations (for example (Barsamian and Hassan, 1997), (Rollet-Miet et al., 1999), (Bouris and Bergeles, 1999), (Benhamadouche and Laurence, 2003), (Hassan and Barsamian, 2004), (Liang and Papadakis, 2007), (Li et al., 2014)). The numerical study in (Gillen and Meskell, 2009) carried out to investigate the fluidelastic instability using the quasi-steady modeling approach, where the unsteady dynamic motion of the cylinder is approximated by the static displacements along the path of cylinder motion. In the context of dynamic fluid-structure interaction, the Arbitrary Lagrangian Eulerian (ALE) method is adopted in (Longatte et al., 2003) and (Berland et al., 2014). The ALE method is used to simulate the dynamic interaction between a single cylinder oscillating in 1-degree-of-freedom and the surrounding flow fields. (Kassera and Strohmeier, 1997) performed 2-dimensional simulations using the $k-\omega$ turbulence modeling and found good agreements with experimental results. Although the dynamic interactions are well predicted, there is no clarity on the onset of fluidelastic instability. In (Shinde et al., 2014), the onset of fluidelastic instability, of a 1-DOF single cylinder in 2-D, is predicted by means of URANS simulations.

In the present article, firstly, air flow through a triangular normal and a triangular parallel arrays at Reynolds numbers $\sim 7\times10^4$ is simulated by means of URANS turbulence models in 2-D. URANS models considered for the analysis are the two equation $k-\varepsilon$ Linear Production ($k-\varepsilon LP$), $k-\omega$ Shear Stress Transport ($k-\omega SST$) and the four equation $k-\varepsilon-\bar{v^2}/k$ turbulence models. The configurations of the triangular arrays and the corresponding experimental results used for the comparison are taken from the published data in (Mahon and Meskell, 2009) and (Mahon and Meskell, 2012). The results of different turbulence models are compared mainly in terms of the azimuthal pressure profile on the surface of the cylinder. In the second part, the dynamic fluidelastic instability in a single cylinder from a square array is simulated using the four equation $k-\varepsilon-\bar{v^2}/k$ turbulence model at Reynolds numbers $\sim 6\times10^4$ in 2-D. Similar to the experimental setup, the cylinder can oscillate in the transverse to the flow direction only. The results are compared in terms of the response frequency, effective damping of the cylinder vibration and critical flow velocity.

2.2 Surface pressure profiles in triangular arrays

The quasi-steady model of the fluidelastic instability in tube arrays by Price and Païdoussis (1984) and (Granger and Païdoussis, 1996) assumes that the forces acting on a dynamically vibrating cylinder are the same as those acting on a statically displaced cylinder (with a correction to the direction of inflow velocity) on its oscillation cycle. The quasi-steady model coefficients are measured experimentally for the triangular arrays in (Mahon and Meskell, 2009) and (Mahon and Meskell, 2012). The fluid forces on a statistically displaced cylinder are measured for different configurations at different Reynolds numbers. The experiments also provide a vital data of the azimuthal surface pressure profiles on the cylinder for a realistic Reynolds numbers ($\sim 7 \times 10^4$), which is used here for the comparison.

2.2.1 Experimental and numerical configurations

The experimental data published in ((Mahon and Meskell, 2009), (Mahon and Meskell, 2012)) provide the azimuthal pressure profiles in various configurations. The wind tunnel used for the experiments is $0.7m$ long with test cross sections of $0.3m \times 0.3m$ and $0.3m \times 0.272m$ for triangular normal (30^o) and triangular parallel (60^o) arrays respectively. In the triangular normal configuration, various pitch ratios ($p^* = 1.32, 1.58$ and 1.97) are used for four rows of cylinders, while as in the triangular parallel arrangement, the pitch ratio $p^* = 1.375$ is used. The cylinder diameter is $D = 38 \times 10^{-3}m$ for both configurations. The tests are performed for various intertube Reynolds numbers, $Re \sim 10 \times 10^4$. For further details on the experimental measurements and validations one can refer to ((Mahon and Meskell, 2009), (Mahon and Meskell, 2012)).

Numerical simulations are performed for each, the triangular normal and triangular parallel configurations at Reynolds number $Re \approx 7 \times 10^4$. The pitch ratio used in the triangular normal test case is $p^* = 1.32$. The $2D$ computational domain is about $0.8m$ long with $\sim 0.2m$ upstream and $\sim 0.6m$ downstream the tube array, in both configurations.

Figure 2.1 shows the geometries of the triangular normal (Figure 2.1(a)) and triangular parallel (Figure 2.1(b)) configurations. The computational mesh is shown in Figure 2.2. Figure 2.2(a) shows the details of mesh for the triangular normal configuration, while Figure 2.2(b) shows the mesh details of the triangular parallel arrangement. The near wall region (boundaries of the cylinders) contains high velocity gradients, hence required to mesh appropriately in order to resolve the Reynolds averaged flow boundary layers. This is achieved by placing the first layer of grid at a distance for which the non-dimensional y^+ value is less 1. The y^+

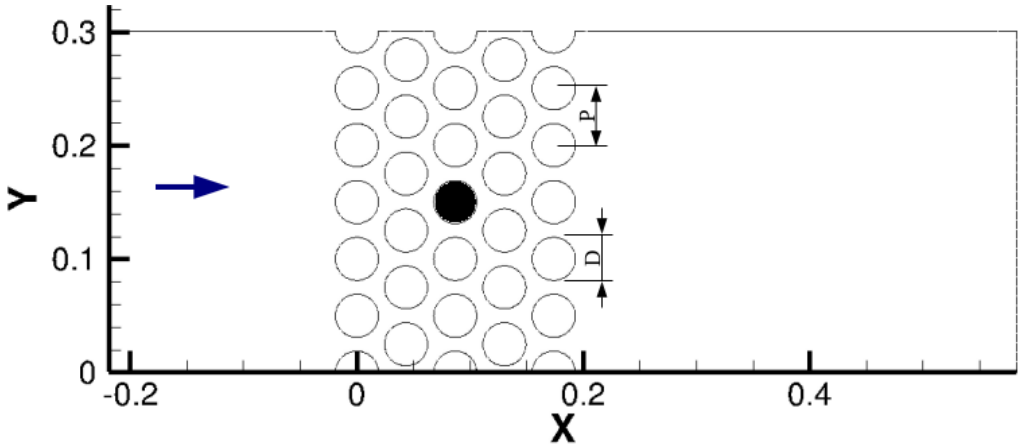

(a) Triangular normal array (30^o)

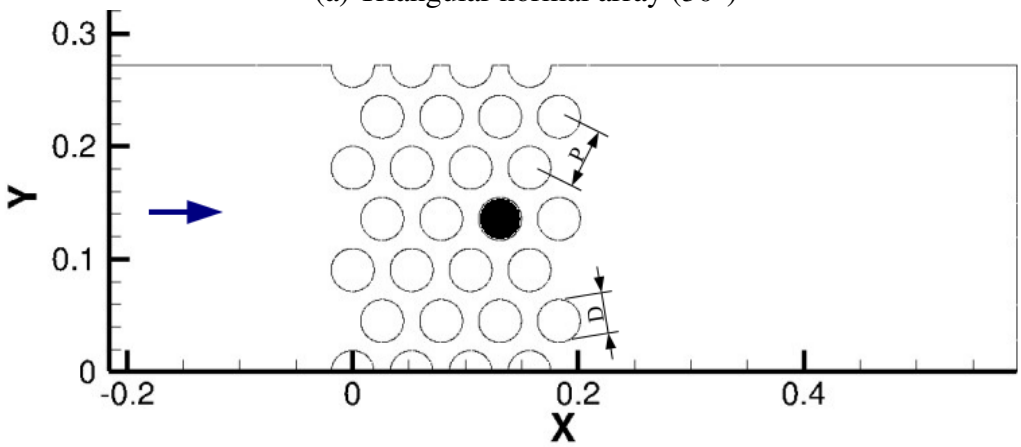

(b) Triangular parallel array (60^o)

Figure 2.1 The computational geometries.

is defined using the fluid kinematic viscosity (ν), actual wall distance (y) and the friction velocity at the wall (u_τ) as $y^+ = yu_\tau/\nu$. In case of the high Reynolds number turbulence models (e..g. $k-\varepsilon$ Linear Production), the boundary layer region is modeled using wall functions. The wall functions provide the values of velocity in the near wall regions for $y^+ \lessapprox 30$, which is approximately in the log region of the boundary layers. The $k-\omega$ *SST* and $k-\varepsilon-\overline{v^2}/k$ are the Low Reynolds number models, which means the near wall boundary layer region is completely descretized by placing the first layer of the mesh below $y^+ = 1$. In addition to the first mesh points, the gradient in the flow velocity needs to be well captured. Thus the mesh size increment away from the wall is usually kept less than 20%.

The simulations are performed using *Code_Saturne*, an open source code developed by Électricité de France (EDF). The code employs co-located finite volume method to solve the Navier-Stokes equations in the incompressible formulation. The calculation are performed

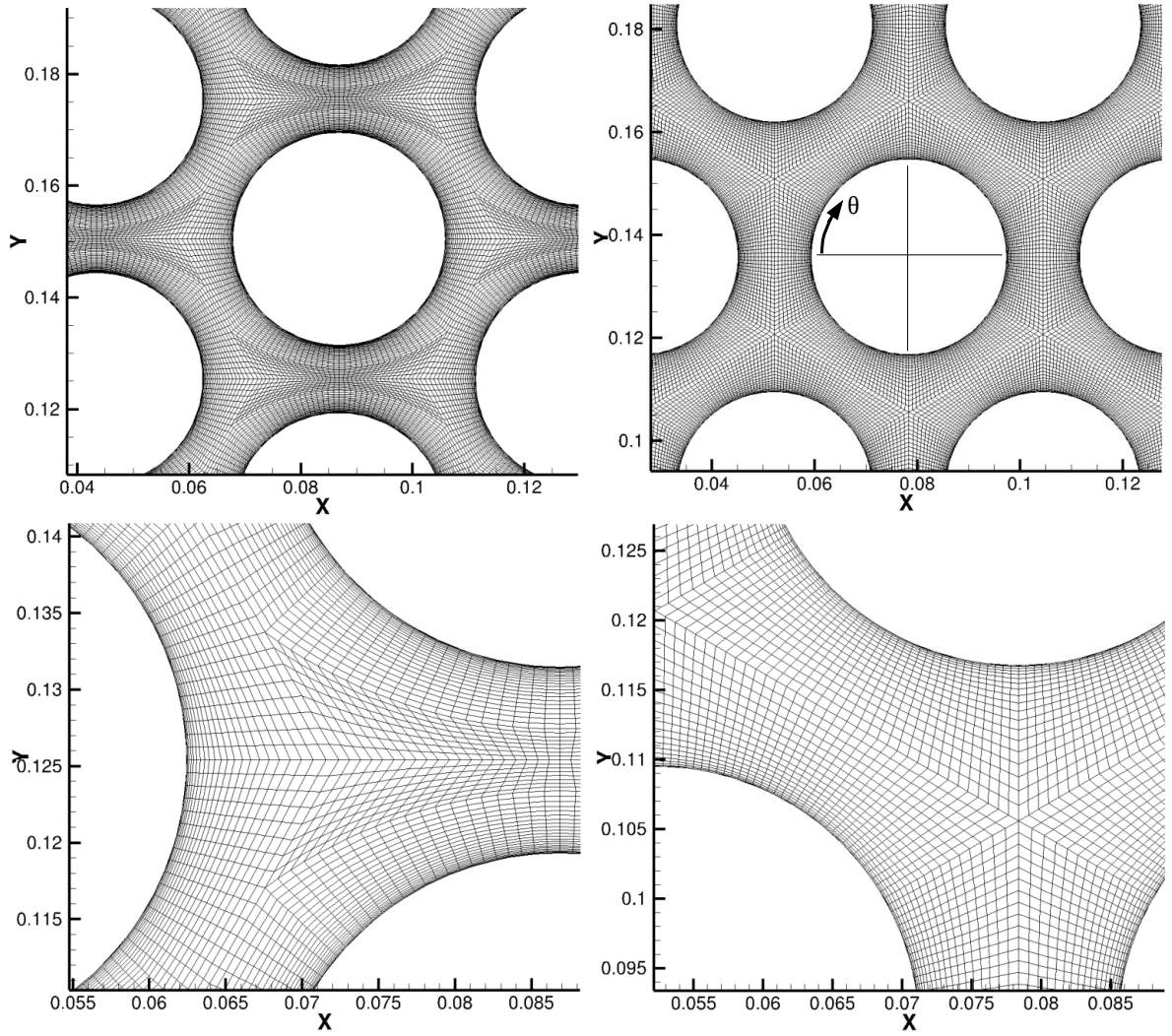

(a) Triangular normal array (30^o)

(b) Triangular parallel array (60^o)

Figure 2.2 Details of the computational meshes.

using a second order central difference scheme for the space discretization and a Cranck-Nicolson method of the time marching. The inlet of computation domain is the Dirichlet boundary condition with a specified constant inflow velocity. The outlet corresponds to a homogeneous Neumann boundary condition for the velocity, while the Dirichlet boundary condition for pressure is employed at the outlet such that $\frac{\partial^2 P}{\partial n \partial \tau} = 0$ for any vector τ collinear with the outlet. P is the pressure and n is the normal to boundary face. The side walls with half wall-mounted cylinder are the no-slip wall boundaries.

Table 2.1 shows the details of the two configurations simulated. $TN30$ and $TP60$ stand for the triangular normal (30^o) and triangular parallel (60^o) respectively. 'Mesh1' and 'Mesh2' are the meshes corresponding to the low Reynolds numbers ($k-\varepsilon-\overline{v^2}/k$ and $k-\omega$) turbu-

Array	pitch ratio (p^*)	u_∞ (m/s)	u_p (m/s)	Re_p	Mesh1	Mesh2
TN30	1.32	7	29.2	7.82×10^4	166370	71792
TP60	1.372	7	25.7	6.88×10^4	165544	57546

Table 2.1 Simulation details.

lence models and the high Reynolds numbers ($k-\varepsilon$ Linear Production) turbulence models respectively.

2.2.2 Results and discussion

The results are mainly comprised of the time averaged pressure profiles on cylinder surface. Furthermore, in addition to the drag and lift coefficients, the instantaneous flow fields are compared between the three turbulence models.

Figure 2.3 shows a comparison of the experimental time-averaged surface pressure profile on cylinder form the triangular tube array with the pressure profiles obtained by using URANS turbulence models. The figure also shows the instantaneous flow fields obtained by the three turbulent models. Figure 2.3(a) shows the azimuthal pressure profiles in terms of the pressure coefficient $C_p(\theta)$ for the three turbulence models in comparison with the experimental data ((Mahon and Meskell, 2009)). The pressure coefficient $C_p(\theta)$ is defined as in the experiments,

$$C_p(\theta) = 1 - \frac{p_{\theta max} - p_\theta}{\frac{1}{2}\rho u_p^2}$$

Where, ρ is air density, u_p represents the gap velocity, while p stands for static pressure. Similar to the experiments, the middle cylinder from the third row is used for measuring the azimuthal surface pressure profile. The convention for the azimuthal position θ on the cylinder surface is shown in Figure 2.2(b) (top figure). The turbulence models $k-\varepsilon$ *LP*, $k-\omega$ *SST* and the $k-\varepsilon-\overline{v^2}/k$ predict the averaged separation locations at $\pm 90^o$, which is in agreement with the experiments. At the locations of flow separation, the pressure coefficient $C_p(\theta)$ is over predicted by the $k-\varepsilon$ *LP* model, while it is underpredicted by the $k-\omega$ *SST*. The $k-\varepsilon-\overline{v^2}/k$ model appears to perform better.

The experimental results show a bistable nature of the flow, which is reported in terms of the two modes of cylinder surface pressure values. The bistable nature of the flow is observed for a higher pitch ratio $p^* = 1.58$. The bistable behaviour of the flow is generally attributed to the mechanism of jet switching (Roberts, 1966) in the flow through tube arrays. At pitch ratio

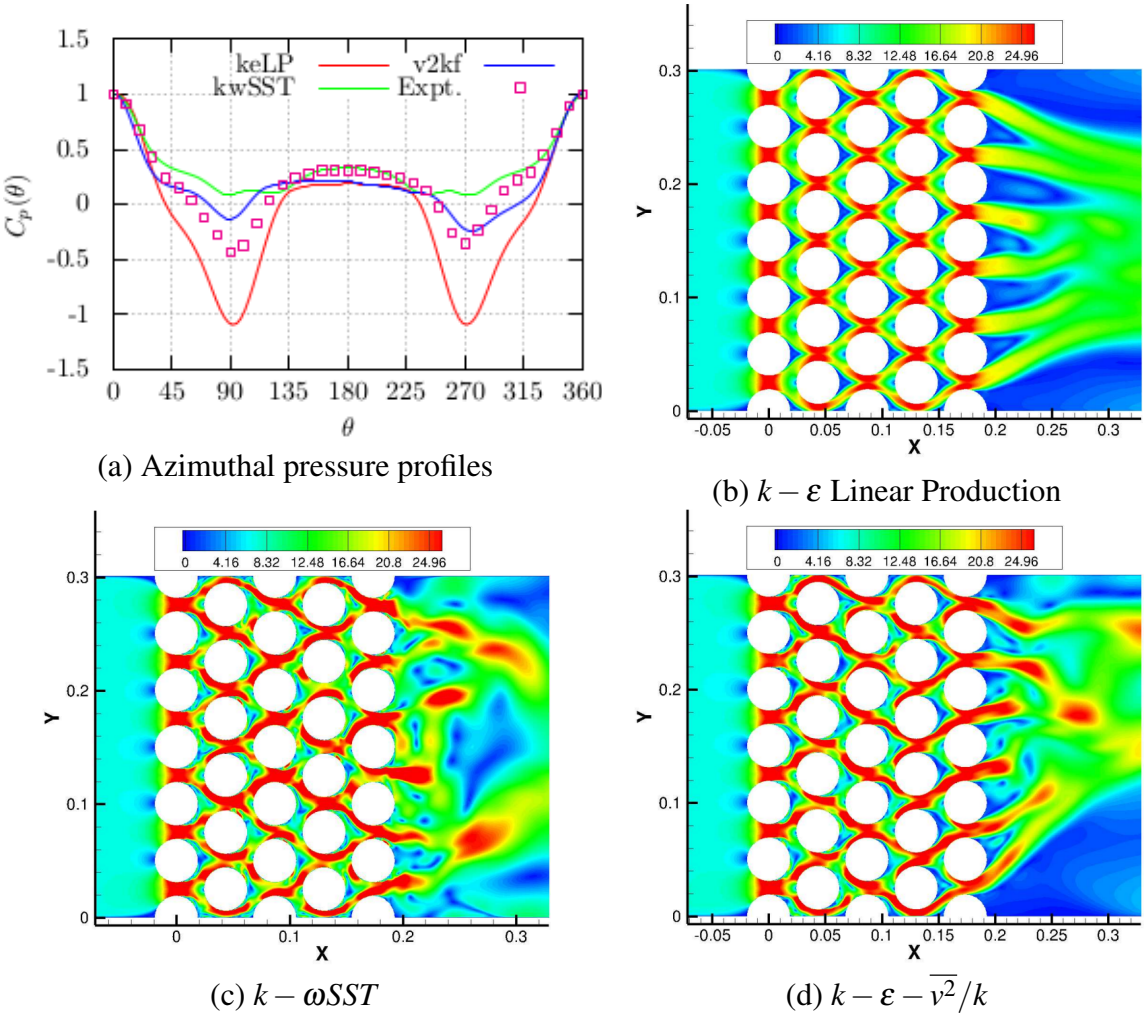

(a) Azimuthal pressure profiles

(b) $k-\varepsilon$ Linear Production

(c) $k-\omega SST$

(d) $k-\varepsilon-\overline{v^2}/k$

Figure 2.3 Comparison of the time averaged pressure profiles and the instantaneous velocity fields in the triangular normal tube array.

$p^* = 1.32$ the pressure profiles are still symmetrical. The instantaneous flow fields predicted by the $k-\omega$ *SST* and $k-\varepsilon-\overline{v^2}/k$ represent the turbulent flow structures, when compared with the flow field obtained with the $k-\varepsilon$ *LP* model (Figures 2.3(b), (c) and (d)).

The cross flow through the triangular parallel array in (Mahon and Meskell, 2012) shows a dominant presence of the jet switching. The time period associated with the bi-stable modes (jet switching) is of the order of tens of second. The time averaged surface pressure profiles in Figure 2.4 are nearly symmetric about $\theta = 180^o$. The surface pressure profile obtained by $k-\varepsilon-\overline{v^2}/k$ model shows a slight asymmetry at the attachment locations, indicating the time $50s$, used for the time averaging, is probably still not sufficient. The time averaged values of the separation and attachment locations are in agreement with the experimental data. The experimental pressure coefficient $C_p(\theta)$ profile in the rear of the cylinder ($90 \lessapprox \theta \lessapprox 270$)

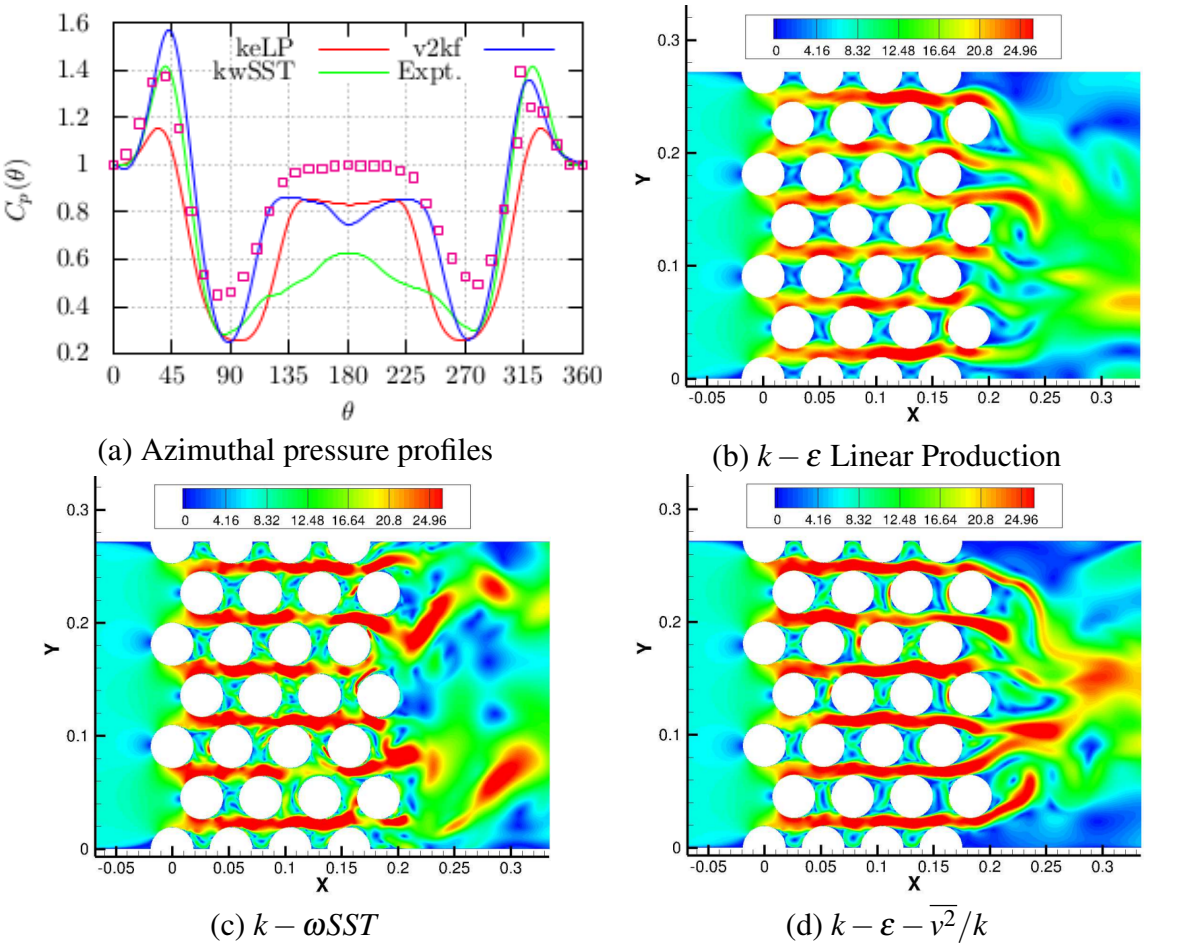

(a) Azimuthal pressure profiles

(b) $k-\varepsilon$ Linear Production

(c) $k-\omega SST$

(d) $k-\varepsilon-\overline{v^2}/k$

Figure 2.4 Comparison of the time averaged pressure profiles data and instantaneous velocity fields in triangular parallel tube array.

shows a considerable difference when compared with the pressure coefficient predicted by the $k-\omega$ *SST* model. Although, the pressure profile ($C_P(\theta)$) is more or less well captured by the $k-\varepsilon$ *LP* model, it underestimates the values by $\approx 20\%$. The $k-\varepsilon-\overline{v^2}/k$ model also overshoots at the separation locations and underpredicts the pressure coefficient near $\theta \approx 180^o$.

The drag and lift coefficients are estimated respectively as,

$$C_D = \frac{F_D}{\frac{1}{2}\rho D u_p^2} = \frac{\int_0^{2\pi} pDcos(\theta)d\theta}{\frac{1}{2}\rho D u_p^2} \quad \text{and} \quad C_L = \frac{F_L}{\frac{1}{2}\rho D u_p^2} = \frac{\int_0^{2\pi} pDsin(\theta)d\theta}{\frac{1}{2}\rho D u_p^2}$$

Table 2.2 shows a quantitative comparison of drag and lift coefficients estimated using the three turbulence models for both the triangular normal and triangular parallel tube arrays with the experimental values. The $k-\omega$ *SST* appears to predict the drag and lift coefficients close

	TN30 C_D	TN30 C_L	TP60 C_D	TP60 C_L
Experiments	0.52	0.0125	0.248	0.025
$k-\varepsilon$ *LP*	0.139	0.000	0.209	0.000
$k-\omega$ *SST*	0.449	-0.008	0.54	0.01
$k-\varepsilon-\overline{v^2}/k$	0.287	-0.107	0.319	-0.045

Table 2.2 Drag and Lift coefficients.

to the experimental data. Contrary, in Figures 2.3(a) and 2.4(a), the experimental pressure profiles are relatively better predicted by the simulations performed using the $k-\varepsilon-\overline{v^2}/k$ turbulence model.

2.3 Dynamic simulation of the fluidelastic instability in a single cylinder of an in-line tube array

A single cylinder from a square array vibrating in only lift direction is simulated using the $k-\varepsilon-\overline{v^2}/k$ turbulence model in 2-D. The interaction between the cylinder and the fluid flow is simulated dynamically by means of the Arbitrary Lagrangian Eulerian (ALE) method. The Reynolds number varies approximately from 1.5×10^4 to $\sim 5.1\times10^4$ at the onset of fluidelastic instability. The numerical results are compared with the experimental results in the same configuration. The results are analysed and compared in terms of the cylinder response frequency, effective damping, oscillation amplitudes and the critical flow velocity.

2.3.1 Experimental and numerical configurations

The experiments are facilitated by the Commissariat à l'énergie atomique et aux énergies alternatives (CEA) via its RESEDA mechanical testing platform. The experimental mockup is shown in Figure (2.5). The tube bundle consists of 5 rows and 5 columns of circular tubes located in the vertical flow channel. The two outer columns are half wall mounted cylinders also named dummy cylinders. As shown in the figure, the cylinders are in a square normal arrangement. All cylinders are rigid and fixed except, the central cylinder, which is flexibly mounted. The central cylinder is supported on a flexible blade at one end. It is allowed to move in the flow normal direction only. The blade is flat, thus restricts its motion in the flow direction. The flexible supporting blade is connected to a strain gauge in order to measure the displacement of cylinder. The channel depth (the length of cylinders) and width are 100×10^{-3} m and 180×10^{-3} m respectively. The tube diameter is $D=30\times10^{-3}$ m. The pitch ratio ($p^*=$

P/D) of the tube arrangement is $p^* = 1.5$ in both (the in-flow and flow normal/lift) directions. The mass of the tube per unit length in air is $m = 0.564\ kg/m$. The natural frequency (f_n) and damping ratio (ζ) of the cylinder in vacuum (practically in air) are 30.78 Hz and 0.334% respectively.

(a) The experimental apparatus

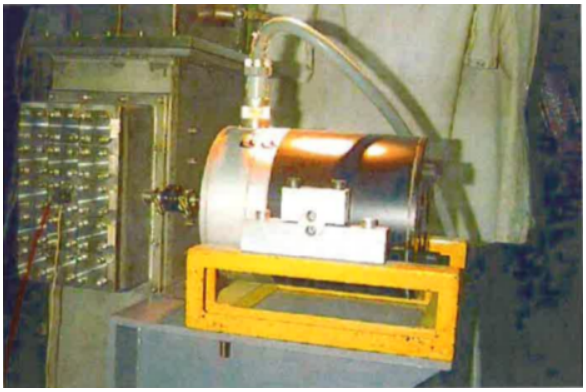

(b) The mockup with an electromagnetic exciter

Figure 2.5 The experimental setup and instrumentation measuring flow induced vibrations.

The experiments are carried out for different volume flow rates in the channel, varying from $9 \times 10^{-3}\ m^3/s$ to $30.6 \times 10^{-3}\ m^3/s$. The velocity at inflow is also measured directly using Laser Doppler Velocimetry (LDV). The vibration in the central instrumented tube is measured for each flow velocity by means of the micro-deformations ($\mu\ def$) at the bottom of the flexible supporting blade induced due to the water flow. A time response signal for about $1000s$ is recorded to perform the time modal analysis, in order to estimate the values of modal frequency and damping ratio for each flow rate. The experiment is stopped for high amplitude oscillations in the cylinder response and the corresponding velocity is considered as the critical flow velocity.

The experimental results are tabulated in Table (2.3). The first three columns of the table show the volume inflow rate (Q), Reynolds number (Re) and the minimum gap velocity respectively. The Reynolds number $Re = \rho u_p D/\mu$ is based on the cylinder diameter (D) and the pitch velocity (u_p). ρ and μ are the density and viscosity of water respectively. The non-dimensional reduced pitch velocity u^* is defined with respect to the response frequency of cylinder in the fluid (water) at rest as $u^* = u_p/(f_n D)$. The values of the reduced velocity are provided in the next column (the fourth column). The vibration in the tube is recorded in terms of the strain in the flexible blade, which holds the tube. The root mean square (rms) displacement in the tube is thus measured in μdef units. The μdef unit deformations are con-

Q $\times 10^{-3}\ m^3/s$	Re	u_p m/s	u^*	y_{rms}/D (%)	ζ_t (%)	$(f_n^*)_t$	ζ_h (%)	$(f_n^*)_h$
9.0	15000	0.5	0.90	0.03	0.78	0.99	1.12	0.99
2.6	21000	0.7	1.26	0.11	1.17	0.99	1.55	0.99
16.2	27000	0.9	1.62	0.30	1.61	0.98	1.74	0.98
19.8	33000	1.1	1.98	0.99	0.42	0.98	0.78	0.98
23.4	39000	1.3	2.34	0.99	2.25	0.98	2.64	0.98
27.0	45000	1.5	2.70	1.48	3.25	0.97	3.43	0.96
30.6	51000	1.7	3.06	2.32	3.08	0.96	3.27	0.96

Table 2.3 Experimental results.

verted in SI units using a gauge factor. The rms displacement y_{rms} is listed in the fifth column of Table (2.3). The next two columns (the sixth and seventh) are the damping ratio (ζ_t) and normalised response frequency ($(f_n^*)_t$) of the cylinder respectively, which are estimated using the Time Modal Analysis. The frequency of the cylinder in still water $f_n = 18.5\ Hz$ is used to non-dimensionalize the cylinder response frequencies. Alternately, the damping ratio (ζ_h) and response frequency ($(f_n^*)_h$) of the cylinder vibration is estimated using the Half Power Bandwidth method. The values are tabulated in the last two column of the Table (2.3). The results of the Time Modal Analysis and the Half Power Bandwidth method show a fairly good agreement.

Figure (2.6)(a) shows the computational domain of the square normal array ($SN90D$). The flow is in the $+X$ direction. The numerical simulations are performed in 2-dimensions ($2D$). The array geometry is similar to the experimental setup (Figure 2.5(a)). The diameter and pitch ratio for the arrangement are $D = 30 \times 10^{-3}\ m$ and $p^* = 1.50$ respectively. There are 5 rows and 5 columns of tubes. The computational domain is about $5D$ upstream from the first row of the tube bundle and about $10D$ downstream from the last row of the tube bundle. The computational domain is discretized in 848892 finite control volumes. The mesh in the near wall regions (i.e. near the cylinders surface and the two side walls) is refined, in comparison with the mesh in the inflow and outflow regions. The details of the mesh near the central cylinder is shown in Figure 2.6(b). Thus the non-dimensional distance (y^+) at these Reynolds numbers remains less than 1. The Reynolds number, similarly to the experiments (Table (2.3)), ranges from 15000 to $\approx$ 60000. The flow turbulence is modeled using the four equation turbulence model $k - \varepsilon - \overline{v^2} - f$.

Simulations are performed with the incompressible flow solver *Code_Saturne*, an open source software developed by Électricité de France (EDF). The algorithm is based on co-located finite volume method to solve the incompressible Navier-Stokes equations. Compu-

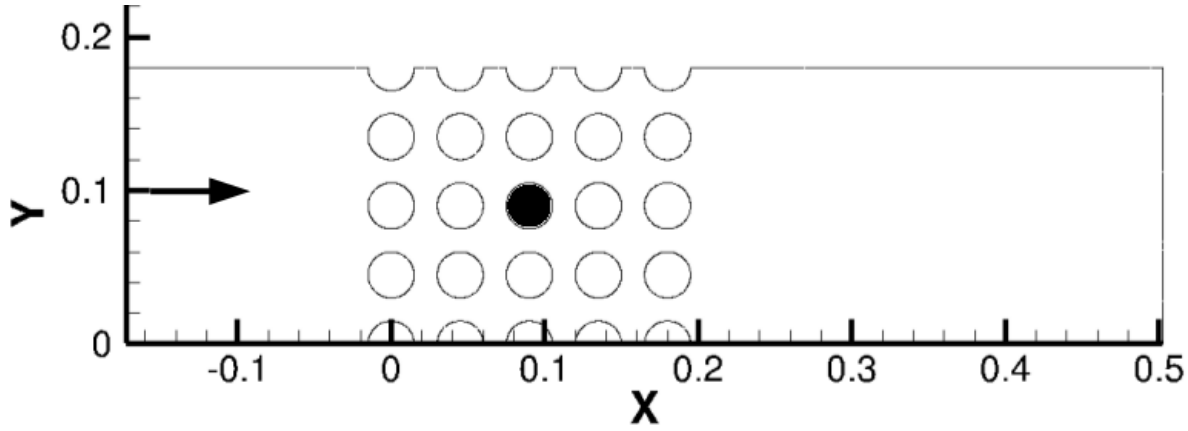

(a) The square normal array (90^o)

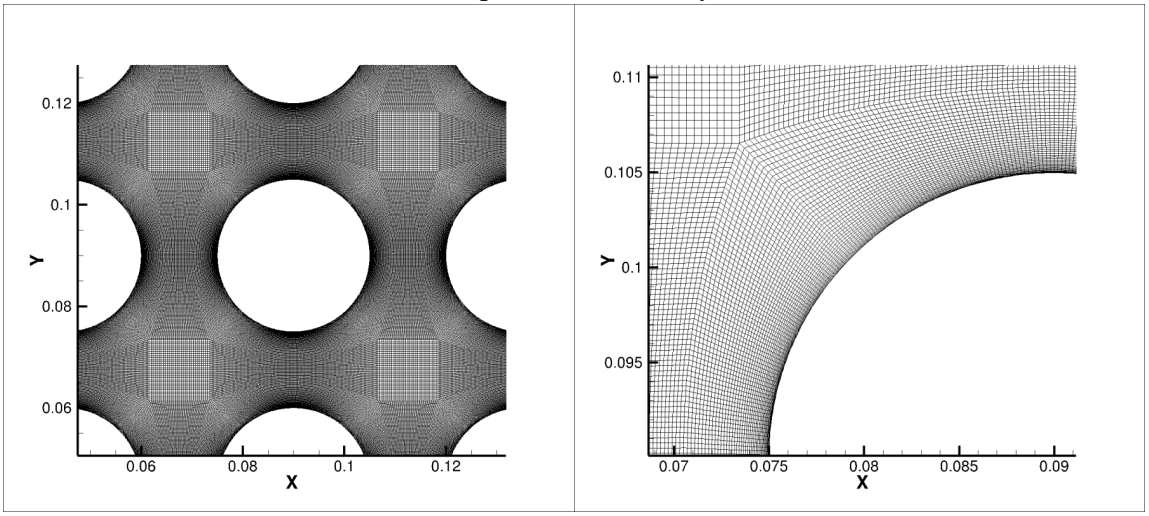

(b) Details of the computational mesh

Figure 2.6 The computational domain.

tations are performed using second order central difference schemes for space discretization and a Cranck-Nicolson scheme for time marching. A Dirichlet boundary condition with specified constant inflow velocity is applied at inlet. At outlet, homogeneous Neumann boundary condition for velocity and a Dirichlet boundary condition for pressure are employed, such that $\frac{\partial^2 P}{\partial n \partial \tau} = 0$ for any vector τ collinear with outlet. P is pressure and n is normal to boundary face. No-slip wall boundary conditions are prescribed on the side walls with cylinders half-mounted.

The cylinder movement is coupled with the fluid flow by the method of Arbitrary-Lagrangian-Eulerian (ALE). The moving mesh (boundary) is considered in flow equations in terms of the mesh velocity. In response, the forces experted by the fluid flow are used to displace the cylinder boundary surface. In experiments, the cylinder is rigid and flexibly mounted. An

equivalent numerical arrangement is shown in Figure (3.3). It is a mass on spring physics, where, m is the mass of cylinder, k and c are the stiffness and damping coefficients of the cylinder.

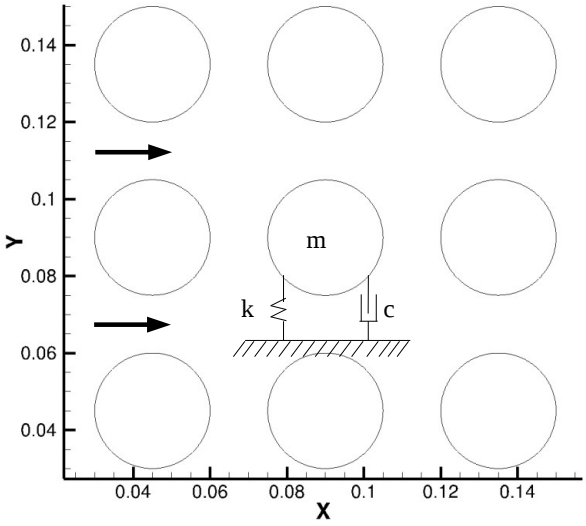

Figure 2.7 The fluid-structure coupling.

The equation of motion of the cylinder is,

$$m\frac{d^2y}{dt^2} + c\frac{dy}{dt} + ky = F_y \tag{2.1}$$

where, y is the displacement of the cylinder in the flow normal direction. F_y is the fluid force in same direction. The experimental values of modal mass and damping ratio can be used to estimate the stiffness and damping coefficients in air, by using the following relations

$$k = (2\pi f_n)^2 m \qquad \text{and} \qquad c = 2\zeta\sqrt{km}$$

The ordinary differential equation (Equation (2.1)) is numerically solved using Newmark HHT algorith, in which the fluid forces are used to estimate the displacement y. The new position of the cylinder is achieved by solving Poisson's equation for re-meshing before the next flow iteration. The deformation of near-wall mesh is controlled by assigning a high value for an artificial mesh viscosity.

The results of numerical simulations are tabulated in Table (2.4). The first two columns show the Reynolds number (Re) and the pitch velocity (u_p) respectively. The pitch velocity (also the gap velocity) is computed using the inflow velocity. The reduced velocity (u^*) is listed in the third column. It is based on the cylinder response frequency with respect to the

fluid medium at rest, which is $f_n = 18.5\,Hz$. The rms response of the cylinder vibration is listed in the fourth column. The cylinder response damping ratio (ζ_h) and the frequency ($(f_n^*)_h$), estimated using the Half Power Bandwidth method is tabulated in the last two columns of the table. The response frequency is normalised by the cylinder frequency in still water. The numerical simulation is diverged in the response for the reduced pitch velocity ($u^* = 3.06$), which is considered as the critical value.

Re	u_p m/s	u^*	y_{rms}/D (%)	ζ_h (%)	$(f_n^*)_h$
15000	0.5	0.90	0.10	3.58	1.025
18000	0.6	1.08	0.13	1.42	0.931
21000	0.7	1.26	0.28	1.94	1.081
24000	0.8	1.44	0.54	1.09	1.037
27000	0.9	1.62	1.26	2.14	1.022
30000	1.0	1.80	2.12	1.06	0.994
33000	1.1	1.98	2.78	4.33	0.993
36000	1.2	2.16	3.87	2.16	1.038
39000	1.3	2.34	4.37	4.10	1.021
42000	1.4	2.52	5.13	2.65	1.023
45000	1.5	2.70	7.17	2.73	0.991
48000	1.6	2.88	9.83	3.23	1.024
51000	1.7	3.06	15.6	-	1.099

Table 2.4 Numerical results.

2.3.2 Results comparison and discussion

The rms response of the cylinder is compared in Figure (2.8) between the experiments and the numerical calculations. The cylinder rms response amplitude grows gradually for increasing reduced pitch velocity (u^*). The critical reduced velocity obtained by the experiments is well predicted by the URANS calculations. The value of critical reduced velocity is $u_c^* \approx 3.06$. There is a factor ≈ 6 in the actual rms values between the experiments and numerical simulations. As discussed in the section on experimental set up, the central tube is mounted on one end of the tube. In addition, in order to avoid the non-linearity in the strain gauge readings and also to avoid breaking of the instrument, the experiments are stopped before large displacements are observed ($\approx 10^{-3}\ m$). Therefore, the results of URANS calculations differ quantitatively with the experiments. Qualitatively, the increase in response of the cylinder shows a good agreement between the experiments and the URANS simulations. The response

curve show a flat region near the reduced velocity $u^* \approx 2$ for the experimental data, which is absent in the numerical data.

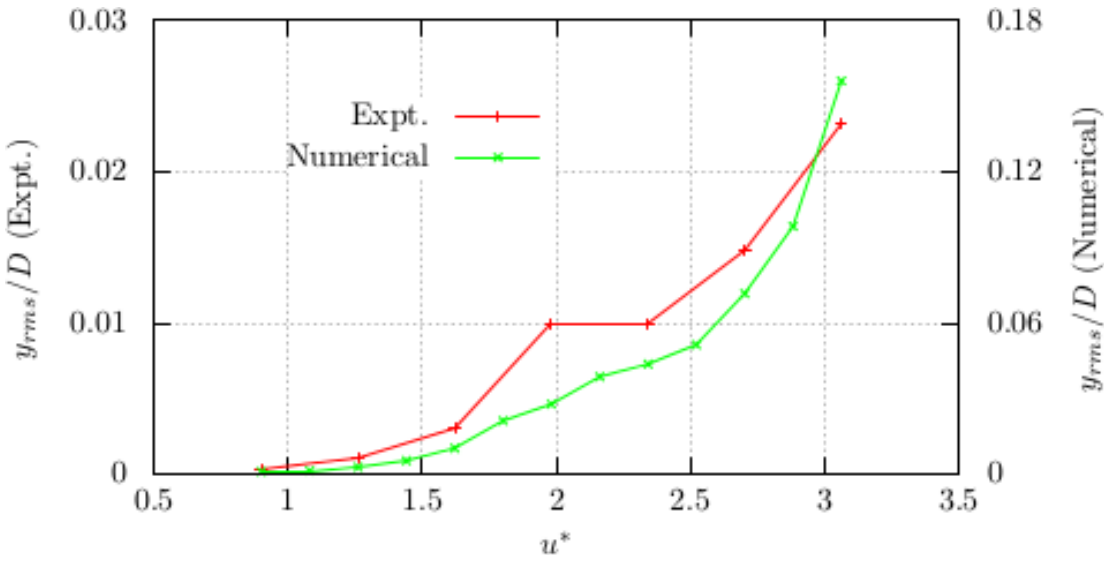

Figure 2.8 Comparison of the cylinder rms response.

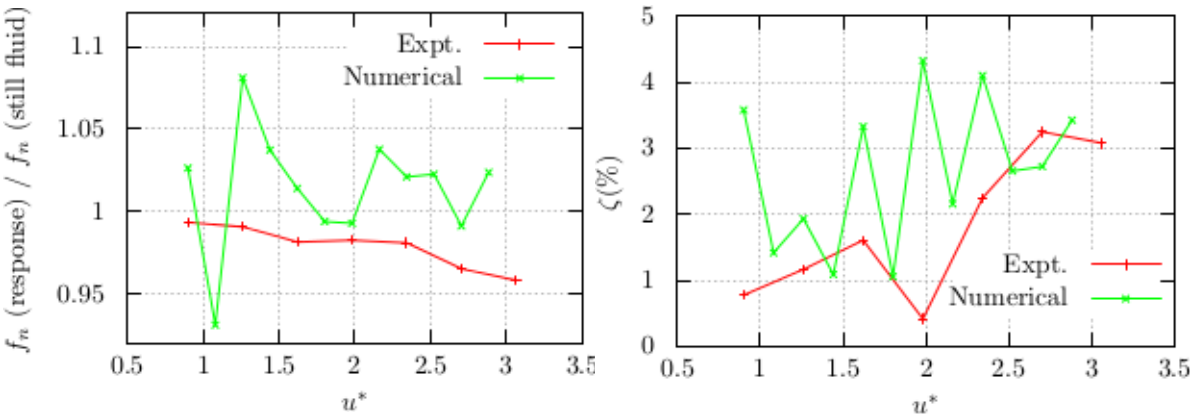

(a) Normalised response frequency

(b) Damping ratio (ζ)

Figure 2.9 Comparison of the response frequency and damping ratio of the cylinder.

The experimental values of the cylinder response frequency (f^*) (Table (2.3)) show a continuous decrease from 1.00 at $u^* = 0.9$ to 0.96 at the onset of the fluidelastic instability at $u_c^* = 3.06$. The Figure 2.9 (a) shows the normalised cylinder response frequency curves for increasing reduced velocity. The response frequency is non-dimensionalized by the frequency of cylinder with respect to fluid at rest. The experimental values observe a plateau at about $u^* = 2$. On the contrary, the experimental effective damping (ζ) increases continuously, except a decrease at $u^* = 2$ (see Figure 2.9(b)). The values of the non-dimensional cylinder response

frequency (f_n) and the effective damping (ζ) obtained by numerical simulations (Table (2.4)) are in close agreement with the experimental data. Although the variations in these values for increasing reduced velocity are not captured by the URANS ($k-\varepsilon-\bar{v^2}/k$) simulations.

2.4 Conclusion

One of the objectives of the surface pressure survey on a cylinder from triangular tube arrays by (Mahon and Meskell, 2009) and (Mahon and Meskell, 2012) is to create a database for the validation of numerical models. There are numerous models for modelling the flow turbulence at higher Reynolds numbers. The predictions of URANS models are often questioned, when it comes to investigation of the transient nature of the flow turbulence. In order to study the dynamic fluid-structure interaction in tube bundles, two two equation models and a four equation model are chosen for the results comparison. The predictions of the turbulence models are satisfactory in predicting overall profiles of the time-averaged surface pressures, while there are discrepancies in actual values, particularly at the separation locations as well as in the rear part of the cylinder. Although, the $k-\varepsilon-\overline{v^2}/k$ model doesn't do distinctly better in comparison with the other two ($k-\varepsilon$ *LP* and $k-\omega$ *SST*) models, it is chosen for the dynamic simulations, since the formulation contains four turbulent scales and it takes in to account the near-wall turbulence anisotropy.

In the dynamic case simulations, the prediction of the critical reduced flow velocity is in agreement with the experimental value of $u_c^* \approx 3.06$. Although, the actual rms response of the cylinder differs with the experimental values, qualitatively the response of the cylinder is well predicted with the increasing flow velocity. The values of the response frequency and effective damping of the cylinder are compare well with experimental values, but the trends of variations in these quantities for increasing flow velocity are not well captured by the URANS calculations.

CHAPTER 3

ANALYSIS OF THE FLUIDELASTIC INSTABILITY BY USING THE LARGE EDDY SIMULATIONS

Abstract

Large Eddy Simulations (LES) are performed to study a flow through an array of cylinders in square normal arrangement. A single phase water under cross flow through a 5×5 tube bundle at low intertube Reynolds numbers (2000 to 6000) is simulated in order to investigate the mechanism of fluid-elastic instability. First, the flow is analysed in static configuration for to reveal the existence of flow periodicities and the nature of fluid forces acting on a cylinder. Second, a cylinder is allowed to oscillate in one degree of freedom (1-DOF) in the flow normal (transverse) direction, which is a replica of the experimental set up. The Arbitrary Lagrangian-Eulerian (ALE) apporach is adopted to simulate the fluid-structure coupling. The sub-grid scale turbulence of the LES is modeled using standard Smagorinsky's eddy-viscosity model. The LES results show good agreement with experimental results in terms of the response frequency and damping ratio of the cylinder. The dynamic case simulations are compared with static cases over the range of Reynolds numbers by means of the probe velocity spectra and pressure profiles on the cylinder surface. The amplitude of cylinder vibration increases with the increase in flow velocity. However, it is characterised by a sinusoidal increase-decrease and followed by a monotonous increase onset of the instability. This typical behaviour of the fluidelastic instability is elucidated as a consequence of the dynamics of fluid forces exerted by two adjacent flow streams on the cylinder and in return the deformations in flow streams produced by the cylinder movement. The time-evolving instantaneous pressure profiles on the cylinder surface show alternating symmetry and antisymmetry with increasing intertube velocity, which is correlated with the distortions (high velocity patches) on the flow streams as well as the variations in the effective damping and natural frequency of the cylinder vibrations.

Keywords

flow induced vibration, heat exchanger tube bundles, fluid-elastic instability, large eddy simulation

Contents

3.1 Introduction

Heat exchangers are important components of any power generation industry, while as they are prone to failures in terms of collision damage, fatigue and fretting wear of the tubes. The cross flow-induced vibrations in heat exchanger tube bundles may lead to serious consequences, especially in nuclear power plants. The safety measures involved as well as the tubes replacement cost involved are very high (Païdoussis et al., 2010, chap. 5). Generally, the vibrations in heat exchanger tube bundles are classified in four types, namely, vibrations induced by flow vortex shedding, acoustic resonance, turbulence buffeting and the fluidelastic instability. Turbulence buffeting exists for a large range of interstitial flow velocities and it causes problems in the long term. The acoustic resonance appears generally in heat exchangers with low density fluids on the shell side of a large container. The excitations generated by flow jets, wake or shear layer instabilities lead to vibrations are generally categorised under Vortex-Induced Vibrations (VIV). The fluidelastic instability, as understood up to date, is a

self excitation mechanism, which comes in play at sufficiently high intertube flow velocities (relative to the range of Strouhal periodicity). The failures of heat exchanger tubes because of the flow vortex shedding and fluidelastic instability occur in a short time span (in a matter of hours). The tubes damage due to fluidelastic instability is severe and devastating. It results in a high amplitude vibration, collision and eventually sudden breakdown of the tubes.

The flow-induced vibrations in tube bundles were mostly attributed to Strouhal periodicity, until (Roberts, 1966) first reported the phenomenon of fluidelastic instability. Following the work by (Connors, 1970), (Connors, 1978) on fluidelastic instability, an extensive research work has been carried out by (Weaver and Grover, 1978), (Chen, 1978), (Tanaka and Takahara, 1981), (Païdoussis, 1981), (Lever and Weaver, 1982), (Price and Païdoussis, 1984), (Pettigrew and Taylor, 1991) and many others, in order to better understand the mechanism of fluidelastic instability. Experiments were performed by (Weaver and Grover, 1978) in order to examine the flow vortex shedding, turbulent buffeting and fluidelastic instability in a large triangular parallel tubes bank. The fluidelastic instability develops at relatively higher velocities, where no distinct flow vortex frequencies are observed in corresponding static configurations. The interaction between the interstitial flow and the tubes are transient in nature. (Tanaka and Takahara, 1981) carried out experiments and obtained the unsteady forces on the vibrating cylinders in order to feed the force coefficients in their theoretical model. Also the dependence of the critical velocity on the fluid density and damping ratio (mass-damping parameter) is studied. An extensive experimental work program is carried out by (Chen and Jendrzejcyk, 1981) to study the influence of different parameters such as mass ratio, pitch ratio, damping ratio and in general the coefficients of the empirical relation, which is developed for the prediction of fluidelastic stability thresholds. Furthermore, multiple critical velocities are observed for a single value of the mass-damping parameter. In (Lever and Weaver, 1982) a simple experimental work is carried with just a single cylinder from an array is used to predict the fluidelastic instability. A theoretical model is derived under simplifying assumptions such as the dominance of fluidelastic instability in the transverse direction, the flow redistribution and the phase lag between the fluid flow and the cylinder motion. A generalized model of fluidelastic instability is proposed in (Chen, 1987), where the model coefficients demanded the transient fluid force data from experiments or numerical simulations. The experimental results by (Païdoussis et al., 1989) showed that in the square rotated arrangement of the tube bundles, the fluidelastic instability appeared dominantly in the flow direction and the cylinder remained statistically displaced. The instability appeared only for the cylinders in first few rows, while as a cylinder from the sixth (second last row) row never became fluidelastically unstable, at least in the configuration they used. Further experiments ((Price and Païdoussis,

1989), Price and Kuran (1991)) on the in-line and triangular normal tube arrays with a single flexible (flexibly mounted) cylinder configuration led to conclusions in accordance with most of the earlier works by other researchers, such as the dominance of vibration in the lift direction, the independence of the onset fluidelastic instability on the Strouhal Periodicity. (Granger et al., 1994) performed experiments in order to measure the motion dependent fluid forces on the tubes. A method for the statistical time domain modal analysis is developed to estimate the transient coupled forces. The low values of mass-damping parameter ($m^*\delta$) lead to the fluid damping controlled instability ((Chen et al., 1998)), which is characterized by the presence of multiple stability boundaries. (Tanaka et al., 2002) found that the mass and damping of the mass-damping parameter must be treated separately for small values of the mass-ratio ($m^* < 10$). The use of a single cylinder and positioning of the cylinder in all types of tube array, in order to predict fluidelastic instability are critically examined in (Khalifa et al., 2012).

Although there have been numerous experimental campaigns, which has enhanced our understanding about the fluidelastic instability to great extent, there remains an unexplained scatter in the stability thresholds. The number of parameters involved in the instability is large. Further, the instability appears due to the transient interaction between the interstitial fluid flow and the cylinder displacements. The non-intrusive accurate experimental simulations of the instability to fully understand its source of excitation is fairly difficult. Computational Fluid Dynamics (CFD) simulations provide a possibility of such non-intrusive accurate simulations. Although the advent of computers has enabled us to perform the high fidelity simulations, the turbulence in fluid flow at high Reynolds numbers (which is typical in an industrial configuration) further makes the problem intractable. There have been several attempts to model the cross flow through tube arrays using the potential or semi potential flow theory, but the predictions of the dynamic fluidelastic instability are not accurate enough (see Païdoussis et al., 2010, chap. 5, pp. 261-264). The importance of the shear layers or the vortex shedding is studied in a comparison with the potential flow modeling approach in (Kevlahan, 2011). The Direct Numerical Simulation (DNS) of the turbulent flow through tube arrays at high Reynolds numbers is impractical considering the available computing resources today. The Unsteady Reynolds Averaged Navier-Stokes (URANS) and the Large Eddy Simulations (LES) are normally adopted to perform the numerical simulations of the flow through tube bundles. A characterization of the flow through tube arrays by comparing with the experimental flow visualization data is done in (Barsamian and Hassan, 1997) by using the Large Eddy Simulations (LES), though not in the context of fluidelastic instability. $2D$ dynamic simulations are performed in (Kassera and Strohmeier, 1997) by adopting the URANS approach of turbulence

modeling at reasonably high Reynolds number ($Re \sim 10^5$). Furthermore, in (Schröder and Gelbe, 1999), (Beale and Spalding, 1999) and (Benhamadouche and Laurence, 2003) numerical simulations (either LES and/or URANS) are performed to study the flow characteristics, fluid-induced vibrations etc. but with no explicit examples of the fluidelastic instability. The numerical study in (Gillen and Meskell, 2009) is performed by statically displacing cylinders in order to obtain coefficients for the quasi-steady modeling approach. The dynamic modeling of fluid-structure interaction using Arbitrary Lagrange Eulerien (ALE) method is employed in (Longatte et al., 2003), (Shinde et al., 2014) in order to investigate the dynamic fluidelastic instability.

In the present work, Large Eddy Simulations (LES) of a flow across cylinders in a square normal arrangement are performed at low Reynolds numbers for approximately 2000 to 6000. A single phase water flow through the array of 5×5 cylinders is simulated. The simulations are performed for a static configuration (all cylinders fixed). The fluid flow is characterized in terms of the flow periodicity, pressure profile on the cylinder surface, attachment and separation locations and force coefficients. A single central cylinder is then allowed to vibrate freely in 1-degree-of-freedom (1-DOF) in the flow normal (transverse) direction. The results of simulations in the static configuration are compared with the dynamic case simulations for the corresponding Reynolds numbers. The root-mean-squared (rms) vibration in the cylinder shows an intermediate peak in the response before it becomes fluidelastically unstable. The total force on the cylinder is split into two parts acting on each half of the cylinder. Thus each force component is associated with an adjacent flow stream. The dynamics between these two forces acting in opposite direction is studied carefully, in order to understand the behaviour of cylinder vibration at the onset of the instability. The article is organized as follow: first, a description of the experimental and LES configurations is provided. Second, the LES results are compared with the experimental results in terms of the cylinder response frequency and effective damping ratio. Third, the static configuration results are analysed and compared with the corresponding dynamic case simulations. Lastly, the development of fluidelastic instability is carefully elucidated by means of several parameters, namely, cylinder displacement response, fluid forces on the cylinder, effective damping ratio and frequency of the cylinder, surface pressure profile evolution and the disturbances appearing on the adjacent flow streams due to cylinder motion.

3.2 Configuration

3.2.1 Experiments

The experiments were facilitated by Commissariat à l'énergie atomique et aux énergies alternatives (CEA) via its RESEDA mechanical testing platform. The tube bundle (5×5) is located in a vertical flow channel as shown in Figure (3.1). The cylinders are in a square normal arrangement. The two side columns are half wall mounted. Only the cylinder located at the center is flexibly mounted, while the remaining cylinders are fixed. The channel depth (the length of cylinders) and width are 100×10^{-3} m and 70×10^{-3} m respectively. The central cylinder is supported on a flexible blade at one end. It is allowed to move in the flow normal direction only. The flexible supporting blade is connected to a strain gauge in order to measure the displacement of cylinder.

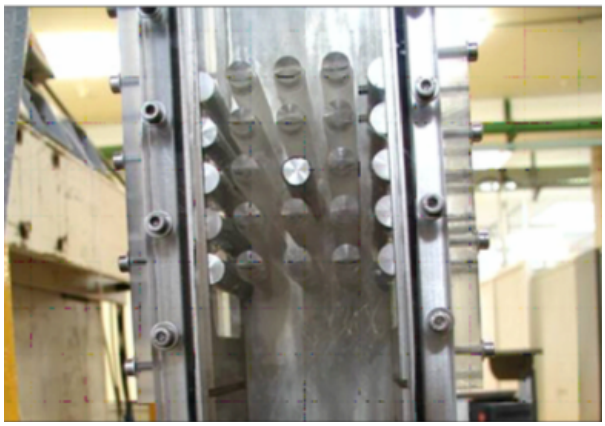

Figure 3.1 Experimental setup.

The tube diameter is $D = 12.15 \times 10^{-3}$ m. The pitch ratio ($p^* = P/D$) of the tube arrangement is $p^* = 1.44$ in both (in-flow and flow normal) directions. The modal mass of the cylinder per unit length is $m = 0.298$ kg/m. The natural frequency (f_n) and damping ratio (ζ) of the cylinder in air are 14.39 Hz and 0.25% respectively.

The experiments are carried out for volume flow rate in the channel from $0.2 \times 10^{-3} m^3/s$ upto $1.1 \times 10^{-3} m^3/s$ by increments of $0.05 \times 10^{-3} m^3/s$. The velocity at inflow is also measured directly with laser doppler velocitimetry (LDV). The vibration in the central instrumented tube is measured for each flow rate by means of micro-deformations (μdef) at the bottom of flexible supporting blade. A time response signal for 1000s is recorded for the modal analysis, in order to estimate the values of modal frequency and damping ratio for each flow rate.

3.2.2 Large Eddy Simulations (LES)

The computational domain for LES is 70×10^{-3} m wide and 48.6×10^{-3} m deep. The cylinders length is thus $4D$ against about $8D$ in the experimental facility. The domain is 269.5×10^{-3} m long in in-flow direction. The inflow boundary is $5D$ upstream the tube bundle, while as the outflow is $10D$ downstream of the tube bundle. The tube diameter (D), array pitch ratio (p) and arrangement of the tube bundle (90^o) is identical to the experiment. The geometry of the LES computational domain is shown in Figure 3.2(a).

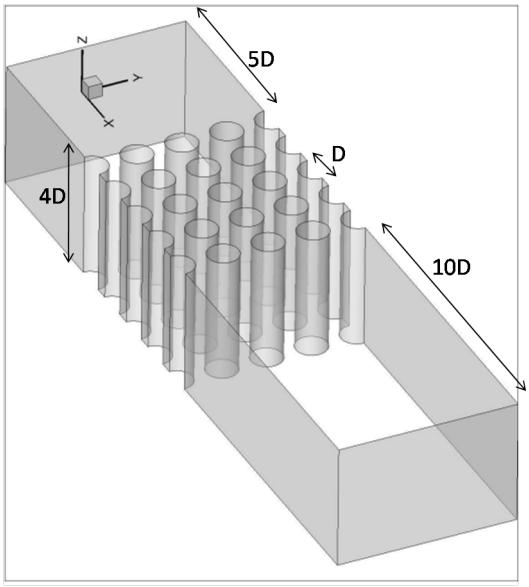

(a) Geometry

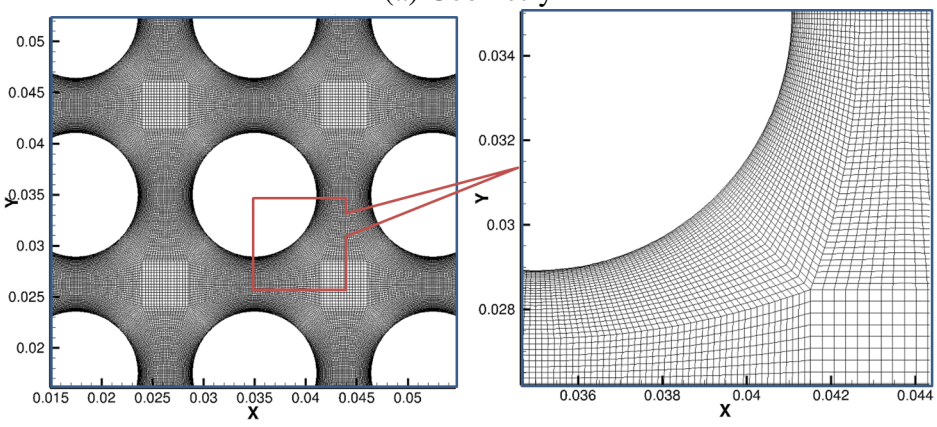

(b) Mesh

Figure 3.2 The computational domain.

The computational domain is descretized in nearly 25.3 million finite volume cells. The mesh near the cylinder surface region is fine enough to resolve the boundary layers of the fluid

flow. The first layer of the mesh is placed at a distance of 1.8×10^{-5} m away from the cylinder surface ensuring the y^+ below 1. The circumference of each cylinder is split in 360 elements. The mesh is coarser (2×10^{-3} m) far upstream and downstream the tube array. Figure 3.2 (b) shows the details of the mesh inside the tube array.

In the Large Eddy Simulations (LES) approach of turbulence modeling, the large eddies (larger than the size of mesh cells) are resolved directly. It contains most of the turbulent energy, however the subgrid scale turbulence needs to be modeled in order to balance the truncated turbulence energy spectrum. The filtered (subgrid) eddies are assumed to be isotropic and they can be modeled by simple Boussinesq type eddy viscosity relations. There exist several models for the subgrid scale turbulence. The standard Smagorinsky model is considered in this work with appropriate value of the model constant. However, the choice of subgrid scale model has little influence on the results ((Rollet-Miet et al., 1999), (Benhamadouche and Laurence, 2003)) of interest for the present configuration.

The computations are performed by using *Code_saturne*, an open-source incompressible Navier-Stokes solver developed by Électricité de France (EDF). It is based on a co-located finite volume method. The second order central difference and Crank-Nicolson schemes are used to perform the space and time descretizations respectively. A time step has a predictor and a correction steps. In the predictor step all physical properties are calculated along with the velocity field, while as in the correction step the pressure equation is accounted implicitly.

The LES computations are performed on a supercomputer of EDF R&D (IVANOE). Every simulation is carried out using 768 MPI-cores, with a memory requirement of about 24 Gb for each run. The four static case simulations are performed at gap Reynolds numbers $Re_p = 2124$, $Re_p = 3186$, $Re_p = 4248$ and $Re_p = 5310$, while the dynamic case simulations are performed at these Reynolds number with additional three intermediate cases at $Re_p = 2655$, $Re_p = 3717$ and $Re_p = 4779$. The dynamic case simulations are run in static configuration until the flow is established (for about 2 times the flow residence time). Then the cylinder is set free to interact with the flow. The simulations are carried out for $40s$ of physical time with a constant time-step of $2 \times 10^{-4}s$. The simulation physical time ($40s$) corresponds to 400 times the period of cylinder oscillations and 20 times the flow residence time approximately.

3.2.3 Fluid-structure coupling

The cylinder movement is coupled with the fluid flow by the method of Arbitrary-Lagrangian-Eulerian (ALE). The moving mesh (boundary) is considered in flow equations in terms of the mesh velocity. In response, the forces exerted by the fluid flow are used to displace the cylinder boundary surface. A detailed discussion on ALE in this context is provided in (Longatte et al.,

2003). In experiments, the cylinder is rigid and flexibly mounted. An equivalent numerical arrangement is shown in Figure (3.3). It is a mass on spring physics, where, m is the mass of cylinder, k and c are the stiffness and damping coefficients of the cylinder oscillations.

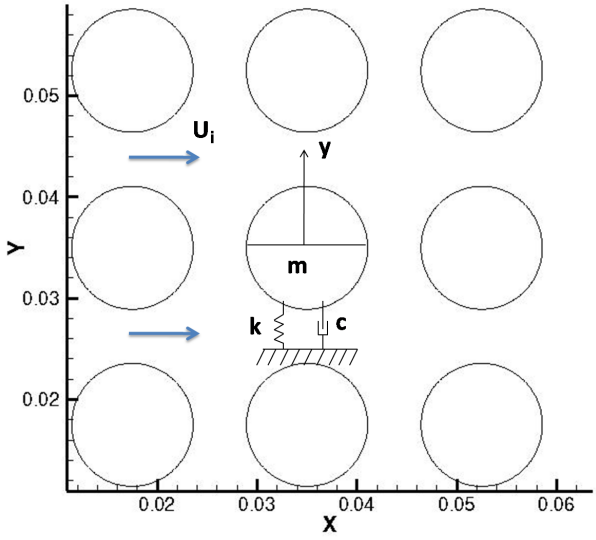

Figure 3.3 The fluid-structure coupling.

The equation of motion for the cylinder can be given by,

$$m\frac{d^2y}{dt^2} + c\frac{dy}{dt} + ky = F_y \tag{3.1}$$

Where, y is the displacement of the cylinder in flow normal direction, while as the fluid force in the same direction is represented by F_y on the right hand side of equation. The experimental values of modal mass and damping ratio can be used to estimate the stiffness and damping coefficients in air, by using following relations

$$k = (2\pi f_n)^2 m \qquad \text{and} \qquad c = 2\zeta\sqrt{km}$$

The ordinary differential equation (Equation (3.1)) is numerically solved using Newmark HHT algorithm, in which the fluid forces are used to estimate the displacement y. The new position of the cylinder is achieved by solving Poisson's equation for re-meshing before the next flow iteration. The deformation of near-wall mesh is controlled by assigning a high value for an artificial mesh viscosity.

3.3 Results comparison

Table (3.1) shows selected experimental results for comparison with the Large Eddy Simulation (LES) results. First three columns of the table enlist the values of volume flow rate (Q) in m^3/s, intertube (gap) velocity (u_p) in m/s and correponding Reynolds number Re_p respectively. The Reynolds number is based on gap velocity (u_p) and the cylinder diameter D. The reduced velocity is defined as $u^* = (u_p)/(f_n D)$, where $f_n = 11.68\ Hz$ is the cylinder response frequency in the fluid medium at rest. The reduced velocity is listed in the third column of the results table (Table (3.1)), while as the reduced response frequency of the cylinder vibration (f_n^*) is in the fourth column. It is non-dimensionalized by the cylinder response frequency in the still fluid medium. Last two columns of the results table show the damping ratio of cylinder vibration in percent estimated by using Time Domain Modal Analysis (ζ_t) and Half Power Bandwidth Method (ζ_h) respectively.

$Q\ (\times 10^{-3} m^3/s)$	$u_p\ (m/s)$	Re_p	u^*	f_n^*	$\zeta_t\ (\%)$	$\zeta_h\ (\%)$
0.35	0.164	1988	1.16	1.03	2.54	–
0.45	0.210	2556	1.48	1.00	0.90	0.73
0.55	0.257	3124	1.81	0.99	0.02	0.09
0.65	0.304	3692	2.14	1.02	1.56	1.43
0.75	0.351	4260	2.47	1.00	3.12	3.12
0.85	0.397	4828	2.80	0.98	1.42	1.62
0.95	0.444	5396	3.13	0.98	0.13	0.14

Table 3.1 Experimental results.

The Time Domain Modal Analysis (TDMA) of Poly Reference (PR) type is used to identify the modes and corresponding damping ratios. It is a statistical modal analysis method for experimental data developed in (Granger, 1990). The method establishes free decays from a transposed correlation matrix formed by using cylinder time response signal. The statistical auto-regression is performed by using the approach of maximum-likelihood estimation. The characteristic modes are predefined by means of characteristic functions. The modal parameters are treated for optimised values by using a non-linear Quasi-Newton method, with an initialization provided by Prony's method. On the other hand, the Half Power Bandwidth Method (HPBM) for estimation of damping ratio is simple in its formation. The Power Spectral Density (PSD) of the response time signal is obtained by Fast Fourier Transform (FFT).

The quality factor Q for a relevant mode is estimated using relation $Q = f_n/\Delta f$, where f_n is a modal frequency and Δf is the difference between two adjacent frequencies representing half power on the frequency (f_n) lobe. The damping ratio is readily calculated by relation $\zeta_h = 1/(2Q)$. The former method (TDMA) is more suited for experimental signals or sufficiently long time signals in order to perform statistical analysis. The damping ratios estimated using both methods are in good agreement (Table (3.1)).

$u_p\ (m/s)$	Re_p	u^*	f_n^*	$\zeta_h\ (\%)$
0.175	2124	1.23	1.00	2.19
0.219	2655	1.54	0.95	1.62
0.262	3186	1.85	1.00	0.20
0.306	3717	2.16	1.03	2.83
0.350	4248	2.47	0.92	3.08
0.393	4779	2.77	0.97	0.27
0.437	5310	3.08	0.98	–

Table 3.2 Numerical results.

The LES results are tabulated in Table (3.2). The simulations are performed for increasing intertube reduced velocity from 1.23 to 3.08, at which the instability occurs. The intertube velocities, corresponding Reynolds numbers and values of reduced velocities are listed in the first three columns respectively. Last two columns of Table (3.2) show the response non-dimensional frequency and damping ratio of the cylinder. The damping ratio is estimated by the Half Power Bandwidth Method only, since the time response signals of LES calculations are still short for the statistical time modal analysis.

The the experimental results in Table (3.1) and the LES results from Table (3.2) can be compared with one-to-one correspondence. The damping ratio of the cylinder vibration decreases with increase in reduced velocity up to $u^* \approx 1.85$ (gap velocity upto $\sim 0.26\ m/s$) in both the experiments and LES simulations. Further increase in the intertube reduced velocity velocity from $u^* \approx 1.80$ to $u^* \approx 0.35\ m/s$ results in increase in the damping ratio upto $\approx 3.1\%$. The cylinder observes a continuous decrease in its damping ratio for further increase in intertube velocity and it becomes zero, where the cylinder vibrations become unstable (Figure 3.4(b)). The experimental value of critical reduced velocity, where the damping ratio of the cylinder reaches zero is $u_c^* = 3.30$ ($u_{pc} = 0.468\ m/s$). The LES computation is already unstable for the reduced pitch velocity $u^* = 3.08$ ($u_{pc} = 0.437\ m/s$). The non-dimensional

response frequency f_n^* shows a general trend of decrease-increase-decrease in both the experimental and numerical results (Figure 3.4(a)). Overall, the results of LES calculations are in a good agreement with the experimental results.

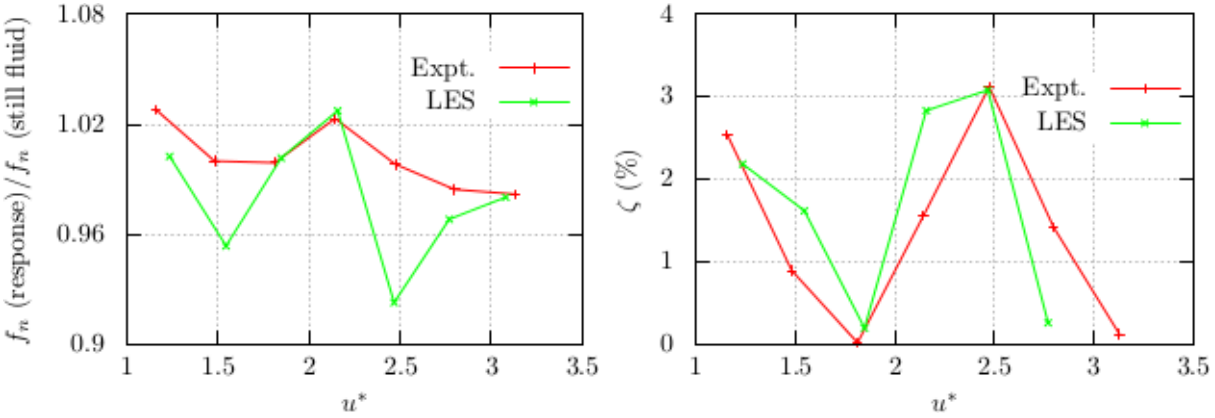

(a) response frequency f_n^* (b) effective damping ratio $\zeta(\%)$

Figure 3.4 The non-dimensional cylinder response frequency and damping ratio vs increasing reduced velocity.

3.4 Flow analysis

In addition to the dynamic case simulations, the static case Large Eddy Simulations (LES) are performed in order to understand the flow development in the array. These simulations are performed at four different values of the pitch Reynolds number increasing from $Re_p =$ 2124 up to $Re_p = 5310$. The particulars of the static case calculations are provided in Table (3.3). The intertube reduced velocities ($u^* = u_p/f_nD$) and corresponding intertube Reynolds numbers (Re_p) are listed in first two columns of the table. In general in tube arrays, the vortex-shedding phenomenon is not obvious, especially in the closely spaced tube arrays (the pitch ratio $p^* \lessapprox 1.50$). The interstitial flow could have the vortex-shedding linked with the shear layer instabilities, wakes or jet switching mechanisms, which may lead to an acoustic resonance (Oengören and Ziada, 1992), (Ziada, 2006). In general, in all the four cases listed in Table (3.3), the turbulence in flow develops as it passes down through the tube rows. Figure (3.5) shows the vorticity plots at Reynolds number $Re_p = 3186$. The spanwise component (Z) of the vorticity Ω_z on the mid-cross section of the tube array is shown in Figure 3.5(a). The shear layers are developed behind the first row of cylinders, which are nicely attached to the second row cylinders. Shortly downstream the second row of cylinders, the shear layers tend to break into turbulent structures. The two probes $P1$ and $P2$ are located along the second row

of cylinders, in the middle of the flow channels in order extract the flow frequencies. Further downstream, the shear layers appear more turbulent. The middle cylinder from the third row is monitored for vibration in the dynamic case calculations. The other two monitoring probes $P3$ and $P4$ are placed in the fourth row of the tube bundle as shown in Figure 3.5(a). There are two plane $L1$ and $L2$ located at upstream and downstream of the middle cylinder respectively. The streamwize (X) flow vorticity Ω_x is compared at these two corss-sectional planes ($L1$, $L2$). The comparison of the stremwize flow vorticity (Ω_x) between Figures 3.5(b) and 3.5(c) indicate the increased level of spanwize flow activity, mostly behind, in the wake region of the cylinders. Similar observations about the development of flow turbulence for the in-line cylinder arrays are reported in (Ziada, 2006).

u^*	Re_p	f^*_{sh}	St	Eu	C_d (rms)	C_l (rms)	Att. (θ^o)	Sep. (θ^o)
1.23	2124	0.56	0.45	0.42	6.28	0.030	64.0	93.6
1.85	3186	0.79	0.43	0.47	2.91	0.028	61.0	92.0
2.47	4248	1.92	0.78	0.55	1.76	0.021	55.0	90.3
3.08	5310	3.30	1.07	0.58	1.22	0.022	54.5	90.0

Table 3.3 Results of the static case LES simulations.

Figure (3.6) shows the flow normal velocity (u_2) spectra at the four probe locations for increasing Reynolds number. The flow frequencies are non-dimensionalized by using the cylinder's natural frequency in water at rest, i.e. $f^*_{sh} = f_{sh}/f_n$, with $f_n = 11.68\ Hz$. The spectra for intertube reduced velocity $u^* = 1.23$ ($u_p = 0.175\ m/s$) is shown in Figure 3.6(a). It shows a distinct frequency of $f^*_{sh} = 0.56$ at all the four probe locations. There are additional peaks at 1.1 and 1.7 in the spectra at the downstream locations ($P3$, $P4$). Generation of such higher harmonics due to non-linear instabilities in such flow configurations is discussed in (Ziada and Rockwell, 1982). In all cases, the spectra at the downstream locations $P3$ and $P4$ are elevated compared to the upstream locations $P1$ and $P2$, indicating an increase in the turbulence level as the eater flows downstream. The spectra at locations in the same row ($P1$ and $P2$ or $P3$ and $P4$) are nearly the same, except for the reduced velocity $u^* = 3.08$ ($u_p = 0.437\ m/s$) at locations $P3$ and $P4$, where the spectra differ in the frequency range 8.56 to 42.80 (Figure 3.6(d)). Figure 3.6(b) shows the spectra at an increased reduced velocity $u^* = 1.85$ ($u_p = 0.262\ m/s$). The dominant first frequency peak is at 0.79, while the second peak is at 1.58. The shapes of the spectra differ for the downstream locations ($P3$ and $P4$) if compared with the upstream locations ($P1$ and $P2$), especially in the frequency range around 8.56. Figures 3.6(c) and 3.6(d)

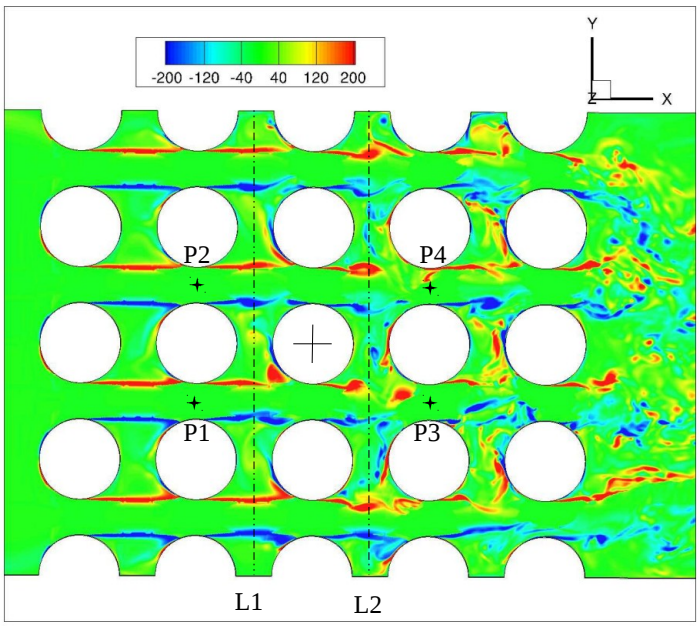

(a) Z vorticity (ω_z) at mid plane

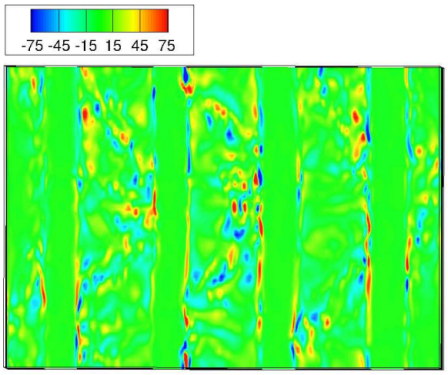

(b) X vorticity (ω_x) at plane L1

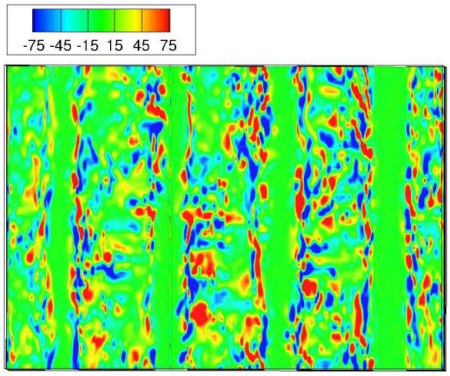

(c) X vorticity (ω_x) at plane L2

Figure 3.5 Vorticity plots for $u^* = 1.85$ ($Re_p = 3186$).

are the velocity (u_2) spectra at the intertube reduced velocities $u^* = 2.47$ ($u_p = 0.35\ m/s$) and $u^* = 3.08$ ($u_p = 0.437\ m/s$) respectively. The spectra at the upstream probe locations show wider peaks, with almost flat spectra (no peaks) at the downstream locations. The shear layer frequency peaks in the spectra in Figures 3.6(c) and 3.6(d) are at non-dimensional frequencies 1.93 and 3.3 respectively. The multiple frequency peaks in the spectra at Reynolds number $Re_p = 2124$ and $Re_p = 3186$ are the higher harmonics of the first frequency peaks. The frequency peaks at the downstream locations almost disappear, indicating the complete breakdown of the shear layers at higher Reynolds numbers. This is also observed experimentally for the in-line arrays with small pitch ratios (Ziada, 2006). The non-dimensional shear

layer frequency (f^*_{sh}) and the corresponding Strouhal number ($St = f_{sh}/(u_p/D)$) of the first dominant peak at increasing reduced intertube velocity are tabulated in the third and fourth columns of Table (3.3) respectively.

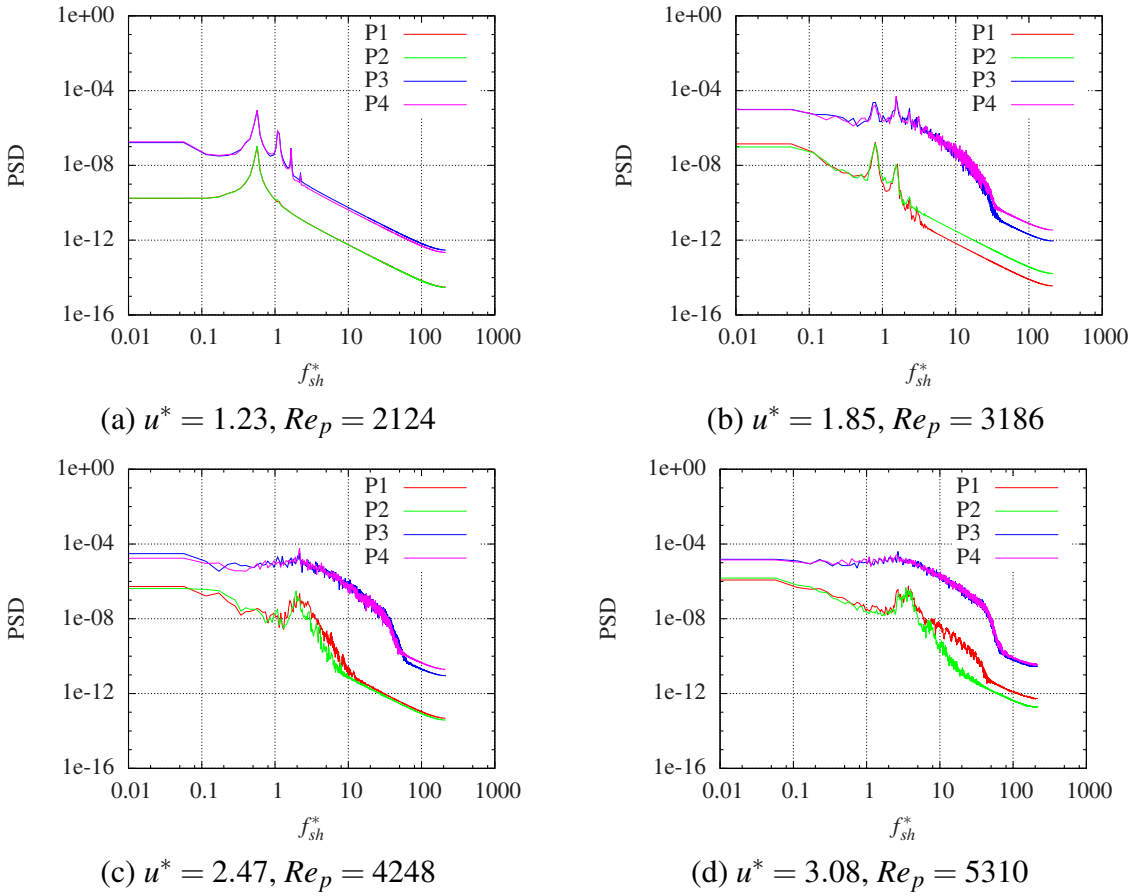

(a) $u^* = 1.23$, $Re_p = 2124$

(b) $u^* = 1.85$, $Re_p = 3186$

(c) $u^* = 2.47$, $Re_p = 4248$

(d) $u^* = 3.08$, $Re_p = 5310$

Figure 3.6 Power Spectral Densities (PSD) of Y velocity (u_2) at locations $P1$, $P2$, $P3$ and $P4$ for increasing intertube reduced velocity (u^*).

The surface pressure profiles in terms of pressure coefficient

$$C_p(\theta) = \frac{\langle p(\theta)\rangle_t - \langle p(\theta = 0)\rangle_{t,length}}{\frac{1}{2}\rho u_p^2}$$

on the monitored cylinder for different reduced velocities are shown in Figure (3.7). The time averaged surface pressure profile at reduced velocity $u^* = 1.23$ is shown in Figure 3.7(a), where the symmetry in the profile indicates that the shear layer sheets generated at the first row of cylinders are probably unbroken upto the third row of cylinders since the Reynolds is lower ($Re_p = 2124$). Figures 3.7(b), 3.7(b) and 3.7(b) show the profiles at Reynolds numbers $Re_p = 3186$, $Re_p = 4248$ and $Re_p = 5310$ respectively. The locations of maximum and

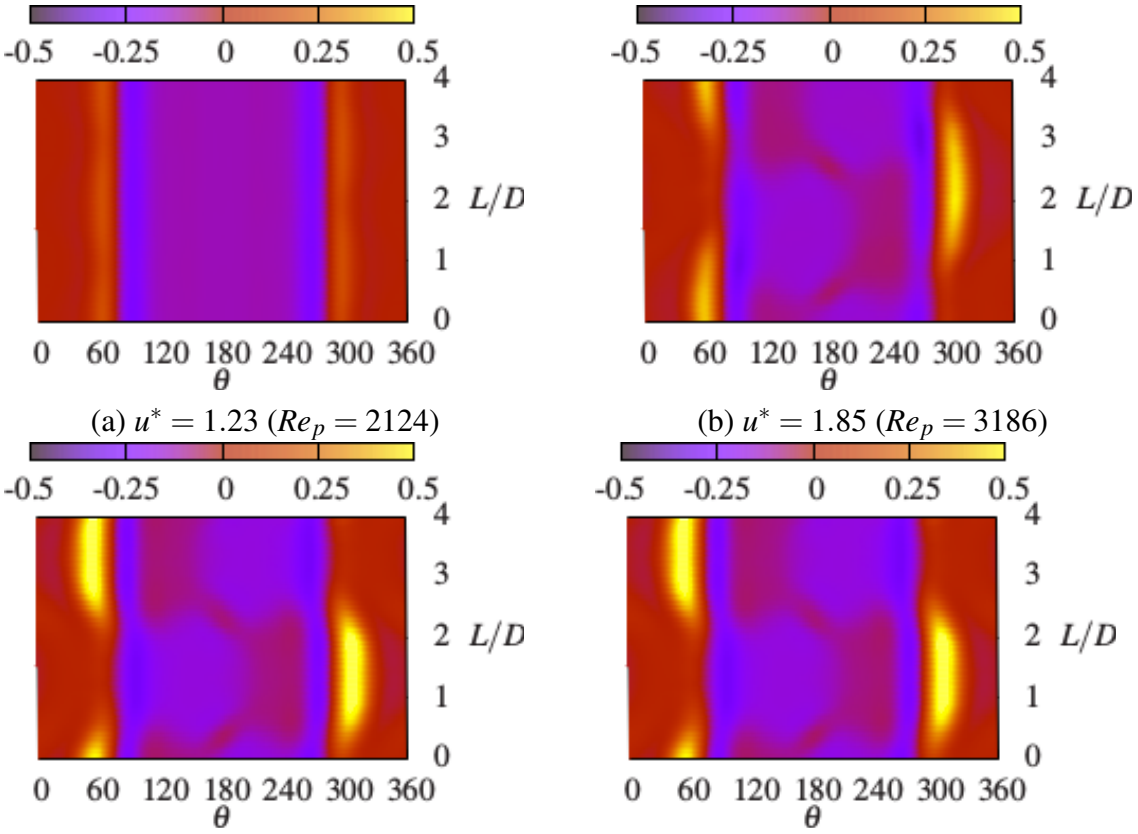

(a) $u^* = 1.23$ ($Re_p = 2124$) (b) $u^* = 1.85$ ($Re_p = 3186$)

(c) $u^* = 2.47$ ($Re_p = 4248$) (d) $u^* = 3.08$ ($Re_p = 5310$)

Figure 3.7 The time-averaged pressure profiles in terms of pressure coefficient ($C_p(\theta)$) for increasing reduced velocity.

minimum of the averaged pressure indicate the flow attachment and separation regions on the cylinder surface. The variations of averaged pressure profiles along the length of cylinder for Reynolds numbers ($Re_p = 3186$, $Re_p = 4248$ and $Re_p = 5310$) in Figures 3.7(b), 3.7(c) and 3.7(d) indicate the spanwize correlation of the flow structures. The spanwize correlation is approximately $\approx 3D$ in length.

Figure (3.8) shows the pressure coefficient

$$C_p(\theta) = \frac{\langle p(\theta)\rangle_{t,length} - \langle p(\theta = 0)\rangle_{t,length}}{\frac{1}{2}\rho u_p^2}$$

on the cylinder surface for various reduced pitch velocities. The pressure drop across a row of cylinder increases with an increase in the intertube velocity. The Euler number (Eu) is

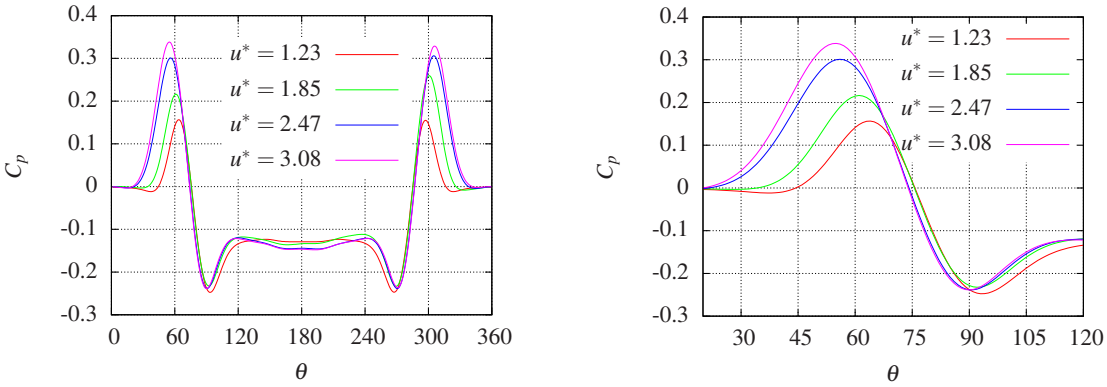

(a) $C_p(\theta)$ at various u^* (b) Attachment and separation points

Figure 3.8 The time-length-averaged azimuthal pressure profiles.

provided in the sixth column of Table (3.3). The Euler number is defined as,

$$Eu = \langle \Delta p_{row} \rangle_t / \left(\frac{1}{2} \rho u_p^2 \right)$$

. The values of the Euler number are in a good agreement with the heat exchanger design handbook data in (Coletti, 1983). Figure 3.8(b) shows the change in the attachment and separation locations due to the increase in the Reynolds number. The values of attachment and separation locations in degree are listed in the last two columns of the result table (Table (3.3)). The flow attachment locations are shifted inward (away from the flow streams) with the increase in flow velocity (u_p). On the contrary, the separation locations are shifted towards 90^o from 93^o. The root mean squared (rms) drag (C_d) and lift (C_l) coefficients for the cylinder (listed in the seventh and eighth columns of the result table) are estimated using relations,

$$C_d = Fx_{rms} / \left(\frac{1}{2} \rho u_p^2 DL \right) \quad \text{and} \quad C_l = Fy_{rms} / \left(\frac{1}{2} \rho u_p^2 DL \right)$$

Where Fx and Fy are the forces on cylinder in inflow and transverse directions, while L represents the length of cylinder.

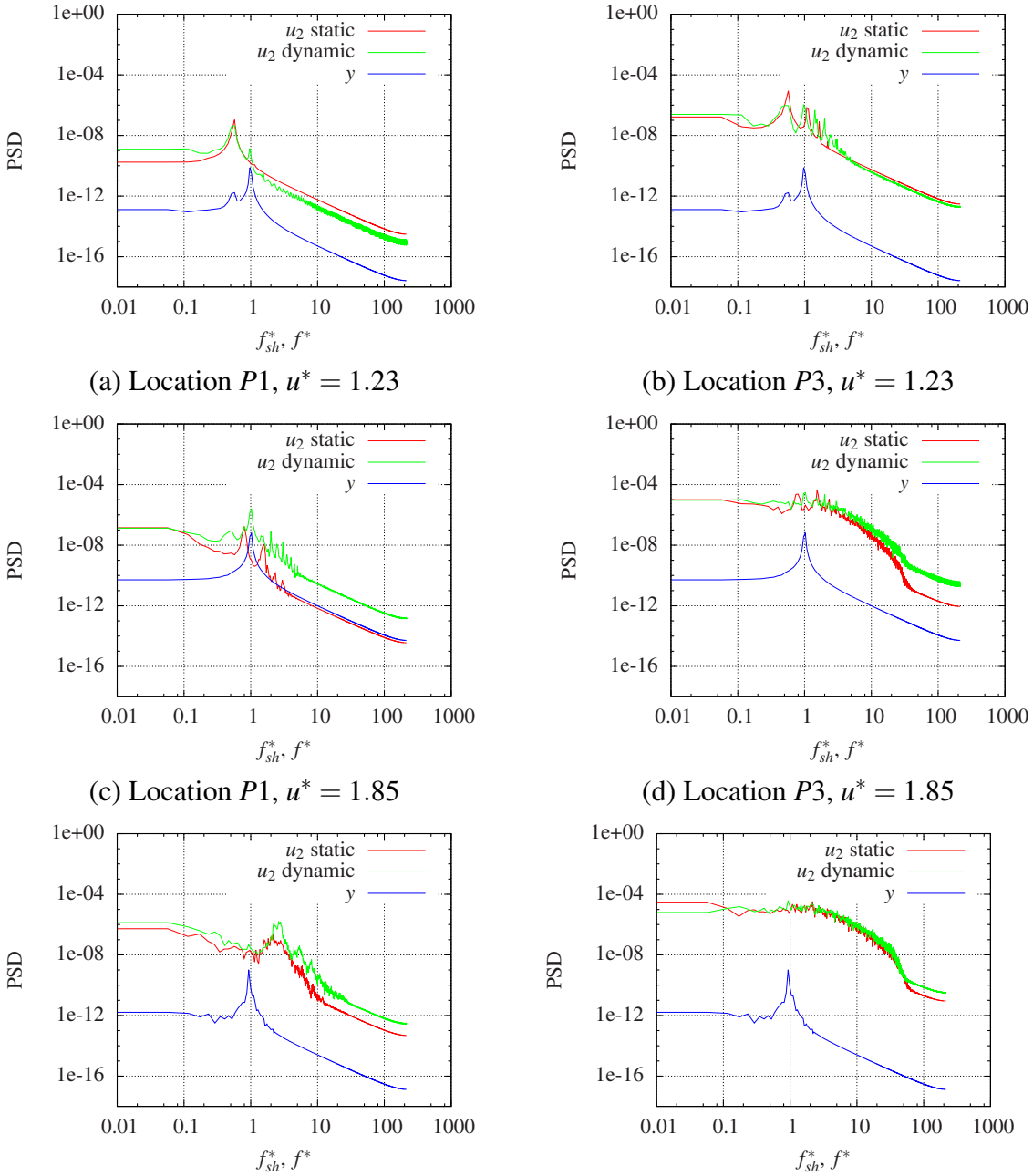

(a) Location $P1$, $u^* = 1.23$

(b) Location $P3$, $u^* = 1.23$

(c) Location $P1$, $u^* = 1.85$

(d) Location $P3$, $u^* = 1.85$

(e) Location $P1$, $u^* = 2.47$

(f) Location $P3$, $u^* = 2.47$

Figure 3.9 Power spectral densities (PSD) of Y velocity in static and dynamic cases at an upstream (P1) and a downstream (P3) locations, in comparison with the cylinder response spectrum for increasing reduced velocity.

3.5 The onset of fluidelastic instability

3.5.1 Comparison between the static and dynamic case simulations

In order to understand the development of fluidelastic instability, the static case Large Eddy Simulations (LES) results are compared with the dynamic case LES computations. The com-

parison is done using the spectra of Y velocity (u_2) at probe locations $P1$ and $P3$ for increasing reduced velocity (u^*). Furthermore, the velocity spectra at these upstream and downstream locations are compared with the spectrum of cylinder vibration (y) in Figure (3.9). In the static case simulations, the red curves in Figures 3.9(a) and 3.9(b), the shear layer frequency at gap reduced velocity $u^* = 1.23$ ($u_p = 0.175\ m/s$) is $f^*_{sh} = 0.56$, which is normalised by the cylinder natural frequency in still water i.e. $f_n = 11.68\ Hz$. There are higher harmonics of this frequency in the spectra computed at the downstream location $P3$. In the dynamic case computations, the green curves in Figures 3.9(a) and 3.9(b), there appears an extra frequency peak at both at the upstream and downstream locations, which corresponds to the response frequency of cylinder. On other hand, the response spectrum of cylinder, the blue curve in Figures 3.9(a) and 3.9(b)) shows a peak at $f^* = 0.56$. Figures 3.9(c) and 3.9(d) show similar comparison for the intertube reduced velocity $u^* = 1.85$ ($u_p = 0.262\ m/s$). The red curves of the static case simulations show two frequency peaks, one at 0.79 and its first harmonic at about 1.63, at both $P1$ and $P2$ locations. On the contrary, the velocity spectra in dynamic case (green curves in Figures 3.9(c) and 3.9(d)) show a distinct frequency at the cylinder response frequency ($f^*_n = 1$). Furthermore, the cylinder response spectrum at this reduced velocity $u^* = 1.85$ is elevated, in terms of the spectral power, compared to the response spectra at both $u^* = 1.23$ and $u^* = 2.47$ reduced pitch velocities, which may be due to a possible synchronization between the shear layer frequencies and the cylinder response frequency. The flow velocity spectra at the gap velocity $u^* = 2.47$ show wider peaks at frequency 1.92, at the upstream ($P1$) location only. The frequency peak corresponding to the cylinder vibration are not distinctly reflected in the velocity spectra (Figures 3.9(e) and 3.9(f)). The shear layer frequencies increase with further increase in the Reynolds number. The fluidelastic instability in the dynamic calculations occurs at Reynolds number $Re_p = 5310$, where the flow frequencies at the upstream locations ($P1$, $P2$) are about 3.3 with no distinct frequency peaks at the downstream locations ($P3$, $P4$). Therefore, the mechanism of the fluidelastic instability must be different than the classical "lock-in" phenomenon.

The interaction between the single cylinder and its adjacent flow streams can be monitored at the fluid-solid interface, i.e. the cylinder surface, for the exchange of the momentum by means of the fluid forces. The pressure force constitutes a major part of the fluid force, even for these low Reynolds numbers ($Re_p \approx 6000$). The time evolution of the pressure coefficient

$$C_p(\theta) = \frac{p(\theta) - \langle p(\theta = 0)\rangle_{t,length}}{\frac{1}{2}\rho u_p^2}$$

on the cylinder surface in both the static and dynamic configurations is presented in Figure

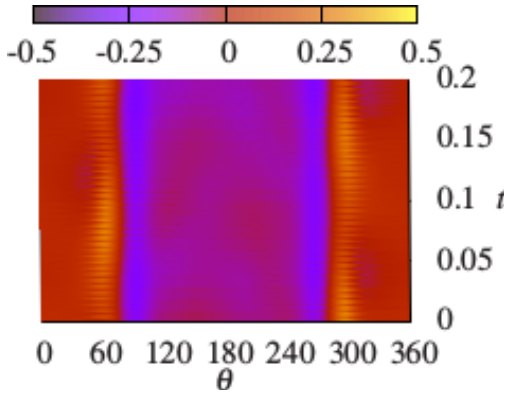

(a) $u^* = 1.23$ static case

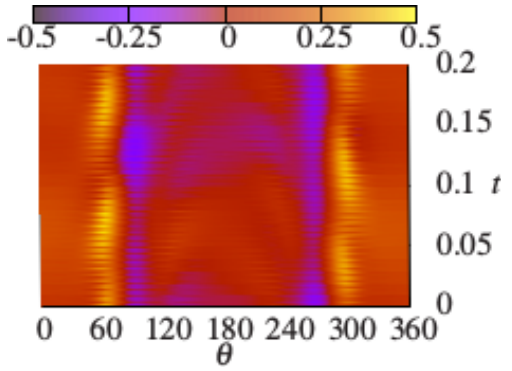

(b) $u^* = 1.23$ dynamic case

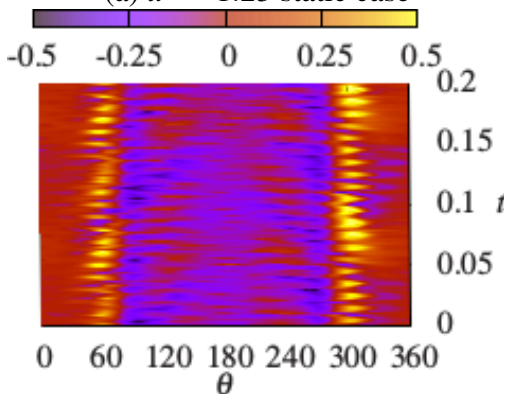

(c) $u^* = 1.85$ static case

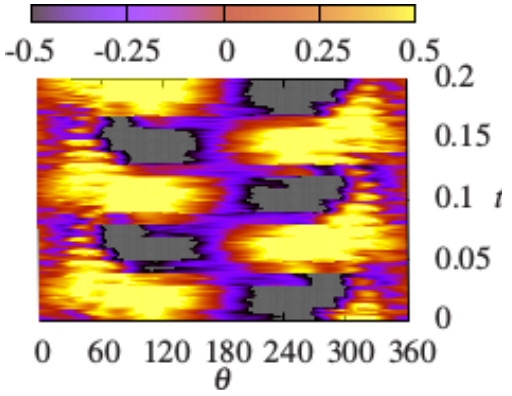

(d) $u^* = 1.85$ dynamic case

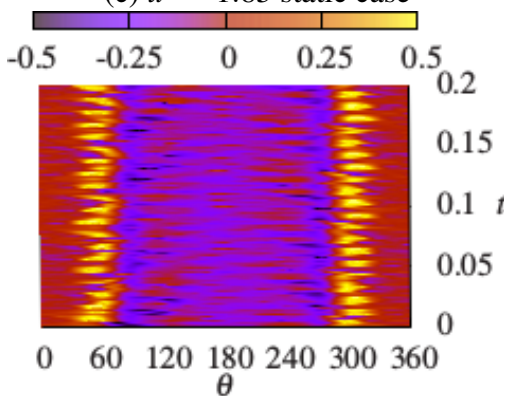

(e) $u^* = 2.47$ static case

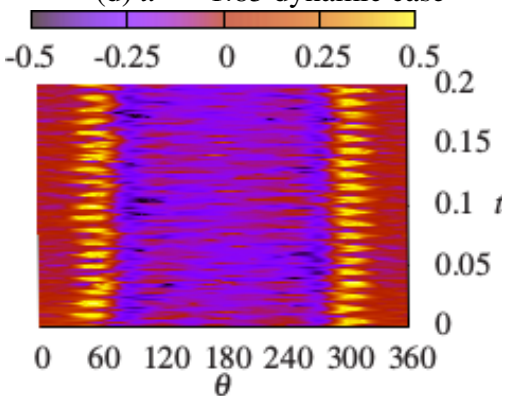

(f) $u^* = 2.47$ dynamic case

Figure 3.10 Comparison of the time evolving instantaneous surface pressure between static and dynamic cases for increasing reduced velocity.

(3.10). The time duration considered (on the y axis) is 0.2 s, which corresponds to approximately two periods of the cylinder oscillations in water (i.e. $\approx 2/f_n$, with $f_n \approx 11.68\ Hz$). In all static case configurations (Figures 3.10(a), 3.10(c), 3.10(e) and 3.10(g)), the pressure profiles evolve in time symmetrically with respect to the azimuthal angle $\theta = 180^o$. The pressure profile in the static case at reduced intertube velocity $u^* = 1.23$ (Figure 3.10(a)) shows more

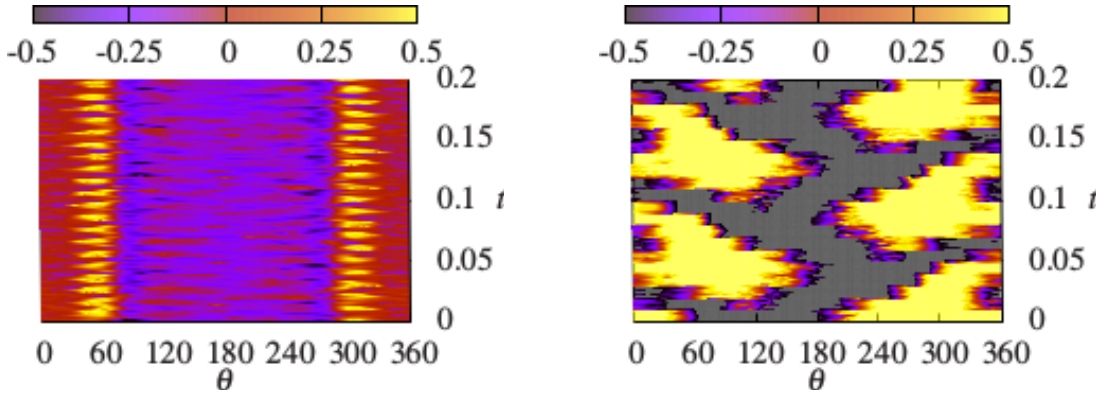

(g) $u^* = 3.08$ static case (h) $u^* = 3.08$ dynamic case

Figure 3.10 Comparison of the time evolving instantaneous surface pressure between static and dynamic cases for increasing reduced velocity.

or less symmetrical time evolution. The corresponding dynamic case (figure 3.10(b)) shows a similar time evolution of the surface pressure profile with $\approx 10\%$ higher values of the pressure coefficient. The time-pressure profiles in the static and dynamic simulations at the reduced gap velocity $u^* = 1.85$ are compared in Figures 3.10(c) and 3.10(d) respectively. The comparison shows a considerable difference in the time-evolution and the values of pressure drop coefficient. The pressure difference in the dynamic case is higher by ≈ 3 times the pressure drop in the static case. The time-evolution pressure profile is changed from the symmetric to nearly anti-symmetric profile with respect to $\theta = 180^o$. It indicates that, when one flow stream adjacent to the cylinder ($\theta = 0^o$ to $\theta = 180^o$) exerts a positive pressure on the cylinder surface, at the same time the other flow stream ($\theta = 180^o$ to $\theta = 360^o$) exerts a negative pressure on the cylinder surface. The increase in the reduced intertube velocity further to $u^* = 2.47$ results in the symmetry of the time-evolving pressure profile the dynamic case simulations (Figures 3.10(f)). Figure 3.10(e) shows the corresponding static case simulation profile. The value of instantaneous pressure drop is higher in the dynamic case by $\approx 14\%$. The cylinder oscillations become unstable at reduced intertube velocity $u^* = 3.08$. The transient development of the cylinder surface pressure profile in the dynamic case is shown in Figure 3.10(h). The pressure profile evolution is antisymmetric (alternating) and there is a sudden increase in the pressure drop value (by ≈ 8 to 10 times) against the symmetrical pressure profile in the corresponding static case (Figure 3.10(g)). The dynamic interaction between the cylinder and the adjacent flow streams result in the variation of the instantaneous surface pressure profiles for the increasing intertube velocity as shown in Figures 3.10(b), 3.10(d), 3.10(f) and 3.10(h). Furthermore, there is a similar trend in variation of the time-length averaged surface profiles for increasing flow velocity. The time-length averaged pressure profiles are almost

equal between the dynamic and static cases, for which the time evolving surface pressure are symmetric about $\theta = 180^o$. On contrary, The time-length averaged surface pressure profiles for the dynamic and static cases significantly differ, if the dynamic case shows an antisymmetry in the time evolution of the instantaneous surface pressure profile. Figure (3.11) shows a comparison of the time-length averaged cylinder surface pressure profiles for the reduced intertube velocities $u^* = 1.85$ and $u^* = 2.47$. In Figure 3.11(a), the flow attachment locations are shifted inwards (away from the flow streams) in the dynamic case, when compared to the static case profile. The pressure profiles in Figure 3.11(b) are nearly indifferent between static and dynamic cases.

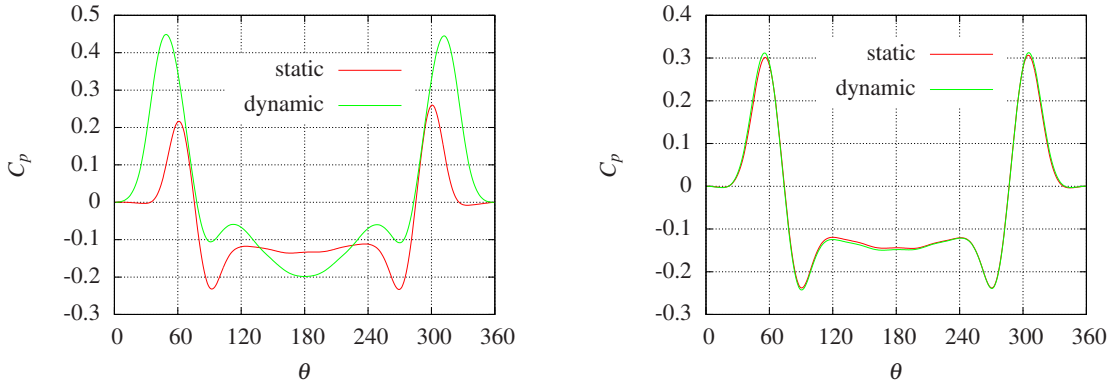

(a) $u^* = 1.85$ (b) $u^* = 2.47$

Figure 3.11 Comparison of the time-length averaged cylinder surface pressure profiles between the static and dynamic cases at $u^* = 1.85$ and $u^* = 2.47$.

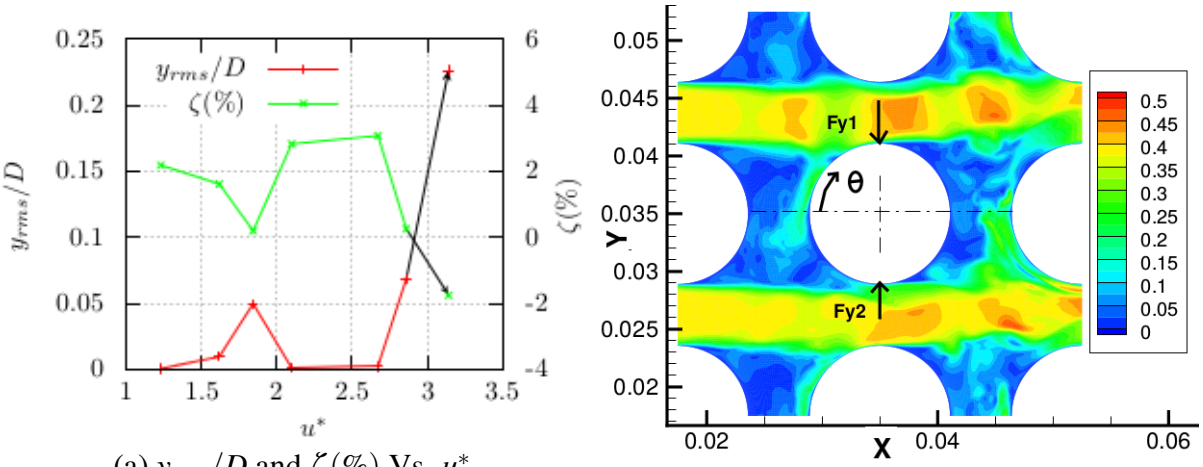

(a) y_{rms}/D and $\zeta(\%)$ Vs. u^* (b) Fy_1, Fy_2 and θ ($u^* = 2.67$)

Figure 3.12 LES results: (a) Cylinder response amplitude (y_{rms}/D) and damping ratio (ζ) with increasing reduced velocity (u^*) (b) Force (y component) on cylinder surface split into $Fy_1(t)$ and $Fy_2(t)$.

In the development of fluidelastic instability, the increasing intertube reduced velocity u^* changes the way fluid forces are imparted to the cylinder dynamically. The time-evolving pressure profiles are nearly symmetric for the reduced velocity $u^* = 1.23$. The symmetric pressure profile becomes anti-symmetry until $u^* = 1.84$. Furthermore the anti-symmetrical pressure profile changes back to symmetrical profile until the reduced velocity becomes $u^* = 2.67$. A further increase in the intertube reduced velocity results in the anti-symmetry of the pressure profiles at the onset of fluidelastic instability. The change in the time-evolving pressure profile on the cylinder surface is also accompanied by the variations in the damping ratio (ζ), cylinder response frequency (f_n) and the amplitude of cylinder vibration (y). The section (Section 3.3) on results comparison shows the details of the variations in the damping ratio and response frequency of the cylinder oscillations. The experimental as well as LES results show an initial decrease of the cylinder response frequency, which is followed by an increase and a decrease until the instability occurs with increasing flow velocity. The damping ratio (ζ) exhibits similar trend, experimentally as well as numerically. Figure 3.12(a) shows the variations in the damping ratio (ζ, in green) and the cylinder rms displacement (y_{rms}/D, in red) against the increasing reduced velocity u^*. The damping ratio of the cylinder decreases gradually up to the reduced velocity $u^* = 1.84$, which results in a gradual increase in the amplitude of cylinder vibration. Further increase in the reduced velocity results in an increase of the damping ratio, while as a decrease in the cylinder response rms amplitude. The damping ratio undergoes a sudden decrease for the higher reduced velocities $u^* \gtrapprox 2.67$, on other hand the vibration in cylinder increases drastically. The Large Eddy Simulations (LES) computations performed for the reduced velocity $u^* = 3.14$ shows a divergence in its response, indicating that the damping ratio becomes negative ($\zeta < 0$) for this value of the reduced velocity.

3.5.2 Dynamics of the fluid forces acting on the cylinder

The higher amplitudes of cylinder vibration and the drop in the damping ratio correspond to the anti-symmetry in the pressure profiles on the cylinder surface. The symmetrical pressure profile means both the flow streams acting a positive or a negative pressure on the cylinder at the same time, while as the anti-symmetric pressure profiles indicate that one flow stream exerts a positive pressure at the same time when other exerts a negative pressure. In order to study this dynamics of the pressure forces exerted by each adjacent flow stream on the cylinder surface, the total force on the cylinder surface $Fy(t)$ is split into two parts $Fy_1(t)$ and $Fy_2(t)$,

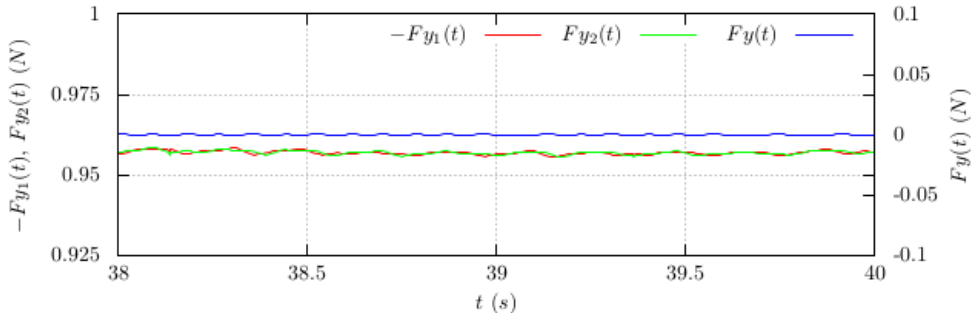

(a) $u^* = 1.23$

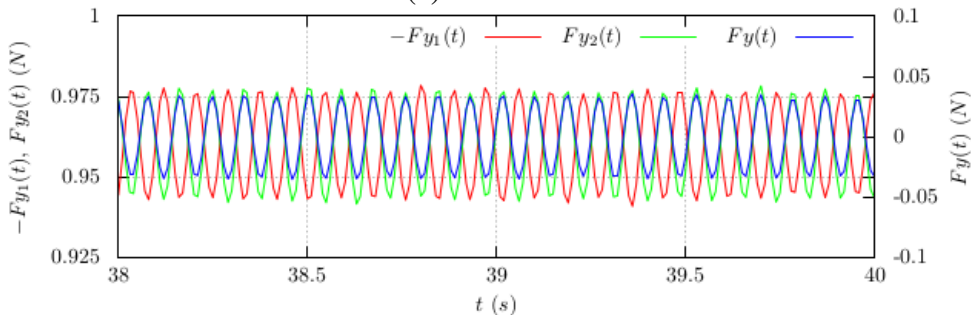

(b) $u^* = 1.85$

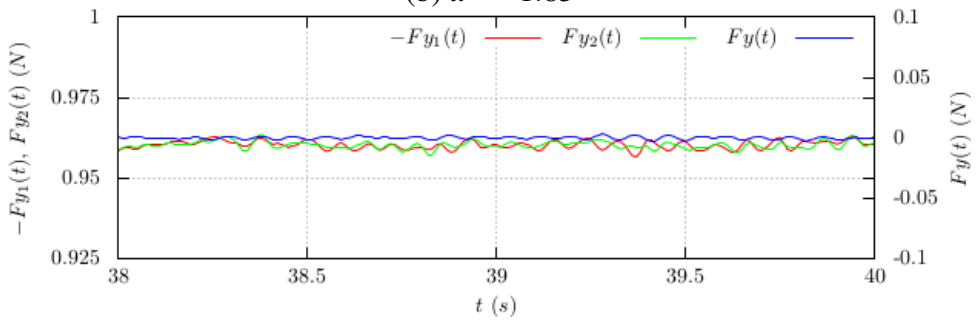

(c) $u^* = 2.16$

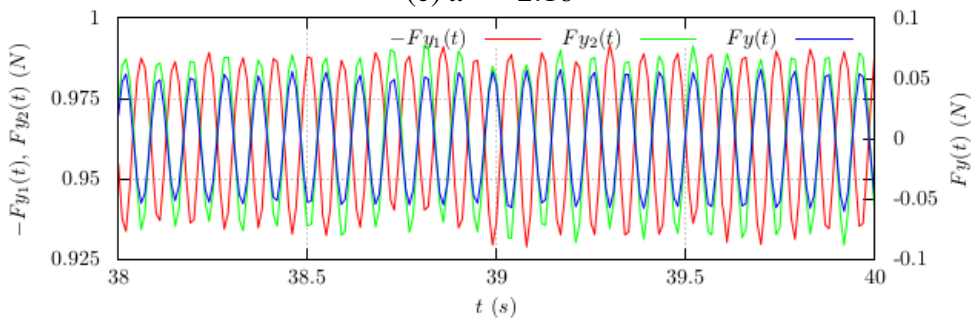

(d) $u^* = 2.77$

Figure 3.13 The time response of the forces acting on cylinder at increasing reduced velocity.

as shown in Figure 3.12(b). The forces are estimated as,

$$Fy_1(t) = \int_{\theta=0}^{180} f_y d\theta \quad \text{and} \quad Fy_2(t) = \int_{\theta=180}^{360} f_y d\theta$$

where f_y is a force on a small elemental surface on the cylinder. The instantaneous time signals of the forces $Fy_1(t)$, $Fy_2(t)$ and $Fy(t)$ are compared in Figure (3.13). The forces plotted in Figures 3.13(a), 3.13(b), 3.13(c) and 3.13(d) are for the increasing reduced velocities $u^* = 1.23$, $u^* = 1.85$, $u^* = 2.16$ and $u^* = 2.77$ respectively. The forces Fy_1 and Fy_2 exerted by the flow streams adjacent to the cylinder are nearly equal in the magnitude and opposite in the direction as shown in Figure 3.12(b). Hence the total force $Fy(t)$ on the cylinder, which is responsible for the cylinder displacement $y(t)$ has a magnitude approximately ≈ 100 times smaller than the individual forces ($Fy_1(t)$ and $Fy_2(t)$). The amplitude of the force increases with an increase in the reduced intertube velocity from $u^* = 1.23$ to $u^* = 1.85$, as shown in Figures 3.13(a) and 3.13(b) respectively. The amplitude of the force $Fy(t)$ observes a decrease with an increase in the reduced intertube velocity from $u^* = 1.85$ to $u^* = 2.16$ (Figures 3.13(b) and 3.13(c)). It is followed by a monotonous increase for further increase in the velocity, a trend similar to the displacement of cylinder (Figure 3.12(a)). The magnitudes of the individual forces $Fy_1(t)$ and $Fy_2(t)$ do not increase much with the increase in the reduced intertube velocity. The dynamics between these two forces play an important role in the behaviour of the total force ($Fy(t)$) change with the increasing reduced velocity. The forces $Fy_1(t)$ and $Fy_2(t)$ become synchronized when the reduced velocity increases from $u^* = 1.23$ (Figure 3.13(a)) to $u^* = 1.85$ (Figure 3.13(b)). The synchronization results in a increase of the total force on cylinder ($Fy(t)$). The increase of the reduced intertube velocity from $u^* = 1.85$ to $u^* = 2.16$ leads to an unsynchronized time response of these two individual forces, which results in the smaller values for the resultant total force (Figure 3.13(c)). Consequently, it results in the smaller displacements of the cylinder (y) at this reduced velocity ($u_p^* = 2.16$). A further increase in the intertube velocity regains the synchronization between the forces $Fy_1(t)$ and $Fy_2(2)$. Thus the resultant force $Fy(t)$ is increased, which eventually leads to the instability.

The dynamic interaction between the cylinder and the flow around is either ways, i.e. the flow induces vibration in the cylinder and as a consequence of the movement of cylinder, the flow streams are modified. Contrary to the static case simulations, it is observed that the time-pressure profiles on the cylinder surface show alternatively the symmetry and anti-symmetry with increasing the flow streams velocity. The dynamics of the forces exerted by the adjacent flow streams results in the variations of the total force acting on the cylinder. The variations in the damping ratio (ζ), response frequency (f_n) and the amplitude of cylinder vibration (y) is a consequence of the resultant force (Fy) on the cylinder. The displacement of the cylinder (y) modifies the flow field abound it, changing the course of the flow streams adjacent to the cylinder. The displacement of cylinder towards a flow stream, results in an increase of the local flow velocity because of the decrease in the cross-sectional flow area. The displacement

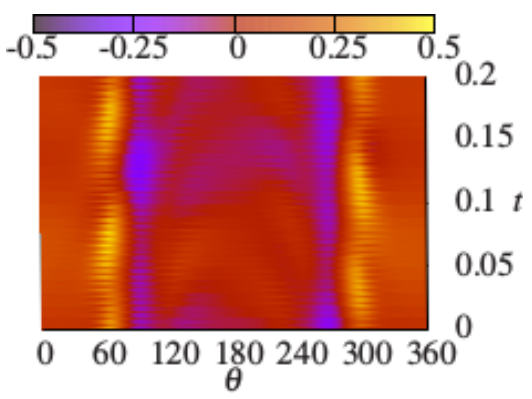

(a) $u^* = 1.23$, $Re_p = 2124$

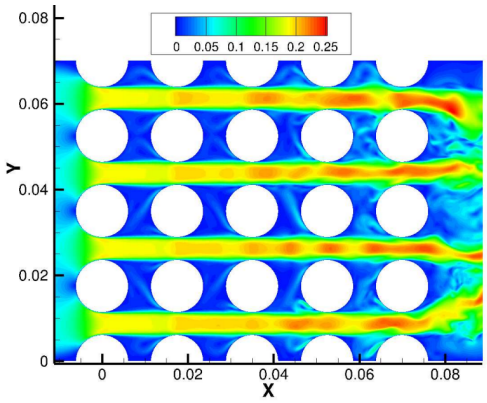

(b) $u^* = 1.23$, $Re_p = 2124$

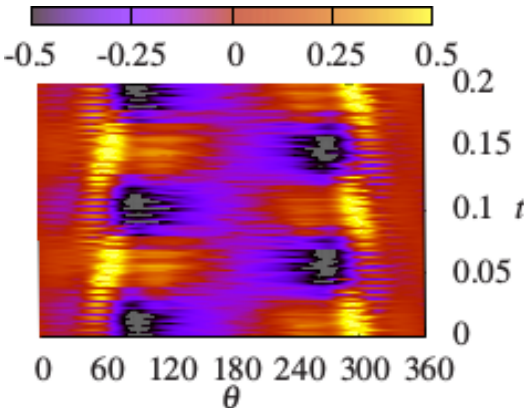

(c) $u^* = 1.54$, $Re_p = 2655$

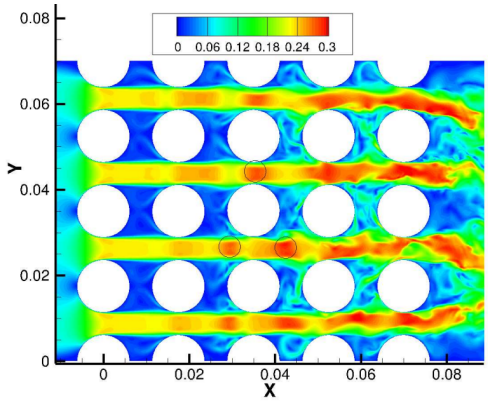

(d) $u^* = 1.54$, $Re_p = 2655$

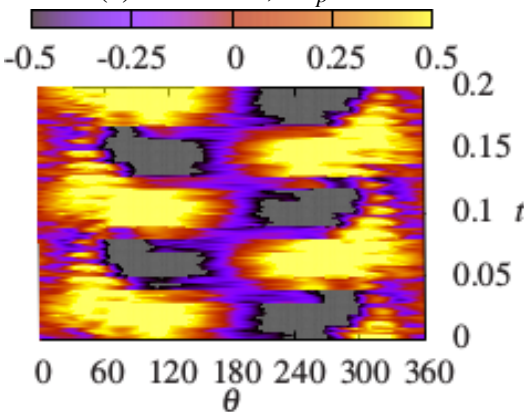

(e) $u^* = 1.85$, $Re_p = 3186$

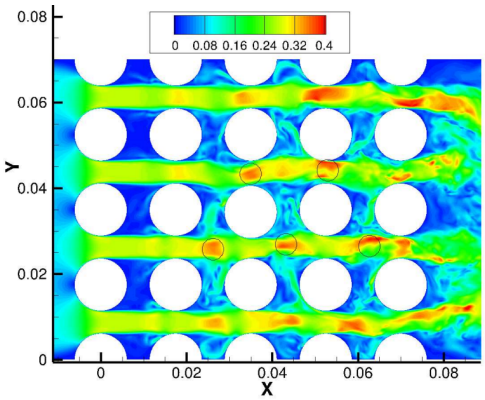

(f) $u^* = 1.85$, $Re_p = 3186$

Figure 3.14 Correspondence between the time evolving pressure profiles with the velocity field adjacent to the cylinder.

of cylinder may introduce a flow retardation or acceleration to the adjacent flow streams. The distortions on the flow streams are carried with the flow (both downstream as well as upstream the cylinder). Figure (3.14) shows the flow distortions (in terms of the high velocity patches) travelling on the flow streams at different reduced velocities. A correspondence between the

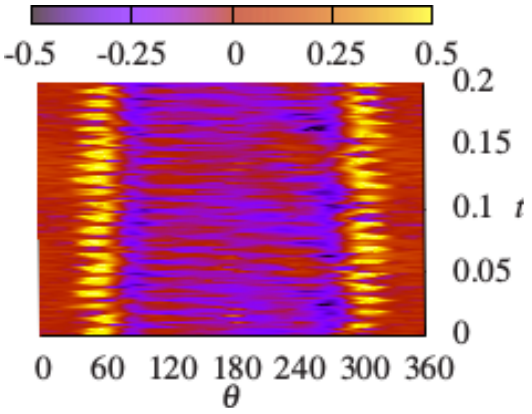

(g) $u^* = 2.16$, $Re_p = 3717$

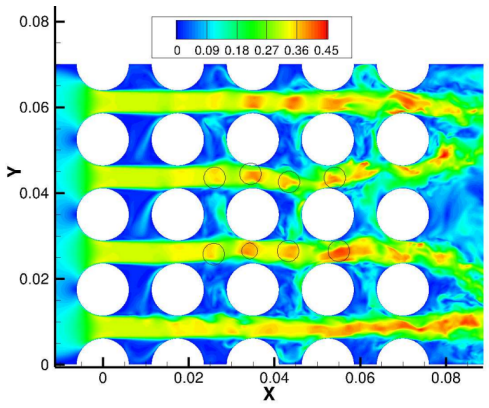

(h) $u^* = 2.16$, $Re_p = 3717$

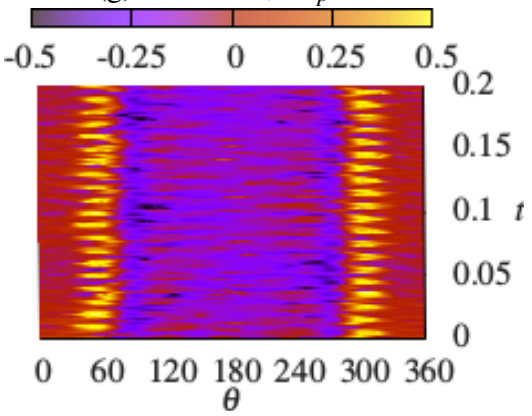

(i) $u^* = 2.47$, $Re_p = 4248$

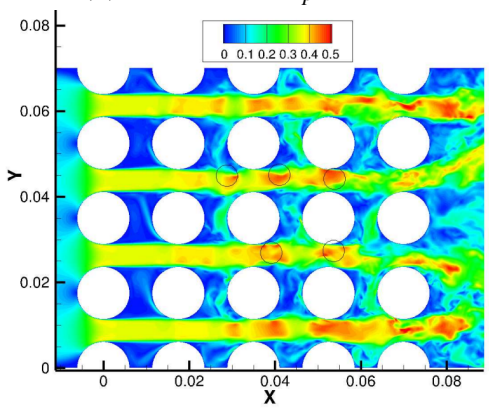

(j) $u^* = 2.47$, $Re_p = 4248$

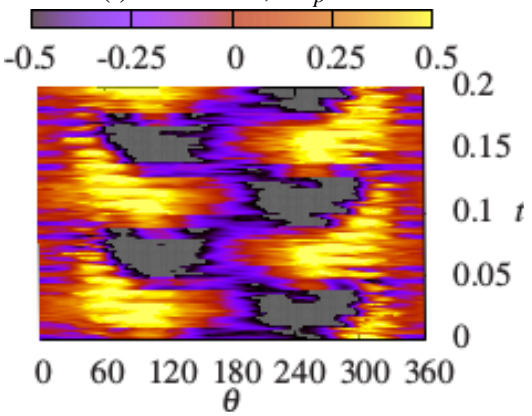

(k) $u^* = 2.77$, $Re_p = 4779$

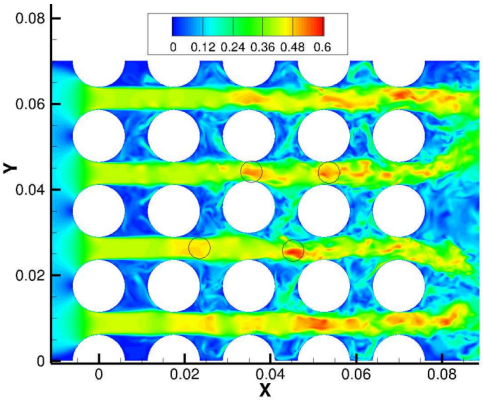

(l) $u^* = 2.77$, $Re_p = 4779$

Figure 3.14 Correspondence between the time evolving pressure profiles with the velocity field adjacent to the cylinder.

appearance of the high velocity patches on the flow streams and the time-evolution of the instantaneous pressure profile on cylinder surface are also shown for the pitch velocities increasing from $u^* = 1.23$ to $u^* = 3.08$. The cylinder vibration for the reduced velocity $u^* = 1.23$

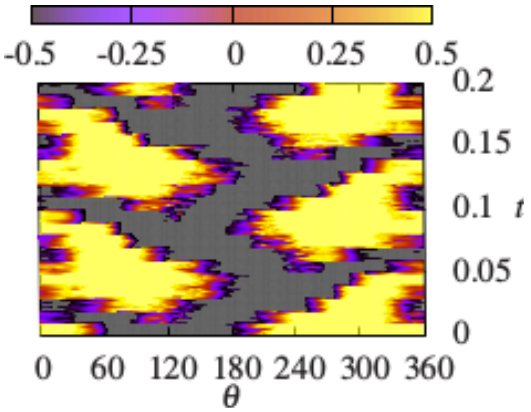

(m) $u^* = 3.08$, $Re_p = 5310$

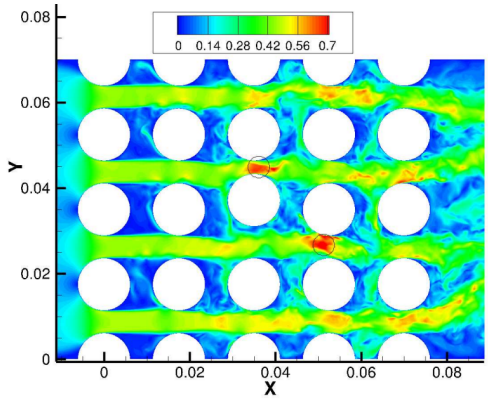

(n) $u^* = 3.08$, $Re_p = 5310$

Figure 3.14 Correspondence between the time evolving pressure profiles with the velocity field adjacent to the cylinder.

results in a symmetrical time-evolution of the surface pressure profile (Figure 3.14(a)). The corresponding flow field is shown in Figure 3.14(b). The high velocity flow patches due to the cylinder displacement are not distinct in this particular case, since the amplitudes of cylinder vibration are small. The time evolving pressure profiles for the reduced velocities $u^* = 1.54$ and $u^* = 1.85$ are anti-symmetrical (Figures 3.14(c) and 3.14(e)). Therefore the high velocity regions on the flow streams due to the cylinder displacement appear alternately, which are marked by circles on the flow streams (Figures 3.14(d) and 3.14(f)). The damping ratio of cylinder vibration decreases upto this reduced velocity ($u^* = 1.85$), while as the amplitude of cylinder oscillations shows an increase. The cylinder displacements at increased reduced velocities $u^* = 2.16$ and $u^* = 2.47$ give rise to a symmetrical appearance of the high velocity patches on the flow streams adjacent to the central cylinder, as shown in Figures 3.14(h) and 3.14(j). The corresponding cylinder surface pressure profiles show a symmetric time evolution (Figures 3.14(g) and 3.14(i)). The damping ratio (ζ) and the cylinder displacement (y) show an increase and a decrease respectively, when compared to the lower reduced velocities $u^* = 1.54$ and $u^* = 1.85$. Further increase in the values of reduced velocities $u^* = 2.77$ and $u^* = 3.08$ brings back the anti-symmetry in the time-pressure profiles on cylinder surface (Figures 3.14(k), 3.14(m) respectively) as well as the alternate appearance of the high velocity patches on flow streams adjacent to the central cylinder (Figures 3.14(l) and 3.14(n)). The damping ratio and the displacement of the cylinder vibration continue monotonously to a decrease and an increase respectively at these reduced velocities. The cylinder becomes unstable and it observes a diverged vibration response at the reduced velocity $u^* = 3.08$.

In figure 3.14(n), the high velocity patches adjacent to the cylinder at center are very clear.

u^*	$\lambda = u_p/f_n$ (m)	$\alpha = \lambda/P$	Note
1.23	0.0149	0.85	symmetry
1.54	0.0200	1.12	anti-symmetry
1.85	0.0224	1.28	anti-symmetry
2.16	0.0255	1.46	symmetry
2.47	0.03247	1.86	symmetry
2.77	0.0347	1.99	anti-symmetry
3.08	0.0382	2.18	anti-symmetry

Table 3.4 The perturbation wavelength (λ) for increasing reduced velocity.

It appears that the stremwise distance between the two high velocity patches nearly equals the pitch distance (P) of the array. The distance (λ) between two consecutive high velocity patches produced on a flow stream due to the cylinder oscillations can by defined as $\lambda = u_p/f_n$. Table (3.4) provides details of the distance between high velocity patches as well as nature of their appearance for increasing reduced velocity. The distance (λ) is normalized using pitch distance (P), given by $\alpha = \lambda/P$. The last column of Table (3.4) provides remarks on the appearance of the high velocity patches, which also corresponds to the time-evolving pressure profiles on the cylinder surface.

Understanding the nature of fluid force acting on a cylinder from a tube array is important in order to develop a theoretical model of the fluidelastic instability. The theoretical approach of (Tanaka and Takahara, 1981) and (Chen, 1983a) is probably the more accurate of all the present theories (Païdoussis et al., 2010). In their approach, the unsteady fluid force coefficients are measured directly using experiments. Although the numerous requirement of experimental data makes this approach less feasible, it signifies the necessity to understand the unsteady interaction between the cylinder and interstitial flow dynamics around cylinder. The analysis presented above aims to elucidate these unsteady fluid forces acting dynamically on the cylinder. The theoretical approach of (Lever and Weaver, 1982) and improved models based on it assume similar interaction between a single cylinder and the adjacent flow streams. In addition, (Khalifa et al., 2013) considered a phase lag between the cylinder vibration and fluid response and obtained improved predictions of the instability limits, although the nature of phase lag was speculated. The nature of total fluid force acting on the cylinder is more intuitive when the force is divided into two forces each due to an adjacent flow channel. The symmetry or antisymmetry in the time evolving pressure profile on the cylinder surface in-

dicates the dynamics of fluid forces imparted by each flow channel for the increasing flow velocity. These features of the interaction between cylinder and interstitial fluid flow of an array appear to be essential in theoretical predictions of the fluidelastic instability.

3.6 Conclusion

The onset of fluidelastic instability in a square normal cylinder array is studied by performing the Large Eddy Simulations (LES) of a single phase water cross-flow through the array. The fluid-structure coupling is achieved by the Arbitrary Lagrangian Eulerien (ALE) method. A single cylinder in 1-degree-of-freedom is allowed to oscillate freely and become fluidelastically unstable in the lift direction. The fluid flow in a static configuration (all cylinders fixed) is characterized by analysing the presence of shear layer instabilities in the interstitial flow, providing the coefficients of pressure, drag and lift forces on the cylinder and also variations in the flow attachment and separation locations with increasing Reynolds number. The dynamic LES results are first validated by a comparison with the experimental results in terms of the cylinder response frequency and the effective damping ratio. The surface pressure profile in the range of flow velocities in static cases are compared with the dynamic cases in order to elucidate the nature of dynamic forces acting on the cylinder. It is observed that the pressure force on the cylinder in the dynamic case simulations evolves either symmetrically or antisymmetrically for a particular value of the intertube velocity. The total force on the cylinder, when split into two components, each associated with an adjacent flow stream shows that the symmetric or antisymmetric pressure profiles are linked with the dynamic interaction between the cylinder and adjacent flow streams. It also explains the variations in the response amplitude, effective damping and the response frequency of the cylinder for increasing intertube velocity. The dynamic interaction between the cylinder and adjacent flow streams also reflects on the flow streams in terms of the distortions (high velocity patches), which travel along the flow through the array. The distortions on the flow streams appear simultaneously or alternately for the respective symmetric or anti-symmetric time evolution of the pressure profile on cylinder surface. Finally, the instability is characterized by the antisymmetric surface pressure profiles and the alternate appearance of the high velocity regions on the flow streams.

CHAPTER 4

A THEORETICAL MODEL OF THE FLUIDELASTIC INSTABILITY IN SQUARE INLINE TUBE ARRAYS

Abstract

An implicit mathematical model to predict the fluidelastic instability in square normal (90^o) tube arrays is presented in this article. The mathematical development is based on the transient interaction between a single cylinder and the flow streams adjacent to the cylinder. The fluid flow is assumed in a single phase. The cylinder is assumed to oscillate in 1-degree-of-freedom in the lift direction only. A small displacement of the cylinder introduces an equivalent perturbation on the surrounding fluid flow. The oscillating cylinder produces timely perturbations, which are carried by the interstitial flow streams. The waveforms of the flow disturbances are assumed to interact with the array pattern. The total force on the cylinder is thus modified due to these interactions. The fluidelastic proportionality constant is obtained as a function of the pitch ratio and the Euler number. The mathematical development results in an implicit model for the critical flow velocity. The model predictions of the critical flow velocity are in fairly good agreement with the experimental results.

Keywords

Flow-induced vibrations, heat exchanger tube arrays, fluidelastic instability, Euler number

Contents

4.1 Introduction

The flow-induced vibrations in the heat exchanger tube arrays exhibit different mechanisms. The vibrations are generally classified under, vortex-induced vibration, turbulent buffeting, acoustic vibration and the fluidelastic vibration. The underlying mechanisms in the first three types of vibrations are more or less well understood, hence the safe operating conditions can be procured by appropriate design guidelines against these instabilities. The exact mechanism underlying the fluidelastic instability is relatively less understood. The damages occurred due to the fluidelastic instability are severe and short term. The phenomenon is given major attention in the recent decades in order to establish the accurate stability thresholds of the critical flow velocities for the flow through tube bundles. There are several mathematical models available for the fluidelastic instability. The presence of the fluidelastic excitations in the context of cylinders was first reported in (Roberts, 1962). A detailed work in (Connors, 1970) and (Connors, 1978) led to a simplified model for the fluidelastic instability,

$$\frac{u_{pc}}{f_n D} = K\left(\frac{m\delta}{\rho D^2}\right)^a \tag{4.1}$$

Where, u_{pc}, f_n and D are the critical pitch (minimum gap) velocity, natural frequency and the diameter of the cylinder respectively. The non-dimensional critical pitch velocity is proportional to the mass m, logarithmic decrement δ of the cylinder vibration in the non-dimension forms with the exponent a. K is the constant of proportionality. ρ is the fluid density. An enormous amount of work is carried out in terms of the experiments and the theoretical developments, since the work of (Connors, 1970), in order to better understand and predict the phenomenon. The topic is well reviewed in (Païdoussis, 1983a), (Weaver and Fitzpatrick, 1988b), (Pettigrew and Taylor, 1991) and more recently in (Païdoussis et al., 2010, Chapter 5). A detailed review on the mathematical models of fluidelastic instability is provided in (Price, 1995).

In this article, a new mathematical model is presented for the fluidelastic instability in square normal tube arrays. The model is based on the dynamic interaction between a single cylinder oscillating in 1-degree-of-freedom (1-DOF) in transverse/lift direction only. The displacement of the cylinder produces small deformations in the flow streams adjacent to the cylinder. The flow perturbations are modeled as a waveforms on top of the flow streams. The flow streams carrying the perturbations interact elastically with the cylinder, especially at the low values of the mass ratio ($m/\rho D^2$). The mathematical development and a procedure to estimate the critical pitch velocity u_{pc} is formulated in the following section. The model predictions are compared with a set of experimental data reported in (Pettigrew and Taylor, 1991) for the square normal tube arrays. In addition, a stability map is established for a pitch ratio $p^* = 1.33$, similar to the stability map of (Tanaka and Takahara, 1981) for the square normal array of pitch ratio $p^* = 1.33$.

4.2 Theory

The fluid flow through a square normal tube array under cross flow forms a typical flow pattern of the interstitial flow. The fluid flowing through channels observes a variation in the flow velocity due to the decrease and increase of the cross-sectional flow area available in the array. The pitch distance is the minimum distance between two cylinders of the array, where the flow accelerates. The displacement of cylinder in transverse direction results in either a decrease or an increase in the adjacent cross-sectional area. Consequently, the flow velocity observes locally either an increase or a decrease respectively. The perturbations on the flow streams are conveyed downstream as well as, to a certain extent, upstream on the flow streams. The change in the flow streams modifies the total force acting on the moving cylinder, which further results in a modification of the cylinder displacement. The streamwise distance between two consecutive perturbations is directly proportional to the intertube flow velocities, assuming the response frequency of cylinder remains more or less constant. In addition to the increased fluid forces due to the increased energy level, the dynamics of the flow disturbances travelling through the non-uniform array pattern has an influence on the total force acting on the cylinder. The mathematical model proposed in the following section is based on these dynamic interactions between the flow streams and a cylinder of the array.

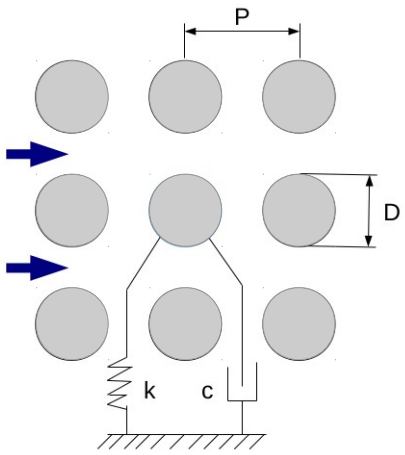

Figure 4.1 The kernel of a square normal cylinder array.

4.2.1 Mathematical Model

The kernel of an in-line array is shown in Figure 4.1. The diameter and pitch distances are represented by D and P respectively. The pitch ratio ($p^* = P/D$) is equal in both the longitudinal (in-flow) and transverse (flow-normal) directions. The flow direction is shown by the bold arrows in the figure. The central cylinder is assumed to oscillate in the flow normal direction only. The schematic of the mass on a spring physics is shown, where k, c stand for the cylinder stiffness and damping respectively. The mass of the cylinder per unit length is represented by m. The mass includes the hydrodynamic mass of the fluid medium at rest. Similarly the stiffness (k) and damping (c) coefficients are defined with respect to the quiescent fluid medium. Equation (4.2) represents the motion of cylinder in the flow normal direction. y is the instantaneous cylinder displacement in the flow normal direction. t represents the time. The right hand term of the equation is a sinusoidal fluid force with an amplitude f_y per unit length of the cylinder and an angular periodicity (ω_{sh}) associated with the force.

$$m\frac{d^2y}{dt^2} + c\frac{dy}{dt} + ky = f_y e^{-\hat{\imath}\omega_{sh}t} \tag{4.2}$$

Where $\hat{\imath} = \sqrt{-1}$. Using the definitions of the natural angular frequency (ω_n) and damping ratio (ζ) of the cylinder, $\omega_n = \sqrt{k/m}$ and $\zeta = c/2\sqrt{km}$, Equation (4.2) can be written as,

$$\frac{d^2y}{dt^2} + 2\zeta\omega_n\frac{dy}{dt} + \omega_n^2 y = \frac{f_y}{m}e^{-\hat{\imath}\omega_{sh}t} \tag{4.3}$$

The general solution can be given as,

$$y = Ye^{-\hat{\imath}(\omega_{sh}t+\theta)} \tag{4.4}$$

Where, Y is the magnitude of cylinder oscillations, while as θ is the phase difference between the fluid force and the cylinder response (y). The magnitude (Y) can be obtained by solving Equation (4.4) and Equation (4.3).

$$-Y\omega_{sh}^2 e^{-\hat{\imath}\omega_{sh}t} + 2\zeta\omega_n Y\left(-\hat{\imath}\omega_{sh}\right)e^{-\hat{\imath}(\omega_{sh}t+\theta)} + \omega_n^2 Y e^{-\hat{\imath}(\omega_{sh}t+\theta)} = \frac{f_y}{m}e^{-\hat{\imath}\omega_{sh}t}$$

$$-Y\omega_{sh}^2 + 2\zeta\omega_n Y\left(-\hat{\imath}\omega_{sh}\right) + \omega_n^2 Y = \frac{f_y}{m}e^{\hat{\imath}\theta}$$

By equating the real and imaginary parts, we can obtain,

$$\left(\omega_n^2 - \omega_{sh}^2\right)Y = \frac{f_y}{m}\cos\left(\theta\right) \tag{4.5}$$

$$\left(-2\zeta\omega_n\omega_{sh}\right)Y = \frac{f_y}{m}\sin\left(\theta\right) \tag{4.6}$$

Thus,

$$Y = \frac{f_y/m}{\sqrt{\left(\omega_n^2 - \omega_{sh}^2\right)^2 + \left(2\zeta\omega_n\omega_{sh}\right)^2}} \tag{4.7}$$

The unsteady response amplitude (Y) of the cylinder is directly proportional to the magnitude of fluid force f_y and it is inversely proportional to the mass and damping terms. The phase difference (θ), between the fluid force acting on the cylinder and cylinder displacement is considered as an important component of the fluidelastic instability, particularly in the theoretical models based on (Lever and Weaver, 1982). The exact physics of the phase lag (θ) is not known. It is approximated by using an expression based on a hydraulic analogy in (Lever and Weaver, 1982). In Equation (4.7), the phase lag (θ) is eliminated in the derivation of the displacement amplitude (Y), although its effect is incorporated in the square-root term.

The fluid force (f_y) in Equation (4.7) can be expressed in terms of the pitch velocity (u_p) by an empirical relation as,

$$f_y = Eu_y\,\frac{1}{2}\rho u_p^2\,D \tag{4.8}$$

Where, Eu_y is the component of the Euler number in the transverse direction. The Euler

number in heat exchanger designs is commonly defined as,

$$Eu = \frac{\Delta p_{row}}{\frac{1}{2}\rho u_p^2} \tag{4.9}$$

Where, Δp_{row} is the pressure drop across a row of an array. Thus the Euler number in the flow direction Eu_x is simply the Euler number Eu. The flow normal component of the Euler number Eu_y is assumed to be based on the instantaneous pressure drop in the lift direction (Δp_y) across the cylinder. Using Equation (4.8) in Equation (4.7) gives,

$$Y = \frac{Eu_y \, \frac{1}{2}\rho u_p^2 \, D}{m\omega_n^2 \sqrt{\left(1 - \left(\frac{\omega_{sh}}{\omega_n}\right)^2\right)^2 + \left(2\zeta \frac{\omega_{sh}}{\omega_n}\right)^2}} \tag{4.10}$$

The term in the square root acts as a mechanical impedance, which signifies the resistivity of the cylinder to the imposed harmonic force. Let the mechanical impedance be,

$$I_m = \sqrt{\left(1 - \left(\frac{\omega_{sh}}{\omega_n}\right)^2\right)^2 + \left(2\zeta \frac{\omega_{sh}}{\omega_n}\right)^2} \tag{4.11}$$

Rearranging the terms in Equation (4.10) leads to,

$$\left(\frac{m}{\rho}\right)\frac{Y}{D} I_m = \left(\frac{Eu_y}{2\,(2\pi)^2}\right)\left(\frac{u_p^2}{f_n^2}\right) \tag{4.12}$$

The amplitude (Y) of the cylinder vibration can be expressed in terms of the fraction (h) of the minimum distance between two cylinders ($P - D$) as,

$$\frac{Y}{D} = \frac{h\,(P-D)}{D} = h\,(p^* - 1) \tag{4.13}$$

The expression for the pitch velocity (u_p) using Equation (4.12) and Equation (4.13) becomes,

$$\frac{u_p}{f_n D} = \sqrt{\frac{8\pi^2 h\,(p^* - 1)}{Eu_y}} \left(\frac{m}{\rho D^2}\right)^{0.5} I_m^{0.5} \tag{4.14}$$

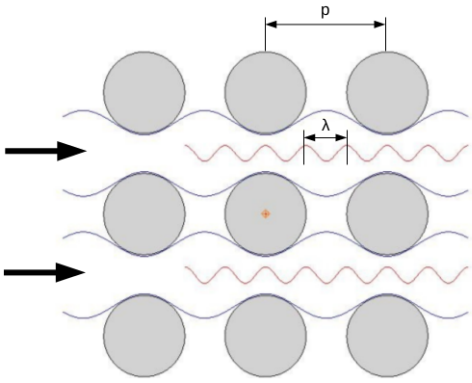

Figure 4.2 Idealized interactions between the central cylinder and adjacent flow-streams.

Modeling the impedance

The impedance I_m represents the dynamics between the flow periodicity (ω_{sh}) and the cylinder natural frequency (ω_n) at a particular flow velocity (u_p). It also contains the damping ratio (ζ). The dynamic interaction between the flow streams and the cylinder oscillations can be modeled using the impedance I_m. The oscillating central cylinder perturbs the adjacent flow streams. The perturbations, in terms of the local high/low velocities, travel on top of the flow streams. The perturbations appear on the stream tubes in a timely manner, since they are generated as a result of the harmonic oscillations of the cylinder. The distance between the two high/low velocity perturbations (or simply the wavelength of the perturbation wave) λ can be defined as,

$$\lambda = 2\pi \frac{u_p}{\omega_n} \tag{4.15}$$

The interstitial flow with the flow perturbation waves is idealised in Figure (4.2). The flow direction is shown by the bold arrows. The smaller waves with a wavelength λ represents the perturbation wave. Similarly the pitch length (P) can be represented in terms of the angular frequency (ω_{sh}), representing the flow periodicity due to the array pattern as,

$$P = 2\pi \frac{u_p}{\omega_{sh}} \tag{4.16}$$

The flow perturbations produced due the cylinder vibration travel with the adjacent flow streams through the non-uniform cross-sectional areas of the array pattern. The wavelength λ linearly increases with the pitch velocity u_p as per Equation (4.15). At a particular value of the velocity (u_p), where λ equals the pitch distance ($\lambda \approx P$), the impedance (I_m) of the system becomes minimum. Thus the cylinder experiences less resistance for the vibration.

The amplitude of oscillations increases as per Equation (4.10), in other words, the effective damping (damping of the cylinder ζ and the fluid damping coefficient) decreases. In a contrary scenario, the increase of impedance results in an increase of the effective damping of the cylinder. The increase or decrease of the effective damping of cylinder reflects in the respective decrease or increase of the amplitudes of cylinder vibration (Equation 4.10). Thus the impedance (I_m) varies dynamically with the increasing flow velocity (u_p). In general, we can consider $n\lambda \approx P$ for $\lambda \leq P$ and $\lambda \approx nP$ for $\lambda \geq P$, where n is a positive integer multiplier. Let α be the ratio of the wavelength λ and the pitch distance P of the array. We can write,

$$\alpha = \frac{\lambda}{P} = \frac{\omega_{sh}}{\omega_n} \tag{4.17}$$

The fluidelastic instability model presented by (Yetisir and Weaver, 1993a), (Yetisir and Weaver, 1993b) is based on the the semi-analytical model of (Lever and Weaver, 1982). The unsteady model is improved (in (Yetisir and Weaver, 1993a), (Yetisir and Weaver, 1993b)) by using a decay function for the perturbations away from an oscillating cylinder, in addition to the phase lag function used in (Lever and Weaver, 1982). In these formulations the flow disturbances are accounted in terms of the perturbations in the area of the flow streamtube. Thus the perturbations in the streamtube area introduced by a moving tube are assumed to decay away from the tube. A simple decay function for the area perturbation is used (refer Equation 2 in (Yetisir and Weaver, 1993b)). On the same ground, here, the influence of the perturbation generated by a cylinder is assumed to decay exponentially as it travels away from the cylinder. The ratio α can be redefined as β, for the multiple synchronizations between λ and P as well as by taking into account the exponential decay as,

$$\beta = 1 + \sin(\pi\alpha)\exp(-\alpha) \tag{4.18}$$

The impedance I_m for the tube array can be redefined using β as,

$$I_m = \sqrt{(1-\beta^2)^2 + (2\zeta\beta)^2} \tag{4.19}$$

Stability criteria and mechanisms

The amplitude of cylinder vibration ($Y = h(p^* - 1)$) increases (or may also decrease depending on the dynamics between the perturbation wave and the array pattern) with the increasing pitch velocity (u_p), as per Equation (4.14). The unsteady and stationary response of the cylinder is expected to follow stable limit cycles, atleast for $h < 0.5$. The limiting value of h is 1, for

which the cylinder strikes the neighbouring cylinders. The critical value of the amplitude of cylinder oscillations can be taken as half the gap distance $(P-D)$, with $h_c = 0.5$. The Euler number (Eu_y) in the lift direction was defined in terms of the flow normal pressure drop (ΔP_y) across the cylinder. The pressure drop in the lift direction across the cylinder remains small for the smaller amplitude oscillations of the cylinder. At the onset of the instability, the cylinder, which oscillates at higher amplitudes, tends to cross the adjacent flow streams. Thus, the upper limit for the pressure drop ΔP_y is the pressure drop (Δp_{row}) across a row of the array. The critical value of the flow normal Euler number (Eu_y) can be used as $Eu_y = Eu_c = Eu$, for the corresponding Reynolds number (Re_c). The Equation (4.14) can be written for the critical pitch velocity (u_{pc}) as,

$$\frac{u_{pc}}{f_n D} = K_c \left(\frac{m}{\rho D^2} \right)^{0.5} I_m^{0.5} \tag{4.20}$$

Where the constant of proportionality K_c is,

$$K_c = \sqrt{\frac{8\pi^2 h_c \left(p^* - 1\right)}{Eu_c}} \tag{4.21}$$

The fluidelastic instability is usually classified under different mechanisms, mainly, in the stiffness controlled and damping controlled mechanisms, as predicted by (Chen, 1983a), (Chen, 1983b) as well as (Price and Païdoussis, 1986a). In the damping controlled mechanism the fluidelastic forces are in phase with the cylinder velocity, while as in the stiffness controlled mechanism the forces are in phase with the cylinder displacement. Furthermore, at a low mass damping parameter $(m\delta^{\dagger}/\rho D^2)$, the instability is said to be damping controlled, while as at a higher mass-damping parameter the instability is said to be stiffness controlled. On the contrary, in (Tanaka et al., 2002) the mechanisms are found to assist each other, and hence the instability is considered to be a combination of both the stiffness and damping controlled mechanisms.

The phase lag (θ) between the cylinder displacement and the forces can be approximated in terms of the modeled mechanical impedance (Equation (4.19)) and the parameter β as,

$$\theta = \arcsin\left(\frac{2\zeta\beta}{I_m} \right) \tag{4.22}$$

At the low values of mass-damping parameter, where the critical flow velocities are low, the parameter β oscillates about 1 with the increasing flow velocity. The phase lag (θ) thus oscillates between 0 and $\pi/2$, which indicates the presence of both stiffness as well as damping

$^{\dagger}\delta = 2\pi\zeta/\sqrt{(1-\zeta^2)}$, for small ζ, $\delta \approx 2\pi\zeta$

controlled mechanisms, an observation similar to the (Tanaka et al., 2002). On the other hand, for high values of the mass-damping parameter (or the higher flow critical velocities) the parameter β converges to 1. It leads to the phase lag value of $\theta = \pi/2$. Although it implies that the fluid forces are in phase with the cylinder velocity, the higher values of mass-ratio ($m/\rho D^2$) result into motion dependant forces (Chen, 1983a) (Chen, 1983b), (Price and Païdoussis, 1986a) on the cylinder. Therefore it is classified under the stiffness controlled mechanism. The paradox is also discussed in (Païdoussis et al., 2010, chapter 5). Furthermore, at higher values of the mass-damping parameter (typically for gaseous flows), the mechanical impedance (I_m) simply becomes $I_m = 2\zeta$. Thus, Equation (4.20) takes the form of Equation (4.1) with a value of the exponent $a = 0.5$, common for both the mass ratio ($m/\rho D^2$) and the damping ratio (ζ).

4.2.2 Estimation of the critical flow velocity

The derivation for the critical pitch velocity (u_{pc}) in Equation (4.20) is in an implicit form. The terms Eu_c in the constant of proportionality (K_c) and the wavelength λ in the impedance I_m term are functions of the pitch velocity u_p itself. The Euler number (Eu) for different Reynolds numbers and array configurations is generally provided in the heat exchanger design handbooks in terms of empirical relations. Equations (4.23), (4.24) represent power series providing the values of Euler number (Eu) at different Reynolds numbers (Re) for the square normal (90^o) and square rotated arrays (40^o). The values of empirical constants c_i varies with the array configuration. The table in Figure (4.3) provides the values of empirical coefficients c_i for the in-line square arrays for different pitch ratios (p^*). Figure 4.3 shows the curves generated using these empirical relations.

$$Eu = \sum_{i=0}^{4} \frac{c_i}{Re^i} \quad \forall \text{ in-line and rotated square arrays} \tag{4.23}$$

$$= \sum_{i=0}^{4} c_i Re^i \quad \forall \text{ in-line arrays, longitudinal pitch ratio } p^* = 2.5 \tag{4.24}$$

An iterative procedure can be followed in order to solve Equation (4.20) for u_{pc}. The structural parameters (m, f_n and ζ) in quiescent fluid medium, fluid density (ρ), fluid viscosity (μ) and the geometrical parameters (D, P) are known beforehand. The critical pitch velocity u_{pc} is thus estimated using Equation (4.20) for an arbitrary value of the pitch velocity u_p, such that $u_{pc} = u_p$. Figure 4.4 shows the flow chart of the procedure to estimate the critical pitch velocity. At first, for an arbitrary value of the pitch velocity (u_p), Reynolds number

p^*	Re range	c_0	c_1	c_2	c_3	c_4
1.25	3 to 2×10^3	0.272	0.207×10^3	0.102×10^3	-0.286×10^3	–
1.25	2×10^3 to 2×10^6	0.267	0.249×10^4	-0.927×10^7	0.1×10^{11}	–
1.50	3 to 2×10^3	0.263	0.867×10^2	-0.202×10^0	–	–
1.50	2×10^3 to 2×10^6	0.235	0.197×10^4	-0.124×10^8	0.312×10^{11}	-0.274×10^{14}
2.00	7 to 800	0.188	0.566×10^2	-0.646×10^3	0.601×10^4	-0.183×10^5
2.00	800 to 2×10^6	0.247	-0.595	0.15	-0.137	0.396

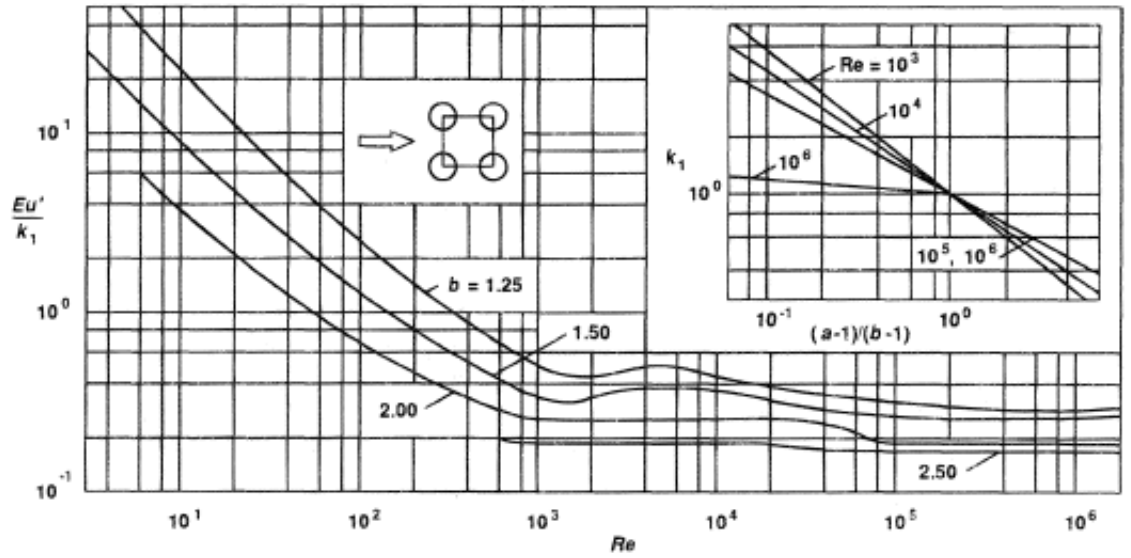

Figure 4.3 The 'pressure drop coefficient vs Reynolds number plot' for in-line tube banks. Source: (Singh and Soler, 1984). (a, b are the pitch ratios in the transverse and in-line direction respectively).

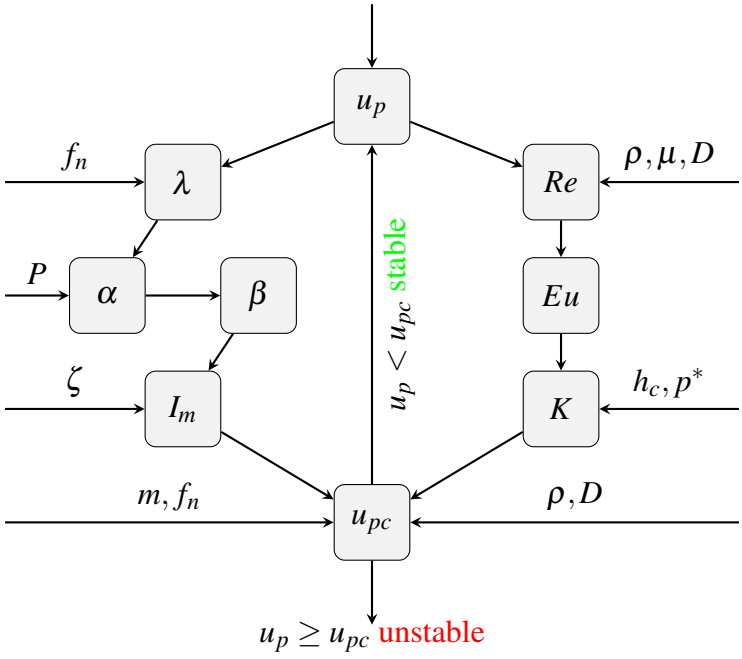

Figure 4.4 Flow chart for an estimation of the critical pitch velocity u_{pc}.

Re is calculated using the density ρ, fluid viscosity μ and the cylinder diameter D. The Euler number is estimated using the value of Reynolds number and the appropriate empirical relation (Equations 4.23 or 4.24). The Euler number (Eu) and the critical value of the fraction (h_c) are used to estimate the critical proportionality constant K_c using Equation (4.21). On the other hand, the perturbation wavelength λ is obtained using the arbitrary pitch velocity u_p and the natural frequency of the cylinder f_n as $\lambda = u_p/f_n$. The parameter α and β can be readily obtained by using Equations (4.17) and (4.18) respectively. The mechanical impedance I_m is estimated by using the damping of cylinder (ζ) and the parameter β in Equation (4.19). Thus for an arbitrary pitch velocity u_p, a critical value of the pitch velocity (u_{pc}) can be obtained using Equation (4.20). The vibrations in cylinder are critical for $u_p = u_{pc}$.

4.3 Model predictions of experimental results

The experimental results of the fluidelastic instability in square normal (90^o) tube arrays are taken from the review article of (Pettigrew and Taylor, 1991). The results of 11 experiments and their model predictions are enlisted in Table (4.1). In the second column of the table, the names of experiment series are listed, which refer to the corresponding data source. Please refer to Table 2 of (Pettigrew and Taylor, 1991) for further details. The last two data sets,

named as AMOVI and DIVA, are unpublished results. All the experiments are carried out with the water flows except the fifth one, which is with the air flow. The pitch ratio (p^*) and the cylinder diameter (D) in m are listed in the third and fourth columns respectively. The cylinder mass per unit length m in kg/m, natural frequency f_n in Hz and the damping ratio ζ are listed in the fifth, sixth and seventh columns respectively. These quantities are defined with respect to the quiescent flow medium. The fluid density ρ in kg/m^3 and viscosity ν in $Pa{\cdot}s$ is tabulated in the eighth and ninth columns of the table. The values of the mass-damping parameter ($m\delta/\rho D^2$) are calculated and listed in the tenth column. The critical pitch velocities (u_{pc}) in m/s for each experiment are provided in the eleventh column of the table. The non-dimensional critical pitch velocities (critical reduced velocities) u^*_{pc} are listed in the twelfth column. The remaining columns of the table provide the results of model predictions. The critical reduced pitch velocity u^*_{pc} and the critical pitch velocity u_{pc} in m/s estimated using Equation (4.20) are listed in the thirteenth and fourteenth columns of the Table (4.1). The corresponding Reynolds number (Re_c), Euler number (Eu_c) and the proportionality constant (K_c) are tabulated in the fifteenth, sixteenth and the seventeenth columns of the table respectively.

It is necessary to note that the experimental results compiled in (Pettigrew and Taylor, 1991) are gathered from different sources. The experimental results can have discrepancies in terms of some parameters such as size of the array, length of the array, exact value of the critical flow velocity and so on. In addition to these parameters, the inflow turbulence, the location of the tube in an array, vibration in all tubes, degrees-of-freedom in vibration are known to have an influence on the value of critical flow velocity. The configuration of AMOVI and DIVA experiments contain tube bundles of 5×5 and similar to the assumptions made in the theoretical development presented in this article, i.e. only the central cylinder is free to oscillate in the lift direction. The instability criteria used in the theory are, first, the amplitude of oscillations becomes half the gap between two adjacent cylinders separated by the pitch and second, the lift component of the Euler number (Eu_y) takes the maximum value based on the pressure drop (Δp_{row}) across a row of the array. Therefore the predicted critical velocities may serve as a general threshold of the instability in the array. The critical reduced velocities (u^*_{pc}) predicted by the theory are in a fair agreement with the experimental results, especially considering the different values of the input parameters.

Figure (4.5) shows the variation in the model (Equation (4.20)) parameters for increasing value of the arbitrary reduced pitch velocity (u^*_p). The Figures 4.5(a), (b) show predictions of the critical flow velocity for a water flow experiment (AMOVI), in which the first plot (Figure 4.5(a)) shows the variation in the critical reduced velocity u^*_{pc}, while the second plot shows the variations in the impedance (I_m), parameter β, the Euler number (Eu) and the fluidelastic

		Expt.								Model			
No.	Test Series[a]	p^*	D	m	f_n	ζ	$\frac{m\delta}{\rho D^2}$	u_{pc}	u^*_{pc}	u^*_{pc}	Re_c	Eu_c	K_c
			$\times 10^{-3} m$	kg/m	Hz	%		m/s					
1	Nak86a (water)	1.42	19.05	1.1000	12.30	0.990	0.1886	0.60	2.56	2.73	12271	0.36	6.85
2	Nak86a (water)	1.42	19.05	1.1000	20.20	1.460	0.2781	1.45	3.77	2.78	20154	0.33	7.14
3	Nak86a (water)	1.42	19.05	1.1000	24.30	1.200	0.2286	1.92	4.15	2.79	24408	0.31	7.27
4	Axisa84 (water)	1.44	19.05	0.4920	51.00	0.700	0.0596	1.10	1.13	1.42	26391	0.30	7.51
5	Axisa84 (air)	1.44	19.05	0.4920	75.00	0.200	14.197	21.0	14.70	15.96	25989	0.31	7.51
6	Pett87 (water)	1.22	13.00	0.5400	25.90	0.930	0.1867	0.81	2.41	2.35	10238	0.44	4.44
7	Pett87 (water)	1.47	13.00	0.5100	26.50	0.840	0.1593	0.87	2.53	2.87	12814	0.34	7.43
8	W&AR85 (water)	1.50	25.40	1.2570	16.90	0.590	0.0722	1.05	2.45	2.89	31593	0.29	8.31
9	Scot87 (water)	1.33	25.40	1.2900	16.20	2.700	0.3393	0.86	2.09	2.55	26552	0.33	6.28
10	AMOVI (water)	1.44	12.15	0.4523	11.68	1.250	0.2407	0.47	3.31	2.82	4816	0.37	6.84
11	DIVA (water)	1.50	30.00	1.4700	18.50	0.920	0.0944	1.70	3.06	2.90	48025	0.27	8.54

Table 4.1 Model predictions against the experimental data.

[a] Please refer Table 2 of (Pettigrew and Taylor, 1991) for the references corresponding to the test series names. The AMOVI and DIVA experiments are unpublished data.

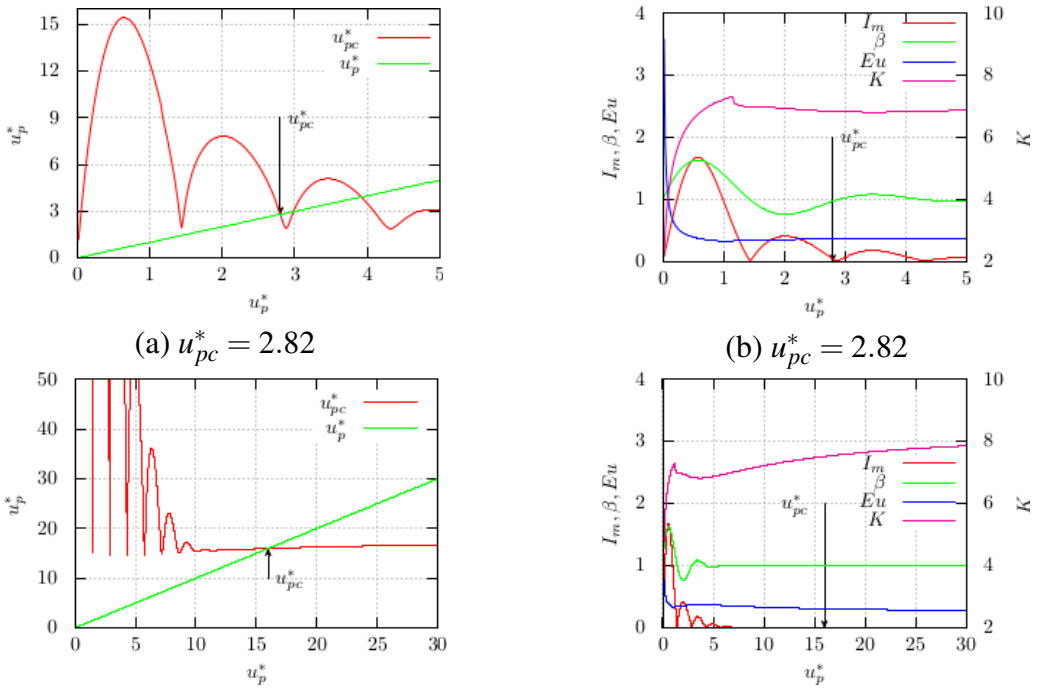

(a) $u^*_{pc} = 2.82$ (b) $u^*_{pc} = 2.82$

(c) $u^*_{pc} = 15.96$ (d) $u^*_{pc} = 15.96$

Figure 4.5 Model predictions of the critical pitch velocity (u_{pc}) for (a), (b) a water flow and (c), (d) an air flow experiments.

proportionality constant (K_c) against the increasing reduced velocity (u^*_p). Similarly, Figures 4.5(c), (d) are the model predictions for the air flow experiment (Axisa84) listed in the Table (4.1). It is clear from the Figures 4.5(a), (b) (as well as from (c), (d)) that the main source of the variation in the critical reduced pitch velocity (u^*_{pc}) is the impedance I_m of the system. The Euler number and the proportionality constant show some variations initially for low Reynolds numbers, but over the large range their values remain nearly constant.

An important difference between the water flow and the air flow experiments in Figure (4.5) is the variations in the critical reduced velocity at the onset of the instability. In Figure 4.5(a) the arbitrary reduced velocity becomes greater than the estimated critical reduced velocity after $u^*_p = u^*_{pc} = 2.82$. Although with further increase of the u^*_p, the critical reduced velocity u^*_{pc} becomes smaller than the u^*_p, indicating a possibility of the restabilization of the vibration in cylinder. On the other hand, the critical reduced velocity (u^*_{pc}) in Figure 4.5(c) remains almost constant for $u^*_p \gtrapprox 10$, providing no possibility of the restabilization. The major difference between these two experiments is the mass ratio ($m^* = m/\rho D^2$), due the difference in the fluid mediums. The influence of the mass ratio (m^*) on the fluidelastic instability thresholds is studied in (Tanaka and Takahara, 1981) for a square normal tube array. In their approach, the critical reduced velocity is estimated using the measured unsteady fluidelastic

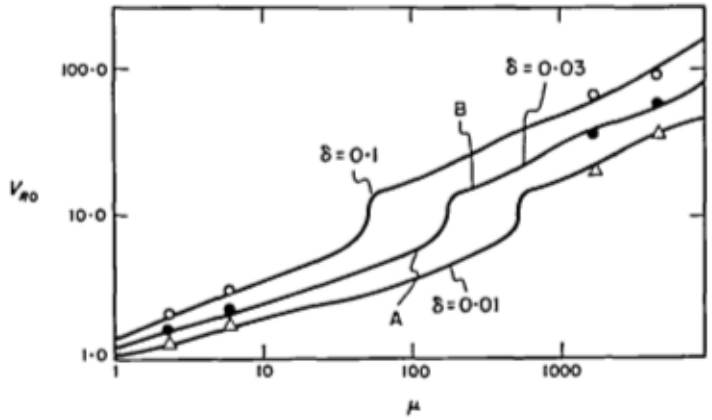

(a) Influence of the mass ratio on the critical reduced velocity (Source: (Tanaka and Takahara, 1981))

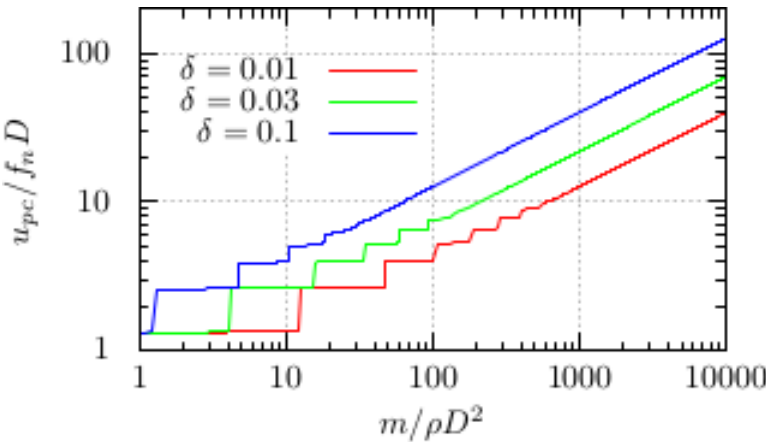

(b) Model prediction of the critical reduced velocity for the same parameters as in (a)

Figure 4.6 Comparison of the stability thresholds, for various mass ratio and three values of the logarithmic decrement, between (Tanaka and Takahara, 1981) and the proposed model (Equation 4.20).

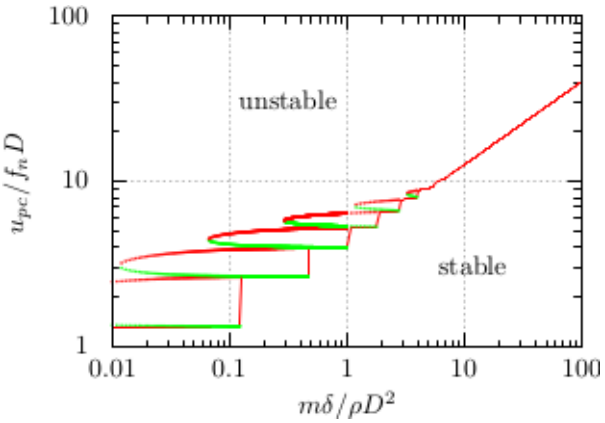

Figure 4.7 Theoretical prediction of the instability boundaries for an in-line array with the pitch ratio $p^* = 1.33$ and the logarithmic decrement $\delta = 0.01$.

forces on a cylinder of the array. Figure 4.6(a) shows the continuous stability boundaries for three values of the logarithmic decrement (δ) and varying mass ratio (m^*) for a small (2×3) square array with the pitch ratio $p^* = 1.33$. In addition, there are some experimental data points on the stability map (Figure 4.6(a)), which are obtained for a bigger (4×7) square normal array with the same pitch ratio ($p^* = 1.33$). The labels 'A' and 'B' indicate the different modes of vibration. The model (Equation (4.20)) prediction of the threshold boundaries for the pitch ratio $p^* = 1.33$ and for different values of the δ and m^*, similar to that of (Tanaka and Takahara, 1981) used in Figure 4.6(a), are shown in Figure 4.6(b). The Figures 4.6(a) and (b) appear to make a match qualitatively and quantitatively, particularly for the higher values of the mass ratio. Further the nature of the stability boundaries changes for $u^*_{pc} \gtrapprox 10$ in both the stability maps of Figure (4.6).

The stability thresholds predicted in Figure 4.6(b) by using Equation (4.20) are the lower stability limits for a particular value of the logarithmic decrement (δ). As discussed above, the variation in the critical reduced pitch velocity at low mass ratio (low velocities) provide a possibility of the restabilization (at least theoretically) for velocities higher than the critical values. The actual stability boundaries predicted by the model include the multiple stability thresholds. For example, Figure (4.7) show the stability map for a square array with pitch ratio $p^* = 1.33$. A constant value of the logarithmic decrement is used ($\delta = 0.01$). The plot shows the critical reduced pitch velocity (u^*_{pc}) as a function of the mass-damping parameter ($m\delta/\rho D^2$). The red curves represent the unstable boundaries for an increasing value of the velocity, while the green curves stand for the restabilization boundary. Further investigation is required for accurate the shapes of the multiple stability boundaries, since it depends on the modeling of mechanical impedance term (I_m) of the implicit model.

4.4 Conclusion

A theoretical model for the fluidelastic instability is developed. The dynamic interaction between the interstitial flow streams and the cylinder vibration is modeled by means of the perturbation waveforms on the flow streams due to cylinder displacements. The influence of the flow perturbations on the cylinder is assumed to decrease exponentially away from the cylinder. The effective damping of the cylinder vibration varies with the increasing flow velocities, this effect is attributed to the synchronization of the perturbations travelling on the flow streams with the non-uniform flow paths of the array geometry. Incorporating these physical aspects of the fluidelastic interactions lead to an implicit mathematical model for the critical flow velocity. The constant of proportionality is a function of the array pitch ratio and the Euler number (which is a function of the Reynolds number). The model predictions show a fair agreement with several experimental data. The multiple stability regions at lower mass-damping parameter are predicted by the model, although there is a need for further investigation in order to precise the shapes of the multiple instability boundaries.

CHAPTER 5

INTRODUCTION TO REDUCED-ORDER MODELING

Abstract

An introduction to Reduced-Order Modeling (or Model Order Reduction) is presented in this article. the model reduction techniques in the field of control theory and analysis of large nonlinear dynamical systems are briefly reviewed. At first, preliminary concepts for the model reduction are defined. Secondly, the common model reduction methods, namely, *Truncated Balanced Approximation*, *Krylov subspace approximations* and *Proper Orthogonal Decomposition* are presented. The ultimate aim of the model reduction methods is to approximate a complex and large dynamical system by a simpler reduced system, while keeping its essential features. Thus the insignificant and unwanted parts of the original system are eliminated in order to reduce the system size and computational time.

Keywords

Reduced-Order Modeling, Singular Value Decomposition, Krylov subspaces, Proper Orthogonal Decomposition, Galerkin projection

Contents

5.1 Introduction

Model reduction techniques has its origin in the control theory and applications. The complex input-output relations of a control systems are simplified by using reduced-order models (ROM) (Benner et al., 2006). In science, mathematical models are regularly used to describe physics of a system, especially with the development of Newtonian mechanics. Often, exact solutions of the mathematical models are impossible because of the complexity of mathematics involved. In such scenarios, model reduction plays an important role in approximating the behaviour of original system. Prior to the development of the computers and computational algorithms, model reduction was performed by using simple trigonometric functions (Fourier's development) and generally using simplified mathematical relations. With the advent of computers and highly efficient algorithms, the complex mathematical models are addressed by means of numerical simulations. Generally the degrees of freedoms involved in such numerical simulations are high, typically of the order $\sim 10^6$. The real time and data storage requirements by the numerical simulations has also led to the development in the model reduction techniques. In linear algebra, the tridiagonalization of a matrix was introduced by (Lanczos, 1950). Further, (Arnoldi, 1951) introduced an algorithm to approximate large matrices by small matrices by means of the concept of Krylov subspaces. (Lanczos, 1950) algorithm deals with symmetric matrices, which is a simplified case of (Arnoldi, 1951) algorithm.

The two commonly used approaches in model reduction are the *method of moments matching* based on the *Krylov subspaces* (Antoulas, 2005) and the *Gaerkin projection* of the *Proper Orthogonal Decomposition* (POD) basis functions (Schilders et al., 2008). The pioneering and formal method of model reduction was proposed by (Moore, 1981b), which is known as

the method of *Truncated balanced realizations*. In this method, a controllable and observable subspace is formed based on the *Principal Component Analysis*. In order to retain the important features of a control system, (Glover, 1984a) proposed the *Hankel-norm reduction*. The Hankel norm provides a measure of the energy of a system state. Thus a reduced subspace is formed based on the states with higher energy content. The well known method of *Padé Via Lanczos* (PVL) was proposed by (Feldmann and Freund, 1995), which showed the relation between the Padè approximations and the Krylov subspaces. The Arnoldi based method called PRIMA was developed by (Odabasioglu et al., 1997) in order to deal with the non-passivity of the control systems. The methods of moments matching are highly efficient and can easily be extended to higher order systems, although they lack in the exact error estimates. The method of Proper Orthogonal Decomposition (POD) (or *Karhunen-Loève* decomposition) (Aubry, 1991) is used for higher order non-linear dynamical systems and analysis of multidimensional data in several fields. (Sirovich, 1987) proposed an important development in the POD method, it is known as the *method of snapshots*. It results in a considerable amount of reduction of the number of degrees-of-freedom compared to the *Direct method* of POD.

Reduce-Order modeling is a developing field, hence several new methods as well as existing methods in modified form are available. The methods *Singular Perturbation Approximation*, *Low-rank Gramian approximants and matrix sign function method* are base on the formulation of *Truncated Balanced Approximation*. The method of *Asymptotic Waveform Evaluation* related to the Krylov subspaces was proposed by (Pillage et al., 1990). It mainly deals with obtaining the Padè approximation rather than the Krylov subspaces. There exist a class of model reduction techniques dealing with parametric (Benner et al., 2013) and weakly-nonlinear dynamical systems (Phillips, 2003). The nonlinear model reduction methods based on Volterra series representation and harmonic balance are presented, in addition to the POD based reduced models in (Lucia et al., 2004). The method of Proper Generalized Decomposition (PGD) promises to construct the reduced subspace without a priori knowledge of the system (Chinesta et al., 2010).

The article is arranged as follow: first, the following section (5.2) is dedicated to the definitions of preliminary concepts in reduced-order modeling. Second, the two commonly used approaches in model reduction based on the Krylov subspaces and POD basis are discussed, in addition to the pioneering balancing and truncation approach.

5.2 Preliminary definitions

5.2.1 Dynamical systems

A state variable (or a set of variables) varying in time, which is described by a set of equations can be termed as a dynamic system. The state vector can be a function of a geometrical space. Every future time state is predicted by the dynamic equations describing the state. The mathematical representations are usually differential equations. Many dynamic systems representing the real world problems are often fairly complicated, for example the Navier-Stokes equations in fluid dynamics. A simple dynamic system can be written in terms of an explicit ordinary differential equation as,

$$\begin{aligned} \frac{d\mathbf{x}}{dt} &= f(\mathbf{x},\mathbf{u}) \\ \mathbf{y} &= g(\mathbf{x},\mathbf{u}) \end{aligned} \tag{5.1}$$

Here, $\mathbf{x}$ is the state variable, $\mathbf{y}$ is the output, $\mathbf{u}$ is the input and functions f, g are the dynamic equations governing the state variable. The objective of model reduction is to decrease the number of degrees-of-freedom (DOF) present in the system while retaining essential dynamics of the system. This can be achieved by reducing the dimension of the state variable $\mathbf{x}$ and also preserving the characteristics of the governing equations f and g. The functions f, g can be of different type (e.g. linear, non-linear, time dependant, time-varying etc.), accordingly the dynamical system can be classified.

5.2.2 Transfer functions

In the context of control theory, a transfer function is defined as the ratio of the output of the system to its input in the Laplace transform domain considering the initial conditions and the zero equilibrium condition. Lets consider the system in Equation (5.1) in the linear time-invariant form as,

$$\begin{aligned} \frac{d\mathbf{x}}{dt} &= \mathbf{A}\mathbf{x} + \mathbf{b}\mathbf{u} \\ \mathbf{y} &= \mathbf{c}^T\mathbf{x} \end{aligned} \tag{5.2}$$

Where, **A**, **b**, **c** are the time-independent coefficients. Applying Laplace transform to the dynamics system using an initial condition $\mathbf{x}(t) = 0$ at $t = t_0$ gives,

$$\begin{aligned}(s\mathbf{I} - \mathbf{A})\mathscr{L}(\mathbf{x}) &= \mathbf{b}\mathscr{L}(\mathbf{u}) \\ \mathscr{L}(\mathbf{y}) &= \mathbf{c}^T\mathscr{L}(\mathbf{x})\end{aligned} \tag{5.3}$$

Where, the parameter s is the 'complex number frequency' in the definition of Laplace transform. $\mathbf{I}$ is the identity matrix. The symbol $\mathscr{L}$ represents the Laplace transform, while the superscript T stands for the matrix transpose. The transfer function $\mathbf{H}(s)$ of the system is then given by,

$$\mathbf{H}(s) = \frac{\mathscr{L}(\mathbf{y})}{\mathscr{L}(\mathbf{u})} = \mathbf{c}^T(s\mathbf{I} - \mathbf{A})^{-1}\mathbf{b} \tag{5.4}$$

The transfer functions can be expanded at $s = 0$ as,

$$\mathbf{H}(s) = \mathbf{M}_0 + \mathbf{M}_1 s + \mathbf{M}_2 s^2 + ... \tag{5.5}$$

The coefficients $\mathbf{M}_0$, $\mathbf{M}_1$, $\mathbf{M}_2$, ... are called the *moments* of the transfer function. The time delay between the input (**u**) and the output (**y**) corresponds to the first moment $\mathbf{M}_1$. The time delay is also called as Elmore delay. The dimensions of the transfer function $\mathbf{H}(s)$ depends on the size of input **u**. The transfer functions of finite-dimensional systems are generally rational functions of s. The roots of denominator ($\mathscr{L}(\mathbf{u})$) are called *poles* and that of numerator ($\mathscr{L}(\mathbf{y})$) are the *zeros* of the dynamical system. The poles and zeros dictate the dynamics of the system.

5.2.3 Controllability and Observability Gramians

Controllability and observability are two important and dual aspects of a control system. In general, controllability is the ability of the input function (**u**) to change the state variable (**x**). The observability of a control system is the possibility of determining the behaviour of the system from the system's output (**y**). Let **E** be the eigenvector space with λ_i as corresponding eigenvalues of the matrix **A** of the dynamic system in Equation (5.2). The system can be transformed in a more intuitive form as,

$$\frac{d\mathbf{z}}{dt} = \mathbf{E}^{-1}\mathbf{A}\mathbf{E}\mathbf{z} + \mathbf{E}^{-1}\mathbf{b}\mathbf{u} = \begin{pmatrix} \lambda_1 & & \\ & \ddots & \\ & & \lambda_n \end{pmatrix}\mathbf{z} + \begin{pmatrix} b_1 \\ \vdots \\ b_n \end{pmatrix}\mathbf{u} \tag{5.6}$$

and

$$\mathbf{y} = \mathbf{c}^T\mathbf{E}\mathbf{z} = (c_1, \cdots, c_n)\,\mathbf{z} \tag{5.7}$$

The transformed dynamic system in Equations (5.6) and (5.7) consists n independent transfer relations. The state variable z_i is controllable for $b_i \neq 0$. If the value of c_i is zero, the the corresponding z_i is unobservable. Thus from the model reduction point of view, it is desirable to eliminate the unobservable and uncontrollable transfer function equations. Thus the reduced dynamical system is known as minimum realization of the original system.

Let $\mathbf{P}$ and $\mathbf{Q}$ be respectively the controllability and observability gramians of the dynamical system in Equation 5.2. The gramians are the solutions of the Lyapunov equations,

$$\begin{aligned} \mathbf{A}\mathbf{P} + \mathbf{P}\mathbf{A}^T &= -\mathbf{b}\mathbf{b}^T \\ \mathbf{A}^T\mathbf{Q} + \mathbf{Q}\mathbf{A} &= -\mathbf{c}^T\mathbf{c} \end{aligned} \tag{5.8}$$

5.2.4 Stability and Passivity

A dynamical system is stable if the output of the system is bounded in time domain. The poles and the eigenvalues of the system are generally used to study the stability of a dynamical system. For instance, the system in Equation (5.6) is stable for all eigenvalues less than or equal to zero ($Re(\lambda_i) \leq 0$). Passivity of a dynamic system is its inability to produce anything that increases the output beyond the input. When a stable system coupled with some non-linear components, it can go unstable. The passive components are incapable of producing energy or gaining power.

5.2.5 Subspace projections

Subspace projection is a very important part of many model reduction techniques for large linear algebraic systems and eigenvalue matrices. Suppose a system of equations $\mathbf{A}\mathbf{x} = \mathbf{b}$ with $\mathbf{A} \in \mathscr{R}^{n\times n}$ and $\mathbf{x}$, $\mathbf{b} \in \mathscr{R}^n$. Here n is the dimension of the problem. The idea is to find an appropriate subspace $\mathscr{R}^r$ such that $r << n$. The original system of equations $\mathbf{A}\mathbf{x} = \mathbf{b}$ is then projected on the reduced subspace $\mathscr{R}^r$. The projection generates a fairly reduced system, which can be solved with much less computational efforts. The dynamical system in Equation (5.6) uses the eigenvector matrix $\mathbf{E}$ of dimension $n \times n$. It can form a subspace, if we reduce its dimension to $r \times r$. This can be achieved by eliminating the uncontrollable, unobservable and insignificant transfer paths from the system. The projection of $\mathbf{A}$ on the subspace $\mathbf{E}_r$ is $\mathbf{A}_r = \mathbf{E}_r^{-1}\mathbf{A}\mathbf{E}_r$, the projection of $\mathbf{b}$ is $\mathbf{b}_r = \mathbf{E}_r^{-1}\mathbf{b}$ and the projection of $\mathbf{c}^T$ on the subspace $(\mathbf{E}_r)$

can be given by $\mathbf{c}_r^T = \mathbf{c}^T\mathbf{E}_r$. The projection here is bi-orthogonal since $\mathbf{E}_r^{-1}\mathbf{E}_r = \mathbf{I}_r$. In general the subspace $\mathbf{E}_r$ need not necessarily be orthogonal.

5.2.6 Hankel singular values

The stability of a control system can be defined in terms of eigenvalues, whereas the Hankel singular values represent the energy associate with each state in the system (Glover, 1984a). The important characteristic properties of a system are preserved with the large Hankel singular values (i.e. with the large energy states of a system). The important properties can be stability, frequency dynamics or a time response of the system. The Hankel values are given by,

$$\sigma_i = \sqrt{\lambda_i(\mathbf{PQ})} \tag{5.9}$$

Where, λ_i are the eigenvalues of the system, while $\mathbf{P}$ and $\mathbf{Q}$ are the controllability and observability gramians satisfying the Lyapunov equations (Equation 5.8).

5.3 Model order reduction techniques

5.3.1 Truncated Balanced Realization

In the balanced truncation method (Moore, 1981b), the projection subspace is obtained by means of the controllability and observability gramians. The balancing transformation can be performed by using the Square-root method. The unobservable and uncontrollable parts of the system are truncated in order to obtain a reduced system. The controllability gramian ($\mathbf{P}$) and the observability gramian ($\mathbf{Q}$) of the dyanmics system in Equation (5.2), which are the solutions of the Lyapunov equations (Equation 5.8). The dynamical system is balanced if, $\mathbf{P} = \mathbf{Q} = diag(\sigma_1, \cdots, \sigma_n)$ with $\sigma_1 \geq \sigma_2 \geq \cdots \sigma_n \geq 0$, where the σ_i are the Hankel singular values of the dynamical system.

In the first step of the necessary balancing transformation, the Cholesky factors ($\mathbf{L}$, $\mathbf{R}$) of the gramians are obtained. The graminas in terms of Cholesky factors are $\mathbf{P} = \mathbf{L}^T\mathbf{L}$ and $\mathbf{Q} = \mathbf{R}^T\mathbf{R}$. In the next step the matrix $\mathbf{LR}^T$ is decomposed by the Singular Value Decomposition as, $\mathbf{LR}^T = \mathbf{L}_0\Sigma\mathbf{R}_0^T$. The truncation of the system (matrices $\mathbf{L}_0$ and $\mathbf{R}_0$) can be performed at this stage based on the Hankel Singular Values. The subspace matrices for model reduction

are given as,

$$\begin{aligned} \mathbf{W}_r^T &= \Sigma^{-\frac{1}{2}} \mathbf{R}_0^T \mathbf{R} \\ \mathbf{V}_r &= \mathbf{L}^T \mathbf{L}_0 \Sigma^{-\frac{1}{2}} \end{aligned} \tag{5.10}$$

The reduced-order system is given as $\mathbf{A}_r = \mathbf{W}_r^T \mathbf{A} \mathbf{V}_r$, $\mathbf{b}_r = \mathbf{W}_r^T \mathbf{b}$ and $\mathbf{c}_r = \mathbf{c}\mathbf{V}_r$. The value of reduced dimension r can be found by formulating an error bound as,

$$||\Sigma - \Sigma_r|| \leq 2||\mathbf{u}|| \sum_{i=r+1}^{n} \sigma_i \tag{5.11}$$

5.3.2 Krylov subspaces

The Krylov subspace is defined for a matrix $\mathbf{A}$ and an initial vector $\mathbf{b}$ as,

$$\mathscr{K}_r(\mathbf{A};\mathbf{b}) = span\left\{\mathbf{b}, \mathbf{A}\mathbf{b}, \cdots, \mathbf{A}^{r-1}\mathbf{b}\right\} \tag{5.12}$$

The dimensions of matrix $\mathbf{A}$ and $\mathbf{b}$ are $n \times n$ and $n \times 1$ respectively. r is a positive integer. The subspace vectors $\mathbf{b}, \mathbf{A}\mathbf{b}, \cdots$ are called basis vectors. Let us define Krylov subspace matrices ($\mathbf{V}$, $\mathbf{W}$) for the dynamic system in Equation (5.2) as,

$$\mathbf{V}_r \rightarrow \mathscr{K}_r(\mathbf{A}^{-1};\mathbf{A}^{-1}\mathbf{b}) = span\{\mathbf{A}^{-1}\mathbf{b}, \cdots, (\mathbf{A}^{-1})^{rv-1}\mathbf{A}^{-1}\mathbf{b}\} \tag{5.13}$$

and

$$\mathbf{W}_r \rightarrow \mathscr{K}_r(\mathbf{A}^{-T};\mathbf{A}^{-T}\mathbf{c}) = span\{\mathbf{A}^{-T}\mathbf{c}, \cdots, (\mathbf{A}^{-T})^{rw-1}\mathbf{A}^{-T}\mathbf{c}\} \tag{5.14}$$

Unlike the subspace spanned by eigenvectors ($\mathbf{E}_r$) the Krylov subspace matrices ($\mathbf{V}_r$, $\mathbf{W}_r$) need not be orthogonal. The model order reduction performed using these subspaces can be two-sided (if both the matrices are specified) or one-sided (if one of the two matrices is specified while the other left arbitrary). In the Krylov subspace transformations, the resulting dynamical system is not guaranteed to a stable reduced system. The stability can be ensured by matching more moments ($\mathbf{M}_0$, $\mathbf{M}_1$, ...) of the transfer function ($\mathbf{H}$(s)) of the original system with the reduced model. The Taylor series expansion for the transfer function in Equation (5.4) at $s_0 = 0$ is,

$$\mathbf{H}(s) = -\mathbf{c}^T\mathbf{A}^{-1}\mathbf{b} - \mathbf{c}^T(\mathbf{A}^{-1})\mathbf{A}^{-1}\mathbf{b}s - \mathbf{c}^T(\mathbf{A}^{-1})^2\mathbf{A}^{-1}\mathbf{b}s^2 - \cdots \tag{5.15}$$

The first moment $\mathbf{M}_0 = -\mathbf{c}^T\mathbf{A}^{-1}\mathbf{b}$ of the original system should equals the first moment of the reduced system $\mathbf{M}_{0r} = -\mathbf{c}_r^T\mathbf{A}_r^{-1}\mathbf{b}_r$. Similarly the equality of the higher moments up to $2r$

moments in two-sided methods and r moments in one-sided methods ensure the stability of the reduced system. The approximation by moment matching can be performed for a non-zero value of s_0. The moments are termed as *Markov parameters* when $s_0 \to \infty$. The reduced system is known as *Padé approximation* for $s_0 \to \infty$. Although the dual (two-sided) method improves the approximation by considering higher moments, the stability of the reduced system is not guaranteed in either methods (Antoulas, 2005).

Arnoldi algorithm

The numerical issues in the moment matching approximations can be refined by using orthogonal basis instead of any basis matrices forming the Krylov subspace. Thus for a Krylov subspace $\mathscr{K}_r(\mathbf{A};\mathbf{b})$ formed using Arnoldi algorithm generates a subspace $(\mathbf{V}_r)$ such that $\mathbf{V}_r^T\mathbf{V}_r = \mathbf{I}_r$. The Krylov subspace generation using Arnoldi algorithm is common in one-sided methods. In an interesting development in Arnoldi algorithm, (Odabasioglu et al., 1997) proposed the PRIMA method, which deal with the non-passivity of a dyanical system by an explicit projection algorithm instead of the Hessenberg matrix formation.

Lanczos procedure

Lanczos procedure is well known for two-sided Krylov subspace methods. It generates an additional orthogonal Krylov subspace $\mathscr{K}_r(\mathbf{A}^T;\mathbf{c})$, in addition to $\mathscr{K}_r(\mathbf{A};\mathbf{b})$ in Arnoldi method by forming another orthogonal matrix $\mathbf{W}_r$ such that $\mathbf{W}_r^T\mathbf{V}_r = \mathbf{I}$. The Lanczos method is unstable, in terms of preserving the orthogonality of both matrices ($\mathbf{V}_r$ and $\mathbf{W}_r$). A re-orthogonalization procedure is often used to stabilize the Lanczos algorithm. The algorithm transforms the system matrices in the tridiagonal form. The method is improved for the stabilization and efficient operations over the years.

5.3.3 Proper Orthogonal Decomposition

POD basis

Let us consider a vector space $\mathbf{V} \in \mathbb{R}^n$. Let $\mathbf{S}$ be a discrete solution set given as $\mathbf{S} = \{\mathbf{s}_1(t), \mathbf{s}_2(t), \cdots, \mathbf{s}_m(t)\}$. A solution $\mathbf{s}_i(t) \in \mathbb{R}^n$, with $i = 1, 2, \cdots, m$ and time $t \in [0, T]$. The objective of POD analysis of the solution set is to perform an orthogonal projection $\Pi_r : \mathbf{V} \to \mathbf{V}_r$ such that $r << n$. The subspace $\mathbf{V}_r \subset \mathbf{V}$ and the projection is constrained to minimize the least-squared distance,

$$||\mathbf{S} - \Pi_r\mathbf{S}||^2 = \sum_{i=1}^{m} \int_0^T ||\mathbf{s}_i(t) - \Pi_r\mathbf{s}_i(t)||^2 dt \tag{5.16}$$

This is achieved by forming a correlation matrix ($\mathbf{R} \in \mathbb{R}^{n \times n}$) of the solution set defined as,

$$\mathbf{R} = \sum_{i=1}^{m} \int_0^T \mathbf{s}_i(t)\mathbf{s}_i(t)^T dt \tag{5.17}$$

The correlation matrix ($\mathbf{R}$) is a symmetric positive semi-definite matrix. Let $\lambda_1 \geq \lambda_2 \geq \cdots \lambda_n \geq 0$ be the (ordered) eigenvalues of the correlation matrix. The corresponding eigenvectors $\boldsymbol{\phi}_i$ are give by,

$$\mathbf{R}\boldsymbol{\phi}_i = \lambda_i \boldsymbol{\phi}_i, \quad i = 1, 2, \cdots, n \tag{5.18}$$

The eigenvectors serve as an orthonormal basis from $\mathbf{V}$. The subspace $\mathbf{V}_r = span\{\boldsymbol{\phi}_1, \boldsymbol{\phi}_2, \cdots, \boldsymbol{\phi}_r\}$ with reduced size r represents the optimal subspace known as the POD reduced basis.

The *method of snapshots* is much efficient method to obtain the POD basis. The correlation matrix ($\mathbf{R}$), which is $n \times n$ in size, is build using a correlation of a time-varying data set (snapshots). The time correlation matrix ($\mathbf{R}$) is thus $m \times m$ in size. The time correlation matrix is given by,

$$\mathbf{R} = SS^T = \sum_{i=1}^{m} \mathbf{s}(t_i)\mathbf{s}(t_i)^T \tag{5.19}$$

The time-correlation matrix is solved for the eigenvalue problem.

$$\mathbf{R}\boldsymbol{\psi}_i = \lambda_i \boldsymbol{\psi}_i, \quad i = 1, 2, \cdots, m \tag{5.20}$$

The eigenvectors ($\boldsymbol{\psi}_i$) are also referred as the POD time modes. The eigenvalues λ_i remain the same. The orthonormal subspace $\mathbf{W}_r = span\{\boldsymbol{\psi}_1, \boldsymbol{\psi}_2, \cdots, \boldsymbol{\psi}_r\}$ is related with the subspace $\mathbf{V}_r = span\{\boldsymbol{\phi}_1, \boldsymbol{\phi}_2, \cdots, \boldsymbol{\phi}_r\}$ by,

$$\boldsymbol{\phi}_i = \lambda_i^{-\frac{1}{2}} \mathbf{S}\boldsymbol{\psi}_i, \quad i = 1, 2, \cdots, r \tag{5.21}$$

The eigenvalues (λ_i) observe an exponential decay in their values, hence the energy content associated with the POD mode. The value of reduced dimension r is usually chosen based on the relative information retained,

$$\%I(r) = \frac{\sum_{i=1}^{r} \lambda_i}{\sum_{i=1}^{n} \lambda_i} \times 100 \tag{5.22}$$

Galerkin projection

Lets assume a dynamical system with the solution $\mathbf{s}(t)$. It is obtained by a finite discretization of non-linear differential equations. The dynamical system can be written as,

$$\frac{d\mathbf{s}}{dt} = f(\mathbf{s}(t)) \tag{5.23}$$

Here $f : \mathbf{V} \to \mathbf{V}$. A reduced-order model is obtained by projecting the dynamical system on the POD orthogonal reduced basis (Π_r) as,

$$\frac{d\mathbf{s}_r}{dt} = \Pi_r f(\mathbf{s}_r(t)) \tag{5.24}$$

Using relations $\Pi_r = \mathbf{V}_r \mathbf{V}_r^T$ and $a_i(t) = \sqrt{\lambda_i}\psi_i(t)$ in Equation (5.24),

$$\frac{da_i(t)}{dt} = \boldsymbol{\phi}_i^T f\left(\sum_{j=1}^{r} \boldsymbol{\phi}_j a_j(t)\right), \quad i = 1, 2, \cdots, r \tag{5.25}$$

The system of ordinary differential equations can be solved using an initial value for the time POD time coefficients ($a_i(0)$). The reduced solution of the system is obtained as,

$$\boldsymbol{s}_r(t) = \sum_{i=1}^{r} \boldsymbol{\phi}_i a_i(t) \tag{5.26}$$

5.4 Conclusion

A brief introduction to reduced-order modeling in the control system and large scale numerical systems is provided. The preliminary concepts in the model reduction are revised. The basis of the most commonly used methods in mode reduction, namely, truncated balanced realization, Krylova subspace apporximations and proper orthogonal decomposition is presented.

CHAPTER 6

A GALERKIN-FREE MODEL REDUCTION APPROACH FOR THE NAVIER-STOKES EQUATIONS

Abstract

Galerkin projection of the Navier-Stokes equations on Proper Orthogonal Decomposition (POD) basis is predominantly used for model reduction in fluid dynamics. The robustness for changing operating conditions, numerical stability in long-term transient behaviour and the pressure-term consideration are generally the main concerns of the Galerkin Reduced-Order Models (ROM). In this article, we present a novel procedure to construct an off-reference solution state by using an interpolated POD reduced basis. A linear interpolation of the POD reduced basis is performed by using two reference solution states. The POD basis functions are optimal in capturing the averaged flow energy. The energy dominant POD modes and corresponding base flow are interpolated according to the change in operating parameter. The solution state is readily built without performing the Galerkin projection of the Navier-Stokes equations on the reduced POD space modes as well as the following time-integration of the resulted Ordinary Differential Equations (ODE) to obtain the POD time coefficients. The proposed interpolation based approach is thus immune from the numerical issues associated with a standard POD-Galerkin ROM. In addition, a posteriori error estimate and a stability analysis of the obtained ROM solution are formulated. A detailed case study of the flow past a cylinder at low Reynolds numbers is considered for the demonstration of proposed method. The ROM results show good agreement with the high fidelity numerical flow simulation.

Keywords

Reduced-Order Modeling, Proper Orthogonal Decomposition, Navier-Stokes equations

Contents

6.1 Introduction

Computational Fluid Dynamics (CFD) simulations is an indispensable element of the engineering research today. Although there is a considerable advancement in the computing power in last couple of decades, the exact flow simulations at high Reynolds numbers are unaffordable in terms of the time and computing cost. The efforts become enormous for research applications (e.g. optimization), where the simulations need to be performed repeatedly. Consequently, reduced-order models (ROM) are developed extensively in recent years. They offer substantial reduction in the degrees of freedom and yet retain the essential features of the flow by means of the reduced basis. The reduced system may lead to a better understanding of the underlying mechanism and thereby improvements in the empirical flow (turbulence) models. The flow control, optimization and stability analysis in hydrodynamics, aero-acoustics are some of the potential applications of model reduction (see for e.g. (Noack et al., 2011)).

The first important step of the model reduction in fluid dynamics is to form an appropriate reduced basis out of a complete set of basis functions. The choice of particular basis functions may be problem specific. The derivation of the reduced basis can be 'a priori' or 'a posteriori'. One can refer to (Joseph, 1976), (Noack and Eckelmann, 1994) for some of the early works on 'a priori' formation of the basis functions. Recently, (Dumon et al., 2013) used 'a priori' derivation of the basis functions, in the context of Proper General Decomposition (PGD).

Besides, the spectral discretization methods are often preferred over the spatial discretization methods in order to gain the accuracy for same computing time and space requirements. In 'a posteriori' formation, the basis functions are derived using the existing solution datasets and methods such as Proper Orthogonal Decomposition (POD) (for e.g. method of Dynamic Mode Decomposition (DMD) in (Rowley et al., 2009) and (Schmid, 2010)). The POD (also Principle Component Analysis) is a popular choice of the empirical basis functions for the Navier-Stokes equations, especially in understanding the onset of bifurcations or instabilities and the spatial-temporal dynamics of the flow structures. The error in time-averaged energy remains minimal compared to every other method for the same number of modes. The convergence in extracting the space structures (topos) and the associated time modes (chronos) is optimum in terms of the flow energy (Aubry, 1991). An elaborated discussion with mathematical derivations on the optimality of the POD method is provided in (Holmes et al., 1990).

The POD-Galerkin ROM are build using a coordinate transformation performed by means of a Galerkin projection of the system of Navier-Stokes equations on the reduced POD basis functions. Generally, the flow velocity ($\mathbf{v}$) is decomposed into the spatial ($\boldsymbol{\phi}_i$) and temporal (a_i) basis functions as shown in Equation (6.1),

$$\mathbf{v}(\boldsymbol{x},t) \approx \mathbf{v}^{[0,1,2,\ldots n]} = \bar{\mathbf{v}}(\boldsymbol{x}) + \sum_{i=1}^{n} \boldsymbol{\phi}_i(\boldsymbol{x}) a_i(t) \tag{6.1}$$

Where $\bar{\mathbf{v}}(\boldsymbol{x})$ is the time-averaged base flow, n is the number of POD modes. This equation holds good under the assumption that the flow is statistically stationary in time. In incompressible flows with Dirichlet type boundary conditions, the basis functions satisfy both the boundary conditions and the divergence-free constrain of the continuity equation. The Galerkin projection of the momentum equations on the basis functions results in the non-linear quadratic Ordinary Differential Equations (ODE) of the form:

$$\frac{da_i}{dt} = \mathbf{C}_i + \sum_{j}^{n} \mathbf{L}_{ij} a_j + \sum_{j,k}^{n} \mathbf{Q}_{ijk} a_j a_k \tag{6.2}$$

Where $\mathbf{C}, \mathbf{L}$ and $\mathbf{Q}$ are the Galerkin ROM coefficients. The indices $i, j, k = 1, \cdots, n$. Equation (6.2) is a reduced model for the Navier-Stokes Equations (NSE) with n spatial modes. The time-integration of Equation (6.2) with an appropriate initial boundary condition gives the temporal coefficients (basis functions), and the flow solution can be easily built by using Equation (6.1). The Galerkin projection ideally should preserve the stability dynamics of the NSE, but generally it is achieved by extrinsic stability enablers. (Rempfer, 2000) showed how the Galerkin ROM are inherently prone to numerical instabilities. The energy associ-

ated with the truncated basis functions keeps piling on, which results in a divergence of the Galerkin-ROM. The concept of artificial viscous dissipation to stabilize the Galerkin ROM was introduced in (Aubry et al., 1988). Later, (Sirisup and Karniadakis, 2004) proposed a spectral viscosity diffusion convolution operator based on a bifurcation analysis. In addition, the stability of Galerkin ROM greatly depends on parameters such as the flow compressibility, pressure-term consideration and time varying boundary conditions. The flow compressibility effect can be considered by means of an energy based inner product while formulating a ROM (Rowley et al., 2004). The POD-penalty method was proposed by (Sirisup and Karniadakis, 2005) to treat the time dependence of the boundary conditions on the POD-Galerkin ROM. The Galerkin projection of the pressure-gradient term of NSE on the reduced basis functions can be neglected in case of the internal flows, but for open flows the pressure term does not disappear (Noack et al., 2005) and it needs to be modeled. The pressure term is accounted in a formulation of the pressure extended Galerkin ROM by (Bergmann et al., 2009). In addition, (Noack et al., 2003) demonstrated that neglecting the interactions between the time-averaged base flow and the fluctuating flow may lead to an unstable Galerkin ROM. The authors also introduced the concept of 'shift mode' correction technique. Further, from the flow control applications point of view (Morzynski et al., 2006) proposed a continuous interpolation based method. In the method, an interpolation between the stability eigenmodes and the POD modes is performed to deal with the changing flow conditions. A detailed discussion on the numerical instabilities and perspectives of the reduced order models in fluid dynamics is provided by (Lassila et al., 2013).

The choice of an appropriate reduced basis, the Galerkin projection of the NSE on the reduced basis and the time-integration of the obtained ODE are the main elements of the POD-Galerkin ROM. The POD basis functions are optimal in terms of flow energy, while as the Galerkin projection of NSE on the reduced basis may not produce a stable ROM as discussed above. In this article, we propose a novel approach, where it is not required to perform the Galerkin projection of NSE on the reduced basis and also the time-integration to obtain the POD time coefficients. The time-averaged base flow and the POD space basis functions (topos) are directly interpolated for the change in operating condition. The POD temporal basis functions (chronos) are also interpolated in phase space. The periodicity (the period of limit-cycles) of the POD temporal modes is accounted for the energy conservation. Furthermore, the method is extended for a continuous transition between two operating conditions. Also a linear extrapolation of the POD reduced basis is performed to widen the range of operating parameter. The article is organised as: Section (7.2) is dedicated to the mathematical formulation and error analysis of the proposed ROM. In Section (6.3), we provide a demon-

stration of the method using a case study of the flow past a cylinder at low Reynolds numbers. At last, the work is summarised in Section (6.4).

6.2 Mathematical formulation

The compressible Navier-Stokes equations (including the continuity and energy equations) are considered here as the High Fidelity Model (HFM). The flow is statistically stationary in time such that Equation (6.1) is applicable to the solution (state) variables. The solution state vector $\boldsymbol{s} = \boldsymbol{s}(\boldsymbol{x},t)$ is spanned on the space $\boldsymbol{x} \in \Omega$, Ω is the spacial flow domain. t is the time in $[0, T_\infty]$. Let H be a Hilbert space and a state variable $\boldsymbol{s}_i(\boldsymbol{x},t) \in H$ with $i = 1,2,\cdots,r(\boldsymbol{s})$. $r(\boldsymbol{s})$ is the number of state variables. The standard inner product of the state variables $\boldsymbol{s}_i(\boldsymbol{x},t_1)$, $\boldsymbol{s}_i(\boldsymbol{x},t_2)$ and the solution state vector $\boldsymbol{s}(\boldsymbol{x},t)$ are respectively,

$$
\begin{aligned}
(\boldsymbol{s}_i(\boldsymbol{x},t_1),\boldsymbol{s}_i(\boldsymbol{x},t_2))_\Omega &= \int_\Omega \boldsymbol{s}_i(\boldsymbol{x},t_1)\cdot\boldsymbol{s}_i(\boldsymbol{x},t_2)d\boldsymbol{x} \\
(\boldsymbol{s}(\boldsymbol{x},t_1),\boldsymbol{s}(\boldsymbol{x},t_2))_\Omega &= \begin{pmatrix} (\boldsymbol{s}_i(\boldsymbol{x},t_1),\boldsymbol{s}_i(\boldsymbol{x},t_2))_\Omega \\ \vdots \\ \left(\boldsymbol{s}_{r(\boldsymbol{s})}(\boldsymbol{x},t_1),\boldsymbol{s}_{r(\boldsymbol{s})}(\boldsymbol{x},t_2)\right)_\Omega \end{pmatrix}
\end{aligned}
\tag{6.3}
$$

The induced norm and time averaging (for time period T_∞) of a state variable and the solution state vector are respectively defined as,

$$
\begin{aligned}
||\boldsymbol{s}_i||_\Omega &= \sqrt{(\boldsymbol{s}_i,\boldsymbol{s}_i)_\Omega} \quad \text{and} \quad \bar{\boldsymbol{s}}_i = \frac{1}{T_\infty}\int_{T_\infty} \boldsymbol{s}_i\, dt = \langle \boldsymbol{s}_i \rangle_{T_\infty} \\
||\boldsymbol{s}||_\Omega &= \begin{pmatrix} \sqrt{(\boldsymbol{s}_i,\boldsymbol{s}_i)_\Omega} \\ \vdots \\ \sqrt{(\boldsymbol{s}_{r(\boldsymbol{s})},\boldsymbol{s}_{r(\boldsymbol{s})})_\Omega} \end{pmatrix} \quad \text{and} \quad \bar{\boldsymbol{s}} = \frac{1}{T_\infty}\int_{T_\infty} \boldsymbol{s}\, dt = \langle \boldsymbol{s} \rangle_{T_\infty}
\end{aligned}
\tag{6.4}
$$

6.2.1 Method of snapshots POD

The POD or Karhunen-Loeve expansion was first introduced in fluid dynamics by (Lumley, 1967) for the analysis of coherent structures in the flow turbulence. Following the development of POD, (Sirovich, 1987) introduced the method of snapshots for the experimental and numerical datasets. It allows further reduction of degrees of freedom, compared to the direct method of POD.

The solution state vector $\boldsymbol{s}$ includes all variables varying in the time and space. Let η be

an operating parameter (e.g. Reynolds number). The state vector of the High Fidelity Model (HFM) solution can be defined as,

$$\boldsymbol{s}(\boldsymbol{x},t;\eta) = \begin{pmatrix} \rho(\boldsymbol{x},t;\eta) \\ \mathbf{v}(\boldsymbol{x},t;\eta) \\ p(\boldsymbol{x},t;\eta) \\ \vdots \end{pmatrix} \tag{6.5}$$

Where ρ, $\mathbf{v}$ and p are the fluid density, velocity vector and static pressure respectively. The state vector can be separated in the time-averaged base flow and the unsteady part as shown in Equation (6.6).

$$\boldsymbol{s}(\boldsymbol{x},t;\eta) = \bar{\boldsymbol{s}}(\boldsymbol{x};\eta) + \boldsymbol{s}'(\boldsymbol{x},t;\eta) \tag{6.6}$$

$$= \bar{\boldsymbol{s}}(\boldsymbol{x};\eta) + \sum_{i=1}^{\infty} \boldsymbol{\phi}_i(\boldsymbol{x};\eta)\boldsymbol{a}_i(t;\eta) \tag{6.7}$$

In Equation (6.7), the unsteady part ($\boldsymbol{s}'(\boldsymbol{x},t;\eta)$) is decomposed into the POD basis functions using the Galerkin expansion. The time invariant orthonormal $\boldsymbol{\phi}_i(\boldsymbol{x};\eta)$ and the space invariant orthogonal $\boldsymbol{a}_i(t;\eta)$ are the POD basis functions (modes). The state vector can be obtained in discrete (N_t) snapshots by performing a CFD simulation. The snapshots can be collected once the flow becomes statistically stationary and using (typically) a constant timestep (Δt_{sn}). Let N_t, N_{pod} be the number of snapshots and number of POD modes respectively, also $N_{pod} \leq N_{t-1}$. The state vector can be approximated by discrete snapshots as,

$$\boldsymbol{s}(\boldsymbol{x},t;\eta) \approx \boldsymbol{s}(\boldsymbol{x},t_1;\eta),.....,\boldsymbol{s}(\boldsymbol{x},t_{N_t};\eta) \tag{6.8}$$

$$\approx \bar{\boldsymbol{s}}(\boldsymbol{x};\eta) + \sum_{i=1}^{N_{pod}} \boldsymbol{\phi}_i(\boldsymbol{x};\eta)\boldsymbol{a}_i(t;\eta) \qquad t_1 \leq t \leq t_{N_t} \tag{6.9}$$

Where t_1 and t_{N_t} are the time coordinates of the first and last snapshots. Also, let $T_{sn} = [t_1,..,t_{N_t}]$ be the time domain of discrete snapshots collection. The time step (Δt_{sn}) of snapshots recording and the number of snapshots (N_t) depend on the desired resolution in the temporal harmonics of the POD modes (Noack et al., 2005).

Let $\boldsymbol{R}(\eta)$ be the two point time-correlation function, given by,

$$\boldsymbol{R}(\eta) = \boldsymbol{R}(t_i,t_j,\eta) = \frac{1}{N_t}\left(\boldsymbol{s}'(\boldsymbol{x},t_i;\eta),\boldsymbol{s}'(\boldsymbol{x},t_j;\eta)\right)_\Omega \qquad i,j = 1,2,.....N_t \tag{6.10}$$

The correlation function $\boldsymbol{R}(\eta)$ is solved for the eigenvalue problem, as in Equation (6.11).

$$\boldsymbol{R}(\eta)\boldsymbol{\psi}_i(t;\eta) = \boldsymbol{\lambda}_i\boldsymbol{\psi}_i(t;\eta) \tag{6.11}$$

where $\boldsymbol{\lambda}_i$ are the eigenvalues. The orthogonal eigenfunctions $\boldsymbol{\psi}_i(t;\eta)$ are then normalized as,

$$\big(\boldsymbol{\psi}_i(t;\eta),\boldsymbol{\psi}_j(t;\eta)\big)_{T_{sn}} = \boldsymbol{\delta}_{ij} \tag{6.12}$$

Where, $\boldsymbol{\delta}_{ij}$ is the Kronecker delta in vector form. The POD modes are arranged in descending order of their energy content (the eigenvalues associated with the modes). i.e $\boldsymbol{\lambda}_1 > \boldsymbol{\lambda}_2 >$ ..... $> \boldsymbol{\lambda}_{N_{pod}} > 0$. The orthonormal 'topos' are obtained using Equation (7.10), such that $(\boldsymbol{\phi}_i(\boldsymbol{x};\eta),\boldsymbol{\phi}_i(\boldsymbol{x};\eta))_\Omega = \boldsymbol{\delta}_{ij}$.

$$\boldsymbol{\phi}_i(\boldsymbol{x};\eta) = \frac{1}{\sqrt{N_t\boldsymbol{\lambda}_i}}\big(\boldsymbol{s}'(\boldsymbol{x},t;\eta),\boldsymbol{\psi}_i(t;\eta)\big)_{T_{sn}} \tag{6.13}$$

The corresponding POD time coefficients are given by,

$$\begin{aligned}\boldsymbol{a}_i(t;\eta) &= \big(\boldsymbol{\phi}_i(\boldsymbol{x};\eta),\boldsymbol{s}'(\boldsymbol{x},t;\eta)\big)_\Omega \\ &= \sqrt{N_t\boldsymbol{\lambda}_i}\boldsymbol{\psi}_i(t;\eta)\end{aligned} \tag{6.14}$$

Generally, the number of reduced POD modes (N_r) is much smaller compared to the total POD modes ($N_r << N_{pod}$). The relative energy captured ($\boldsymbol{Ec}$) by the most energetic (first few) POD modes is substantial. It can be given as,

$$\%\boldsymbol{Ec} = \frac{\sum_{i=1}^{N_r}\boldsymbol{\lambda}_i}{\sum_{i=1}^{N_{pod}}\boldsymbol{\lambda}_i} \times 100 \tag{6.15}$$

6.2.2 Periodicity of POD temporal modes

The total energy [†] $\boldsymbol{E}(\eta)_{pod}$ of the unsteady part of the discrete state vector can be given by,

$$\boldsymbol{E}(\eta)_{pod} = \frac{1}{2}\int_\Omega \big\langle \boldsymbol{s}'(\boldsymbol{x},t,\eta)^2\big\rangle_{T_{sn}}\, d\boldsymbol{x} = \frac{1}{2}\sum_{i=1}^{N_{pod}}\boldsymbol{\lambda}_i = \frac{1}{2}\sum_{i=1}^{N_{pod}}\big\langle \boldsymbol{a}_i(t;\eta)^2\big\rangle_{T_{sn}} \tag{6.16}$$

[†] An appropriate term for the non-velocity variables (e.g. density, pressure) be the 'variance'.

The space domain (Ω) is limited by a boundary ($\partial\Omega$). Similarly, let T_{min} be the minimum time window for which the total energy in Equation (7.13) remains the same, such that,

$$\boldsymbol{E}(\eta)_{pod} = \frac{1}{2}\int_{\Omega} \left\langle \boldsymbol{s}'(\boldsymbol{x},t,\eta)^2 \right\rangle_{T_{min}} d\boldsymbol{x} = \frac{1}{2}\sum_{i=1}^{N_{pod}} \boldsymbol{\lambda}_i = \frac{1}{2}\sum_{i=1}^{N_{pod}} \left\langle \boldsymbol{a}_i(t;\eta)^2 \right\rangle_{T_{min}} \tag{6.17}$$

In statistically stationary flows, the POD temporal basis functions observe the stable limit cycles in phase space (see for e.g. (Sirisup and Karniadakis, 2004), (Ma and Karniadakis, 2002), (Aubry, 1991)). Let T_η be the time period of the limit-cycle of first POD time coefficient $\boldsymbol{a}_1(t;\eta)$. The higher (well resolved by snapshots) POD time modes for the state vector are periodic with the time T_η. The characteristic POD time coefficients can be defined as,

$$\tilde{\boldsymbol{a}}_i(t;\eta) = \boldsymbol{a}_i(t;\eta) \qquad for \;\; t \in [t_a, t_a + T_\eta] \tag{6.18}$$

Where $t_a \in [0, (T_{sn} - T_\eta)]$ is an arbitrary time. Further, the total energy in Equation (6.17) becomes,

$$\boldsymbol{E}(\eta)_{pod} = \frac{1}{2}\sum_{i=1}^{N_{pod}} \left\langle \tilde{\boldsymbol{a}}_i(t;\eta)^2 \right\rangle_{T_\eta} = \frac{1}{2}\sum_{i=1}^{N_{pod}} \left\langle \boldsymbol{a}_i(t;\eta)^2 \right\rangle_{T_{min}} = \frac{1}{2}\sum_{i=1}^{N_{pod}} \boldsymbol{\lambda}_i \tag{6.19}$$

It also implies that the minimum time window (T_{min}) is the time period of the first POD temporal mode (T_η).

Under the statistically stationary flow assumption and using the periodic characteristic POD temporal modes (Equation 7.14), one can reconstruct the flow with reduced number (N_r) of POD basis even outside the snapshots time domain (T_{sn}) as,

$$\boldsymbol{s}(\boldsymbol{x},t;\eta) \approx \bar{\boldsymbol{s}}(\boldsymbol{x};\eta) + \sum_{i=1}^{N_r} \boldsymbol{\phi}_i(\boldsymbol{x};\eta)\tilde{\boldsymbol{a}}_i(t;\eta) \qquad t \geq 0 \tag{6.20}$$

6.2.3 Linear interpolation

A linear interpolation is used to interpolate the right hand side terms of Equation (6.20) for the change in operating parameter η. The interpolation of the characteristic POD temporal modes ($\tilde{\boldsymbol{a}}_i$) ensures the appropriate flow energy ($\boldsymbol{E}(\eta)$) levels in the interpolated state.

Let $\boldsymbol{s}(\boldsymbol{x},t;\eta_j)$ with $j = 1, 2$ be the two reference states. In order to build a solution state vector at an operating parameter $\eta \in [\eta_1, \eta_2]$, the time-averaged base flow $\bar{\boldsymbol{s}}(\boldsymbol{x};\eta)$, the POD spacial modes ($\boldsymbol{\phi}_i(\boldsymbol{x};\eta)$) and the associated time coefficients $\tilde{\boldsymbol{a}}_i(t;\eta)$ are obtained by the linear interpolation of the reference states. The interpolation is formulated using a vector $\boldsymbol{\Gamma}(\boldsymbol{\beta};\eta)$ in

Equation (7.16). It stands for the solution state average ($\bar{\boldsymbol{s}}(\boldsymbol{x};\eta)$) and the POD modes ($\boldsymbol{\phi}_i(\boldsymbol{x};\eta)$ and $\tilde{\boldsymbol{a}}_i(t;\eta)$).

$$\boldsymbol{\Gamma}(\boldsymbol{\beta};\eta) = \boldsymbol{\Gamma}(\boldsymbol{\beta};\eta_1) + \left[\frac{(\boldsymbol{\Gamma}(\boldsymbol{\beta};\eta_2) - \boldsymbol{\Gamma}(\boldsymbol{\beta};\eta_1))}{(\eta_2 - \eta_1)}\right](\eta - \eta_1) \tag{6.21}$$

Here $\boldsymbol{\beta}$ is either $\boldsymbol{x}$, for $\bar{\boldsymbol{s}}$, $\boldsymbol{\phi}_i$ or $t \in [0, T_\eta]$ for $\tilde{\boldsymbol{a}}_i$. A priori, the condition in Equation (7.17) is satisfied so that the interpolated quantities (RHS of Equation (6.20)) follow the signs of any of the two (η_1 and η_2) reference cases.

$$(\boldsymbol{\Gamma}(\boldsymbol{\beta};\eta_1), \boldsymbol{\Gamma}(\boldsymbol{\beta};\eta_2))_{\boldsymbol{\beta}} \geq 0 \tag{6.22}$$

The time-averages of the state vectors ($\bar{\boldsymbol{s}}(\boldsymbol{x};\eta_j)$ for $j = 1,2$) generally do not alter their sign for the change in operating parameter (η_j). A symmetry in the flow geometry can lead to a phase difference of π between the corresponding POD space modes ($\boldsymbol{\phi}_i(\boldsymbol{x};\eta_j)$) for different operating conditions (η_j). The constrain in Equation (7.17) ensures that they do not cancel out, while performing the interpolation. In addition, the reference states η_j need to be close enough, in order to perform the linear interpolation (Equation 7.16). The characteristic POD time coefficients ($\tilde{\boldsymbol{a}}_i(t;\eta)$) are brought in minimal phase difference by using Equation 7.17. The interpolated base solution and the POD modes follow any one of the reference states for the phase. The characteristic time period (T_η) is also linearly interpolated for the change in operating parameter (η). The interpolation ROM solution, with the reduced number (N_r) of POD interpolated basis and for the change of parameter (η) in $[\eta_1, \eta_2]$, can be written as,

$$\boldsymbol{s}(\boldsymbol{x},t;\eta) \approx \bar{\boldsymbol{s}}(\boldsymbol{x};\eta) + \sum_{i=1}^{N_r} \boldsymbol{\phi}_i(\boldsymbol{x};\eta)\tilde{\boldsymbol{a}}_i(t;\eta) \qquad t \geq 0 \;\;\&\;\; \eta \in [\eta_1, \eta_2] \tag{6.23}$$

A smooth transition of a ROM solution from one flow state to another is useful in the flow control applications. A continuous mode interpolating technique developed in (Morzynski et al., 2006) uses a parameter κ for a continuous transition between the stability matrices at a steady state to an unsteady (with periodic limit cycle) state. Similarly, a smooth transition between two interpolated off-reference states (η^n, η^{n+1}) can be achieved by,

$$\boldsymbol{\Gamma}(\boldsymbol{\beta};\eta^{n+1}) = \kappa\boldsymbol{\Gamma}(\boldsymbol{\beta};\eta^{n+1}) + (1-\kappa)\boldsymbol{\Gamma}(\boldsymbol{\beta};\eta^n) \tag{6.24}$$

$$T_{\eta^{n+1}} = \kappa T_{\eta^{n+1}} + (1-\kappa)T_{\eta^n} \tag{6.25}$$

Here n is an integer indicator for a flow state. The transition parameter κ varies from 0 to 1.

A simple linear function with an appropriate time delay parameter (c_τ) can be used to obtain a real time transition. Equation (6.26) shows such a function.

$$\kappa = c_\tau \left(t - t_0^{n+1}\right) / T_{\eta^{n+1}} \tag{6.26}$$

Where, t_0^{n+1} represents the time of control parameter change. The time delay constant (c_τ) can be used to control the transition time.

In addition to the linear interpolation, a linear extrapolation of the reference states (η_1 and η_2) can also be used to widen the range of controlling parameter, with a caution of the presence of major flow transitions in the vicinity.

6.2.4 A posteriori error estimate

Snapshots POD and truncation errors

The High Fidelity Model (HFM) solution can be an accurate CFD solution to the full NSEs or the experimental datasets for the flow under consideration. The HFM solution state vector can be expressed in terms of POD basis functions by Equation (6.7). The method of snapshots leads to an approximation (similar to Equation 6.9),

$$\boldsymbol{s}(\boldsymbol{x},t;\eta)_{hf} \approx \bar{\boldsymbol{s}}(\boldsymbol{x};\eta)_{pod} + \sum_{i=1}^{N_{pod}} \boldsymbol{\phi}_i(\boldsymbol{x};\eta)_{pod} \tilde{\boldsymbol{a}}_i(t;\eta)_{pod} \tag{6.27}$$

The subscript 'hf' stands for a high fidelity solution, while as the subscript 'pod' stands for quantities estimated using POD. A posteriori the error in POD discretization can be given by,

$$\boldsymbol{\varepsilon}_{ps}(\boldsymbol{x},t;\eta) = \boldsymbol{s}(\boldsymbol{x},t;\eta)_{hf} - \boldsymbol{s}(\boldsymbol{x},t;\eta)_{pod} \tag{6.28}$$

Where the subscript '$p\boldsymbol{s}$' stands for a POD based error in the solution state vector $\boldsymbol{s}$. The POD error depends mainly on the timestep of snapshots collection (ΔT_{sn}), number of snapshots (N_t) and the time-window of snapshots collection (T_{sn}). A rigorous parametric analysis and error estimate study of the POD method was performed by Kunisch and Volkwein (2002). In order to normalise the errors, let us represent the element wise division of vectors $\boldsymbol{u}$ and $\boldsymbol{v}$ as $\boldsymbol{u} \oslash \boldsymbol{v}$, for no element of vector $\boldsymbol{v}$ is zero ($v_i \neq 0$). Further, the total variance can be defined for the high fidelity state vector $\boldsymbol{s}(\boldsymbol{x},t;\eta)$ as,

$$\boldsymbol{\sigma}^2(\eta) = \int_\Omega \left\langle \boldsymbol{s}'(\boldsymbol{x},t;\eta)_{hf}^2 \right\rangle_{T_\infty} d\boldsymbol{x} \tag{6.29}$$

A posteriori, normalized error in POD discretization can be given by,

$$\varepsilon_p(t;\eta) = \left|\left| \int_\Omega \boldsymbol{\varepsilon}_{ps}(\boldsymbol{x},t;\eta)^2 d\boldsymbol{x} \oslash \boldsymbol{\sigma}^2(\eta) \right|\right|_{r(\boldsymbol{s})} \tag{6.30}$$

In addition, the error introduced by the truncation of the higher ($> N_r$) POD modes can be obtained as,

$$\boldsymbol{\varepsilon}_{ts}(\boldsymbol{x},t;\eta) = \sum_{i=N_r+1}^{N_{pod}} \boldsymbol{\phi}_i(\boldsymbol{x};\eta)_{pod}\, \tilde{\boldsymbol{a}}_i(t;\eta)_{pod} \tag{6.31}$$

The normalized truncation error becomes,

$$\varepsilon_t(t;\eta) = \left|\left| \int_\Omega \boldsymbol{\varepsilon}_{ts}(\boldsymbol{x},t;\eta)^2 d\boldsymbol{x} \oslash \boldsymbol{\sigma}^2(\eta) \right|\right|_{r(\boldsymbol{s})} \tag{6.32}$$

Interpolation error

The interpolation errors associated with each term of the ROM solution (Equation 6.23) with respect to the POD solution can be defined,

$$\begin{aligned}
\boldsymbol{\varepsilon}_{\bar{\boldsymbol{s}}}(\boldsymbol{x};\eta) &= \bar{\boldsymbol{s}}(\boldsymbol{x};\eta)_{pod} - \bar{\boldsymbol{s}}(\boldsymbol{x};\eta) \\
\boldsymbol{\varepsilon}_{\boldsymbol{\phi}_i}(\boldsymbol{x};\eta) &= \boldsymbol{\phi}_i(\boldsymbol{x};\eta)_{pod} - \boldsymbol{\phi}_i(\boldsymbol{x};\eta) \\
\boldsymbol{\varepsilon}_{\tilde{\boldsymbol{a}}_i}(t;\eta) &= \tilde{\boldsymbol{a}}_i(t;\eta)_{pod} - \tilde{\boldsymbol{a}}_i(t;\eta)
\end{aligned} \tag{6.33}$$

Let $\boldsymbol{\varepsilon}_{is}(\boldsymbol{x},t;\eta)$ be the total interpolation error in solution state vector ($\boldsymbol{s}$) with respect to the POD solution. It can be given as,

$$\boldsymbol{\varepsilon}_{is}(\boldsymbol{x},t;\eta) = \boldsymbol{s}(\boldsymbol{x},t;\eta)_{pod} - \boldsymbol{s}(\boldsymbol{x},t;\eta) \tag{6.34}$$

$$\boldsymbol{\varepsilon}_{is}(\boldsymbol{x},t;\eta) = \left(\bar{\boldsymbol{s}}(\boldsymbol{x};\eta)_{pod} + \sum_{i=1}^{N_r} \boldsymbol{\phi}_i(\boldsymbol{x};\eta)_{pod} \tilde{\boldsymbol{a}}_i(t;\eta)_{pod} \right) - \left(\bar{\boldsymbol{s}}(\boldsymbol{x};\eta) + \sum_{i=1}^{N_r} \boldsymbol{\phi}_i(\boldsymbol{x};\eta) \tilde{\boldsymbol{a}}_i(t;\eta) \right) \tag{6.35}$$

Using the individual error definitions from Equation (6.33) and the total interpolation error in Equation (6.35) we obtain,

$$\boldsymbol{\varepsilon}_{i\boldsymbol{s}}(\boldsymbol{x},t;\eta) = \boldsymbol{\varepsilon}_{\bar{\boldsymbol{s}}}(\boldsymbol{x};\eta) + \sum_{i=1}^{N_r} \boldsymbol{\phi}_i(\boldsymbol{x};\eta)\boldsymbol{\varepsilon}_{\tilde{\boldsymbol{a}}_i}(t;\eta) + \boldsymbol{\varepsilon}_{\boldsymbol{\phi}_i}(\boldsymbol{x};\eta)\tilde{\boldsymbol{a}}_i(t;\eta) + \boldsymbol{\varepsilon}_{\boldsymbol{\phi}_i}(\boldsymbol{x};\eta)\boldsymbol{\varepsilon}_{\tilde{\boldsymbol{a}}_i}(t;\eta) \quad (6.36)$$

A priori, the maximum error bound in the linear interpolation can be given by Equation (6.37), for each interpolation error term from Equation (6.36). The second derivatives ($\boldsymbol{\alpha}_*$) must exist.

$$\begin{aligned}
|\boldsymbol{\varepsilon}_{\bar{\boldsymbol{s}}}(\boldsymbol{x};\eta)| &\leq \frac{1}{8}(\Delta\eta)^2 \sup_{\eta\in[\eta_1,\eta_2]} |\boldsymbol{\alpha}_{\bar{\boldsymbol{s}}}(\boldsymbol{x};\eta)| \quad \text{where } \boldsymbol{\alpha}_{\bar{\boldsymbol{s}}}(\boldsymbol{x};\eta) = \frac{\partial^2}{\partial\eta^2}(\bar{\boldsymbol{s}}(\boldsymbol{x};\eta)_{pod}) \\
\left|\boldsymbol{\varepsilon}_{\boldsymbol{\phi}_i}(\boldsymbol{x};\eta)\right| &\leq \frac{1}{8}(\Delta\eta)^2 \sup_{\eta\in[\eta_1,\eta_2]} \left|\boldsymbol{\alpha}_{\boldsymbol{\phi}_i}(\boldsymbol{x};\eta)\right| \quad \text{where } \boldsymbol{\alpha}_{\boldsymbol{\phi}_i}(\boldsymbol{x};\eta) = \frac{\partial^2}{\partial\eta^2}(\boldsymbol{\phi}_i(\boldsymbol{x};\eta)_{pod}) \\
|\boldsymbol{\varepsilon}_{\tilde{\boldsymbol{a}}_i}(t;\eta)| &\leq \frac{1}{8}(\Delta\eta)^2 \sup_{\eta\in[\eta_1,\eta_2]} |\boldsymbol{\alpha}_{\tilde{\boldsymbol{a}}_i}(t;\eta)| \quad \text{where } \boldsymbol{\alpha}_{\tilde{\boldsymbol{a}}_i}(t;\eta) = \frac{\partial^2}{\partial\eta^2}(\tilde{\boldsymbol{a}}_i(t;\eta)_{pod})
\end{aligned} \quad (6.37)$$

The error is $\mathcal{O}(\Delta\eta^2)$. Here $\Delta\eta = (\eta_2 - \eta_1)$. The value of $\Delta\eta$ can be chosen based on the total interpolation error bound $|\boldsymbol{\varepsilon}_{i\boldsymbol{s}}(\boldsymbol{x},t;\eta)|$. The total interpolation error in the solution state vector $\boldsymbol{s}(\boldsymbol{x},t;\eta)$ is in bounds as,

$$|\boldsymbol{\varepsilon}_{i\boldsymbol{s}}(\boldsymbol{x},t;\eta)| \leq \frac{1}{8}(\Delta\eta)^2 \sup_{\eta\in[\eta_1,\eta_2]} \left| \boldsymbol{\alpha}_{\bar{\boldsymbol{s}}}(\boldsymbol{x};\eta) + \sum_{i=1}^{N_r} \boldsymbol{\phi}_i(\boldsymbol{x};\eta)\boldsymbol{\alpha}_{\tilde{\boldsymbol{\alpha}}_i}(t;\eta) + \boldsymbol{\alpha}_{\boldsymbol{\phi}_i}(\boldsymbol{x};\eta)\tilde{\boldsymbol{a}}_i(t;\eta) + \frac{1}{8}(\Delta\eta)^2\boldsymbol{\alpha}_{\boldsymbol{\phi}_i}(\boldsymbol{x};\eta)\boldsymbol{\alpha}_{\tilde{\boldsymbol{\alpha}}_i}(t;\eta) \right| \quad (6.38)$$

On the other hand, a posteriori interpolation error can be directly given by Equation (6.34. The normalized interpolation error will be,

$$\varepsilon_i(t;\eta) = \left|\left| \int_\Omega \boldsymbol{\varepsilon}_{i\boldsymbol{s}}(\boldsymbol{x},t;\eta)^2 d\boldsymbol{x} \oslash \boldsymbol{\sigma}^2(\eta) \right|\right|_{r(\boldsymbol{s})} \quad (6.39)$$

Energy based error

Generally, the error in Galerkin ROM is quantified based on the quadratic flow energy terms. The POD basis functions (topos and chronos) are the optimal basis for a ROM in fluid dynamics, hence it provides an upper bound for the error in Gelerkin ROM ((Balajewicz and Dowell,

2012), (Demmel, 1997)). The normalized error in ROM based on the kinetic energy can be expressed as,

$$\begin{aligned}\varepsilon_e(t;\eta) &= \left|\left|\left(\boldsymbol{E}(t;\eta)_{pod} - \boldsymbol{E}(t;\eta)\right) \oslash \boldsymbol{\sigma}^2(\eta)\right|\right|_{r(\boldsymbol{s})} \\ &= \left|\left|\left(\sum_{i=1}^{N_{pod}} \tilde{\boldsymbol{a}}_i(t;\eta)^2_{pod} - \sum_{i=1}^{N_r} \tilde{\boldsymbol{a}}_i(t;\eta)^2\right) \oslash \boldsymbol{\sigma}^2(\eta)\right|\right|_{r(\boldsymbol{s})}\end{aligned} \tag{6.40}$$

Where $\boldsymbol{E}(t;\eta)$ is the energy of ROM solution. In the presented formulation of ROM, the energy based error ($\varepsilon_e(t;\eta)$) does not account for the error in interpolation of the time-averaged base flow ($\bar{\boldsymbol{s}}(\boldsymbol{x};\eta)$) as well as the POD space modes ($\boldsymbol{\phi}_i(\boldsymbol{x};\eta)$). Therefore the total error relevant to the interpolation ROM can be defined as,

$$\varepsilon_{it}(t;\eta) = \varepsilon_i(t;\eta) + \varepsilon_t(t;\eta) \tag{6.41}$$

6.2.5 Stability of the interpolation ROM

Almost all the Galerkin ROM are unstable and need stabilization techniques such as addition of the artificial viscosity terms, increasing the order of ROM. This way, either the high fidelity Navier-Stokes equation are altered or the computational efforts are increased (Balajewicz and Dowell, 2012). On the contrary, the interpolation based approach of ROM uses the flow statistical stationarity assumption for the energy balance instead of balancing the energy of truncated POD modes by means of the empirical turbulence models. The time average of the total error $\varepsilon_{it}(t;\eta)$ in the interpolation ROM (Equation (6.41)) can be given by,

$$\varepsilon(\eta) = \langle \varepsilon_{it}(t;\eta) \rangle_{T_\infty} = \langle \varepsilon_{it}(t;\eta) \rangle_{T_\eta} \tag{6.42}$$

it implies,

$$\frac{\partial \varepsilon(\eta)}{\partial T_\eta} = 0 \tag{6.43}$$

The errors ($\boldsymbol{\varepsilon}_{p\boldsymbol{s}}(\boldsymbol{x},t;\eta)$, $\boldsymbol{\varepsilon}_{t\boldsymbol{s}}(\boldsymbol{x},t;\eta)$ and $\boldsymbol{\varepsilon}_{i\boldsymbol{s}}(\boldsymbol{x},t;\eta)$) in the interpolation ROM are in bounds under the stationary flow assumption for all time. The total normalized error $\varepsilon(\eta)$ remains a function of the parameters ΔT_{sn}, N_t, N_{pod}, N_r, $\Delta\eta$ and the second derivatives $\boldsymbol{\alpha}_{\bar{\boldsymbol{s}}}$, $\boldsymbol{\alpha}_{\boldsymbol{\phi}_i}$ and $\boldsymbol{\alpha}_{\tilde{\boldsymbol{a}}_i}$.

Floquet stability analysis

Let N_o be the number of POD time modes with the time period T_η. The periodic base flow for the Floquet instability can be given as,

$$\boldsymbol{s}_o(\boldsymbol{x},t;\eta) = \bar{\boldsymbol{s}}(\boldsymbol{x};\eta) + \sum_{i=1}^{N_o} \boldsymbol{\phi}_i(\boldsymbol{x};\eta)\boldsymbol{a}_i(t;\eta) \tag{6.44}$$

Let $\boldsymbol{s}'_o(\boldsymbol{x},t;\eta)$ be the small perturbation in the base flow. It is can be represented in terms of the POD basis as,

$$\boldsymbol{s}'_o(\boldsymbol{x},t;\eta) \approx \sum_{i=N_o+1}^{N_r} \chi_i = \sum_{i=N_o+1}^{N_r} \boldsymbol{\phi}_i(\boldsymbol{x};\eta)\boldsymbol{a}_i(t;\eta) \tag{6.45}$$

The perturbation $\boldsymbol{s}'_o(\boldsymbol{x},t;\eta)$ in the base flow is periodic with the period T_η. Therefore we can consider Equation (6.45) for the Floquet analysis. The T_η periodic functions χ_i can be represented in the form, $\tilde{\chi}_i \exp(\varsigma_i t)$. Where $\tilde{\chi}_i$ are also T_η periodic and known as Floquet modes. The exponents ς_i are called the Floquet exponents. Generally, the Floquet multipliers $\xi_i \equiv \exp(\varsigma_i T_\eta)$ are used in the stability analysis. The perturbation $(\boldsymbol{s}'_o(\boldsymbol{x},t;\eta))$ grows exponentially for $|\xi_i| > 1$ and the periodic base flow is unstable. On the other hand the perturbation decays exponentially for $|\xi_i| < 1$ and the periodic base flow is stable ((Barkley and Henderson, 1996)).

The Floquet modes $(\tilde{\chi}_i)$ at a time instance after n time periods (T_η) can be written as,

$$\tilde{\chi}_i^n = \boldsymbol{\phi}_i(\boldsymbol{x};\eta)\tilde{\boldsymbol{a}}_i(t;\eta)^n \tag{6.46}$$

Where, $\tilde{\boldsymbol{a}}_i(t;\eta)^n = \tilde{\boldsymbol{a}}_i(t_0 + nT_\eta;\eta)$ are the POD time modes at n time periods (T_η) after an initial time t_0. The characteristic POD time modes, as defined in Equation (7.14), are periodic with time T_η. Therefore $\tilde{\boldsymbol{a}}_i(t_0 + nT_\eta;\eta) = \tilde{\boldsymbol{a}}_i(t_0 + (n+1)T_\eta;\eta)$, which leads to $\tilde{\chi}_i^n = \tilde{\chi}_i^{n+1}$. Furthermore, the number of POD modes (N_r) used to build the ROM solution follow stable limit cycles with time period T_η. Thus the value of Floquet multipliers $|\xi_i| = 1$ and the corresponding Floquet exponents $\varsigma_i = 0$. The perturbation $\boldsymbol{s}'_o(\boldsymbol{x},t;\eta)$ neither grows nor decays with the time at a particular operating condition (η).

6.3 Flow past a cylinder at low Reynolds number - a case study

The flow past a cylinder at low Reynolds number ($Re = 125 \sim 150$) in 2-dimension (2D) is considered for the demonstration of the proposed Reduced-Order Model (ROM). Figure (7.1) shows the flow domain and the instantaneous flow fields (u, v and p) at Reynolds number $Re = 125$ ($Re = \rho u_\infty D/\mu$). The cylinder of diameter $D = 1$ is at the center of the computational domain. The inflow streamwise (along $+x$ axis) velocity (u_∞) as well as the temperature (θ_∞) far upstream are set to 1. The density of the fluid (calorically perfect gas) is $\rho = 1$. The Mach number upstream is $M_\infty = 0.18$, while as the specific heat ratio of 1.4 (for air) is taken. The gas constant R and the inflow pressure p_∞ are 22.05. The dynamic viscosity (μ) is constant, it is estimated using the Reynolds number (Re_∞) as, $\mu = (\rho \mathbf{v}_\infty D)/(Re_\infty)$. The inflow transverse velocity is $v_\infty = 0$. The internal energy (e) and the enthalpy (h) are given by $C_v\theta$ and $C_p\theta$ respectively, where C_v, C_p are the specific heats at constant volume and constant pressure respectively. The total energy (E) and the internal energy (e) are related by

$$e = E - \frac{1}{2}\left(u^2 + v^2\right)$$

6.3.1 Governing flow equations and numerical methods

A compressible Navier-Stokes flow solver (Navier-Stokes Multi Block - NSMB) is used with a preconditioning for the incompressible flow at low Mach number. The NSMB solver is developed in collaboration between several European organizations which mainly includes Airbus, KTH, EPFL, IMFT, ICUBE, CERFACS, University of Karlsruhe and ETH-Ecole Polytechnique de Zurich. The code has been developed since early 90's. It is coordinated by CFS Engineering in Lausanne, Switzerland. NSMB is a structured code including a variety of high-order numerical schemes and turbulence modeling such as LES, URANS, RANS-LES hybrid turbulence modeling, especially DDES (Delayed Detached Eddy Simulations).

The compressible unsteady Navier-Stokes equations in 2D can be written as,

$$\frac{\partial}{\partial t}(\boldsymbol{w}) + \frac{\partial}{\partial x}(\boldsymbol{f} - \boldsymbol{f}_v) + \frac{\partial}{\partial y}(\boldsymbol{g} - \boldsymbol{g}_v) = 0 \tag{6.47}$$

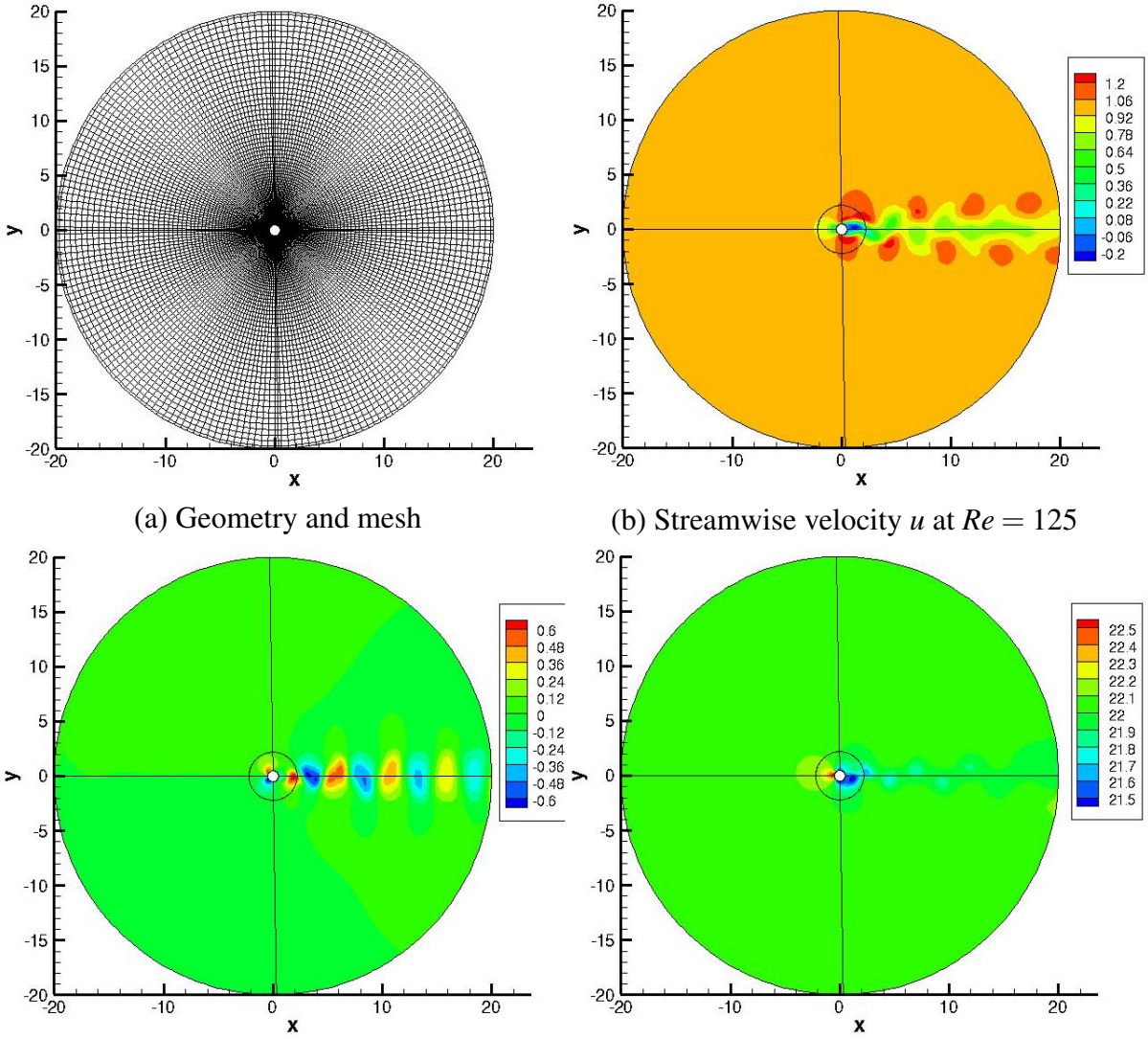

(a) Geometry and mesh

(b) Streamwise velocity u at $Re = 125$

(c) Transverse velocity v at $Re = 125$

(d) Pressure p at $Re = 125$

Figure 6.1 Computational domain and instantaneous flow fields at $Re = 125$.

Where,

$$\boldsymbol{w} = \begin{pmatrix} \rho \\ \rho u \\ \rho v \\ \rho E \end{pmatrix}, \boldsymbol{f} = \begin{pmatrix} \rho u \\ \rho u^2 + p \\ \rho uv \\ u(\rho E + p) \end{pmatrix}, \boldsymbol{g} = \begin{pmatrix} \rho v \\ \rho vu \\ \rho v^2 + p \\ v(\rho E + p) \end{pmatrix}$$

$$\boldsymbol{f}_v = \begin{pmatrix} 0 \\ \tau_{xx} \\ \tau_{xy} \\ [\boldsymbol{\tau}, \mathbf{v}]_x - q_x \end{pmatrix}, \boldsymbol{g}_v = \begin{pmatrix} 0 \\ \tau_{yx} \\ \tau_{yy} \\ [\boldsymbol{\tau}, \mathbf{v}]_y - q_y \end{pmatrix}$$

Here $\boldsymbol{w}$ is the state vector. $\boldsymbol{f}, \boldsymbol{g}$ are the convective fluxes, while as $\boldsymbol{f}_v, \boldsymbol{g}_v$ are the viscous fluxes. The components of shear stress tensor $\boldsymbol{\tau}$ in the viscous fluxes are given by Equation (6.48).

$$\tau_{xx} = \frac{2}{3}\mu\left(2\frac{\partial u}{\partial x} - \frac{\partial v}{\partial y}\right), \tau_{yy} = \frac{2}{3}\mu\left(-\frac{\partial u}{\partial x} + 2\frac{\partial v}{\partial y}\right)$$
$$\tau_{xy} = \tau_{yx} = \mu\left(\frac{\partial u}{\partial y} + \frac{\partial v}{\partial x}\right) \tag{6.48}$$

The heat flux is calculated using Fourier's law as,

$$q_x = -k\frac{\partial \theta}{\partial x}, q_y = -k\frac{\partial \theta}{\partial y} \qquad \text{with } k = \mu C_p/Pr \tag{6.49}$$

Where k is the thermal conductivity. The Prandtl number (Pr) is taken 0.72 (for air).

The second order fully implicit LU-SGS (Lower-Upper Symmetric Gauss-Seidel) backward A-stable scheme with a dual-time stepping is used for the time marching. The space discretization is done using forth order central finite volume scheme in a skew-symmetric form. The preconditioning method proposed in (Turkel et al., 1996) to impose the incompressibility is used, for the flows at low speed (mach number).

6.3.2 Results and discussion

The state vector $\boldsymbol{s}$ in the case study (2-D, incompressible flow) can be considered as,

$$\boldsymbol{s}(\boldsymbol{x}, t; \eta) = \begin{pmatrix} u(\boldsymbol{x}, t; \eta) \\ v(\boldsymbol{x}, t; \eta) \\ p(\boldsymbol{x}, t; \eta) \end{pmatrix} \tag{6.50}$$

Where $\boldsymbol{x}$ is the space domain with x and y dimensions. t represents the time. The operating parameter η is the Reynolds number Re. The two reference cases are considered at Reynolds numbers $\eta_1 = Re_1 = 125$ and $\eta_2 = Re_2 = 150$. The number of snapshots taken for each reference case is $N_t = 900$, this constitutes ≈ 14 vortex shedding periods. The time step for snapshots collection is $\Delta t_{sn} = 0.05$. The correlation matrix was built for each reference case and solved for the eigenvalue problem as detailed in Section (6.2.1). The off-reference case is considered at $\eta = Re = 140$. The linear interpolation of the state vector time-averages and POD modes (both topos and chronos) using the reference states is performed as per Section (6.2.3). The results are build using first 10 POD modes ($N_r = 10$) out of 500 POD modes ($N_{pod} = 500$) and compared with the Navier-Stokes High Fidelity Model (HFM) simulation

results at the same Reynolds number.

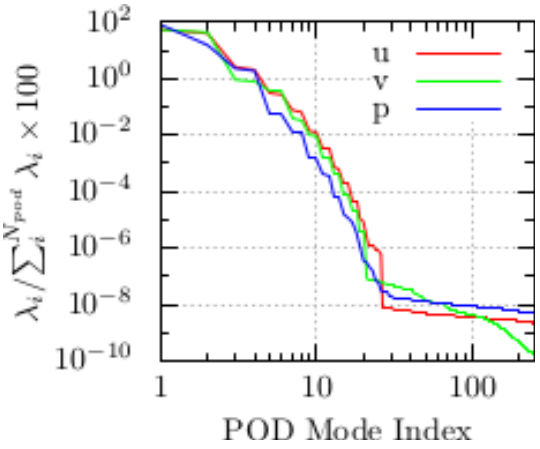

(a) % energy associated with each POD mode of u, v and p.

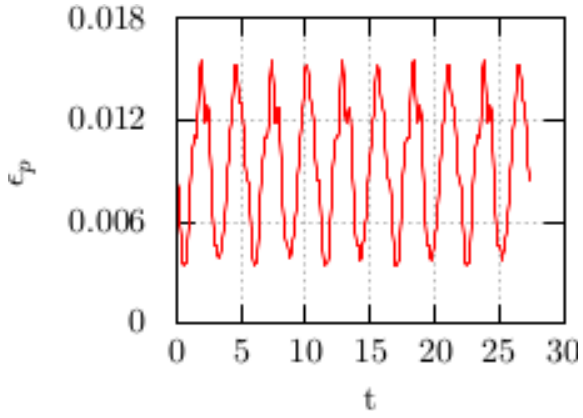

(b) The POD discretization error ($\varepsilon_p(t;Re)$, as defined in Equation (6.30))

Figure 6.2 POD analysis of the flow at $Re = 140$ (η).

The results of POD analysis at $Re = 140$ are shown is Figure (6.2), in terms of the eigenvalues and the time evolution of the discretization error involved in the method of snapshots POD. Figure 6.2(a) shows the % energy associated with each POD mode of the state variables. It also indicates that the $\approx 99.99\%$ of total energy is contained in first 10 modes of each state variables. Therefore the number of reduced basis $N_r = 10$ is chosen for the interpolation (ROM). The discretization error in the method of snapshots POD ($\varepsilon_p(t;\eta)$), as defined in Equation (6.30) is plotted in Figure 6.2(b). The root-mean-srquared (rms) of the error is $\approx 0.25\%$ of the variance of the state variable.

Interpolation of the POD reduced basis

In this case study, the POD space modes ($\boldsymbol{\phi}_i(\boldsymbol{x};\eta)$) are either symmetric or antisymmetric about the x axis. The preconditioning in Equation (7.17) is needed for the antisymmetric modes, only when they observe a flip of sign in changing operating condition (η). Figure (6.3) shows the linear interpolation performed for the fifth space mode of the streamwise velocity (ϕ_5^u). Figures 6.3(a) and 6.3(b) are the fifth POD space modes of the reference cases at $Re_1 = 125$ and $Re_2 = 150$ respectively. The result of interpolation at $Re = 140$ for $\phi_5^u(\boldsymbol{x};Re)$ is shown in Figure 6.3(d). Figure 6.3(c) shows the actual POD mode (ϕ_5^u) at $Re = 140$, computed using the method of snapshots POD for comparison with the interpolated mode.

Similarly, the remaining topos from the reduced basis were interpolated at Reynolds number $Re = 140$. Figure (6.4) shows comparison of the first four interpolated (ROM) modes

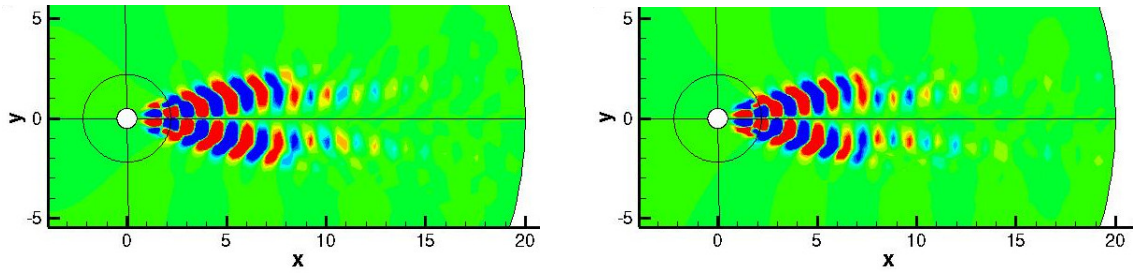

(a) $\phi_5^u(\boldsymbol{x};Re_1)$ (POD)

(b) $\phi_5^u(\boldsymbol{x};Re_2)$ (POD)

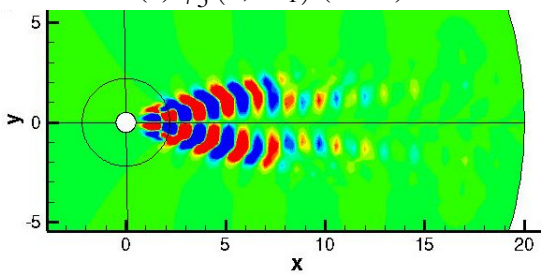

(c) $\phi_5^u(\boldsymbol{x};Re)$ (POD)

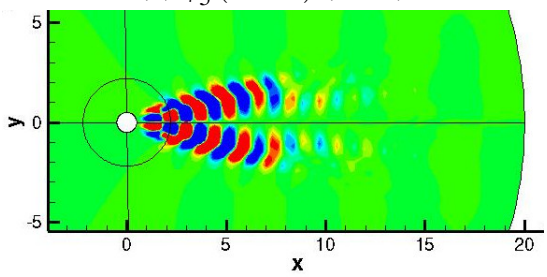

(d) $\phi_5^u(\boldsymbol{x};Re)$ (ROM)

Figure 6.3 The interpolation of $\phi_5^u(\boldsymbol{x},\cdot)$.

(Figures 6.4(b), 6.4(d), 6.4(f), 6.4(h)) versus the snapshots POD modes (Figures 6.4(a), 6.4(c), 6.4(e), 6.4(g) respectively). One can notice that the POD modes act in pairs. The first pair of POD modes of streamwise velocity u (mode number 1 & 2) is antisymmetric, while the second one is symmetric about the x axis. In general here, the odd pairs of POD modes of u are antisymmetric and the even pairs are symmetric. The antisymmetry of the modes about x axis is dealt by the constrain in Equation (7.17) before interpolating the modes. The POD is a biorthogonal decomposition of the flow in space and time, there is one-to-one correspondence between topos and chronos (Aubry, 1991). The change in symmetry of a topo reflects in the corresponding chrono. Although this change of sign (of $\boldsymbol{\phi}_i$ and $\tilde{\boldsymbol{a}}_i$ for the same operating condition) does not alter the value of flow reconstruction by Equation (6.23). The phase information is anyway lost because of the second order statistics used in the POD basis functions (Schmid, 2010). In addition to the phase information, the change of operating condition (Re) leads to the change in orientation of the POD basis functions. The interpolation procedure ensures an appropriate orientation of the POD reduced basis for an intermediate operating conditions between the reference states.

In Galerkin ROMs the time coefficients often need corrections in their amplitudes. The common source of error is due to the truncation of higher POD modes and the formulation of the ROM without pressure-term representation. For instance, the Galerkin ROMs without pressure-term consideration leads to higher amplitudes of the POD time coefficients (Noack

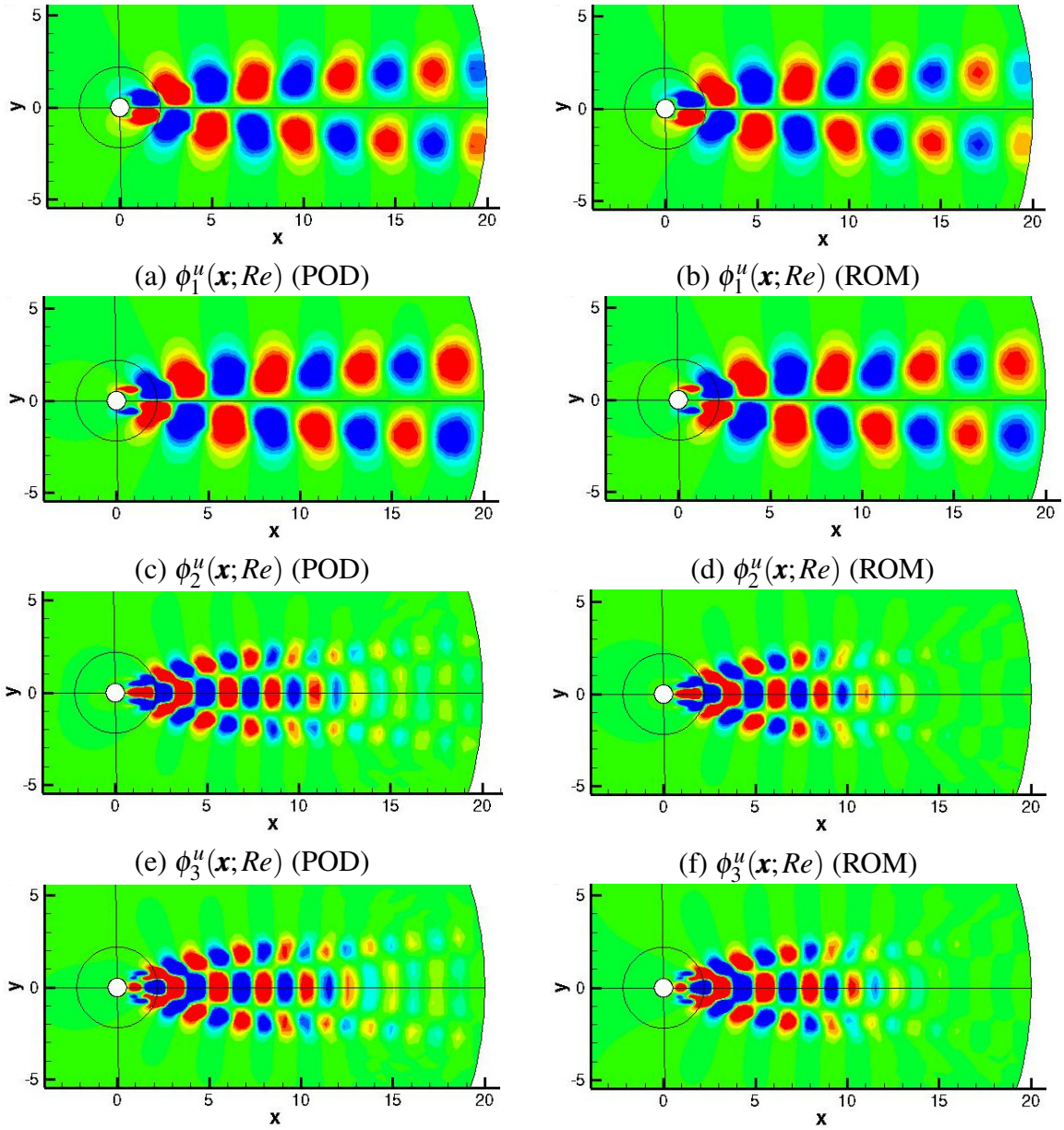

(a) $\phi_1^u(\boldsymbol{x};Re)$ (POD) (b) $\phi_1^u(\boldsymbol{x};Re)$ (ROM)

(c) $\phi_2^u(\boldsymbol{x};Re)$ (POD) (d) $\phi_2^u(\boldsymbol{x};Re)$ (ROM)

(e) $\phi_3^u(\boldsymbol{x};Re)$ (POD) (f) $\phi_3^u(\boldsymbol{x};Re)$ (ROM)

(g) $\phi_4^u(\boldsymbol{x};Re)$ (POD) (h) $\phi_4^u(\boldsymbol{x};Re)$ (ROM)

Figure 6.4 Comparison of $\phi_1^u(\boldsymbol{x},Re)$ to $\phi_4^u(\boldsymbol{x},Re)$ modes obtained by the snapshots POD against the modes obtained by using linear interpolation at $Re = 140$.

et al., 2005). The characteristic POD time coefficients ($\tilde{\boldsymbol{a}}_i(t;Re)$) are immune from the truncation and pressure-term errors, since they are extracted from the time coefficients of the POD ($\boldsymbol{a}_i(t;Re)$) itself as per Equation (7.14) for the reference cases (η_1 and η_2). The characteristic time coefficients, similar to the fellow spacial modes act in pairs. The interpolation results for the characteristic time coefficients (chronos) are shown in Figure (6.5). It shows the com-

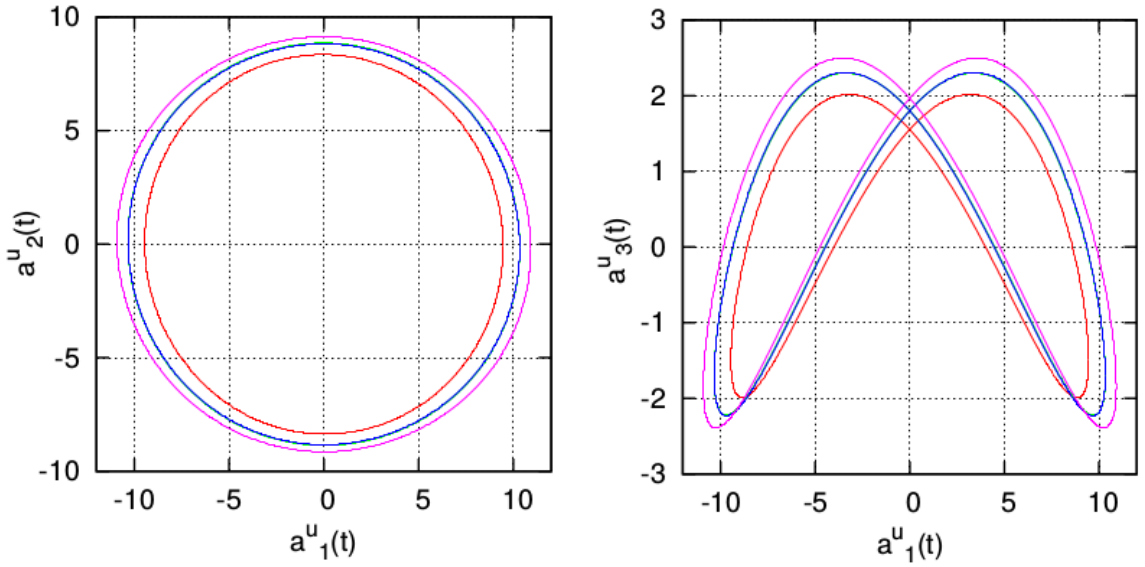

(a) $\left(\tilde{a}_1^u(t;\cdot)\right)$ versus $\left(\tilde{a}_2^u(t;\cdot)\right)$

(b) $\left(\tilde{a}_1^u(t;\cdot)\right)$ versus $\left(\tilde{a}_3^u(t;\cdot)\right)$

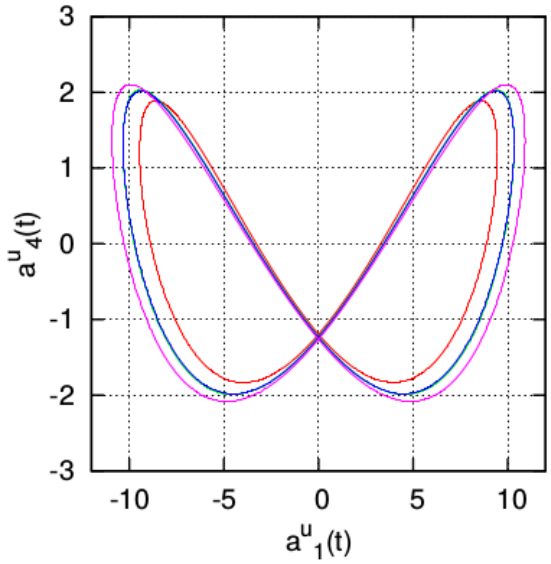

(c) $\left(\tilde{a}_1^u(t;\cdot)\right)$ versus $\left(\tilde{a}_4^u(t;\cdot)\right)$

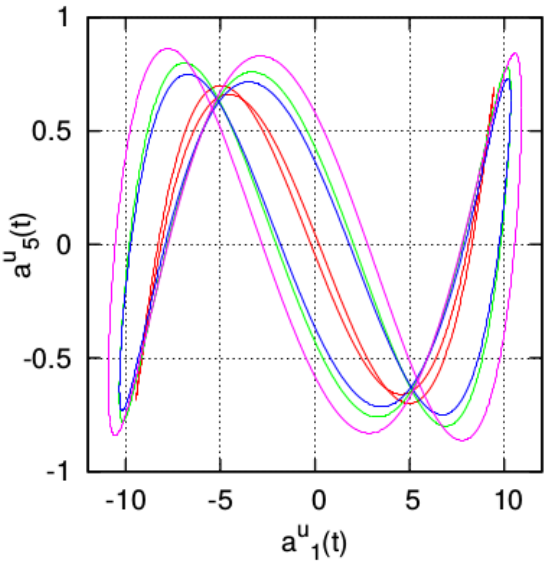

(d) $\left(\tilde{a}_1^u(t;\cdot)\right)$ versus $\left(\tilde{a}_5^u(t;\cdot)\right)$

Figure 6.5 Comparison of the time coefficients $\tilde{a}_i^u(T;\cdot)$ of the first five Chronos. The blue curve in each plot is an interpolated mode (ROM) at $Re = 140$ against the snapshot POD mode at $Re = 140$ in green. The other color correspondence with Reynolds numbers is: Red $\rightarrow Re_1 = 125$ and Pink $\rightarrow Re_2 = 150$

parison of interpolation results in phase space for the first five characteristic time coefficients. The curves in each plot (Figures 6.5(a), 6.5(b), 6.5(c) and 6.5(d)) expand in size, with the increase of Reynolds number. The limit-cycles represented in red color are for the reference state $Re_1 = 125$, while the ones in pink color are for the reference state $Re_2 = 150$. The limit-

cycles at $Re = 140$, in blue color are interpolated using the reference states Re_1 and Re_2. It can be compared with the characteristic POD time modes obtained using snapshots POD at $Re = 140$ in green color.

In addition, the characteristic times (T_η) of the reference states $Re_1 = 125$ and $Re_2 = 150$ are $T_{Re_1} = 5.647$ and $T_{Re_2} = 5.400$ respectively. The linearly interpolated characteristic time at $Re = 140$ is $T_{Re} = 5.499$ against the value 5.489 obtained in POD analysis.

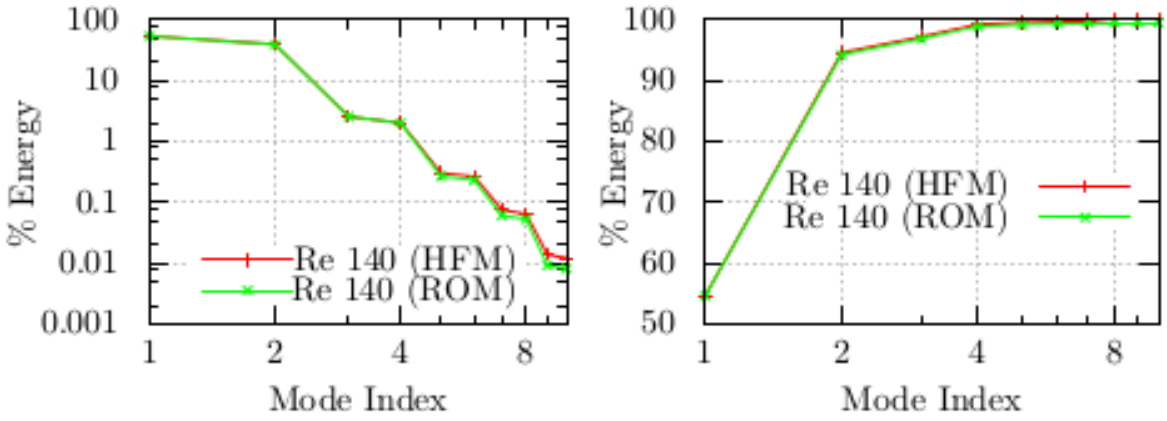

(a) Energy (eigen values) comparison (b) Cumulative energy comparison

Figure 6.6 Energy comparison of the interpolated (ROM) modes with the snapshots POD modes.

The eigenvalues of the interpolation ROM solution at $Re = 140$ were estimated using relation,

$$\boldsymbol{\lambda}_i = \left\langle \tilde{\boldsymbol{a}}_i(t;Re)^2 \right\rangle_{T_{Re}} \tag{6.51}$$

Figure 6.6(a) shows the energy (in %) associated with the reduced interpolated (ROM) modes at $Re = 140$, it is compared with the energy (in %) of the corresponding snapshots POD modes (cumulative plot in Figure 6.6(b)). The time-averaged flow energy estimation using the interpolated POD time modes (Equation 6.51) evinces the orthogonality of the interpolated modes (Balajewicz and Dowell, 2012). An additional orthogonality check is performed a posteriori on the interpolated reduced basis. The angle ($\theta_{\boldsymbol{\gamma},\boldsymbol{\beta}}$) between interpolated modes ($\boldsymbol{\gamma}$, $\boldsymbol{\beta} \in L^2(\Omega)$) is calculated by means of their inner product as,

$$\theta_{\boldsymbol{\gamma},\boldsymbol{\beta}} = \arccos\left(\frac{(\boldsymbol{\gamma},\boldsymbol{\beta})_\Omega}{||\boldsymbol{\gamma}||_\Omega ||\boldsymbol{\beta}||_\Omega}\right) \tag{6.52}$$

The angles (in degree) between the interpolated reduced basis of streamwise velocity (u) are tabulated in Table (6.1). It clearly demonstrates that the interpolation of the POD modes retains the orthogonality of both the topos ($\boldsymbol{\phi}_i$) and chronos ($\tilde{\boldsymbol{a}}_i$).

The errors quantification, as formulated in Section (6.2.4) is plotted in Figure (6.7). The

	ϕ_1^u	ϕ_2^u	ϕ_3^u	ϕ_4^u	ϕ_5^u	ϕ_6^u	ϕ_7^u	ϕ_8^u	ϕ_9^u	ϕ_{10}^u
ϕ_1^u	00.0	89.9	89.9	90.4	90.1	90.0	90.0	90.0	90.0	90.1
ϕ_2^u	89.9	00.0	90.4	90.1	89.8	90.0	90.0	90.0	90.0	90.0
ϕ_3^u	89.9	90.4	00.0	90.4	89.8	90.5	90.1	89.9	90.0	90.0
ϕ_4^u	90.4	90.2	90.4	00.0	90.5	90.3	90.1	89.8	90.0	90.0
ϕ_5^u	90.1	89.8	89.8	90.5	00.0	89.8	90.3	89.7	90.5	89.9
	$\tilde{a}_1^u$	$\tilde{a}_2^u$	$\tilde{a}_3^u$	$\tilde{a}_4^u$	$\tilde{a}_5^u$	$\tilde{a}_6^u$	$\tilde{a}_7^u$	$\tilde{a}_8^u$	$\tilde{a}_9^u$	$\tilde{a}_{10}^u$
$\tilde{a}_1^u$	00.0	90.1	89.0	89.3	90.2	89.7	89.5	90.4	90.4	90.3
$\tilde{a}_2^u$	90.1	00.0	88.7	90.3	91.6	91.3	90.1	90.5	90.3	88.3
$\tilde{a}_3^u$	89.0	88.7	00.0	90.5	91.7	88.3	90.2	88.0	90.3	89.7
$\tilde{a}_4^u$	89.3	90.3	90.5	00.0	88.1	88.0	90.8	89.6	89.6	91.0
$\tilde{a}_5^u$	90.2	91.6	91.7	88.1	00.0	89.9	87.8	94.0	91.4	90.3

Table 6.1 Orthogonality (angle between the modes in degree) of the interpolated reduced basis.

truncation error ($\varepsilon_t(t;Re)$) is nothing but the contribution of higher order POD basis functions ($N_{pod} - N_r$) to the fluctuations in state variables. The maximum truncation error is $\approx 0.25\%$ of the variance (σ^2) for each state variable (Figure 6.7(a)). The interpolation error ($\varepsilon_i(t;Re)$) is relatively high, the maximum of it is about 2% of the variance, for $\Delta\eta = \Delta Re = 25$. The total error relevant to the interpolation ROM ($\varepsilon_{it}(t;Re)$) is also ~ 10 times the truncation error. Figure 6.7(b) shows the errors (ε_i, ε_t & ε_{it}) in phase space. The limit cycles illustrate the boundedness of errors amplitude with the time evolution. On the other hand, maximum of the energy based error $\varepsilon_e(t;Re)$ (as defined in Equation (6.40)) is $\approx 22\%$ of the variance (Figure 6.7(c)). Further, the phase diagrams in Figure 6.7(b) and Figure 6.7 (d) show that the errors follow the stable limit cycles, demonstrating the stability of interpolation ROM method.

High fidelity solution comparisons

Figure 6.8(a) shows the average of streamwise velocity $\bar{u}(\boldsymbol{x};Re)$ obtained using the high fidelity computational fluid dynamics (CFD) simulation at Reynolds number $Re = 140$. The interpolated time-average of the streamwise velocity at same Reynolds number ($Re = 140$) using the reference states at $Re = 125$ and $Re = 150$ is shown in Figure 6.8(b). Generally, the time-averaged base flow shows little variation over the long range of Reynolds numbers. In addition, the dimensionless quantities of practical importance such as Drag, Lift coefficients vary with the logarithmic change in Reynolds number. Therefore the second derivatives $\boldsymbol{\alpha}_*$ in Equation (6.38), contributing to the error bounds for the interpolation error can expected to be small, providing the possibility to have larger $\Delta\eta$. Figure 6.9(a) shows the phase plot

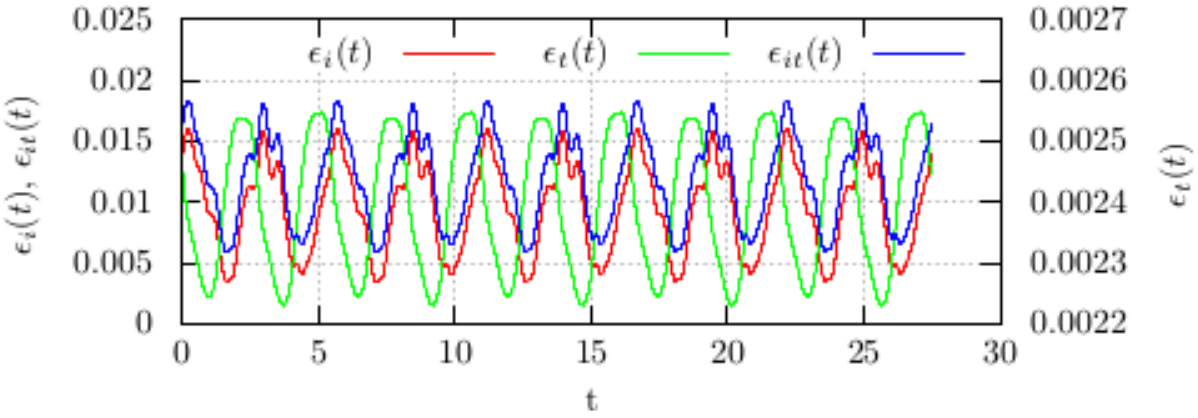

(a) ε_i, ε_t & ε_{it} - a time evolution

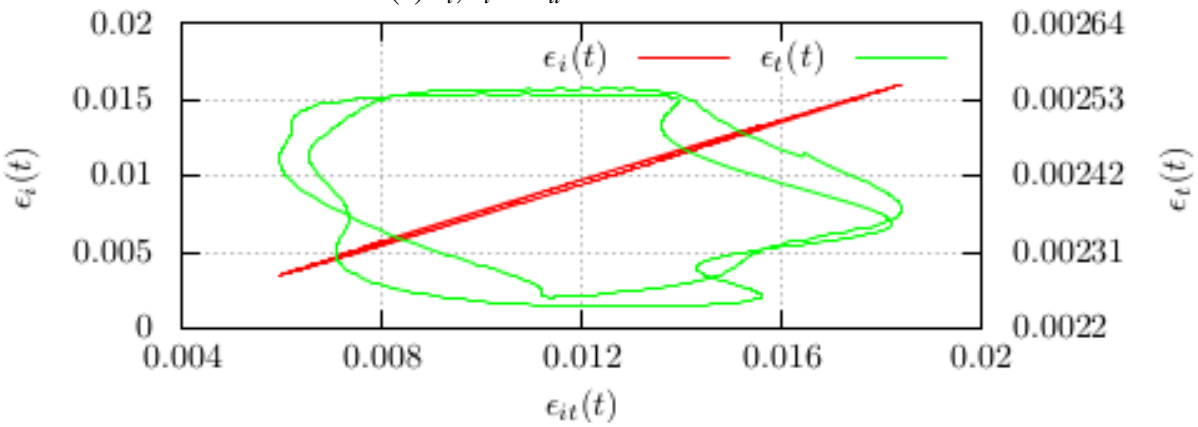

(b) ε_i, ε_t & ε_{it} - in phase space

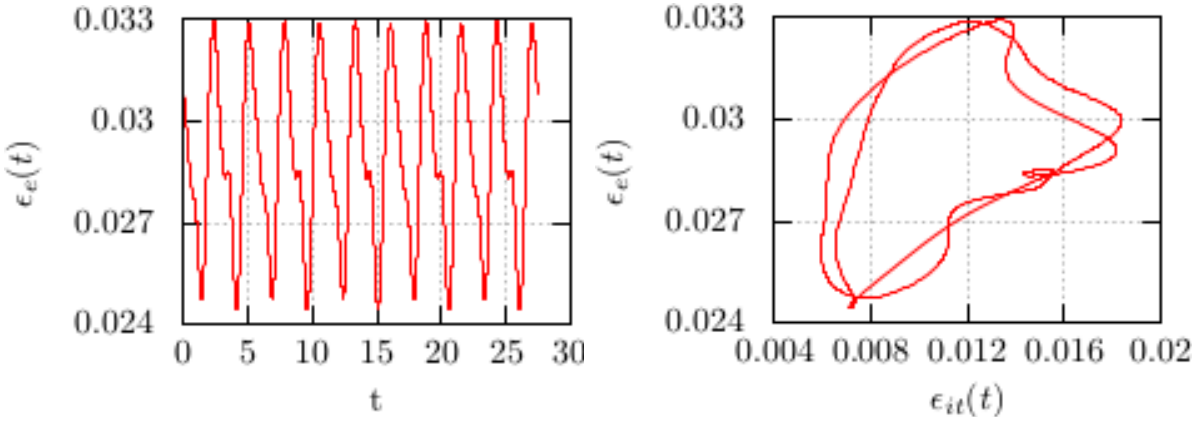

(c) $\varepsilon_e(t;Re)$ (d) ε_e in phase space with ε_{it}

Figure 6.7 Time evolution and phase diagrams of the errors.

of the Drag versus Lift coefficients estimated using pressure force, for both the high fidelity (HFM) and interpolation ROM solutions at $Re = 140$. Figure 6.9(b) shows the comparison of time-averaged pressure coefficient profile on the surface of cylinder at $Re = 140$. The Drag,

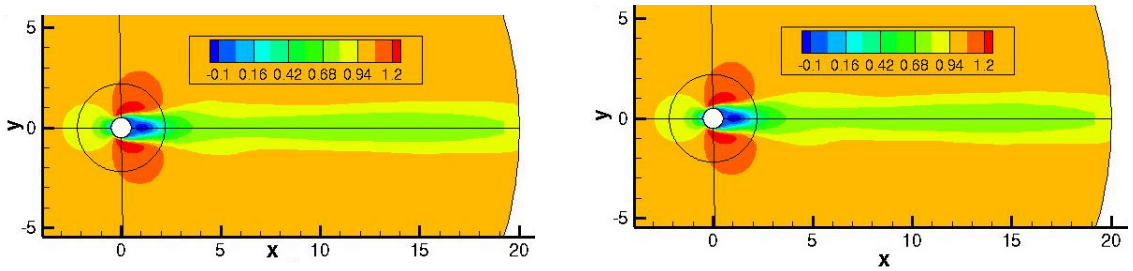

(a) $\bar{u}(\boldsymbol{x};Re)$ (HFM) (b) $\bar{u}(\boldsymbol{x};Re)$ (ROM)

Figure 6.8 Time-averaged base flow comparison at $Re = 140$ ($\bar{u}(\boldsymbol{x},Re)$).

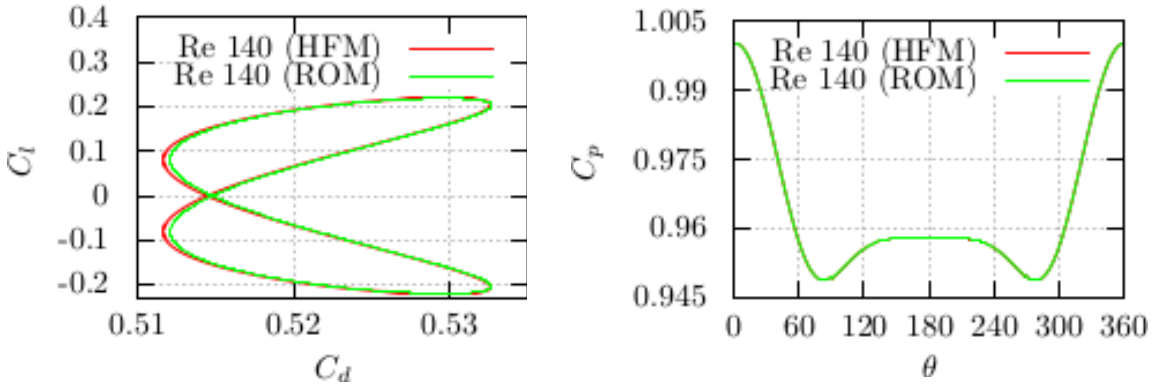

(a) Drag versus Lift coeff. comparison (b) Time-averaged pressure profile

Figure 6.9 The phase plot of Drag vs Lift coefficient and surface pressure profile comparison.

Lift and pressure coefficients are estimated (respectively) as,

$$C_d = 2\int_{L_p} p_l \hat{x} dl; \;\; C_l = 2\int_{L_p} p_l \hat{y} dl \;\text{ and }\; C_p = 2(p - p_\infty) \tag{6.53}$$

Where L_p is the perimeter of cylinder, p_l is the pressure on the small segment (dl) of the perimeter. $\hat{x}$, $\hat{y}$ are the projections of the unit vector normal to a length segment dl along the inflow (x) and flow normal (y) directions respectively.

The time signal of streamwise velocity in Figure 6.10(a) is probed at $x = 5, y = 0$. The time evolution of the Drag and Lift coefficients for unit cylinder length (estimated using pressure force only) is compared in Figure 6.10(b). It shows a fairly good agreement with the high fidelity CFD simulation results. The ROM time signals are $\sim 27\ T_{Re}$ long and they persist for any time duration (T_∞).

A smooth transition between the two off-reference ROM solution is shown in Figure 6.11 (a). The figure shows the drag and lift coefficients plot. The continuous transition of the ROM solution states from $Re = 140$ to $Re = 160$ is obtained by using Equations (6.24), (6.25)

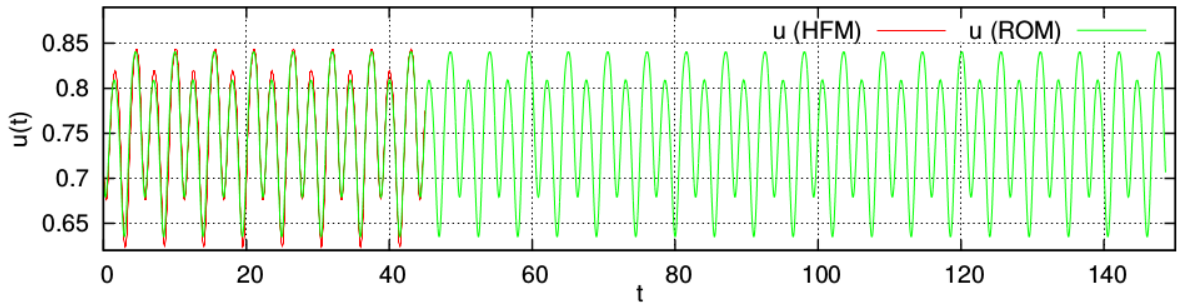

(a) Streamwise velocity at $x = 5, y = 0$

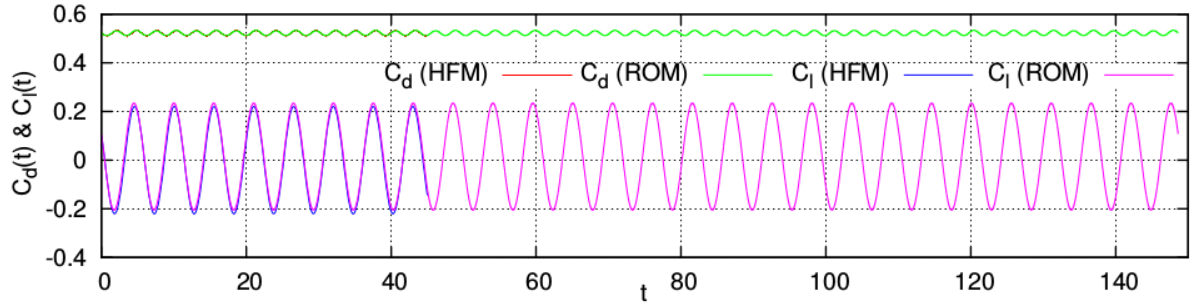

(b) Drag and Lift (pressure) force coeff.

Figure 6.10 Comparison of the time signals of u, C_d and C_l.

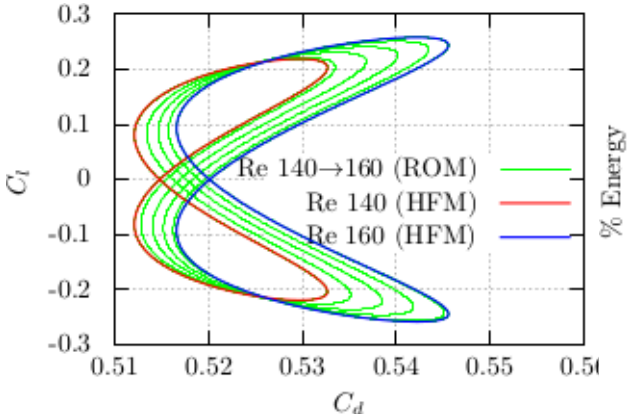

(a) $C_d(t)$ Vs $C_l(t)$

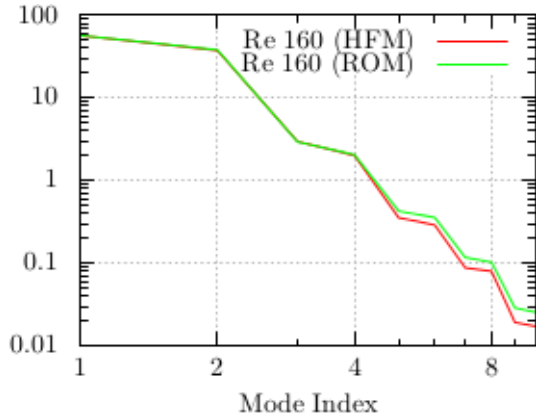

(b) Energy comparison

Figure 6.11 (a) Drag vs Lift coefficient plot showing a smooth transition from $Re = 140$ to $Re = 160$ and (b) energy comparison between HFM ($Re = 160$) and the ROM solution ($Re = 160$) built using a linear extrapolation.

and (6.26). The time coefficient parameter in Equation (6.26) is taken as $c_\tau \approx 0.27$, in order to have the transition between the two operating conditions in $20s$. The value of c_τ varies linearly with time period $T_{\eta^{n+1}}$, for a fixed input of the transition time. The ROM solution at an off-reference operating condition ($Re = 160$) is computed by using a linear extrapolation of

the reference solution states at $Re = 125$ and $Re = 150$. The result of linear extrapolation are compared in Figure 6.11(b), in terms of the % of streamwise velocity (u) fluctuations captured. The plot shows that the ROM solution captures $\approx 98\%$ of the streamwise energy accurately.

6.4 Conclusion

A simple and robust approach to the model reduction of Navier-Stokes equations is presented. In contrast to the Galerkin Reduced-Order Models (ROMs), the method is based on the periodicity of the Proper Orthogonal Decomposition (POD) time coefficients - a beautiful feature of the POD temporal basis functions (chronos) - in statistically stationary flows. In order to cope with the changing operating condition (such as Reynolds number) the reduced POD basis is interpolated using a linear interpolation of the reference operating conditions. The error and stability analysis suggests that the errors in the snapshots POD, truncation of the higher order POD modes and the linear interpolation are bounded for the time evolution. The total absolute error mainly depends on the difference in the two reference states ($\Delta\eta$) and a sensitivity of the flow to the operating parameter. The results of high fidelity CFD simulation of the flow past a cylinder show good agreement with the proposed method. The stable limit-cycles of the errors and the linear interpolation of reduced basis for changing operating condition ensure respectively the stability and robustness of the interpolation ROM. Although the considered case study is in 2-dimensional (2-D) and for an incompressible flow, the mathematical formulation is developed for the full 3-D compressible Navier-Stokes equations. Further, each state variable is treated independently, therefore we anticipate the applicability of the method for a wide range of the problems with coupled phenomena (e.g. flow around aerofoil at high Mach, fluid-structure interaction).

CHAPTER 7

MODEL REDUCTION OF FLUID-STRUCTURE INTERACTIONS BY USING THE GALERKIN-FREE POD APPROACH

Abstract

Reduced-order modeling (ROM) of fluid-structure interaction (FSI) systems is essential, since the applications such as aeroelastic flutter, haemodynamics involve complex physics. In the present work, the Galerkin-free POD-ROM approach is extended to FSI problems. The moving computational mesh in FSI is considered as a part of the solution state vector. The grid deformation is decomposed into Proper Orthogonal Decomposition (POD) modes by using the snapshots POD. In addition to the POD modes of flow variables, the POD modes of grid deformation are also interpolated/extrapolated to an off-referenced solution state. The vortex-induced vibration in a cylinder at Reynolds number $Re = 100$ in 2-dimensions (2-D) for low mass ratios ($m^* = [1.5, 20]$) (mass of the cylinder/mass of the fluid displaced) is considered for discussion. The fluid-structure coupling is simulated using the Arbitrary Lagrangian Eulerian (ALE) approach, where the cylinder is allowed to oscillate only in the flow normal or lift (Y) direction using the mass on a spring motion physics. The mass ratio is considered as the controlling (or changing) parameter of the FSI-ROM. A priori, 10 reference case simulations are performed for different mass ratios, such that a reduced-order solution can be provided for the cylinder displacements ranging approximately between 0 and $1D$. A posteriori estimate of an energy based error in the FSI-ROM remained under 2% of the total variance.

Keywords

Reduced-Order Modeling, Fluid-Structure Interaction, Proper Orthogonal Decomposition, Navier-Stokes equations

Contents

7.1 Introduction

Computing science is addressing more and more complex problems with the benefit of advanced computing algorithms and technology. Computational Fluid Dynamics (CFD) simulations are still a costly endeavour in terms of the computing cost involved in the large scale real world problems (Lucia et al., 2004). Reduced-Order Models (ROM) provide a computationally inexpensive possibility to perform the same computations at a minimum possible complexity and also keep the essential features of system intact. Although, ROM were initially developed for the dynamic systems and control theory, now model reduction is popular in almost every discipline of the computing science and engineering. There exist different approaches for model reduction that are specific to the problem in hand and can be based on the selection of the reduced basis functions. The method of balanced truncation ((Moore, 1981a), (Li et al., 2008)) is based on the controllability and observability of a control system. The Hankel-norm reduction ((Glover, 1984b)) method is applied for the approximation of transfer functions. These methods are originated in the context of the systems and control theory. Although the Proper Orthogonal Decomposition (POD) or Karhunen-Loève expansion was originally developed in statistics, it is commonly used in fluid dynamics ((Lumley,

1967), (Sirovich, 1987)) in order to build reduced order models, to study the flow structures, flow stability and so on. The POD basis serves as an optimal choice (in terms of the flow energy) of the reduced basis ((Holmes et al., 1990)). A traditional procedure to build a ROM in fluid dynamics is by a Galerkin projection of the Navier-Stokes Equations (NSE) on the POD time-invariant reduced basis. The resulting reduced system of the Ordinary Differential Equations (ODE) is then time integrated to obtain the space-invariant POD modes (also known as the POD time coefficients). Thus, the solution is readily built using the POD reduced basis functions.

In addition to the numerical issues associated with Galerkin ROM, a principal difficulty in building a ROM for FSI problems is the dynamic moving mesh (computational grid). In a general strategy, two separate ROM are derived each for the fluid flow and structure domains. The two ROM are then coupled to form a FSI-ROM ((Dowell and Hall, 2001), (Beran et al., 2004), (Vierendeels et al., 2007), Kalashnikova et al. (2013)). This procedure to build a FSI-ROM benefits in terms of reducing the number of parameters and also keeping them independent. In addition to the individual ROM for either domains, sometimes the interface between fluid and solid domains is also modeled using a ROM ((Vierendeels et al., 2007)). The FSI-ROM are developed mainly for the Computational Aeroelasticity analysis or Aeroelastic Flutter and for Haemodynamics applications. In aerodynamics, the weakly coupled flutter analysis is studied with the help of FSI-ROM ((Silva and Bartels, 2004), (Beran et al., 2004), (Raveh, 2005)). In this context, the recent advancement in the ROM based on Proper Orthogonal Decomposition, Volterra series and the method of Harmonic balance are discussed in (Lucia et al., 2004), (Raveh, 2005). On the other hand, the blood flow through the arteries and heart is a strongly coupled FSI problem, where ROM are expected to provide simplistic models ((Colciago et al., 2014), (Gerbeau and Vidrascu, 2003), (Vierendeels et al., 2007)).

The influence of mesh deformation on the POD modes is studied in (Anttonen et al., 2003), where the Multi-POD technique is adopted in order to select the POD basis depending on the grid displacement. The method of Multi-POD is applied to a flow around a pitching and plunging airfoil in (Anttonen et al., 2005), where the blended POD/ROM based on a forced deformation analysis resulted in an accurate and effective FSI-ROM. A Galerkin POD-ROM of FSI is also developed in (Bourguet et al., 2011) for small imposed domain deformations to capture the transition features of a compressible transonic flow. An aeroelastic ROM for wings in transonic flow is obtained through a transonic full-potential aerodynamic model, its transfer functions and a structural dynamic operator for the fluid-structure coupling in (Iemma and Gennaretti, 2005). A general framework for constructing an optimization oriented ROM is presented in (Bui-Thanh et al., 2007), with an example of a subsonic blade row. A FSI-ROM

for a steady FSI problem is presented in (Lassila and Rozza, 2010), where a free-boundary problem is reduced to a low-dimensional parameter space.

In the present work, separate POD modes are obtained for the moving mesh in addition to the flow variables. The reduced number of POD modes are formed by using the energy dominant POD modes of the mesh deformation and flow variables. The POD subspaces are obtained a priori for certain values of the controlling parameters such as Reynolds number (Re), mass ratio (m^*). The POD subspace is directly interpolated (or extrapolated) linearly for the changing controlling parameter in order to obtain an off-referenced reduced solution. A test case of the Vortex-Induced Vibration (VIV) of a single cylinder in 2-D at Reynolds number $Re = 100$ for changing mass ratio (mass of the cylinder/ mass of the fluid displaced) is considered. In the following section (Section 7.2), the mathematical formulation of the procedure including a posteriori error estimate is provided. In Section 7.3, results of the VIV test case are presented.

7.2 Mathematical formulation

The accurate Computational Fluid Dynamics (CFD) simulations coupled with the moving solid boundaries are considered as the High Fidelity Model (HFM). Thus the solution state vector is composed of the mesh deformation in addition to the solution of Navier-Stokes equations. The solution state vector $\boldsymbol{s} = \boldsymbol{s}(\boldsymbol{x},t)$ is spanned on the space $\boldsymbol{x} \in \Omega$, Ω is the spacial flow domain. t is the time in $[0, T_\infty]$. Let H be a Hilbert space and a state variable $\boldsymbol{s}_i(\boldsymbol{x},t) \in H$ with $i = 1,2,\cdots,r(\boldsymbol{s})$. $r(\boldsymbol{s})$ is the number of state variables. The standard inner product of the state variables $\boldsymbol{s}_i(\boldsymbol{x},t_1)$, $\boldsymbol{s}_i(\boldsymbol{x},t_2)$ and the solution state vector $\boldsymbol{s}(\boldsymbol{x},t)$ are respectively,

$$
\begin{aligned}
(\boldsymbol{s}_i(\boldsymbol{x},t_1),\boldsymbol{s}_i(\boldsymbol{x},t_2))_\Omega &= \int_\Omega \boldsymbol{s}_i(\boldsymbol{x},t_1)\cdot\boldsymbol{s}_i(\boldsymbol{x},t_2)d\boldsymbol{x} \\
(\boldsymbol{s}(\boldsymbol{x},t_1),\boldsymbol{s}(\boldsymbol{x},t_2))_\Omega &= \begin{pmatrix} (\boldsymbol{s}_i(\boldsymbol{x},t_1),\boldsymbol{s}_i(\boldsymbol{x},t_2))_\Omega \\ \vdots \\ \left(\boldsymbol{s}_{r(\boldsymbol{s})}(\boldsymbol{x},t_1),\boldsymbol{s}_{r(\boldsymbol{s})}(\boldsymbol{x},t_2)\right)_\Omega \end{pmatrix}
\end{aligned}
\tag{7.1}
$$

Although the spacial flow domain Ω deforms in its shape, the volume of the elemental flow domain $d\boldsymbol{x}$ is assumed to be conserved. The induced norm and time averaging (for time period

T_∞) of a state variable and the solution state vector are respectively defined as,

$$||\boldsymbol{s}_i||_\Omega = \sqrt{(\boldsymbol{s}_i,\boldsymbol{s}_i)_\Omega} \text{ and } \bar{\boldsymbol{s}}_i = \frac{1}{T_\infty}\int_{T_\infty} \boldsymbol{s}_i \, dt = \langle \boldsymbol{s}_i \rangle_{T_\infty}$$

$$||\boldsymbol{s}||_\Omega = \begin{pmatrix} \sqrt{(\boldsymbol{s}_i,\boldsymbol{s}_i)_\Omega} \\ \vdots \\ \sqrt{(\boldsymbol{s}_{r(\boldsymbol{s})},\boldsymbol{s}_{r(\boldsymbol{s})})_\Omega} \end{pmatrix} \text{ and } \bar{\boldsymbol{s}} = \frac{1}{T_\infty}\int_{T_\infty} \boldsymbol{s} \, dt = \langle \boldsymbol{s} \rangle_{T_\infty} \tag{7.2}$$

7.2.1 The Snapshots POD

The method of Proper Orthogonal Decomposition (POD) is brought in fluid mechanics by (Lumley, 1967) in order to analyse the turbulent flow structures. Later, (Sirovich, 1987) proposed the snapshots POD approach to further considerably reduce the degrees of freedom. In the Arbitrary Lagrangian Eulerian (ALE) formulation of fluid-structure coupling the computational mesh is repositioned in accordance with the moving solid boundaries. Therefore, in the solution state vector $\boldsymbol{s}(\boldsymbol{x},t;\eta)$ we can consider the deforming mesh in addition to the flow state variables. The solution state vector can be written as,

$$\boldsymbol{s}(\boldsymbol{x},t;\eta) = \begin{pmatrix} \boldsymbol{x}(t;\eta) \\ \rho(\boldsymbol{x},t;\eta) \\ \mathbf{v}(\boldsymbol{x},t;\eta) \\ p(\boldsymbol{x},t;\eta) \\ \vdots \end{pmatrix} \tag{7.3}$$

Where, η represents the controlling parameter. The variables ρ, $\mathbf{v}$ and p are density, flow velocity and pressure respectively. The solution state vectors at discrete time steps (snapshots) are obtained by performing the accurate HF CFD calculations. The state vector can be decomposed by using the Reynolds decomposition as,

$$\boldsymbol{s}(\boldsymbol{x},t;\eta) = \bar{\boldsymbol{s}}(\bar{\boldsymbol{x}};\eta) + \boldsymbol{s}'(\boldsymbol{x},t;\eta) \tag{7.4}$$

$$= \bar{\boldsymbol{s}}(\bar{\boldsymbol{x}};\eta) + \sum_{i=1}^{\infty} \boldsymbol{\phi}_i(\bar{\boldsymbol{x}};\eta)\boldsymbol{a}_i(t;\eta) \tag{7.5}$$

Where $\boldsymbol{s}'(\boldsymbol{x},t;\eta)$ represents the unsteady part of the Reynolds decomposition. The flow solution is assumed to be statistically stationary. The unsteady part of the state vector in Equation (7.4) is equivalently represented by means of the POD time-invariant (topos) and time-dependent POD modes (chronos) (Equation 7.5). The time-averaged state vector $\bar{\boldsymbol{s}}$ and the

POD time-invariant (or space) modes ($\boldsymbol{\phi_i}$) can be plotted on a time-averaged space vector $\bar{\boldsymbol{x}}$.

$$\boldsymbol{s}(\boldsymbol{x},t;\eta) \approx \bar{\boldsymbol{s}}(\bar{\boldsymbol{x}};\eta) + \sum_{i=1}^{\boldsymbol{N_r}} \boldsymbol{\phi}_i(\bar{\boldsymbol{x}};\eta)\boldsymbol{a}_i(t;\eta) \qquad t_1 \leq t \leq t_{sn} \tag{7.6}$$

The solution state vector can be built using a reduced number of the dominant POD modes ($\boldsymbol{\phi_i}$) and corresponding time coefficients ($\boldsymbol{a_i}$) as shown in Equation (7.6). The solution can be rebuilt in the time interval of snapshots collection i.e. for $[t_1, t_{sn}]$. Where $\boldsymbol{N}_r$ is the reduced number of POD modes, which can be different for each variable of the solution state vector. t_1 and t_{sn} represent the time of first and last snapshots respectively. Let $\boldsymbol{R}(\eta)$ be the two point time-correlation function, given by,

$$\boldsymbol{R}(\eta) = \boldsymbol{R}(t_i,t_j,\eta) = \frac{1}{N_t}\left(\boldsymbol{s}'(\boldsymbol{x},t_i;\eta),\boldsymbol{s}'(\boldsymbol{x},t_j;\eta)\right)_\Omega \qquad i,j = 1,2,.....N_t \tag{7.7}$$

Where N_t stands for the number of snapshots used to estimate the time-correlation tensor. The correlation function $\boldsymbol{R}(\eta)$ is solved for the eigenvalue problem, as in Equation (7.8).

$$\boldsymbol{R}(\eta)\boldsymbol{\psi}_i(t;\eta) = \boldsymbol{\lambda}_i\boldsymbol{\psi}_i(t;\eta) \tag{7.8}$$

where $\boldsymbol{\lambda}_i$ are the eigenvalues. The orthogonal eigenfunctions $\boldsymbol{\psi}_i(t;\eta)$ are then normalized as,

$$\left(\boldsymbol{\psi}_i(t;\eta),\boldsymbol{\psi}_j(t;\eta)\right)_{T_{sn}} = \boldsymbol{\delta}_{ij} \tag{7.9}$$

Where, $\boldsymbol{\delta}_{ij}$ is the Kronecker delta in vector form. The POD modes are arranged in descending order of their energy content (the eigenvalues associated with the modes). i.e $\boldsymbol{\lambda}_1 > \boldsymbol{\lambda}_2 >$ ..... $> \boldsymbol{\lambda}_{N_{pod}} > 0$. The orthonormal 'topos' are obtained using Equation (7.10), such that $(\boldsymbol{\phi}_i(\bar{\boldsymbol{x}};\eta),\boldsymbol{\phi}_i(\bar{\boldsymbol{x}};\eta))_\Omega = \boldsymbol{\delta}_{ij}$.

$$\boldsymbol{\phi}_i(\bar{\boldsymbol{x}};\eta) = \frac{1}{\sqrt{N_t\boldsymbol{\lambda}_i}}\left(\boldsymbol{s}'(\boldsymbol{x},t;\eta),\boldsymbol{\psi}_i(t;\eta)\right)_{T_{sn}} \tag{7.10}$$

The corresponding POD time coefficients are given by,

$$\begin{aligned}\boldsymbol{a}_i(t;\eta) &= \left(\boldsymbol{\phi}_i(\bar{\boldsymbol{x}};\eta),\boldsymbol{s}'(\boldsymbol{x},t;\eta)\right)_\Omega \\ &= \sqrt{N_t\boldsymbol{\lambda}_i}\boldsymbol{\psi}_i(t;\eta)\end{aligned} \tag{7.11}$$

Generally, the number of reduced POD modes ($\boldsymbol{N}_r$) is much smaller compared to the total POD modes ($N_r << N_{pod}$). The relative energy captured ($\boldsymbol{Ec}$) by the most energetic (first few)

POD modes is substantial. It can be given as,

$$\%\boldsymbol{Ec} = \frac{\sum_{i=1}^{\boldsymbol{N_r}} \boldsymbol{\lambda}_i}{\sum_{i=1}^{N_{pod}} \boldsymbol{\lambda}_i} \times 100 \tag{7.12}$$

7.2.2 The POD time modes (Chronos)

The total energy of the system can be estimated by Equation (7.13). It also provides an approximate estimate for the energy in terms of the reduced number of POD time coefficients ($\boldsymbol{a_i}$).

$$\boldsymbol{E}(\eta) = \frac{1}{2}\int_{\Omega} \left\langle \boldsymbol{s}'(\boldsymbol{x},t,\eta)^2 \right\rangle_{T_{sn}} d\boldsymbol{x} \approx \frac{1}{2}\sum_{i=1}^{N_r} \boldsymbol{\lambda}_i = \frac{1}{2}\sum_{i=1}^{N_r} \left\langle \boldsymbol{a}_i(t;\eta)^2 \right\rangle_{T_\eta} \tag{7.13}$$

Here T_{sn} is the time period of the snapshots collection. The approximate total energy can be equivalently obtained for the minimum value of time T_η. T_η is a time-period of the first POD time mode for the operating parameter η. It corresponds to the minimum frequency of a POD time mode present in the coupled system, which is captured in the snapshots. The characteristic chronos are obtained using Equation (7.14). Where t_a is an arbitrary time ($t_a = [0, (t_{sn} - T_\eta)]$).

$$\tilde{\boldsymbol{a}}_i(t;\eta) = \boldsymbol{a}_i(t;\eta) \qquad \text{for } t \in [t_a, t_a + T_\eta] \tag{7.14}$$

The POD modes are organized based on their energy content i.e. simply based on the associated eigenvalues. The energy dominant POD modes are retained as the reduced basis for the model reduction. In addition, the retained reduced basis functions should follow the stable limit cycles in their dynamics. Therefore, we can use the periodicity of the POD time modes resulted from Equation (7.14). Equation (7.6) can be reframed as,

$$\boldsymbol{s}(\boldsymbol{x},t;\eta) \approx \bar{\boldsymbol{s}}(\bar{\boldsymbol{x}};\eta) + \sum_{i=1}^{\boldsymbol{N_r}} \boldsymbol{\phi}_i(\bar{\boldsymbol{x}};\eta)\tilde{\boldsymbol{a}}_i(t;\eta) \quad t \geq 0 \tag{7.15}$$

7.2.3 Linear interpolation

The average of state vector ($\bar{\boldsymbol{s}}$) and the POD modes ($\boldsymbol{\phi_i}$, $\tilde{\boldsymbol{a}}_i$) are linearly interpolated for the change in operating parameters such as Reynolds number, mass ratio (mass of solid/mass of displaced fluid medium) in fluid-structure interaction systems by using Equation (7.16).

$$\boldsymbol{\Gamma}(\boldsymbol{\beta};\eta) = \boldsymbol{\Gamma}(\boldsymbol{\beta};\eta_1) + \left[\frac{(\boldsymbol{\Gamma}(\boldsymbol{\beta};\eta_2) - \boldsymbol{\Gamma}(\boldsymbol{\beta};\eta_1))}{(\eta_2 - \eta_1)}\right](\eta - \eta_1) \tag{7.16}$$

Where η_1, η_2 are the values of controlling parameter for the two high fidelity reference cases. A priori, the standard inner product in Equation (7.17) is satisfied so that the interpolated quantities (RHS of Equation (7.15)) track the signs of η_1 reference case.

$$(\boldsymbol{\Gamma}(\boldsymbol{\beta};\eta_1),\boldsymbol{\Gamma}(\boldsymbol{\beta};\eta_2))_{\boldsymbol{\beta}} \geq 0 \tag{7.17}$$

The linear interpolation can be easily extended for a linear extrapolation using the reference state solutions, in order to broaden the range of operating conditions. Furthermore a smooth transition from an operating condition to another can be achieved by using a linear transition similar to the one used in (Morzynski et al., 2006).

7.2.4 Error estimate

The error estimated is based on the quadratic energy terms, since it provides an upper bound for the error for a Galerkin POD-ROM ((Balajewicz and Dowell, 2012), (Demmel, 1997)). The normalized error ($\varepsilon(t;\eta)$) can be given by,

$$\begin{aligned}\varepsilon(t;\eta) &= \left|\left|\left(\boldsymbol{E}(t;\eta)_{pod} - \boldsymbol{E}(t;\eta)\right) \oslash \boldsymbol{\sigma}^2(\eta)\right|\right|_{r(\boldsymbol{s})} \\ &= \left|\left|\left(\sum_{i=1}^{N_{pod}} \tilde{\boldsymbol{a}}_i(t;\eta)^2_{pod} - \sum_{i=1}^{N_r} \tilde{\boldsymbol{a}}_i(t;\eta)^2\right) \oslash \boldsymbol{\sigma}^2(\eta)\right|\right|_{r(\boldsymbol{s})}\end{aligned} \tag{7.18}$$

Where the subscript *pod* stands for the energy of the POD solution. The symbol '$\oslash$' represents an element to element division of the vectors. The total variance is computed using HF model as,

$$\boldsymbol{\sigma}^2(\eta) = \int_{\Omega} \left\langle \boldsymbol{s}'(\boldsymbol{x},t;\eta)^2_{hf} \right\rangle_{T_\infty} d\boldsymbol{x}$$

7.3 Vortex induced vibration of a cylinder at $Re = 100$ for various mass ratios

The flow past a cylinder in 2-D is considered as the fluid-structure coupled system to build the Galerkin-free FSI ROM. The cylinder (with a natural frequency $f_n = 0.17\ Hz$) undergoes Vortex Induced Vibration (VIV) at Reynolds number $Re = 100$, with $Re = \rho u D/\mu$. Where ρ, μ are the fluid density and fluid dynamic viscosity respectively. D is the cylinder diameter. The fluid velocity at inflow is u (the streamwise velocity component of the velocity). Figure 7.1 (a) shows the extent of computational domain (mesh). The mean flow is in $+x$ direction.

Figure 7.1(b) shows an instantaneous streamwise velocity (u) plotted around the oscillating cylinder.

7.3.1 The flow equations

A compressible flow solver[†] with an appropriate preconditioning scheme for the incompressibility is used to perform the high fidelity CFD simulations.

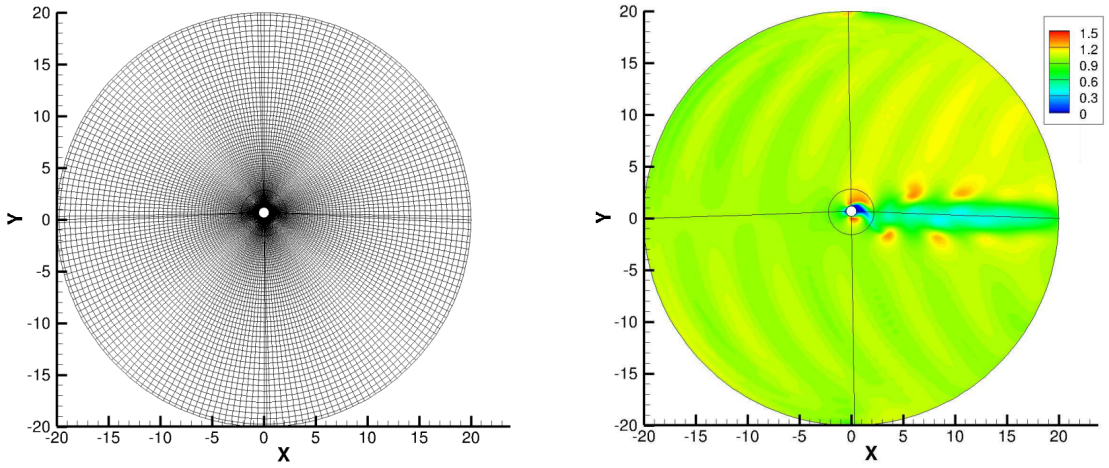

(a) Geometry and mesh

(b) Instantaneous streamwise velocity u

Figure 7.1 Computational domain and instantaneous flow field at $Re = 100$ and mass ratio $m^* = 2.50$.

The full NSE are described from Equation (7.19) through Equation (7.21).

$$\frac{\partial}{\partial t}(\boldsymbol{w}) + \frac{\partial}{\partial x}(\boldsymbol{f} - \boldsymbol{f}_v) + \frac{\partial}{\partial y}(\boldsymbol{g} - \boldsymbol{g}_v) = 0 \tag{7.19}$$

Where,

$$\boldsymbol{w} = \begin{pmatrix} \rho \\ \rho u \\ \rho v \\ \rho E \end{pmatrix}, \boldsymbol{f} = \begin{pmatrix} \rho u \\ \rho u^2 + p \\ \rho uv \\ u(\rho E + p) \end{pmatrix}, \boldsymbol{g} = \begin{pmatrix} \rho v \\ \rho vu \\ \rho v^2 + p \\ v(\rho E + p) \end{pmatrix}$$

$$\boldsymbol{f}_v = \begin{pmatrix} 0 \\ \tau_{xx} \\ \tau_{xy} \\ [\boldsymbol{\tau}, \mathbf{v}]_x - q_x \end{pmatrix}, \boldsymbol{g}_v = \begin{pmatrix} 0 \\ \tau_{yx} \\ \tau_{yy} \\ [\boldsymbol{\tau}, \mathbf{v}]_y - q_y \end{pmatrix}$$

[†]Navier-Stokes Multi Block - NSMB solver

Here $\boldsymbol{w}$ is the state vector. $\boldsymbol{f}, \boldsymbol{g}$ are the convective fluxes, while as $\boldsymbol{f}_v, \boldsymbol{g}_v$ are the viscous fluxes. The components of shear stress tensor $\boldsymbol{\tau}$ in the viscous fluxes are given by Equation (7.20).

$$\begin{aligned} \tau_{xx} &= \frac{2}{3}\mu\left(2\frac{\partial u}{\partial x} - \frac{\partial v}{\partial y}\right), \tau_{yy} = \frac{2}{3}\mu\left(-\frac{\partial u}{\partial x} + 2\frac{\partial v}{\partial y}\right) \\ \tau_{xy} &= \tau_{yx} = \mu\left(\frac{\partial u}{\partial y} + \frac{\partial v}{\partial x}\right) \end{aligned} \tag{7.20}$$

The heat flux is calculated using Fourier's law as,

$$q_x = -k_\theta \frac{\partial \theta}{\partial x}, q_y = -k_\theta \frac{\partial \theta}{\partial y} \qquad \text{with } k_\theta = \mu C_p / Pr \tag{7.21}$$

Where k_θ, θ are the thermal conductivity, temperature respectively. The Prandtl number (Pr) is taken 0.72 (for air).

The second order fully implicit LU-SGS (Lower-Upper Symmetric Gauss-Seidel) backward A-stable scheme is used for time marching. The space discretization is done using forth order central finite volume scheme in a skew-symmetric form. The preconditioning method proposed in (Turkel et al., 1996) to impose the incompressibility is used for the flows at low speed (mach number).

7.3.2 Fluid-structure coupling

The Algebraic Lagrangian Eulerian (ALE) method is used to simulate the fluid-structure coupling. The motion of cylinder is considered as the mass on a spring system as shown in Figure (7.2). The cylinder is allowed to oscillate only in flow normal/lift (Y) direction.

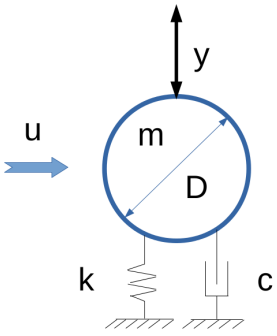

Figure 7.2 The coupling between the cylinder and surrounding fluid.

The equation of motion of the cylinder in flow normal (Y) direction, under VIV can be

written as,

$$m\frac{d^2y}{dy^2} + c\frac{dy}{dy} + ky = F_y \tag{7.22}$$

Here y is the displacement in the cylinder in the lift direction. m is the mass of cylinder per unit length, while c, k are the damping and stiffness coefficients respectively. The cylinder is driven by the fluid force (F_y) per unit length, which is on the right hand side of Equation (7.22). Table (7.1) specifies the values of the simulation parameters. $u^* = u/(f_n D)$, f_n and $\zeta = c/(2\sqrt{km})$ are the reduced velocity, cylinder natural frequency (vacuum) and the damping ratio of the cylinder oscillations (vacuum) respectively. The cylinder's and flow density are $D = 1\ m$ and $\rho = 1\ kg/m^3$ respectively.

Re	u^*	$f_n\ (Hz)$	$\zeta\ (\%)$
100	5.88	0.17	20

Table 7.1 Simulation Parameters.

The mass ratio ($m^* = m/(\rho D^2)$) of the system is taken as the controlling parameter for the system ($\eta = m^*$). The high fidelity simulations are simulated at Reynolds number $Re = 100$ for different values of the mass-ratio (m^*). The mass ratio is changed in order to have the amplitude of oscillations of the cylinder varying approximately from $y = 0$ to $y = 1D$.

7.3.3 POD analysis

The solution state vector ($\boldsymbol{s}(\boldsymbol{x},t;\eta)$, in Equation 7.3) becomes,

$$\boldsymbol{s}(\boldsymbol{x},t;m^*) = \begin{pmatrix} y(t;m^*) \\ u(\boldsymbol{x},t;m^*) \\ v(\boldsymbol{x},t;m^*) \\ p(\boldsymbol{x},t;m^*) \end{pmatrix} \tag{7.23}$$

The number of snapshots of the solution state vector taken is 576. They are collected with a timestep of $\Delta t = 0.05$. A time-correlation tensor is formed by using the unsteady part ($\boldsymbol{s}'$) of the state vector, which is then solved for the eigenvalue problem. The % energy ($\lambda_i/\sum_i \lambda_i \times 100$) associated with the POD modes of the different state variables is plotted in Figure (7.3). The POD modes are sorted based on their energy content. The percentage of energy associated with the first POD modes of the mesh deformation is almost 100% (Figure 7.3 (a)). Therefore, just one mode ($N_r^y = 1$) is sufficient for the reconstruction of mesh movement. On the other

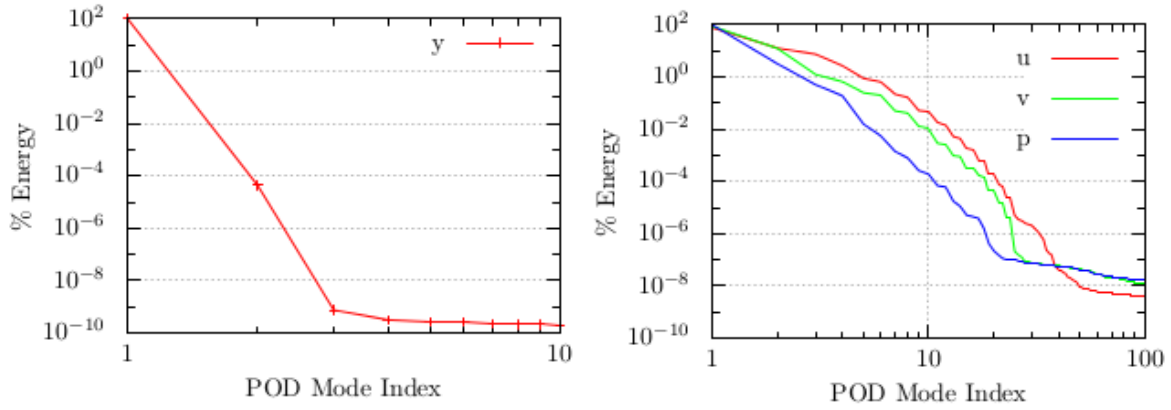

(a) POD modes energy (y) (b) POD modes energy (u, v and p)

Figure 7.3 % energy associated with the POD modes at $Re = 100$, $m^* = 2.50$.

hand, the first 10 POD modes of the flow variables contain most of the energy. Thus the number of reduced modes used for the flow variables i.e. velocity (u, v) and pressure (p) is $N_r = 10$. Figure 7.4(a) shows the normalized, time-invariant, first POD mode ($\phi_1^y(\bar{\boldsymbol{x}}; m^*)$)

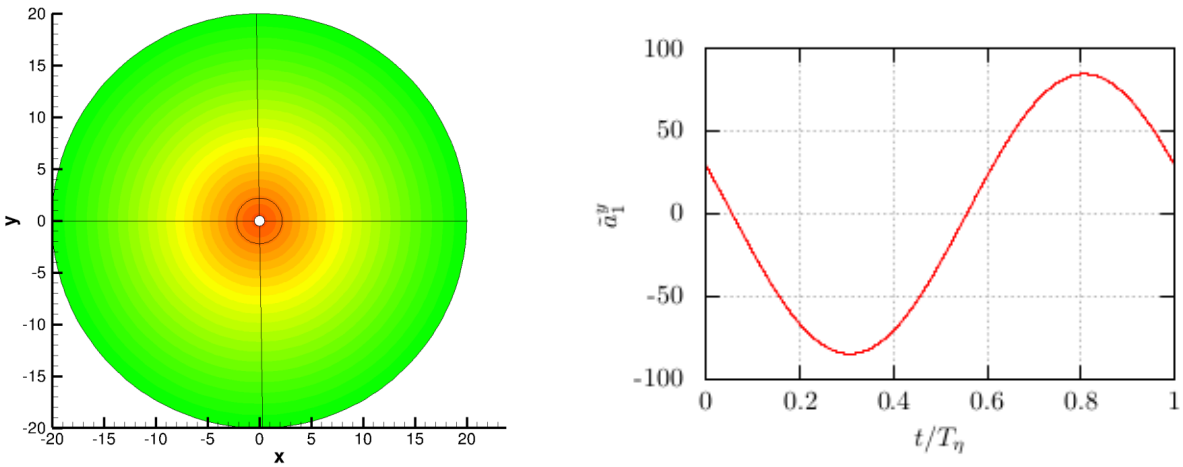

(a) Space mode ($\phi_1^y(\bar{\boldsymbol{x}}; m^*)$) (b) Time mode ($a_1^y(t; m^*)$)

Figure 7.4 The pair of first POD mode of the mesh deformation in y direction at $Re = 100$, $m^* = 2.50$.

of the mesh deformation for mass ratio $m^* = 2.50$. The corresponding first POD time mode (chrono) $a_1^y(t; m^*)$ is shown in Figure 7.4(b) over one time period $T_{m^*} = 5.79622s$.

7.3.4 ROM solution states

The reference case simulations are performed for 10 different values of the mass ratio (m^*), in order to have the cylinder response (y) varying from 0 upto $1D$. Table (7.2) shows the details of reference cases simulated for various mass ratios (listed in first row) and the corresponding Root Mean Squared (rms) response of cylinder per unit diameter ($y^*_{rms} = y_{rms}/D$) in the second row.

Mass ratio (m^*)	1.5	1.75	2	2.5	3	3.5	5	7	10	20
Cylinder response (y^*_{rms})	.69	.64	.59	.51	.44	.38	.25	.21	.10	.04

Table 7.2 Reference case simulations.

The vortex-induced free vibrations in a circular cylinder are extensively studied. The progress on the topic is well reviewed in (Williamson and Govardhan, 2004). There exist a minimum value for the mass ratio (m^*) as discussed in (Williamson and Govardhan, 2004) ($m^* \approx 0.5$, the value changes with other system parameters). The damping ratio (ζ) used in the present work is very high (20%), in order to obtain the desired amplitudes of cylinder oscillations. Thus the mass-damping parameter $m^*\zeta$ varies from 0.2 upto 4. The physics of the problem at small and very small mass-damping parameter is studied in (Khalak and Williamson, 1997) and (Khalak and Williamson, 1999). The non-dimensional (reduced) frequency $f^* = f_n \times T_{m^*} = 1.015$, for $m^* = 2.5$.

The reduced number of POD modes ($\boldsymbol{N}_r$) with high energy content are selected to form the POD subspace. There exist two main problems in constructing the ROM of this FSI system, first, the traditional Galerkin projection of the Navier-Stokes equations on the POD time invariant modes (or space modes) does not lead to set of ordinary differential equations, since the space (fluid domain) is time dependent. Second, the validity of a ROM based on POD is generally limited to a small range of controlling parameter. The POD reduced basis depends non-linearly on the controlling parameter. In an interesting work, (Bui-Thanh et al., 2003) proposed a gappy POD procedure to construct the off-reference ROM solutions, thereby dealing with the change of controlling parameters. Further, the method uses the POD coupled with an interpolation method, which avoid the Galerkin projection of governing equations. In (Lieu et al., 2006) a ROM for a complete aircraft is formulated based on a Mach-adaptation strategy, where the angle between the POD subspace is interpolated in order to deal with the changes in the controlling parameter. The interpolation of the reduced basis for the change in controlling parameter is performed in a tangent space to a Grassmann manifold in (Amsallem and Farhat, 2008) and further on matrix manifolds in (Amsallem and Farhat, 2011). In the

present work, the periodic construction of the POD time modes as per Equation (7.14) is used to avoid the Galerkin projection and the solution including the mesh deformation is readily built using Equation (7.15). A direct linear interpolation of the POD space as well time modes is performed in order to predict an off-reference solution state by using the pre-simulated reference cases. An extrapolation of the reference states can be used to broaden the range of controlling parameter.

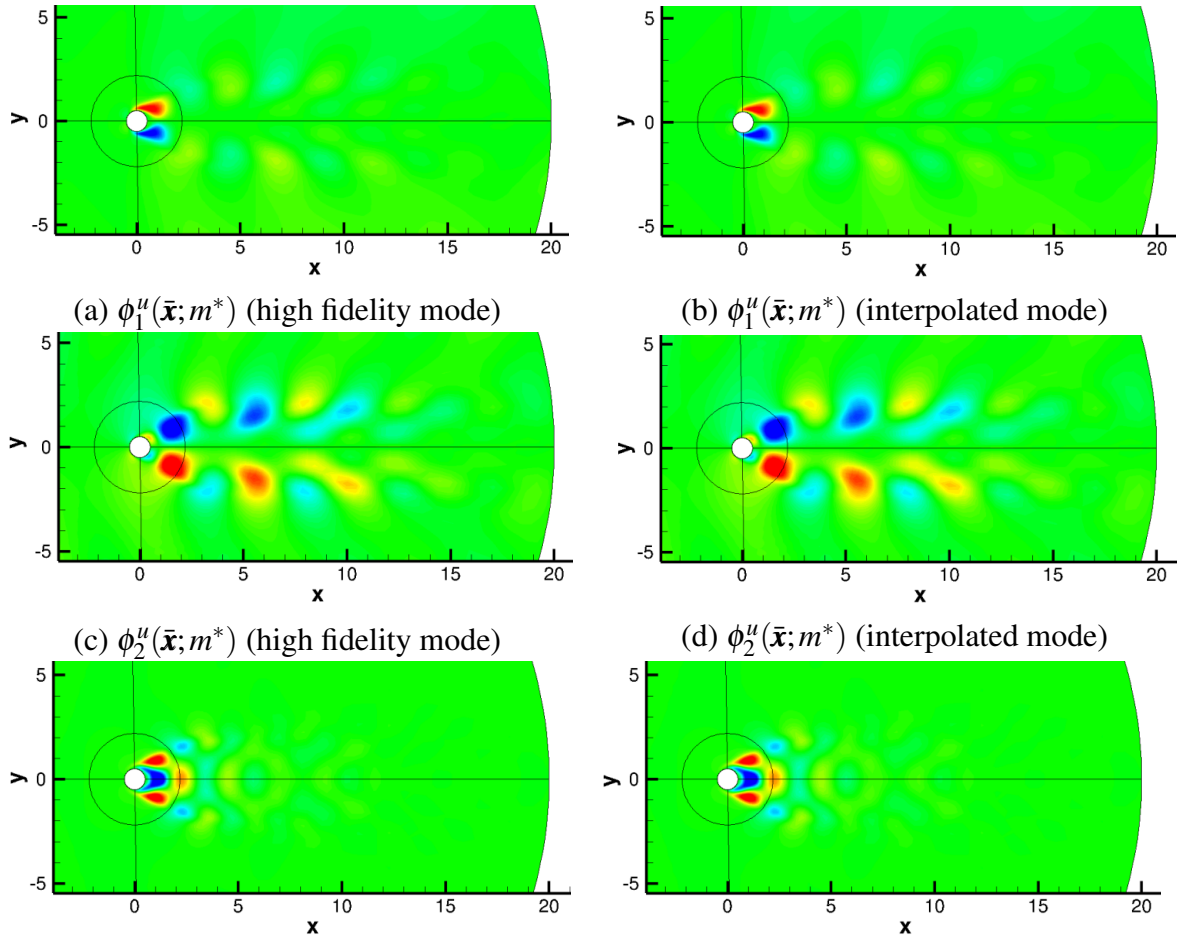

(a) $\phi_1^u(\bar{\boldsymbol{x}};m^*)$ (high fidelity mode) (b) $\phi_1^u(\bar{\boldsymbol{x}};m^*)$ (interpolated mode)

(c) $\phi_2^u(\bar{\boldsymbol{x}};m^*)$ (high fidelity mode) (d) $\phi_2^u(\bar{\boldsymbol{x}};m^*)$ (interpolated mode)

(e) $\phi_3^u(\bar{\boldsymbol{x}};m^*)$ (high fidelity mode) (f) $\phi_3^u(\bar{\boldsymbol{x}};m^*)$ (interpolated mode)

Figure 7.5 Comparison of the POD space modes computed using the high fidelity model with the interpolated modes at $Re = 100$, $m^* = 2.75$.

The linear interpolation of the energy dominant ($\boldsymbol{N}_r$) POD modes is performed for the intermediate values of mass ratio using the reference cases tabulated in Table (7.2). The comparison of the interpolated POD modes with the high fidelity POD modes at an off-reference case (mass ratio $m^* = 2.75$) is shown in Figure (7.5). The figure compares the first three time-invariant POD modes (topos) of the streamwise velocity (u). Figure 7.5 (a), (c) and (e) show

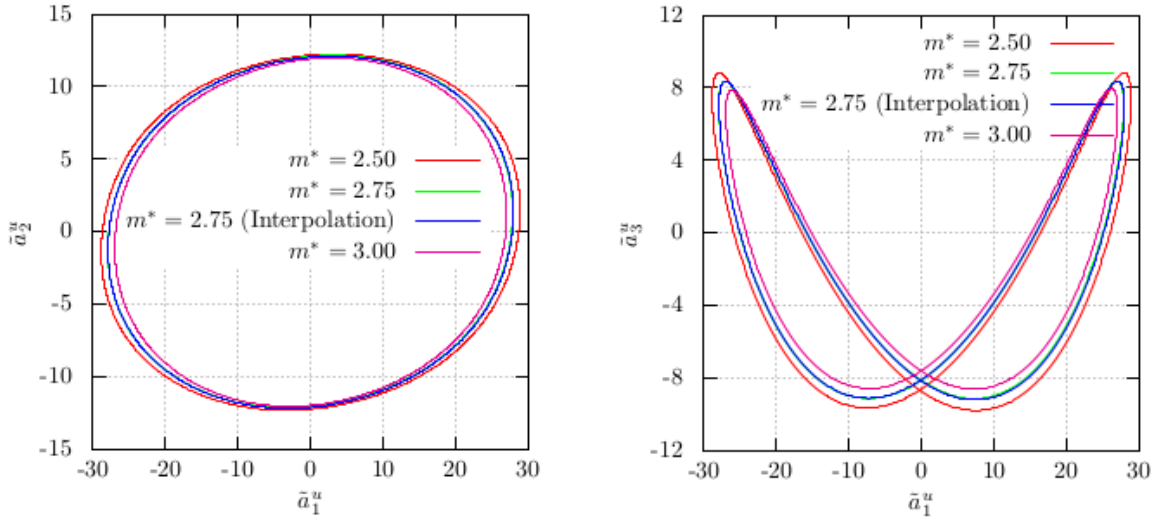

(a) $\tilde{a}_1^u(t;m^*)$ Vs. $\tilde{a}_2^u(t;m^*)$ (b) $\tilde{a}_1^u(t;m^*)$ Vs. $\tilde{a}_3^u(t;m^*)$

Figure 7.6 Comparison of the POD time modes computed using the high fidelity model with the interpolated modes at $Re = 100$, $m^* = 2.75$.

the first three energy dominant POD modes (ϕ_1^u, ϕ_2^u and ϕ_3^u) respectively, which are obtained by using the high fidelity simulation. In comparison, the POD modes in Figure 7.5 (b), (d) and (f) are the corresponding linearly interpolated POD space modes, obtained by using the reference state POD subspaces at $m^* = 2.50$ and $m^* = 3.00$. The modes are shown on a time-averaged computational grid. A similar configuration at Reynolds number $Re = 1690$ is treated in (Liberge and Hamdouni, 2010). A non-linear FSI ROM based on a multiphase formulation of the Navier-Stokes and its extension in the solid domain is presented. The Reynolds number is considered as the controlling parameter.

In addition to the interpolation of the POD space modes, the POD time modes are also linearly interpolated in phase space. The interpolation of the first three POD time modes (chronos) in phase space is shown in Figure (7.6). The interpolated chronos (in blue color, Figure (7.6)) coincide with the high fidelity modes beneath (in green color, Figure (7.6)), which indicates the accuracy of the FSI ROM. The plot of the normalized energy based error ($\varepsilon(t)$), as defined in Equation (7.18), is shown in Figure (7.7)(b). It is bounded under 2%. A ROM solution can be built within a minute on a single processor using the interpolated POD reduced basis, while as the corresponding high fidelity CFD simulation takes about 20 hours on 8 processors to provide the solution. Figure (7.8) shows a comparison of instantaneous streamwise velocity plots between HF CFD model and the FSI ROM, built at a time $t = 10s$.

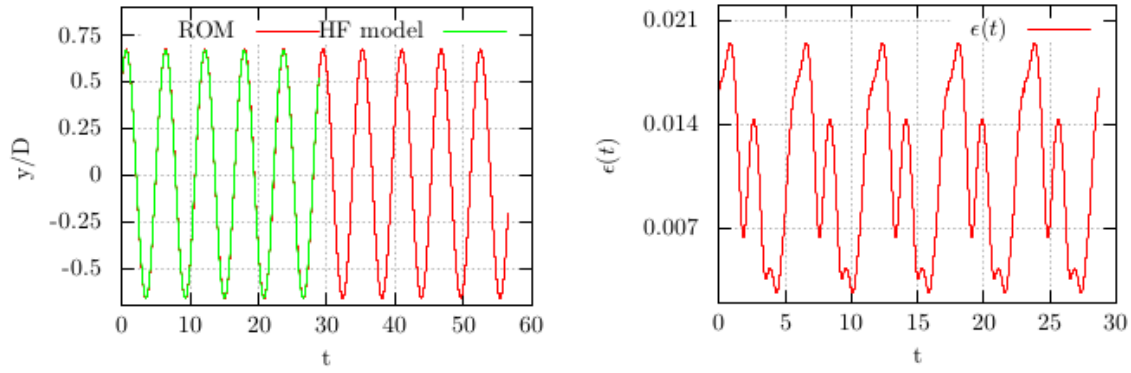

(a) Cylinder timely response at $m^* = 2.75$ (b) Error $\varepsilon(t)$

Figure 7.7 Comparison of the ROM solution with high fidelity CFD solution at $Re = 100$, $m^* = 2.75$.

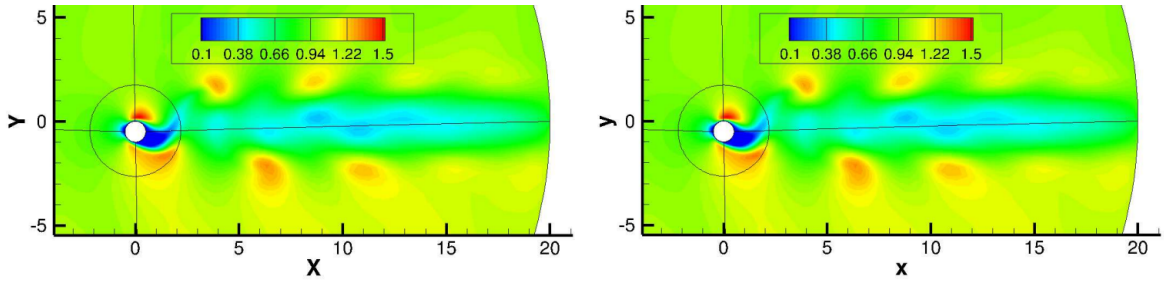

(a) u at $t = 10s$ (High Fidelity) (b) u at $t = 10s$ (ROM)

Figure 7.8 Comparison of the streamwise velocity (u) at $t = 10s$ for $m^* = 2.75$.

7.4 Conclusion

A Galerkin-free approach to model reduction of fluid-structure coupled problems based on the POD modes interpolation is developed. The mesh deformation is considered in the solution state. The snapshots POD analysis is performed on the mesh deformation in addition to the flow variables. The time periodicity of the POD time modes is used to extract the characteristic POD modes. A linear interpolation of the POD subspace is performed to cope with the changing controlling parameter. A case study of the Vortex Induced Vibration of a cylinder placed in external flow is considered. The high fidelity CFD simulations are performed at Reynolds number $Re = 100$. The mass ratio (m^*) is used as an operating parameter for the FSI-ROM. The FSI-ROM solutions are built using 10 reference case simulations for different values of mass ratio such that the range of amplitudes of the cylinder oscillations is from 0 to $1D$. Only 1 POD mode of the mesh deformation and 10 POD modes of the flow variables (velocity, pressure) are required to build a solution with an error less than 2% of the total

variance.

CHAPTER 8

CONCLUSIONS AND OUTLOOK

Contents

8.1 Conclusions

The flow induced vibrations in tube arrays under cross flow arrangement, particularly the fluidelastic vibration is investigated in this thesis work. Numerical simulations of the cross-flow through tube arrays are performed by using the URANS and LES calculations. A mathematical model for the fluidelastic instability is developed. In addition, the second part of thesis deals with reduced-order modeling of the fluid flow dynamical systems. A novel Galerkin-free technique for model reduction of the Navier-Stokes equations is developed and extended to the fluid-structure interaction problems. Below are the concluding remarks and an outlook on the thesis results.

1. In the beginning of thesis, a detailed introduction to the flow induced vibrations in heat exchanger tube bundles is provided. There are several excitation mechanisms for the vibrations in tube bundles, namely, vortex induced vibrations, turbulent buffeting, acoustic resonance in addition to the fluidelastic excitation mechanism. Historical developments of these excitation mechanisms is provided in the context of tube arrays. The excitation mechanism of the fluidelastic instability is not crystal clear, even after the enormous experiments performed by many researchers. The different theoretical approaches are

mainly based on the experimental observations. A detailed review on the mathematical models of the fluidelastic instability is also provided.

2. There are less number of numerical studies on the fluidelastic instability in tube arrays in comparison with the experimental studies. The results of Computational Fluid Dynamics (CFD) models (except for the Direct Numerical Simulations (DNS), which are limited to the low Reynolds number flows) are often criticized for their inability to model the flow turbulence accurately. The potential flow modeling approach is far from the reality, since in the tube arrays almost all the flows of practical interest are turbulent in nature. In this work, the Unsteady Reynolds Averaged Navier-Stokes (URANS) turbulence models, namely, $k-\varepsilon$, $k-\omega$ and $k-\varepsilon-\bar{v^2}/k$ are used to study the time averaged pressure profiles on the cylinder surface, in static configurations. Although, the results of $k-\varepsilon$ and $k-\omega$ models, in static configurations, are fair and comparable with the the four equation $k-\varepsilon-\bar{v^2}/k$ turbulence model, the $k-\varepsilon-\bar{v^2}/k$ is used for the further investigation of fluidelastic instability in the dynamic configuration. The critical flow velocity (u_{pc}) is well predicted by the $k-\varepsilon-\bar{v^2}/k$ model by means of performing the dynamic fluid-structure interaction simulations. The values of resultant quantities, the cylinder response frequency (f_n) and the damping ratio (ζ), are in a good order of magnitudes. Although the stability threshold is well predicted, the trends of variation in the quantities f_n and ζ with increasing flow velocity are missed, when compared with the experimental data.

3. In order to investigate the transient interaction between the interstitial flow through an array and a single tube of the array, the fluid flow is simulated using the Large Eddy Simulations (LES). Although the LES are computationally expensive and restricted to relatively low Reynolds numbers, the results obtained are encouraging. The transient nature of the flow and fluid-structure interaction are well captured by the LES. The development of fluidelastic instability with the increasing flow velocity, in terms of the variations in the cylinder vibration frequency (f_n) and the effective damping ratio (ζ), shows a fairly good agreement with the experiential results.

4. A theoretical model of the fluidelastic instability is proposed based on the dynamics between the interstitial flow and the cylinder vibration. The mathematical formulation yields an implicit expression for the critical flow velocity, which accounts for the influence of the pitch ratio (p^*) and the Reynolds number (Re) through the Euler number (Eu). The model is developed for the square normal tube arrays with a single vibrating tube in 1-degrees-of-freedom (in the flow lift or transverse direction). The model

predictions are promising, even though compared with a limited experiential data.

5. A short review on reduced order modeling in the context of fluid dynamics systems is provided. Traditionally, model reduction is extensively used in the control designs and systems. In fluid dynamics, the method of Proper Orthogonal Decomposition (POD) via Galerkin projections is commonly followed to generate reduced order models. In this thesis, a new methodology for constructing a reduced order solution of the Navier-Stokes equations at an off-reference solution state is proposed. A linear interpolation of the reduced POD space and time modes leads to a Galerkin-free formulation. In the mathematical formulation, the variables forming the state vector are treated separately, hence the model is suited for the multi-physics problems. The model reduction technique is extended to a fluid-structure interaction problem. The flow past a cylinder at low Reynolds numbers ($Re \approx 100$) in static and dynamic configurations are used to demonstrate the method.

8.2 Outlook

The number of parameters involved in the flow induced vibrations of the heat exchanger tube bundles is large. The existing mathematical models of the fluidelastic instability are generally valid for a particular range of parameters. The proposed implicit model of fluidelastic instability is also developed under several simplifying assumptions. The model is developed for the square normal tube arrays under cross flow of a single phase fluid. Only a single inner cylinder is free to oscillate in the flow lift or transverse direction. The influence of parameters such as, array orientation, vibration in all tube bundle instead of a single tube, two phase fluid flow, different values of the longitudinal and transverse pitch ratios etc. need to be incorporated in order to generalize the implicit model. The dynamic interaction between the interstitial flow and the cylinder vibrations are modeled in terms of the mechanical impedance term (I_m). The coupling of the cylinder natural frequency with the fluid (including the effect of flow channel boundaries) frequencies is modeled under simple assumptions, which can be improved based on a detailed analysis and quantification of the interactions. The model is capable of predicting the multiple stability boundaries at the lower values of mass-damping parameter. There is a need to further exploration of the exact shapes of the multiple stability thresholds. The instability is assumed to occur when the fractional length h_c becomes 0.5 as well as when the pressure drop across the cylinder in the lift direction (Δp_y) equals the pressure drop (Δp_{row}) across the cylinder in the flow direction. The exact occurrence of these transitions and the

interrelation between the two events will be useful in refining the model.

The Galerkin-free model reduction technique developed in this thesis work is a posteriori formulation, since it deals with the solution sets obtained and not the equations itself. The linear interpolation technique is robust, although it puts limit on the distance between two reference states. The interpolation can be improved to an interpolation based on the Grassmann manifolds.

APPENDIX A

TURBULENCE MODELING

Contents

Navier-Sokes equations (NSE) describe the flow of viscous fluids. The equations are derived using laws of conservation of mass, momentum and energy as well. The fluid is continuum and undergoes Newton's second law of motion. In addition, the Cauchy stress tensor defined for fluids, which is the addition of a velocity gradient term and a pressure term for the Newtonian fluids. A general form of Navier-Stokes equations (with continuity of mass and momentum) in Einstein's index notation can be written as,

$$\frac{\partial(\rho)}{\partial t} + \frac{\partial(\rho u_i)}{\partial x_i} = 0 \tag{A.1}$$

$$\frac{\partial(\rho u_i)}{\partial t} + \frac{\partial(\rho u_i u_j)}{\partial x_j} = \frac{\partial(\sigma_{ij})}{\partial x_j} + f_i \tag{A.2}$$

Where ρ is the fluid density, u_i is the i^{th} component of instantaneous velocity, t and x_i represents time and space respectively. f_i is a body force. The stress tensor σ_{ij} is given by,

$$\sigma_{ij} = -p\delta_{ij} + \tau_{ij} \tag{A.3}$$

Where p is the static pressure and τ_{ij} is the shear stress tensor. δ_{ij} is the Kronecker delta. τ_{ij} is formulated by using the Newton's law of viscosity and Stokes assumptions as,

$$\tau_{ij} = \mu\left(\frac{\partial u_i}{\partial x_j} + \frac{\partial u_j}{\partial x_i} - \frac{2}{3}\delta_{ij}\frac{\partial u_k}{\partial x_k}\right) + \delta_{ij}\lambda\frac{\partial u_k}{\partial u_k} \tag{A.4}$$

Where, μ and λ are the first and second coefficients of viscosity, also know as dynamic viscosity and bulk viscosity respectively. The equations are simplified significantly for incompressible fluids. By considering the incompressibility and not accounting for body forces, the resulting equations can be written as,

$$\frac{\partial u_i}{\partial x_i} = 0 \tag{A.5}$$

$$\frac{\partial u_i}{\partial t} + u_j\frac{\partial u_i}{\partial x_j} = -\frac{1}{\rho}\frac{\partial p}{\partial x_i} + \nu\frac{\partial^2 u_i}{\partial x_j \partial x_j} \tag{A.6}$$

Where $\nu = \mu/\rho$ is the kinematic viscosity of fluid.

The dimensionless Reynolds number (*Re*) for a fluid flow is defined as the ratio of fluid inertial forces to viscous forces. The flow at high Reynolds number (normally) becomes turbulent and appears chaotic. The Direct Numerical Simulations (DNS) of Navier-Stokes Equations (NES) at higher Reynolds number is computationally expensive endeavour. Turbulence modeling is useful in obtaining numerical solutions of the NSE at high Reynolds number. The DNS approach resolves all the energy scales of the turbulent energy spectra, otherwise the unresolved turbulence need to be modeled.

A.1 Unsteady Reynolds Averaged Navier-Stokes (URANS)

The instantaneous flow velocity is decomposed into the average and fluctuating parts in Reynolds Averaged Navier-Stokes (RANS) approach of turbulence modeling. All the turbulent scales present in the flow are modeled. The NSE are replaced by the averaged NSE and separate equations modeling turbulence in the flow. The Reynolds decomposition can be written as,

$$u_i = \overline{u}_i + u'_i \tag{A.7}$$

Where $\overline{u}_i$ and u_i' are the time averaged i^{th} component of velocity and associated fluctuating component respectively. The Reynolds averaged Navier-Stokes equations become,

$$\frac{\partial \overline{u}_i}{\partial x_i} = 0 \tag{A.8}$$

$$\frac{\partial \overline{u}_i}{\partial t} + \overline{u}_j \frac{\partial \overline{u}_i}{\partial x_j} = -\frac{1}{\rho}\frac{\partial \overline{p}}{\partial x_i} + \nu \frac{\partial^2 \overline{u}_i}{\partial x_j \partial x_j} - \frac{\partial \overline{u_i' u_j'}}{\partial x_j} \tag{A.9}$$

An extra term appears in this operation, $\overline{u_i' u_j'}$ which is known as Reynolds stress tensor. The system of equations remains open with 10 unknowns in 4 equations. One can write 6 separate transport equations for the Reynolds stress tensor, which further produces 34 unknowns. ((Manceau, 2015)). Depending upon the number of equations solved for turbulent quantities, in addition to the mean flow quantities, the turbulence models can be classified.

A generalised eddy-viscosity model for Reynolds stress tensor ($\overline{u_i' u_j'}$) is written as,

$$\overline{u_i' u_j'} = -2\nu_t \overline{s}_{ij} + \frac{2}{3} k \delta_{ij} \tag{A.10}$$

Where ν_t, k are the turbulence viscosity and kinetic energy respectively, while $\overline{s}_{ij}$ is the averaged strain rate tensor, represented as,

$$\overline{s}_{ij} = \frac{1}{2}\left(\frac{\partial \overline{u}_i}{\partial x_j} + \frac{\partial \overline{u}_j}{\partial x_i}\right)$$

A.1.1 Linear eddy viscosity models

The standard $k-\varepsilon$ model is a two-equation turbulence model, as separate transport equations are solved for the turbulent kinetic energy k and the turbulent dissipation ε. This model is the most commonly used in industry, since it was first proposed by Launder and Spalding (1974). The turbulence length scale and time scale are evaluated as $k^{3/2}/\varepsilon$ and k/ε respectively. The effective turbulence viscosity (ν_t) is estimated as,

$$\nu_t = C_\mu k^2/\varepsilon \tag{A.11}$$

The equations for turbulence dissipation (ε) and the turbulence kinetic energy (k) are given as,

$$\frac{\partial \varepsilon}{\partial t} + \overline{u}_j \frac{\partial \varepsilon}{\partial x_j} = \frac{\partial}{\partial x_j}\left[\left(\nu + \frac{\nu_t}{\sigma_\varepsilon}\right)\frac{\partial \varepsilon}{\partial x_j}\right] + \frac{C_1 \varepsilon}{k} P_{k\varepsilon} - C_2 \frac{\varepsilon^2}{k} \tag{A.12}$$

$$\frac{\partial k}{\partial t} + \overline{u}_j \frac{\partial k}{\partial x_j} = \frac{\partial}{\partial x_j}\left[\left(\nu + \frac{\nu_t}{\sigma_k}\right)\frac{\partial k}{\partial x_j}\right] + P_{k\varepsilon} - \varepsilon \tag{A.13}$$

Where $P_{k\varepsilon}$ is the rate of production of turbulent energy (k). It is given by,

$$P_{k\varepsilon} = 2\nu_t \bar{s}_{ij}\bar{s}_{ij} \tag{A.14}$$

The empirical constants appearing in the Standard $k-\varepsilon$ equations are experimentally evaluated ((Launder and Sharma, 1974)) to be,

$$C_\mu = 0.09 \quad C_1 = 1.44 \quad C_2 = 1.92 \quad \sigma_k = 1.0 \quad \sigma_\varepsilon = 1.3$$

The near wall treatment is necessary for the Standard $k-\varepsilon$ model, since the Prandtl-Kolmogorov relation for the turbulent viscosity in Equation (A.11) is not valid in the proximity of wall. An approach of wall-functions modeling is generally opted for near-wall correction ((Patankar and Spalding, 1972), (Launder and Spalding, 1974)).

$k-\varepsilon$ Linear Production

Although, Standard $k-\varepsilon$ is widely used turbulence model, it has some serious limitations ((Manceau, 2015)), stagnation point anomaly is one of them. The production term $P_{k\varepsilon}$ has a quadratic dependency on the mean strain rate tensor ($\bar{s}_{ij}$), which results in overproduction of the turbulent kinetic energy. In Linear Production $k-\varepsilon$ turbulence model (proposed in (Guimet and Laurence, 2002)), the turbulent energy generation rate is linearised based on turbulence anisotropy. The formulation is based on the fact that the anisotropy in fluid does not grow linearly for large values of strain rate tensor. Therefore the value of improved coefficient $\overline{C}_\mu$ is evaluated from the measure of anisotropy in the near wall region. The anisotropy tensor is defined ((Rotta, 1951)) as,

$$a_{ij} = \frac{\overline{u_i' u_j'}}{k} - \frac{2}{3}\delta_{ij} \tag{A.15}$$

Thus by using measurements of the anisotropic tensor in the log layer and the turbulent energy production and dissipation terms, the improved coefficient $\overline{C}_\mu$ is modeled as,

$$\overline{C}_\mu = [a_{12}]^2_{log\ layer}\frac{\varepsilon}{P_{k\varepsilon}} \tag{A.16}$$

Further modeling $[a_{12}]^2_{log\ layer}$ term, allows to return to the original isotropic formulation (quadratic production terms). Several validation case studies are also provided in ((Guimet

and Laurence, 2002)).

$k-\omega$ SST

In most of the two-equation models, turbulent kinetic energy (k) is used as first variable, while the choice of second variable differs from one model to another. Although the two independent turbulent scales are used in these models, they are interrelated and their choice make no difference beforehand. In (Wilcox, 1988), the author presented a frequency scale (ω), based on hypothesis similar to Kolmogorov. The turbulent energy dissipation (ε) linked to the frequency parameter as $\omega = \varepsilon/k$. The model is integrable up to the wall boundary faces, contrary to the $k-\varepsilon$ formulation. On the other hand the model ($k-\omega$) predictions are not not satisfactory in external flows, as compared to Standard $k-\varepsilon$ model. An approach combining merits of both the $k-\varepsilon$ and $k-\omega$ turbulence model is proposed by (Menter, 1994). The first equation of turbulent kinetic energy is given as,

$$\frac{\partial k}{\partial t} + \overline{u}_j \frac{\partial k}{\partial x_j} = \frac{\partial}{\partial x_j}\left[(\nu + \sigma_k \nu_t)\frac{\partial k}{\partial x_j}\right] + P_{k\omega sst} - \beta^* k\omega \tag{A.17}$$

$$\frac{\partial \omega}{\partial t} + \overline{u}_j \frac{\partial \omega}{\partial x_j} = \frac{\partial}{\partial x_j}\left[(\nu + \sigma_\omega \nu_t)\frac{\partial \omega}{\partial x_j}\right] + \frac{\alpha}{\nu_t} P_{k\omega sst} - \beta\omega^2 + 2(1-F_1)\frac{\sigma_{\omega 2}}{\omega}\frac{\partial k}{\partial x_j}\frac{\partial \omega}{\partial x_j} \tag{A.18}$$

Where $P_{k\omega sst}$ is the turbulent kinetic energy production rate. The function F_1 controls the model depending on the region in the computational domain. In the near wall region it tends to value 1, where the $k-\omega$ model should dominate the physics, while away from the boundary layers $k-\varepsilon$ formulation is effective. The closure coefficients and auxiliary relations (α, β^*, β, σ_k, σ_ω, $\sigma_{\omega 2}$ and F_1) can be referred in (Menter, 1994).

A.1.2 Non-linear eddy viscosity models

A generalised formulation for Reynolds stress tensor is postulated in (Wallin and Johansson, 2000), where a non-linear relation between the turbulence stresses and strain rate and mean vorticity tensors is proposed. The eddy viscosity models with inclusion of higher order terms from the general equation leads to non-linear eddy viscosity models.

$k-\varepsilon-\overline{v^2}/k$ elliptic blending turbulence model

The $\overline{v^2}$-f model ((Durbin, 1995)) is similar to the Standard $k-\varepsilon$ model. In addition to the k and ε, two additional variables are solved, namely $\overline{v^2}$ and f. Where $\overline{v^2}$ is a velocity scale, nothing but the ratio of wall normal Reynolds stresses to the turbulent kinetic energy (which represents near-wall anisotropy in turbulence). The second variable f is solved in the form of an elliptic relaxation equation.

A numerically robust form of the model is proposed in (Laurence et al., 2005). A new variable is proposed as $\varphi = \overline{v^2}/k$ in place of $\overline{v^2}$, while a function $\bar{f}$ is newly formulated instead of f as,

$$f = \bar{f} - \frac{2\nu}{k}\frac{\partial\varphi}{\partial x_i}\frac{\partial k}{\partial x_i} - \nu\frac{\partial^2\varphi}{\partial x_i^2} \tag{A.19}$$

such that, $\bar{f} \to 0$ as the distance from wall tends to zero. The transport equations for the new variables are written as,

$$\frac{\partial\varphi}{\partial t} + \overline{u}_j\frac{\partial\varphi}{\partial x_j} = \frac{\partial}{\partial x_j}\left[\frac{\nu_t}{\sigma_k}\frac{\partial\varphi}{\partial x_j}\right] + \bar{f} - P_{v2f}\frac{\varphi}{k} + \frac{2\nu_t}{k\sigma_k}\frac{\partial\varphi}{\partial x_j}\frac{\partial k}{\partial x_j} \tag{A.20}$$

$$L^2\frac{\partial^2\bar{f}}{\partial x_i} - \bar{f} = \frac{1}{T}(C_1 - 1)\left[\varphi - \frac{2}{3}\right] - C_2\frac{P_{v2f}}{k} - 2\frac{\nu}{k}\frac{\partial\varphi}{\partial x_j}\frac{\partial k}{\partial x_j} - \nu\frac{\partial^2\varphi}{\partial x_i^2} \tag{A.21}$$

Where L and T represent length and time scales of turbulence, defined as,

$$L = C_L\max\left[\frac{k^{3/2}}{k}, C_\eta\frac{\nu^{3/4}}{\varepsilon^{1/4}}\right] \qquad T = \max\left[\frac{k}{\varepsilon}, 6\sqrt{\frac{\nu}{\varepsilon}}\right]$$

The constant coefficients of the equations are used as,

$$C_L = 0.25, C_\eta = 110, C_1 = 1.4, C_2 = 0.3$$

Contrary to the earlier ($\overline{v^2} - f$) formulations, the dissipation rate ε is not used directly in the equation for $\bar{f}$. The modified transport equation for ε in $\overline{v^2} - f$ model propositions is of the form,

$$\frac{\partial\varepsilon}{\partial t} + \overline{u}_j\frac{\partial\varepsilon}{\partial x_j} = \frac{\partial}{\partial x_j}\left[\left(\nu + \frac{\nu_t}{\sigma_\varepsilon}\right)\frac{\partial\varepsilon}{\partial x_j}\right] + \frac{C_{\varepsilon1}P_{v2f} - C_{\varepsilon2}\varepsilon}{T} \tag{A.22}$$

The eddy viscosity (ν_t) is modeled as,

$$\nu_t = C_\mu\varphi kT$$

The values of constants for the turbulent kinetic energy (k) and dissipation rate (ε) equations are,

$$C_\mu = 0.22, \sigma_k = 1, \sigma_\varepsilon = 1.3, C_{\varepsilon 2} = 1.9 \text{ and } C_{\varepsilon 1} = 1.4\left(1 + 0.05\sqrt{\frac{1}{\varphi}}\right)$$

The wall boundary conditions for the four variables are,

$$k = 0, \varepsilon \rightarrow \frac{2\nu k}{y^2}, \varphi = 0, \bar{f} = 0$$

Where y is a distance normal to the wall. The boundary conditions $\varphi = 0, \bar{f} = 0$ allow to solve the system of equations separately.

A.2 Large Eddy Simulations (LES)

Increase of inertial forces in fluid flow over viscous forces lead to flow instabilities. Although, flow appears chaotic for increased Reynolds numbers, the turbulence is organized in multi scale flow structures in space and time. The largest scale space structures contain most of the turbulent kinetic energy, which flows down to the smallest scales (Kolmogorov length scale) of turbulence. Thus the flow contained with large eddies, which are characteristic of the flow geometry. The large eddies give rise to small eddies and so on, until the smallest eddies dissipate the turbulent energy against the viscous forces. Numerical simulations of such a flow require huge computing resources. Large Eddy Simulations (LES) was proposed by (Smagorinsky, 1963), wherein the large eddy structures from the flow are resolved (low-pass filtered) and directly solved, while the smaller (or unresolved) eddies are modeled using Boussinesq type eddy viscosity relation.

An LES filter, which can be applied in space or time can be defined as,

$$\widetilde{u_i(\boldsymbol{x},t)} = \int_{-\infty}^{\infty}\int_{-\infty}^{\infty} u_i(\boldsymbol{r},t')G(\boldsymbol{x}-\boldsymbol{r},t-t')dt'd\boldsymbol{r} \tag{A.23}$$

Where G is the filter convolution kernel. Generally, the computational grid is used as a default length scale filter. The governing equations for Large Eddy Simulations are the Navier-Stokes equations convoluted with the LES filter. The velocity field can be split up using the LES filter as, $u_i = \tilde{u}_i + u_i'$. The incompressible Navier-Stokes equations (Equations A.5, A.6) become,

$$\frac{\partial \tilde{u}_i}{\partial x_i} = 0 \tag{A.24}$$

$$\frac{\partial \tilde{u}_i}{\partial t} + \tilde{u}_j \frac{\partial \tilde{u}_i}{\partial x_j} = -\frac{1}{\rho}\frac{\partial \tilde{p}}{\partial x_i} + \nu \frac{\partial^2 \tilde{u}_i}{\partial x_j \partial x_j} - \frac{\partial \widetilde{u_i' u_j'}}{\partial x_j} \tag{A.25}$$

Where $\widetilde{u_i' u_j'}$ is known as sub-grid scale stress tensor. Similar to the Reynolds stress tensor, the sub-grid scale stress tensor is a difference between the non-linear convection term (NSE) and the resolved convection term (LES). It is given by,

$$\widetilde{u_i' u_j'} = \widetilde{u_i u_j} - \tilde{u}_i \tilde{u}_j \tag{A.26}$$

The sub-grid scale tensor needs to be modeled. Boussinesq hypothesis is usually employed to model $\widetilde{u_i' u_j'}$, similar to the Reynolds stress tensor (in Equation A.10).

$$\widetilde{u_i' u_j'} = -2\nu_t \tilde{s}_{ij} + \frac{2}{3}\widetilde{u_k' u_k'}\delta_{ij} \tag{A.27}$$

The sub-grid scale energy term ($\widetilde{u_k' u_k'}/2$) is added to the pressure term ($\tilde{p}$) (Pope, 2000) of filtered LES equations.

A.2.1 Smagorinsky-Lilly Model

The simple and very first model for sub-grid scale eddy viscosity was proposed by (Smagorinsky, 1963). It was used in a numerical simulation first time in (Deardorff, 1970). The turbulent eddy viscosity is modeled as,

$$\nu_t = (C_s \Delta_g)^2 \sqrt{2\tilde{s}_{ij}\tilde{s}_{ij}} \tag{A.28}$$

Where the proportionality constants Δ_g and C_s are the effective grid size and a Smagorinsky constant based on Kolmogorov's hypothesis respectively. It assumes that the production of the turbulent energy and its dissipation are equal. $C_s = 0.18$ in isotropic flows, while it needs to be adjusted depending on a flow (e.g. in channel flow $C_s = 0.065$).

APPENDIX B

MODAL ANALYSIS

Contents

In the Operational Modal Analysis (OMA), the forces acting on structures are unknown beforehand, contrary to the traditional Experimental Modal Analysis (EMA), where the system is provided with known excitation force. Thus, the former method (OMA) is non intrusive compared to the later (EMA) method. The method is significant especially in stability analysis of a system. A recent review on operational modal analysis can be found in (Brincker, 2014). There are two methods presented here to post process the random time response signals in order to estimate the modal parameters such as natural frequency, damping ratio, mode shapes etc.

B.1 Half-Power Bandwidth Method (HBM)

The half-power bandwidth method is commonly used to estimate the damping ratio (ζ) of vibration response signal. The method is fairly simple and accurate for smaller values of

the damping ratio ($\zeta \lessapprox 10\%$). The method is applicable for single as well as multi-degree-of-freedom systems as long as the frequency response spectra has distinct frequency peaks. Although there exist several formats of the method, the estimation of damping using the amplification or quality factor (Q) is most common. One can refer (Green, 1955) for elaborated discussion on origin, applications of the factor Q.

The quality factor (Q) of any under-damped oscillator represents the energy stored per unit energy dissipated in one cycle at a resonant frequency f_n. It also characterizes the sharpness of resonance. High values of Q represent sharp spectral peaks and small bandwidth of the resonant frequencies near the modal frequency. On the other hand, low values of Q means a broad range of resonance frequencies, indicating higher energy dissipation per cycle. The non-dimensional quality factor and damping ratio are related as,

$$Q = \frac{1}{2\zeta} \tag{B.1}$$

The Q factor is also represented in terms of the center resonance frequency f_n and the bandwidth Δf at half the value of peak power at f_n.

$$Q = \frac{f_n}{\Delta f} \tag{B.2}$$

The half-bandwidth Δf is calculated using two adjacent frequencies f_1 and f_2 on the frequency lobe f_n at half power as $\Delta f = f_2 - f_1$.

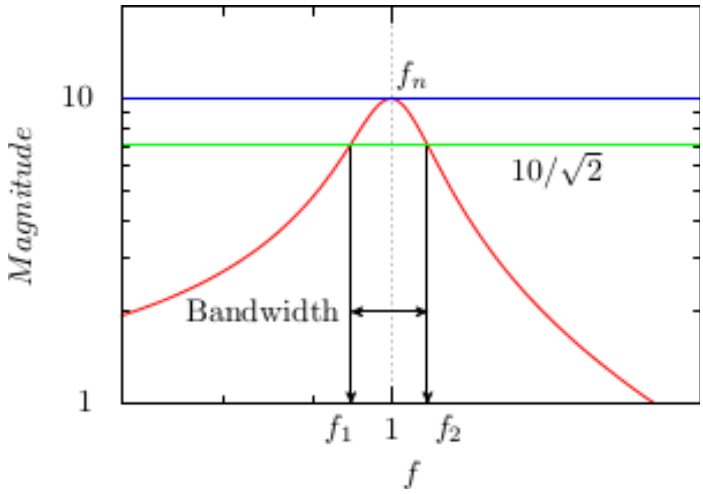

Figure B.1 Estimation of damping using the Half Power Bandwidth Method (HBM).

Figure (B.1) shows a frequency response spectrum of a damped oscillator with $f_n = 1$. The peak value of power at $f_n = 1$ is 10. The half power $(10/\sqrt{2})$ is represented on the frequency

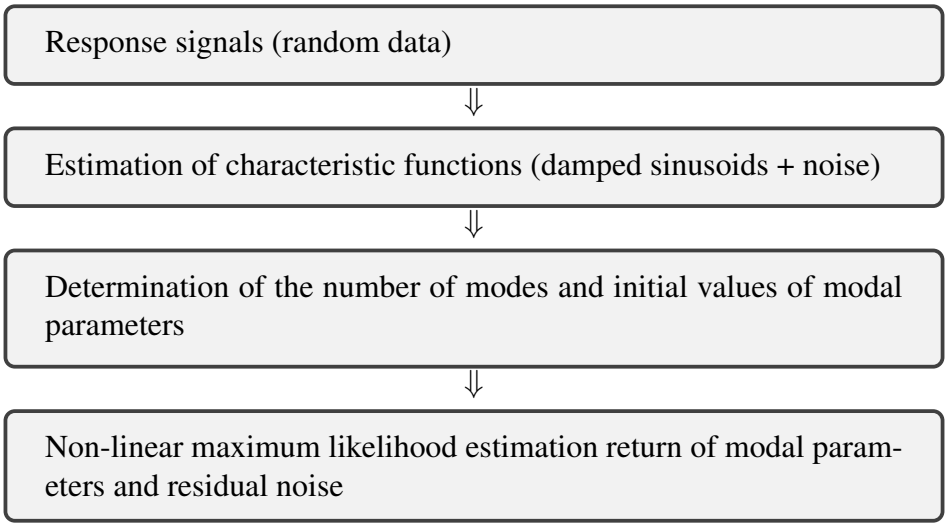

Figure B.2 The IMENE flow chart.

lobe by $f_1 = 0.946962$ and $f_2 = 1.046961$. The quality factor Q of the oscillations using Equation (B.2) is 10. The damping ratio calculated using Equation (B.1) is $\zeta = 5\%$.

A correction to the half power bandwidth method for calculating higher damping ratios ($\zeta \gtrapprox 10\%$) is proposed in (Wu, 2014).

B.2 Time Domain Modal Analysis (TMA)

The time domain method described here for the modal identification is known as Identification Modale Excitation Non Evaluée (IMENE). The method is proposed by (Granger, 1990). It is developed in the context of obtaining indirectly the unmeasured fluid-elastic forces on tube bundle. The flow chart in Figure (B.2) shows the procedure to estimate the modal parameters of a system.

B.2.1 The characteristic functions

The time response signals measured at N_o locations are represented using sampled characteristic functions $c_k(n)$. Where n and k are indices for the sample number and measurement location. The model of $c_k(n)$ consists of a deterministic part $a_k(n)$ and a random part $w_k(n)$. The deterministic part is sum of N sampled damped sinusoids with each sinusoid corresponds to a vibration mode. The damped modal frequency is given by $\omega_i\sqrt{1-\zeta_i}$, where ω_i, ζ_i are the angular frequency and damping ratio of i^{th} mode respectively. The sampled random part $w_k(n)$ is the output of an autoregressive-moving-average(ARMA) filter with an input of a sampled

Gaussian white noise $e_k(n)$. The characteristic functions are expressed as,

$$c_k(n) = a_k(n) + w_k(n), \quad 0 \leq n \leq N_s - 1 \tag{B.3}$$

Where N_s is a number of samples.

$$a_k(n) = \sum_{i=1}^{2N} D_{ki} z_i^n, \quad with \quad D_{ki} z_i^n = \overline{D_{ki-N} z_{i-N}^n} \quad for \quad N+1 \leq i \leq 2N \tag{B.4}$$

Where D_{ki} is a complex amplitude of the damped sinusoid and z_i is the characteristic parameter which provides the natural frequency and damping ratio of a mode. The complex amplitude (D_{ki}) is used to estimate the mode shape coefficient (V_{ki}). The derivation is provided in Appendix A of (Granger, 1990). The random part ($w_k(n)$) of the characteristic functions is expressed as,

$$w_k(n) = \sum_{s=1}^{p} \phi_{ks} w_k(n-s) + e_k(n) + \sum_{s=1}^{q} \theta_{ks} e_k(n-s) \tag{B.5}$$

Thus the modal features are defined in analytical forms using the characteristic functions. The random time signals at several locations are treated using cross-correlations between a reference location and the rest locations, in order to evaluate the characteristic functions.

B.2.2 The number of modes and parameters of the characteristics functions

A nonlinear optimization of the characteristic functions is preformed in order to identify the parameters of characteristic functions and thereby estimate of the modal parameters. An iterative process is followed to improve the values of characteristic parameters successively. An initial approximation of the parameters is obtained using first, the Z-transforms of Equation (B.4) and Equation (B.3) to provide polynomials and second, the polynomials are solved to obtain roots which lead to natural frequency and associated damping ratio. The Z-transform of $a_k(n)$ is,

$$A_k(z) = \sum_{n=0}^{+\infty} a_k(n) z^{-n} = \frac{P_k(z)}{Q(z)}$$

With,

$$P_k(z) = \sum_{i=1}^{2N} D_{ki} z \prod_{s=1, s\neq i}^{2N} (z - z_i)$$

$$Q(z) = \prod_{i=1}^{2N} (z - z_i) \tag{B.6}$$

Rewriting $Q(z)$ in polynomial form

$$Q(z) = z^{2N} + \sum_{i=1}^{2N} q_i z^{2N-i} \tag{B.7}$$

shows that

$$z^{2N} A_k(z) + \sum_{i=1}^{2N} q_i z^{2N-i} A_k(z) = P_k(z) \tag{B.8}$$

The inverse Z-transform of Equation (B.8) and similar treatment of $c_k(n)$ give following finite-difference equations,

$$a_k(n) + \sum_{i=1}^{2N} q_i a_k(n-i) = 0 \quad n \geq 2N$$

$$c_k(n) + \sum_{i=1}^{2N} q_i c_k(n-i) = w_k(n) + \sum_{i=1}^{2N} q_i w_k(n-i) \quad n \geq 2N \tag{B.9}$$

A detailed treatment of Equation (B.9) using a modified Prony's method is presented in Appendix B of (Granger, 1990), which enables to select number of modes N. The polynomial coefficients q_i are estimated using a set of extended Yule-Walker equations by means of the linear least-squares method. The roots of polynomial $Q(z)$ (Equation B.7) are obtained using a standard root-solver. The equations,

$$z_i = e^{\lambda_i \Delta t}$$

$$\lambda_i = \omega_i \left(-\zeta_i + \hat{\imath} \sqrt{1 - \zeta_i^2} \right)$$

leads to initial values of the natural frequencies and damping ratios. Where $\hat{\imath}$ stands for $\sqrt{-1}$. The initial values of the complex amplitude function D_{ki} is then obtained using the linear least-squares fit technique. In addition, the parameters of the random part $w_k(n)$ of the characteristic functions, namely ϕ_k and θ_k are obtained by a set of Yule-Walker equations and Wilson's nonlinear algorithm ((Box et al., 2013)) respectively.

B.2.3 Statistical estimation of the modal parameters

The initial values of the modal parameters in hand are optimized by performing the maximum-likelihood estimation procedure coupled with an iterative Gauss-Newton approach. A statistical model is formulated for the modal parameters of the characteristic functions. The likelihood function of the model is defined as in (Box et al., 2013). The optimization procedure assumes that the time signals are sufficiently long to perform statistical analysis. The residues (errors) are minimized using an iterative Gauss-Newton algorithm. The method provides a confidence interval for each modal parameter, what makes this method more reliable. The test cases of detailed validation are provided in (Granger, 1990).

REFERENCES

Abd-Rabbo, A. and Weaver, D. (1986). A flow visualization study of flow development in a staggered tube array. *Journal of Sound and Vibration*, 106(2):241–256.

Amsallem, D. and Farhat, C. (2008). Interpolation method for adapting reduced-order models and application to aeroelasticity. *AIAA journal*, 46(7):1803–1813.

Amsallem, D. and Farhat, C. (2011). An online method for interpolating linear parametric reduced-order models. *SIAM Journal on Scientific Computing*, 33(5):2169–2198.

Andjelic, M. and Popp, K. (1989). Stability effects in a normal triangular cylinder array. *Journal of Fluids and Structures*, 3(2):165–185.

Antoulas, A. C. (2005). *Approximation of large-scale dynamical systems*, volume 6. Siam.

Anttonen, J., King, P., and Beran, P. (2003). Pod-based reduced-order models with deforming grids. *Mathematical and Computer Modelling*, 38(1):41–62.

Anttonen, J. S., King, P. I., and Beran, P. S. (2005). Applications of multi-pod to a pitching and plunging airfoil. *Mathematical and Computer Modelling*, 42(3):245–259.

Arnoldi, W. E. (1951). The principal of minimized iterations in the solution of the matrix eigenvalue problem. *Quarterly of Applied Mathematics*, 9(17–29).

Aubry, N. (1991). On the hidden beauty of the proper orthogonal decomposition. *Theoretical and Computational Fluid Dynamics*, 2(5-6):339–352.

Aubry, N., Holmes, P., Lumley, J. L., and Stone, E. (1988). The dynamics of coherent structures in the wall region of a turbulent boundary layer. *Journal of Fluid Mechanics*, 192:115–173.

Austermann, R. and Popp, K. (1995). Stability behaviour of a single flexible cylinder in rigid tube arrays of different geometry subjected to cross-flow. *Journal of Fluids and Structures*, 9(3):303–322.

Balajewicz, M. and Dowell, E. (2012). Stabilization of projection-based reduced order models of the navier–stokes. *Nonlinear Dynamics*, 70(2):1619–1632.

Barkley, D. and Henderson, R. D. (1996). Three-dimensional floquet stability analysis of the wake of a circular cylinder. *Journal of Fluid Mechanics*, 322:215–241.

Barsamian, H. and Hassan, Y. (1997). Large eddy simulation of turbulent crossflow in tube bundles. *Nuclear Engineering and Design*, 172(1):103–122.

References

Beale, S. and Spalding, D. (1999). A numerical study of unsteady fluid flow in in-line and staggered tube banks. *Journal of Fluids and Structures*, 13(6):723–754.

Benhamadouche, S. and Laurence, D. (2003). Les, coarse les, and transient rans comparisons on the flow across a tube bundle. *International Journal of Heat and Fluid Flow*, 24(4):470–479.

Benner, P., Freund, R. W., Sorensen, D. C., and Varga, A. (2006). Special issue on "order reduction of large-scale systems". *Linear Algebra and Its Applications*, 2(415):231–234.

Benner, P., Gugercin, S., and Willcox, K. (2013). A survey of model reduction methods for parametric systems. Technical Report MPIMD/13-14, Max Planck Institute Magdeburg.

Beran, P. S., Lucia, D. J., and Pettit, C. L. (2004). Reduced-order modelling of limit-cycle oscillation for aeroelastic systems. *Journal of Fluids and Structures*, 19(5):575–590.

Bergmann, M., Bruneau, C.-H., and Iollo, A. (2009). Enablers for robust pod models. *Journal of Computational Physics*, 228(2):516–538.

Berland, J., Deri, E., and Adobes, A. (2014). Large-eddy simulation of cross-flow induced vibrations of a single flexible tube in a normal square tube array. In *ASME 2014 Pressure Vessels and Piping Conference*, pages V004T04A037–V004T04A037. American Society of Mechanical Engineers.

Blevins, R. (1974). Fluid elastic whirling of a tube row. *Journal of Pressure Vessel Technology*, 96(4):263–267.

Blevins, R. (1979a). Buffeting of heat exchanger tube arrays in a cross flow. In *Vibration in nuclear plant. Proceedings of international conference held at Keswick, UK in May 1978*, pages 327–330.

Blevins, R. (1979b). Flow-induced vibration in nuclear reactors: a review. *Progress in Nuclear Energy*, 4(1):25–49.

Blevins, R. (1979c). Fluid damping and the whirling instability of tube arrays. *Flow-Induced Vibrations*, pages 35–39.

Blevins, R. (1984). Review of sound induced by vortex shedding from cylinders. *Journal of Sound and Vibration*, 92(4):455–470.

Blevins, R. (1986). Acoustic modes of heat exchanger tube bundles. *Journal of Sound and Vibration*, 109(1):19–31.

Blevins, R., Gibert, R., and Villard, B. (1981). Experiments on vibration of heat-exchanger tube arrays in cross flow. Technical report, General Atomic Co., San Diego, CA (USA); CEA Centre d'Etudes Nucleaires de Saclay, 91-Gif-sur-Yvette (France).

Bourguet, R., Braza, M., and Dervieux, A. (2011). Reduced-order modeling of transonic flows around an airfoil submitted to small deformations. *Journal of Computational Physics*, 230(1):159 – 184.

Bouris, D. and Bergeles, G. (1999). Two dimensional time dependent simulation of the subcritical flow in a staggered tube bundle using a subgrid scale model. *International journal of heat and fluid flow*, 20(2):105–114.

Box, G., Jenkins, G., and Reinsel, G. (2013). *Time Series Analysis: Forecasting and Control*. Wiley Series in Probability and Statistics. Wiley.

Brincker, R. (2014). Some elements of operational modal analysis. *Shock and Vibration*, 2014.

Bui-Thanh, T., Damodaran, M., and Willcox, K. (2003). Proper orthogonal decomposition extensions for parametric applications in compressible aerodynamics. In *Proceedings of 21st AIAA Applied Aerodynamics Conference, Orlando, Florida*, pages 1–11.

Bui-Thanh, T., Willcox, K., Ghattas, O., and van Bloemen Waanders, B. (2007). Goal-oriented, model-constrained optimization for reduction of large-scale systems. *Journal of Computational Physics*, 224(2):880–896.

Chen, S. (1978). Crossflow-induced vibrations of heat exchanger tube banks. *Nuclear Engineering and Design*, 47(1):67–86.

Chen, S. (1983a). Instability mechanisms and stability criteria of a group of circular cylinders subjected to cross-flow. part i: theory. *Journal of Vibration and Acoustics*, 105(1):51–58.

Chen, S. (1983b). Instability mechanisms and stability criteria of a group of circular cylinders subjected to cross-flow—part 2: Numerical results and discussions. *Journal of Vibration and Acoustics*, 105(2):253–260.

Chen, S. (1984). Guidelines for the instability flow velocity of tube arrays in crossflow. *Journal of Sound and Vibration*, 93(3):439–455.

Chen, S. (1987). A general theory for dynamic instability of tube arrays in crossflow. *Journal of Fluids and Structures*, 1(1):35–53.

Chen, S., Cai, Y., and Srikantiah, G. (1998). Fluid damping controlled instability of tubes in crossflow. *Journal of Sound and Vibration*, 217(5):883–907.

Chen, S. and Chung, H. (1976). Design guide for calculating hydrodynamic mass. part i. circular cylindrical structures. Technical report, Argonne National Lab., Ill.(USA).

Chen, S. and Jendrzejcyk, J. (1981). Experiments on fluid elastic instability in tube banks subjected to liquid cross flow. *Journal of Sound and Vibration*, 78(3):355–381.

Chen, S. and Jendrzejczyk, J. (1981). Flow velocity dependence of damping in tube arrays subjected to liquid cross-flow. *Journal of Pressure Vessel Technology*, 103(2):130–135.

Chen, S. and Jendrzejczyk, J. (1983). Stability of tube arrays in crossflow. *Nuclear Engineering and Design*, 75(3):351–373.

Chen, Y. (1968). Flow-induced vibration and noise in tube-bank heat exchangers due to von karman streets. *Journal of Manufacturing Science and Engineering*, 90(1):134–146.

Chinesta, F., Ammar, A., and Cueto, E. (2010). Recent advances and new challenges in the use of the proper generalized decomposition for solving multidimensional models. *Archives of Computational methods in Engineering*, 17(4):327–350.

Colciago, C., Deparis, S., and Quarteroni, A. (2014). Comparisons between reduced order models and full 3d models for fluid-structure interaction problems in haemodynamics. *Journal of Computational and Applied Mathematics*, 265(0):120–138. Current Trends and Progresses in Scientific Computation Dedicated to Professor Ben-yu Guo on His 70th Birthday.

Coletti, F., editor (1983). *Heat Exchanger Design Handbook*, volume 1-4. Hemisphere, New York.

Connors, H. (1970). Fluidelastic vibration of tube arrays excited by cross-flows. *Flow-Induced Vibration in Heat Exchangers*, pages 42–56.

Connors, H. (1978). Fluidelastic vibration of heat exchanger tube arrays. *Journal of Mechanical Design*, 100(2):347–353.

Deardorff, J. W. (1970). A numerical study of three-dimensional turbulent channel flow at large reynolds numbers. *Journal of Fluid Mechanics*, 41(02):453–480.

Demmel, J. (1997). *Applied Numerical Linear Algebra*. Society for Industrial and Applied Mathematics.

Dowell, E. H. and Hall, K. C. (2001). Modeling of fluid-structure interaction. *Annual Review of Fluid Mechanics*, 33(1):445–490.

Dumon, A., Allery, C., and Ammar, A. (2013). Proper generalized decomposition method for incompressible navier–stokes equations with a spectral discretization. *Applied Mathematics and Computation*, 219(15):8145 – 8162.

Durbin, P. (1995). Separated flow computations with the k-epsilon-v-squared model. *AIAA journal*, 33(4):659–664.

Feenstra, P., Weaver, D., and Eisinger, F. (2005). Acoustic resonance in a staggered tube array: Tube response and the effect of baffles. *Journal of fluids and structures*, 21(1):89–101.

Feldmann, P. and Freund, R. W. (1995). Efficient linear circuit analysis by padé approximation via the lanczos process. *Computer-Aided Design of Integrated Circuits and Systems, IEEE Transactions on*, 14(5):639–649.

Fitzpatrick, J. (1985). The prediction of flow-induced noise in heat exchanger tube arrays. *Journal of Sound and Vibration*, 99(3):425–435.

Fitzpatrick, J., Donaldson, I., and McKnight, W. (1988). Strouhal numbers for flows in deep tube array models. *Journal of Fluids and Structures*, 2(2):145–160.

Gerbeau, J.-F. and Vidrascu, M. (2003). A quasi-newton algorithm based on a reduced model for fluid-structure interaction problems in blood flows. *ESAIM: Mathematical Modelling and Numerical Analysis-Modélisation Mathématique et Analyse Numérique*, 37(4):631–647.

Gibert, R., Chabrerie, J., and Sagner, M. (1977). Vibrations of tube arrays in transversal flow. *International conference on structural mechanics in reactor technology, Commission of the European Communities (CEC)*, pages 1–13.

Gillen, S. and Meskell, C. (2009). Numerical analysis of fluidelastic instability in a normal triangular tube array. In *ASME 2009 Pressure Vessels and Piping Conference*, pages 447–455. American Society of Mechanical Engineers.

Glover, K. (1984a). All optimal hankel-norm approximations of linear multivariable systems and their l,$^{\infty}$ -error bounds. *International journal of control*, 39(6):1115–1193.

Glover, K. (1984b). All optimal hankel-norm approximations of linear multivariable systems and their l^{∞} -error bounds. *International Journal of Control*, 39(6):1115–1193.

Gorman, D. (1976). Experimental development of design criteria to limit liquid cross-flow-induced vibration in nuclear reactor heat exchange equipment. *Nuclear Science and Engineering*, 61(3):324–336.

Gorman, D. (1977). Experimental study of peripheral problems related to liquid flow induced vibration in heat exchangers and steam generators. In *Structural mechanics in reactor technology*, pages 1–13. Structural mechanics in reactor technology.

Granger, S. (1990). A new signal processing method for investigating fluidelastic phenomena. *Journal of Fluids and Structures*, 4(1):73–97.

Granger, S., Campistron, R., and Lebret, J. (1994). Motion-dependent excitation mechanisms in a square in-line tube bundle subject to water cross flow: an experimental modal analysis. Technical report, Electricite de France (EDF), 92-Clamart (France).

Granger, S. and Païdoussis, M. (1996). An improvement to the quasi-steady model with application to cross-flow-induced vibration of tube arrays. *Journal of Fluid Mechanics*, 320:163–184.

Green, E. I. (1955). The story of q. *American Scientist*, pages 584–594.

Gross, H. G. (1975). *Untersuchung aerodynamischer Schwingungs-mechanismen und deren Berücksichtigung bei der Auslegung von Rohrbundelwarmetauschern*. PhD thesis, Technical University of Hannover, Germany.

Guimet, V. and Laurence, D. (2002). A linearised turbulent production in the k- ε model for engineering applications. In *Proc. 5th Int. Symp. Engng. Turb. Modelling and Measurements, Mallorca, Spain*.

Hanson, R. and Ziada, S. (2011). Effect of acoustic resonance on the dynamic lift of tube arrays. *Journal of Fluids and Structures*, 27(3):367–382.

Hassan, Y. and Barsamian, H. (2004). Tube bundle flows with the large eddy simulation technique in curvilinear coordinates. *International Journal of Heat and Mass Transfer*, 47(14):3057–3071.

Heilker, W. and Vincent, R. (1981). Vibration in nuclear heat exchangers due to liquid and two-phase flow. *Journal of Engineering for Gas Turbines and Power*, 103(2):358–366.

Hodge, R., LeSurf, J., and Hilborn, J. (1974). Steam generator reliability: the canadian approach. Technical report, Chalk River Nuclear Labs., Ont.

Holmes, P., Berkooz, G., and Lumley, J. L. (1990). Turbulence, dynamical systems and the unreasonable effectiveness of empirical eigenfunctions. In *Proceedings of the International Congress of Mathematicians, Kyoto*, pages 1607–1617.

Iemma, U. and Gennaretti, M. (2005). Reduced-order modeling for linearized aeroelasticity of fixed wings in transonic flight. *Journal of fluids and structures*, 21(3):243–255.

Joseph, D. D. (1976). Stability of fluid motions. i, ii. *NASA STI/Recon Technical Report A*, 77:12423.

Kakaç, S., Liu, H., and Pramuanjaroenkij, A. (2002). *Heat Exchangers: Selection, Rating, and Thermal Design, Second Edition*. Designing for heat transfer. Taylor & Francis.

Kalashnikova, I., Barone, M., and Brake, M. (2013). A stable galerkin reduced order model for coupled fluid-structure interaction problems. *International Journal for Numerical Methods in Engineering*, 95(2):121–144.

Kassera, V. and Strohmeier, K. (1997). Simulation of tube bundle vibrations induced by cross-flow. *Journal of fluids and structures*, 11(8):909–928.

Kevlahan, N.-R. (2011). The role of vortex wake dynamics in the flow-induced vibration of tube arrays. *Journal of Fluids and Structures*, 27(5):829–837.

Khalak, A. and Williamson, C. (1997). Fluid forces and dynamics of a hydroelastic structure with very low mass and damping. *Journal of Fluids and Structures*, 11(8):973–982.

Khalak, A. and Williamson, C. (1999). Motions, forces and mode transitions in vortex-induced vibrations at low mass-damping. *Journal of fluids and Structures*, 13(7):813–851.

Khalifa, A., Weaver, D., and Ziada, S. (2012). A single flexible tube in a rigid array as a model for fluidelastic instability in tube bundles. *Journal of Fluids and Structures*, 34:14–32.

Khalifa, A., Weaver, D., and Ziada, S. (2013). Modeling of the phase lag causing fluidelastic instability in a parallel triangular tube array. *Journal of Fluids and Structures*, 43:371–384.

Kunisch, K. and Volkwein, S. (2002). Galerkin proper orthogonal decomposition methods for a general equation in fluid dynamics. *SIAM Journal on Numerical analysis*, 40(2):492–515.

Lanczos, C. (1950). An iteration method for the solution of the eigenvalue problem of linear differential and integral operators1. *Journal of Research of the National Bureau of Standards*, 45(4).

Lassila, T. and Rozza, G. (2010). Reduced formulation of a steady fluid-structure interaction problem with parametric coupling. *arXiv preprint arXiv:1005.3384*.

Lassila, T. M., Manzoni, A., Quarteroni, A., and Rozza, G. (2013). Model order reduction in fluid dynamics: challenges and perspectives. In Quarteroni, A. and Rozza, G., editors, *Reduced Order Methods for modeling and computational reduction*, MS&A, pages 235–273. Springer, Milano. EPFL MATHICSE report 22.2013.

Launder, B. and Sharma, B. (1974). Application of the energy-dissipation model of turbulence to the calculation of flow near a spinning disc. *Letters in heat and mass transfer*, 1(2):131–137.

Launder, B. E. and Spalding, D. (1974). The numerical computation of turbulent flows. *Computer methods in applied mechanics and engineering*, 3(2):269–289.

Laurence, D., Uribe, J., and Utyuzhnikov, S. (2005). A robust formulation of the v2- f model. *Flow, Turbulence and Combustion*, 73(3-4):169–185.

Lever, J. and Weaver, D. (1982). A theoretical model for fluid-elastic instability in heat exchanger tube bundles. *Journal of Pressure Vessel Technology*, 104(3):147–158.

Lever, J. and Weaver, D. (1986a). On the stability of heat exchanger tube bundles, part i: Modified theoretical model. *Journal of Sound and vibration*, 107(3):375–392.

Lever, J. and Weaver, D. (1986b). On the stability of heat exchanger tube bundles, part ii: Numerical results and comparison with experiments. *Journal of Sound and Vibration*, 107(3):393 – 410.

Li, D., Tan, S., and McGaughy, B. (2008). Etbr: Extended truncated balanced realization method for on-chip power grid network analysis. In *Design, Automation and Test in Europe, 2008.*, pages 432–437.

Li, X., Wu, X., and He, S. (2014). Numerical investigation of the turbulent cross flow and heat transfer in a wall bounded tube bundle. *International Journal of Thermal Sciences*, 75:127–139.

Liang, C. and Papadakis, G. (2007). Large eddy simulation of cross-flow through a staggered tube bundle at subcritical reynolds number. *Journal of Fluids and Structures*, 23(8):1215–1230.

Liberge, E. and Hamdouni, A. (2010). Reduced order modelling method via proper orthogonal decomposition (pod) for flow around an oscillating cylinder. *Journal of Fluids and Structures*, 26(2):292–311.

Lieu, T., Farhat, C., and Lesoinne, M. (2006). Reduced-order fluid/structure modeling of a complete aircraft configuration. *Computer methods in applied mechanics and engineering*, 195(41):5730–5742.

Longatte, E., Bendjeddou, Z., and Souli, M. (2003). Methods for numerical study of tube bundle vibrations in cross-flows. *Journal of Fluids and Structures*, 18(5):513–528.

Lucia, D. J., Beran, P. S., and Silva, W. A. (2004). Reduced-order modeling: new approaches for computational physics. *Progress in Aerospace Sciences*, 40(1):51–117.

Lumley, J. L. (1967). The Structure of Inhomogeneous Turbulent Flows. In Yaglom, A. M. and Tatarski, V. I., editors, *Atmospheric turbulence and radio propagation*, pages 166–178. Nauka, Moscow.

Ma, X. and Karniadakis, G. E. (2002). A low-dimensional model for simulating three-dimensional cylinder flow. *Journal of Fluid Mechanics*, 458:181–190.

Mahon, J. and Meskell, C. (2009). Surface pressure distribution survey in normal triangular tube arrays. *Journal of Fluids and Structures*, 25(8):1348–1368.

Mahon, J. and Meskell, C. (2012). Surface pressure survey in a parallel triangular tube array. *Journal of Fluids and Structures*, 34:123–137.

Manceau, R. (2015). Leacture notes on industrial codes for cfd. , pages 1–234.

Menter, F. R. (1994). Two-equation eddy-viscosity turbulence models for engineering applications. *AIAA journal*, 32(8):1598–1605.

Moore, B. (1981a). Principal component analysis in linear systems: Controllability, observability, and model reduction. *Automatic Control, IEEE Transactions on*, 26(1):17–32.

Moore, B. C. (1981b). Principal component analysis in linear systems: Controllability, observability, and model reduction. *Automatic Control, IEEE Transactions on*, 26(1):17–32.

Moretti, P. and Lowery, R. (1976). Hydrodynamic inertia coefficients for a tube surrounded by rigid tubes. *Journal of Pressure Vessel Technology*, 98(3):190–193.

Morzynski, M., Stankiewicz, W., Noack, B. R., Thiele, F., King, R., and Tadmor, G. (2006). Generalized mean-field model for flow control using a continuous mode interpolation. In *Proceedings of the Third AIAA Flow Control Conference*, pages 1–11.

Nelms, H. and Segaser, C. (1969). Survey of nuclear reactor system primary circuit heat exchangers. Technical report, Oak Ridge National Lab., Tenn.

Nicolet, J., Sagner, M., and Regis, G. (1976). Vibrations de faisceaux de tubes sous excitation aerodynamique. *Revue Générale de Thermique*, 128:869–891.

Noack, B. R., Afanasiev, K., Morzynski, M., Tadmor, G., and Thiele, F. (2003). A hierarchy of low-dimensional models for the transient and post-transient cylinder wake. *Journal of Fluid Mechanics*, 497:335–363.

Noack, B. R. and Eckelmann, H. (1994). A low-dimensional galerkin method for the three-dimensional flow around a circular cylinder. *Physics of Fluids (1994-present)*, 6(1):124–143.

Noack, B. R., Morzynski, M., and Tadmor, G. (2011). *Reduced-order modelling for flow control*, volume 528. Springer.

Noack, B. R., Papas, P., and Monkewitz, P. A. (2005). The need for a pressure-term representation in empirical galerkin models of incompressible shear flows. *Journal of Fluid Mechanics*, 523:339–365.

Odabasioglu, A., Celik, M., and Pileggi, L. T. (1997). Prima: passive reduced-order interconnect macromodeling algorithm. In *Proceedings of the 1997 IEEE/ACM international conference on Computer-aided design*, pages 58–65. IEEE Computer Society.

Oengören, A. and Ziada, S. (1992). Vorticity shedding and acoustic resonance in an in-line tube bundle part ii: Acoustic resonance. *Journal of Fluids and structures*, 6(3):293–309.

Owen, P. (1965). Buffeting excitation of boiler tube vibration. *Journal of Mechanical Engineering Science*, 7(4):431–439.

Païdoussis, M. (1981). Fluidelastic vibration of cylinder arrays in axial and cross flow: state of the art. *Journal of Sound and Vibration*, 76(3):329–360.

Païdoussis, M. (1982). Flow-induced vibration of cylindrical structures: a review of the state of the art. Technical report, McGill Univ., Montreal, Quebec (Canada).

Païdoussis, M. (1983a). A review of flow-induced vibrations in reactors and reactor components. *Nuclear Engineering and Design*, 74(1):31 – 60.

Païdoussis, M. (1983b). A review of flow-induced vibrations in reactors and reactor components. *Nuclear Engineering and Design*, 74(1):31–60.

Païdoussis, M. et al. (2006). Real-life experiences with flow-induced vibration. *Journal of fluids and structures*, 22(6):741–755.

Païdoussis, M., Price, S., Nakamura, T., Mark, B., and Mureithi, W. N. (1989). Flow-induced vibrations and instabilities in a rotated-square cylinder array in cross-flow. *Journal of Fluids and Structures*, 3(3):229–254.

Païdoussis, M. P., Price, S. J., and De Langre, E. (2010). *Fluid-structure interactions: Cross-flow-induced instabilities*. Cambridge University Press.

Parker, R. (1978). Acoustic resonances in passages containing banks of heat exchanger tubes. *Journal of Sound and Vibration*, 57(2):245–260.

Patankar, S. V. and Spalding, D. B. (1972). A calculation procedure for heat, mass and momentum transfer in three-dimensional parabolic flows. *International Journal of Heat and Mass Transfer*, 15(10):1787–1806.

Pettigrew, M. and Gorman, D. (1973). Experimental studies on flow induced vibration to support steam generator design. In *Proc. Int. Symp. on Vibration Problems in Industry*, pages 1–20.

Pettigrew, M. and Gorman, D., editors (1978). *Vibration of heat exchanger tube bundles in liquid and two-phase cross-flow*.

Pettigrew, M., Platten, J., and Sylvestre, Y. (1973). Experimental studies on flow induced vibration to support steam generator design. In *Proc. Int. Symp. on Vibration Problems in Industry*, pages 1–20.

Pettigrew, M., Sylvestre, Y., and Campagna, A. (1978). Vibration analysis of heat exchanger and steam generator designs. *Nuclear Engineering and Design*, 48(1):97–115.

Pettigrew, M. and Taylor, C. (1991). Fluidelastic instability of heat exchanger tube bundles: review and design recommendations. *Journal of pressure vessel technology*, 113(2):242–256.

Phillips, J. R. (2003). Projection-based approaches for model reduction of weakly nonlinear, time-varying systems. *Computer-Aided Design of Integrated Circuits and Systems, IEEE Transactions on*, 22(2):171–187.

Pillage, L. T., Rohrer, R., et al. (1990). Asymptotic waveform evaluation for timing analysis. *Computer-Aided Design of Integrated Circuits and Systems, IEEE Transactions on*, 9(4):352–366.

Polak, D. and Weaver, D. (1995). Vortex shedding in normal triangular tube arrays. *Journal of Fluids and Structures*, 9(1):1–17.

Pope, S. B. (2000). *Turbulent flows*. Cambridge university press.

Popp, K. and Romberg, O. (1998). Tube bundle vibrations due to cross flow under the influence of turbulence. In Rath, H. and Egbers, C., editors, *Advances in Fluid Mechanics and Turbomachinery*, pages 99–114. Springer Berlin Heidelberg.

Price, S. (1995). A review of theoretical models for fluidelastic instability of cylinder arrays in cross-flow. *Journal of Fluids and Structures*, 9(5):463–518.

Price, S. and Kuran, S. (1991). Fluidelastic stability of a rotated square array with multiple flexible cylinders, subject to cross-flow. *Journal of fluids and structures*, 5(5):551–572.

Price, S. and Païdoussis, M. (1983). Fluidelastic instability of an infinite double row of circular cylinders subject to a uniform cross-flow. *Journal of Vibration and Acoustics*, 105(1):59–66.

Price, S. and Païdoussis, M. (1984). An improved mathematical model for the stability of cylinder rows subject to cross-flow. *Journal of Sound and Vibration*, 97(4):615–640.

Price, S. and Païdoussis, M. (1986a). A constrained-mode analysis of the fluidelastic instability of a double row of flexible circular cylinders subject to cross-flow: A theoretical investigation of system parameters. *Journal of sound and Vibration*, 105(1):121–142.

Price, S. and Païdoussis, M. (1986b). A single-flexible-cylinder analysis for the fluidelastic instability of an array of flexible cylinders in cross-flow. *Journal of Fluids Engineering*, 108(2):193–199.

Price, S. and Païdoussis, M. (1989). The flow-induced response of a single flexible cylinder in an in-line array of rigid cylinders. *Journal of fluids and structures*, 3(1):61–82.

Raveh, D. E. (2005). Computational-fluid-dynamics-based aeroelastic analysis and structural design opimization – a researcher's perspective. *Computer Methods in Applied Mechanics and Engineering*, 194(30-33):3453–3471. Structural and Design Optimization.

Rempfer, D. (2000). On low-dimensional galerkin models for fluid flow. *Theoretical and Computational Fluid Dynamics*, 14(2):75–88.

Roberts, B. (1966). *Low Frequency, Aeroelastic Vibrations in a Cascade of Circular Cylinders*. Mechanical engineering science. Institution of Mechanical Engineers.

Roberts, B. W. (1962). *Low Frequency, self-excited vibration in a row of circular cylinders mounted in an airstream*. PhD thesis, University of Cambridge.

Rollet-Miet, P., Laurence, D., and Ferziger, J. (1999). Les and rans of turbulent flow in tube bundles. *International Journal of Heat and Fluid Flow*, 20(3):241–254.

Romberg, O. and Popp, K. (1998). The influence of upstream turbulence on the stability boundaries of a flexible tube in a bundle. *Journal of fluids and structures*, 12(2):153–169.

Rotta, J. (1951). Statistische theorie nichthomogener turbulenz. *Zeitschrift für Physik*, 129(6):547–572.

Rottmann, M. and Popp, K. (2003). Influence of upstream turbulence on the fluidelastic instability of a parallel triangular tube bundle. *Journal of fluids and structures*, 18(5):595–612.

Rowley, C. W., Colonius, T., and Murray, R. M. (2004). Model reduction for compressible flows using pod and galerkin projection. *Physica D: Nonlinear Phenomena*, 189(1):115–129.

Rowley, C. W., MEZIĆ, I., Bagheri, S., Schlatter, P., and Henningson, D. S. (2009). Spectral analysis of nonlinear flows. *Journal of Fluid Mechanics*, 641:115–127.

Schilders, W. H., Van der Vorst, H. A., and Rommes, J. (2008). *Model order reduction: theory, research aspects and applications*, volume 13. Springer.

Schmid, P. J. (2010). Dynamic mode decomposition of numerical and experimental data. *Journal of Fluid Mechanics*, 656:5–28.

Schröder, K. and Gelbe, H. (1999). Two-and three-dimensional cfd-simulation of flow-induced vibration excitation in tube bundles. *Chemical Engineering and Processing: Process Intensification*, 38(4):621–629.

Shin, Y. and Wambsganss, M. (1977). Flow-induced vibration in lmfbr steam generators: a state-of-the-art review. *Nuclear Engineering and Design*, 40(2):235–284.

Shinde, V., Marcel, T., Hoarau, Y., Deloze, T., Harran, G., Baj, F., Cardolaccia, J., Magnaud, J.-P., Longatte, E., and Braza, M. (2014). Numerical simulation of the fluid–structure interaction in a tube array under cross flow at moderate and high reynolds number. *Journal of Fluids and Structures*, 47:99–113.

Silva, W. A. and Bartels, R. E. (2004). Development of reduced-order models for aeroelastic analysis and flutter prediction using the cfl3dv6. 0 code. *Journal of Fluids and Structures*, 19(6):729–745.

Singh, K. P. and Soler, A. I. (1984). *Mechanical design of heat exchangers and pressure vessel components*. Springer Science & Business Media.

Sirisup, S. and Karniadakis, G. (2004). A spectral viscosity method for correcting the long-term behavior of pod models. *Journal of Computational Physics*, 194(1):92–116.

Sirisup, S. and Karniadakis, G. (2005). Stability and accuracy of periodic flow solutions obtained by a pod-penalty method. *Physica D: Nonlinear Phenomena*, 202(3):218–237.

Sirovich, L. (1987). Turbulence and the dynamics of coherent structures. part i: Coherent structures. *Quaterly of Applied Mathematics*, XLV(3):561–571.

Smagorinsky, J. (1963). General circulation experiments with the primitive equations: I. the basic experiment*. *Monthly weather review*, 91(3):99–164.

Southworth, P. and Zdravkovich, M. (1975). Cross-flow-induced vibrations of finite tube banks in in-line arrangements. *Journal of Mechanical Engineering Science*, 17(4):190–198.

Takahara, S. and Ohta, K. (1982). Flow-induced vibration of tube arrays with various pitch-to-diameter ratios. *Journal of Pressure Vessel Technology*, 104:169.

Tanaka, H. and Takahara, S. (1980). Unsteady fluid dynamic force on tube bundle and its dynamic effect on vibration. In *ASME century 2 emerging technology conference*, pages 77–92.

Tanaka, H. and Takahara, S. (1981). Fluid elastic vibration of tube array in cross flow. *Journal of sound and vibration*, 77(1):19–37.

Tanaka, H., Tanaka, K., Shimizu, F., and Takahara, S. (2002). Fluidelastic analysis of tube bundle vibration in cross-flow. *Journal of fluids and structures*, 16(1):93–112.

Teh, C. and Goyder, H. (1981). Measurement of vibratory fluid forces on a tube in a bundle subjected to crossflow. *Atomic Energy Research Establishment Report AERE*, 11259.

Turkel, E., Vatsa, V. N., and Radespiel, R. (1996). Preconditioning methods for low-speed flows. *National Aeronautics and Space Administration*. NASA CR 201605.

Vierendeels, J., Lanoye, L., Degroote, J., and Verdonck, P. (2007). Implicit coupling of partitioned fluid-structure interaction problems with reduced order models. *Comput. Struct.*, 85(11-14):970–976.

Wallin, S. and Johansson, A. V. (2000). An explicit algebraic reynolds stress model for incompressible and compressible turbulent flows. *Journal of Fluid Mechanics*, 403:89–132.

Weaver, D. and El-Kashlan, M. (1981). The effect of damping and mass ratio on the stability of a tube bank. *Journal of Sound and Vibration*, 76(2):283–294.

Weaver, D. and Fitzpatrick, J. (1988a). A review of cross-flow induced vibrations in heat exchanger tube arrays†. *Journal of Fluids and Structures*, 2(1):73 – 93.

Weaver, D., Fitzpatrick, J., and ElKashlan, M. (1987). Strouhal numbers for heat exchanger tube arrays in cross flow. *Journal of pressure vessel technology*, 109(2):219–223.

Weaver, D. and Grover, L. (1978). Cross-flow induced vibrations in a tube bank—turbulent buffeting and fluid elastic instability. *Journal of Sound and Vibration*, 59(2):277–294.

Weaver, D. and Lever, J. (1977). Tube frequency effects on cross flow induced vibrations in tube arrays. In *Proceedings of the Fifth Biennial Symposium on Turbulence*, volume 1, pages 323–331. University of Missouri-Rolla Rolla, Missouri.

Weaver, D. and Yeung, H. (1984). The effect of tube mass on the flow induced response of various tube arrays in water. *Journal of Sound and Vibration*, 93(3):409–425.

Weaver, D. t. and Fitzpatrick, J. (1988b). A review of cross-flow induced vibrations in heat exchanger tube arrays. *Journal of Fluids and Structures*, 2(1):73–93.

Whiston, G. and Thomas, G. (1982). Whirling instabilities in heat exchanger tube arrays. *Journal of Sound and Vibration*, 81(1):1–31.

Wilcox, D. C. (1988). Reassessment of the scale-determining equation for advanced turbulence models. *AIAA journal*, 26(11):1299–1310.

Williamson, C. and Govardhan, R. (2004). Vortex-induced vibrations. *Annu. Rev. Fluid Mech.*, 36:413–455.

Wu, B. (2014). A correction of the half-power bandwidth method for estimating damping. *Archive of Applied Mechanics*, 85(2):315–320.

Yetisir, M. and Weaver, D. (1988). On an unsteady theory for fluidelastic instability of heat exchanger tube arrays. In *1988 International Symposium on Flow-Induced Vibrations and Noise*, volume 3, pages 181–195.

Yetisir, M. and Weaver, D. (1993a). An unsteady theory for fluidelastic instability in an array of flexible tubes in cross-flow. part i: Theory. *Journal of Fluids and Structures*, 7(7):751–766.

Yetisir, M. and Weaver, D. (1993b). An unsteady theory for fluidelastic instability in an array of flexible tubes in cross-flow. part ii: Results and comparison with experiments. *Journal of Fluids and Structures*, 7(7):767–782.

Ziada, S. (2006). Vorticity shedding and acoustic resonance in tube bundles. *Journal of the Brazilian Society of Mechanical Sciences and Engineering*, 28(2):186–189.

Ziada, S. et al. (1998). An in-depth study of vortex shedding, acoustic resonance and turbulent forces in normal triangle tube arrays. *Journal of Fluids and Structures*, 12(6):717–758.

Ziada, S. and Oengören, A. (1992). Vorticity shedding and acoustic resonance in an in-line tube bundle part i: Vorticity shedding. *Journal of Fluids and structures*, 6(3):271–292.

Ziada, S. and Oengören, A. (1993). Vortex shedding in an in-line tube bundle with large tube spacings. *Journal of Fluids and Structures*, 7(6):661–687.

Ziada, S. and Oengören, A. (2000). Flow periodicity and acoustic resonance in parallel triangle tube bundles. *Journal of Fluids and Structures*, 14(2):197–219.

Ziada, S., Oengören, A., and Bühlmann, E. (1989a). On acoustical resonance in tube arrays part i: Experiments. *Journal of Fluids and Structures*, 3(3):293–314.

Ziada, S., Oengören, A., and Bühlmann, E. (1989b). On acoustical resonance in tube arrays part ii: Damping criteria. *Journal of Fluids and Structures*, 3(3):315–324.

Ziada, S. and Rockwell, D. (1982). Generation of higher harmonics in a self-oscillating mixing layer-wedge system. *AIAA Journal*, 20(2):196–202.